EVIDENCE OF LEFT VENTRICULAR WALL MOVEMENT ACTIVELY DECELERTING AORTIC BLOOD FLOW

A thesis submitted for the degree of Doctor of Philosophy

By
Chloe May Page
Brunel Institute for Bioengineering

Brunel University

August 2009

Declaration of Authenticity

I hereby declare that the work presented in this thesis is my own.

Chloe Page

Abstract

Efficient function of the left ventricle (LV) is achieved by coherent behaviour of its circumferential and longitudinal myocardial components. Little was known about the direct association between the long and minor axis velocities and the overall haemodynamics generated by ventricular systolic function such as aortic waves.

The forward running expansion wave (FEW) during late systole contains important information about the condition of the LV and its interaction with the arterial system. The aim of this thesis was to underpin the mechanics and timing of the LV wall velocities, which are associated with the deceleration of flow. Both invasive and non-invasive data have been analysed in canines and humans and the following conclusions can be drawn.

LV long axis peak shortening velocity lags consistently behind the minor axis, representing a degree of normal asynchrony. The FEW is seen to have a slow onset before a rapid increase in energy. The slow onset corresponds with the time that the long axis reaches its peak velocity of shortening. After both axes reach their respective maximum shortening velocity they continue to contract, although at a slow steady velocity until late ejection when there is a sudden simultaneous change of shortening velocity of both axes. This time corresponds with peak aortic pressure and the rapid increase in energy of the FEW. The time that the minor axis reaches its maximum velocity of shortening interestingly coincides with the arrival of the reflected wave at the LV during mid-systole. During canine aortic manipulation through the introduction of total occlusions along the aorta, the sequence of events observed in control conditions remains unchanged.

In humans both LV wall movement and carotid wave intensity can be measured successfully using non-invasive methods. The FEW is generated when the last long axis segment begins to slow. The minor axis begins to slow before this time and corresponds to the time of peak aortic flow.

Acknowledgements

I would like to mention a number of people who have made writing this thesis possible for me. Firstly I would like to thank my mum and dad for all their help and support. I would also like to thank my husband Mike for putting up with me while I wrote this thesis.

I would like to thank Dr Ashraf Khir for giving me the opportunity to study towards a PhD and for being there when I needed guidance. I am very grateful for the canine data that makes up the bulk of this thesis.

I have very much enjoyed being a part of the Brunel Institute for Bioengineering, where I always felt very welcome. I especially would like to thank Giovanni, Marcel, Jiling, Lyn and Christina for being great friends.

I would additionally like to thank Professor Alun Hughes and Professor Kim Parker for their words of wisdom when I needed them.

Special thanks to Katherine March, Dr Justin Davies and Dr Nearchos Hadjiloizou for collecting all the human data for me and having the patience to deal with my many questions.

Contents

List of Figures

List of Tables

List of equations

Chapter 1:
Background Information

1.1 Introduction

Cardiovascular disease is the largest cause of mortality in the western world. In the United Kingdom alone more than 1 out of every 3 people (35%) will die of cardiovascular disease (CVD) (British Heart foundation website) and CVD is responsible for 48% of all deaths in Europe (Allender at al. 2008). To successfully prevent, treat and manage all CVD cases it is vital to understand how the cardiovascular system works both in normal conditions and in disease. The flow of blood within the circulation (haemodynamics) is critical to the nutrition recovery rate of the cardiovascular system. The following literature review will examine a variety of techniques that have been developed to quantify haemodynamics and will discuss the key findings to date.

1.2 The heart

1.2.1 Structure

The heart is comprised of 4 chambers: The right atrium (RA), left atrium (LA), right ventricle (RV) and left ventricle (LV). All chambers are enclosed within the fluid filled pericardium and their wall myoarchitecture consists of several layers: the outer obliquely arranged epicardium, circular myocardium and innermost longitudinally arranged endocardium (Pettigrew 1865). The layers of the wall have been studied for centuries, dating back to William Harvey (1628), Stensen (1664), Winslow (1711) and Senac (1749). These investigations revealed that the epicardium and endocardium are arranged in a helical manner while the mid-myocardial fibres are more circumferential. More recently Torrent Guasp (2005) has suggested that cardiac muscle fibres adopt a twisted rope or figure of eight configuration, this suggestion, while not universally accepted is provocative and attractive.

1.2.2 Electrical sequence

The electrical activity of the heart has been investigated since the late 19th century and is the most widely measured cardiac function in clinical practise. The electrical sequence of the heart can be interpreted due to the development of the electrocardiogram (ECG). The interpretation of an ECG was made possible by the breakthrough Nobel Prize winning investigations of Willem Einthoven in 1901 in which he assigned the letters P, Q, R, S and

T to describe the different waves. This notation is still used today. **Figure 1.1**. Electrical activity begins in the RA at the natural pacemaker known as the sino-atrial (SA) node; the electrical impulse is conducted to the atrioventricular node (AV). Atrial excitation is evident as the P wave in the ECG and depolarization of the atrial myocytes results in atrial contraction which contributes to ventricular filling. Electrical depolarization is conducted via the AV node and the bundle of His to the apex of the fascicular branches, which lead to the Purkinje fibres found beneath the endocardium of the ventricle walls. There are three bundle branches (the right anterior bundles and the left anterior and posterior bundle branches) that assist conduct of depolarization within the ventricle. The LV myocardial wall is first activated at the septal and anterior free wall. The activation sequence then travels from the apex to the base (Scher AM 1995). Ventricular depolarisation during the cycle produces electrical gradients that result in the QRS complex of the ECG. The T wave represents ventricular repolarisation. ECG recordings can be used to diagnose many cardiac problems and a high-quality ECG recording is also a very important part of research as the R wave is often used as a reference point indicating the start of electrical systole.

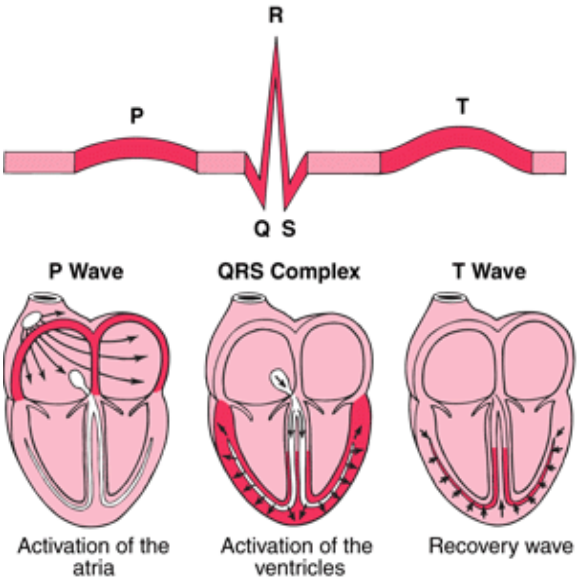

Figure 1.1: A typical ECG recording showing the pressure (P) wave representing activation of the atria, the QRS complex representing activation of the ventricles and the T wave representing depolarisation of the ventricles. Taken from www.merck.com

1.3 The left ventricle

In 1628 William Harvey suggested that LV fibre orientation had a functional significance (Harvey W. 1976). The form and function of the LV are now considered inseparable attributes. Global myocardial performance cannot be fully understood without the knowledge of regional LV structure. The LV is described as prolate ellipsoidal in shape with a central transmurual continuum surrounded by two helical arrangements where subendocardial fibres in the right helix graduate into subepicardial fibres in the left helix (Sengaputa et al. 2000). Fibre orientation is a function of location; longitudinal fibres are more predominant in the endocardium and epicardium while circumferential fibres are located mainly in the mid-wall region (Sengaputa et al. 2007). This is demonstrated in **Figure 1.2.**

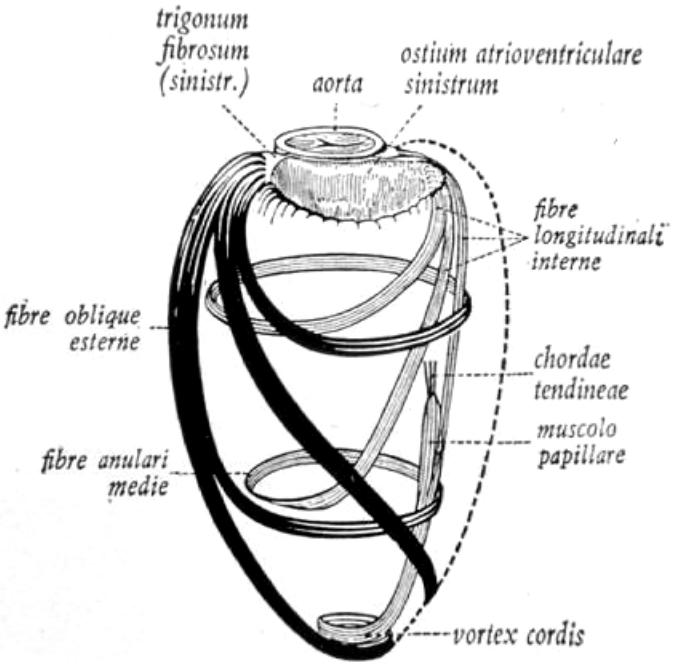

Figure 1.2: A diagram showing the fibre orientation of the left ventricle (LV). The inner fibres (fibre longitudinale interne) and superficial fibres (fibre oblique esterne) are longitudinally arranged. While the fibres in the myocardial mid wall (ibre anulri medie) are circumferentially arranged. The image can be located at www.biomed.brown.edu and http://www.natureinstitute.org/pub/ic/ic7/heart.htm

The LV walls are not uniform, the septum is significantly thinner than the posterolateral wall and the LV base is the thickest circumferential fibre region. Mid-wall fibres become progressively thinner as they progress from the base towards the apex (Greenbaum et al. 1981), however strain rates are greater at the apex than the base. Strain rate is a measure of global deformation. The long axis runs from the apex to the base of the LV and the short axis runs from the septum to the free wall. Circumferential fibres make up the majority of the LV short axis and as they are more abundant than longitudinal fibres it would be logical to assume that the extent and velocity of their shortening would control myocardial performance (Henein and Gibson 1999a). However, the dimensional fall of the short axis during ejection was found to be 15-20% greater than that of the shortening ability of a normally loaded sarcomere (Heinen and Gibson 1999a). The percentage of posterior wall thickening is also much more than expected. The only explanation for this increase in myocardial mass is the additional shortening and transverse thickening of the longitudinal fibres (Henein and Gibson 1999a). In the ventricle the interrelated longitudinally and circumferentially orientated myocardial fibres work together to give co-ordinated LV contraction. The circumferential fibres are responsible for transverse shortening and the longitudinal fibres enable the movement of the mitral annulus towards the apex. Even though the longitudinal fibres only comprise a small percentage of the myocardial mass they are now recognised to play a major role in maintaining normal ejection fraction and changes in LV shape (Henein and Gibson 1999a, Henein and Gibson 1999b). A strong correlation has been observed between impaired LV ejection fraction and reduction in long axis function in a variety of disease states (Henein and Gibson 1999b).

Normal changes along the short axis during ejection are dependent on both circumferential and longitudinal fibres; however long axis shortening is only dependent on longitudinal fibres. While the short axis shortens by 25% the long axis only shortens by 10-12% (Rushmer 1952, Hawthorne 1961). This asymmetry is responsible for the loss of spherical LV cavity shape during ejection. The LV also rotates and twists during ejection due the spiral arrangement of the myofibres (Sengaputa et al. 2007). During isovolumic contraction the subenodcardial fibres shorten while the subepicardial fibres stretch resulting in clockwise rotation of the LV (Sengaputa et al 2005). During ejection the subepicardial fibres dominate and the base rotates clockwise as the apex rotates anti-clockwise resulting

in a ‘wringing’ motion (Ingels et al 1989, Taber et al 1996). Unlike during ejection when myofibres in each helix shorten from the apex to the base the helixes relax in opposite directions. During isovolumic relaxation the right-handed helix relaxes from the apex to the base while the left-handed helix relaxes from the base to the apex. The twisted fibres recoil resulting in a clockwise rotation. The recoil releases stored potential energy that when combined with the different directions of relaxation creates a transmural gradient, which aids diastolic filling (Taber et al. 1996, Davis et al. 2001). It is evident from these findings that LV structure has a direct and dramatic effect on its function. In a normal LV the counter-directional helical arrangement enables strain to be distributed in an energy efficient manner (Sengaputa et al. 2000). Any alterations in fibre orientation and shortening ability decrease optimal energy transfer from the LV wall to the blood. Structural disorganisation of the LV associated with a variety of disease states such as ventricular hypertrophy and coronary ischemia leads to impaired cardiac function (Greenbaum et al. 1981).

1.4 Left ventricle wall movement measurement: Echocardiography

Echocardiography is one of the most commonly used procedures in cardiology and provides valuable insights into cardiac structure and function in health and disease. Since the fifties and sixties when Edler (1955) first displayed A-mode and M-mode ultrasound images of bovine hearts and Bom et al. (1974) developed the first linear array transducers, 2D M-mode and B-mode echocardiography have been increasingly used to assess the size and shape of the heart, the spatial relationship of its structures and to look for abnormal wall and valve motion (Edler 1955, Edler and Gustafson 1957, Popp et al. 1969, Born et al. 1974, Heger et al. 1979, Picard 2008). In more recent years a variety of new technologies have been established that can provide a wealth of additional diagnostic information. (Picard 2008).

Doppler echocardiography can detect the velocity and direction of both blood flow and wall movement. Myocardial velocities can be analysed by pulsed wave (PW), and colour Tissue Doppler Imaging (TDI). TDI is slowly being introduced to supplement the conventional techniques. TDI has the potential to evaluate both regional and global wall motion in a more quantitative way (Yu et al. 2007, Price et al. 2000).

TDI relies on the same principle as all Doppler echocardiography; it requires the detection of the shift in frequency of ultrasound signals that are reflected from the object of interest (Ho and Soloman 2006). Unlike conventional Doppler echocardiography which detects low amplitude, high-velocity red-blood cells, TDI measures high amplitude, low-velocity signals reflected from myocardial tissue motion. Using TDI permits the calculation of radial and longitudinal, systolic and diastolic function in addition to the haemodynamics of filling. While M-mode echocardiography can be used to measure the displacement distance of the base from the apex as a marker of systolic function TDI can measure the rate of displacement. Wall speed measurements are made at different sites and averages are calculated to give global LV function. Regional LV function can also be analysed by measurements of segmental wall velocity. Regional dysfunction can be easily detected this way. TDI velocities are related to the rate of wall thickening and overall cardiac movement.

A shortcoming of TDI is that abnormal function in one LV segment affects the function in other segments. Strain-rate imaging is a method of overcoming this limitation (Smiseth and Ihlen 2003). Strain is the percentage of LV deformation and strain-rate is the velocity of this deformation. A negative strain indicates shortening and thickening of fibres and a positive strain indicates lengthening and thinning. Longitudinal strain rate is calculated from the regional shortening fraction and circumferential strain rate is measured from myocardial thickening. Strain rate measured by tissue Doppler (Urheim et al. 2000) enables quantification of LV segments and can detect akinetic segments and regional myocardial ischemia.

A further limitation to Doppler based studies is their dependency on angle (Price 2000). A newer non-angle dependent technique known as speckle tracking echocardiography (STE) can also be used to calculate strain rates in addition to the assessment of LV rotation (Teske et al. 2007, Edvardsen et al. 2006, Helle-Valle et al. 2005). Speckles are acoustic markers arising from ultrasound interference back scattered from structures smaller than the wavelength of the applied ultrasound. They are distributed in a certain pattern over the myocardium as seen clearly with conventional grey B-mode ultrasound and can be followed throughout the cardiac cycle. Speckle tracking can be used to calculate strain, strain-rate, velocities and displacement (Edvardsen et al. 2006). STE directly measures

myocardial deformation in the longitudinal and short axis and is a quick angle independent method to assess systolic and diastolic heart function.

More recently real-time 3-D echocardiography has been introduced. It can be used in conjunction with strain and speckle tracking techniques (Fonseca et al. 2004) which have already provided numerous insights into the structure and function of the heart (Binder 2002, Monaghn 2006, Lang et al. 2006, Picard et al.2007), especially at a regional level but until recently this method has only be used in combination with limited 2-D echocardiography, and time consuming MRI tissue tagging (Edvardsen et al. 2000, Moore et al. 2000). The use of real-time 3-D echocardiography is the next step forward and will solve the shortcomings of previous methods. 3-D echocardiography has significantly advanced both the accuracy and reproducibility of cardiac assessment (Galderis et al. 2007, Sugeng et al. 2006). Quantification of LV volume, mass and ejection fraction no longer rely on inaccurate modelling and 3-D echocardiography generates fast, reliable and reproducible results, which should ensure that 3D imaging is integrated into routine examinations. When combined with real time 3-D imaging, 3-D speckle tracking can provide a much more comprehensive visualisation of both regional and global LV function. The future of echocardiography is very exciting.

1.5 Blood flow in vessels

1.5.1 Arterial system models

For centuries the intricate structure, mechanisms and physiology of the cardiovascular system have attracted vast interest. It is universally recognised that blood flows around the body in a continuous circular pathway (Harvey 1976) and that blood pressure and flow in the arteries is pulsatile. Numerous techniques have been developed over the years to both measure and analyse the characteristic shapes of pressure and flow waveforms. The human cardiovascular system is a complex 3 dimensional structure that behaves in a non-linear manner; and currently a comprehensive numerical model based on a complete solution of the Navier Stokes equations for the entire circulation is not feasible. The analysis of the arterial system is therefore often simplified by using lower order-dimensional linear (and occasionally non-linear) models.

The first example of a simplified model of the circulation is the air chamber or Windkessel, which was originally proposed by Stephen Hales in 1733 and later formulated mathematically by Otto Frank in 1899 (Frank 1899). This model was inspired by the pumps in ancient fire engines as shown in **Figure 1.3** that converted intermittent pumping into relatively steady flow by means of an air chamber.

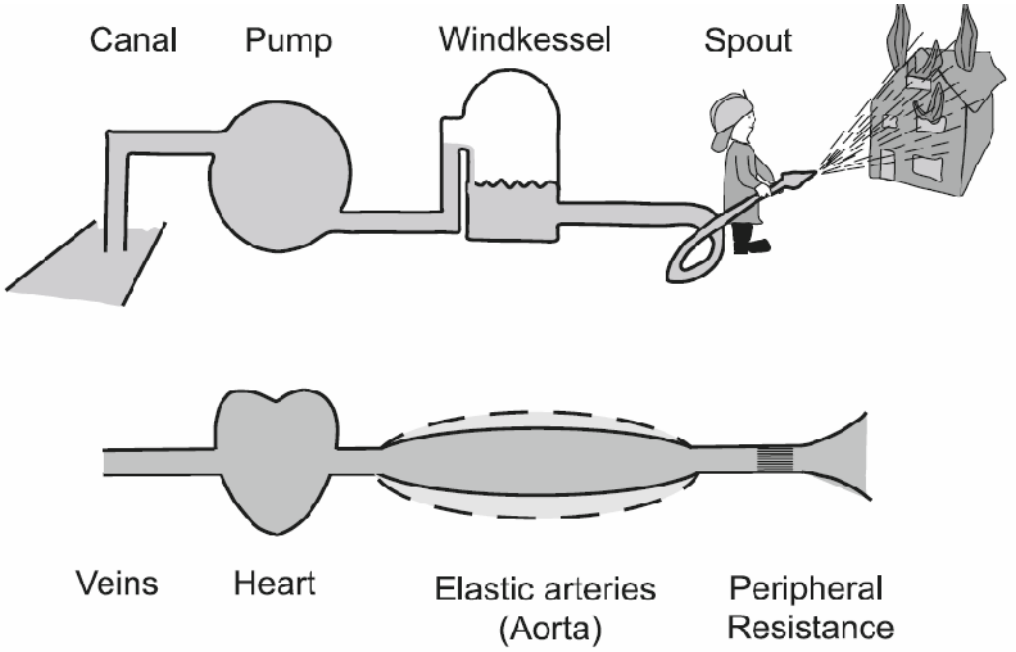

Figure 1.3: The concept of the aortic Windkessel taken from Westerhof et al. 2009. The sketch shows that the simple 2-element Windkessel model can be compared to an old fire engine pump and described in terms of arterial compliance of the aorta and elastic arteries, and the peripheral resistance.

By analogy, the heart is described as a hydraulic pump connected to a compliant chamber (the aorta) in a closed circuit, as shown in **Figure 1.3**. The classical 2-element Windkessel model accounts for pressure and flow over the cardiac cycle in terms of the interaction between arterial compliance and peripheral vascular resistance (PVR). The compliance of an artery is calculated as the ratio of volume (or cross sectional area) change to pressure change and assumes a linear relationship between these variables. The resistance to flow (PVR) is analogous to electrical resistance in Ohm's law and is calculated as the ratio of the mean pressure gradient (usually assumed to be mean arterial pressure since right pressure is negligible) to the flow in the circulation, i.e. cardiac output. Resistance to flow is largely due to viscous losses in the circulation and while total PVR is attributable to a combination of resistance from large conduit arteries and smaller arterioles, the smaller vessels contribute to most of the peripheral resistance as one would expect according to Poiseuilles law for steady laminar flow in a uniform tube which states that resistance is inversely proportional to the tube radius to the fourth power.

$$\Delta P = \frac{8\mu LQ}{\pi r^4} \qquad \textbf{(1.1)}$$

where ΔP is the pressure gradient, μ is the dynamic viscosity, L is the length of the tube, Q is the volumetric flow rate and r is the radius of the tube.

The compliance of the circulation does not affect the relationship between mean pressure and flow, but influences the pulsatility of the pressure and flow waveforms. This is commonly understood in terms of another electrical analogue – capacitance, and the two element Windkessel model of Frank is commonly formulated in electrical terms employing a capacitor and a resistor (**Figure 1.4**). During systole the compliant aorta effectively operates as a capacitor, storing blood. During diastole the stored volume of blood is then discharged through the resistance vasculature due to the elastic recoil of the aorta and elastic arteries.

The classical 2-element model was initially intended to be used in the determination of stroke volume; but it has also proved of some use in computing cardiac output and investigating peripheral resistance (Westerhof et al. 2009). Although it is a very simple model it provides an attractive explanation for the shape of the decline in aortic pressure in diastole, but fails to accurately predict the pressure waveform in systole (Westerhof et al.

2009). Consequently, there have been numerous modifications to this design over the years. Some recent models shown in **Figure 1.4** now attempt to take resistance across the aortic valve (3-element model, Ferreia et al. 2003) and arterial inertance (4-element model, Stergiopulos et al.1996) into consideration, although strictly it is probably inappropriate to draw too close physical analogies between the electrical elements in these models and anatomical structures in the circulation. The 4-element Windkessel model is better able to predict the relationship between pressure and flow in the circulation, however, the major defect in all Windkessel models is that, being non-dimensional models they neglect wave travel in the arterial system.

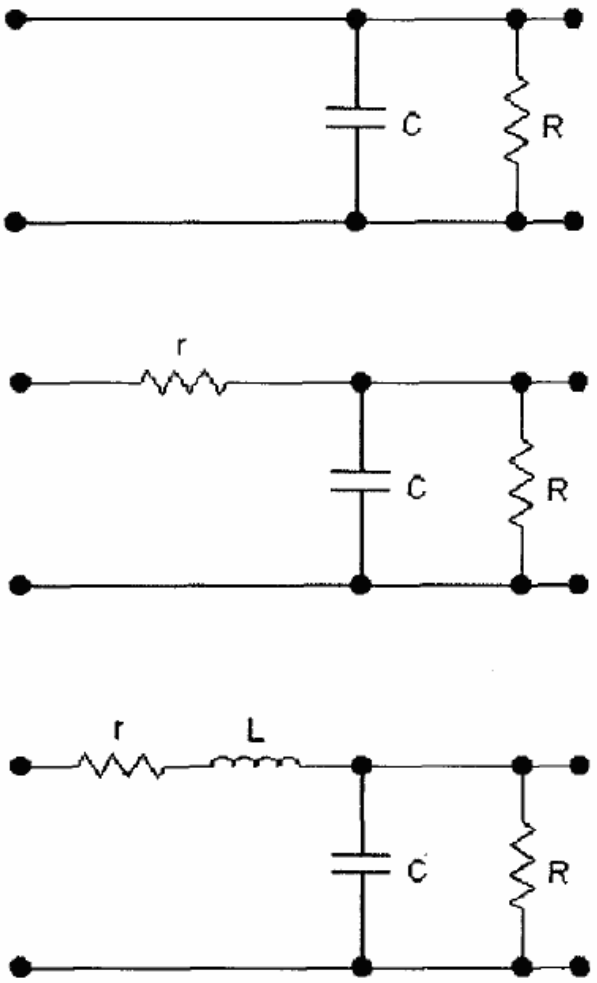

Figure 1.4: Examples of 2-element (top), 3-element (middle) and 4-element (bottom) Windkessel Model taken and modified from Ferreia et al. 2003. R= peripheral resistance, C= arterial compliance. R and C are the original elements used in the 2-element Windkessel model. The 3-element model additionally includes the resistance to blood flow due to the aortic valve (r). While the 4-element model also includes an inductance that equates to the inertia of blood (L).

1.5.2 Wave propagation

A wave is a disturbance that propagates in space and time. Wave propagation depends on the balance of a restoring force and the inertia of the system and involves the exchange of energy between one form and another as the wave passes. Waves propagate in arteries as a consequence of the balance between the inertial force of the blood and the restoring force of the walls (since blood is relatively incompressible the contribution for fluid compressibility is usually neglected in arterial wave analysis). For example, ventricular contraction generates a forward travelling wave (or series of wavefronts) that propagates distally through the aorta to the rest of the circulation. Such a wave will propagate unaltered in a uniform tube containing an inviscid fluid, but non-uniformities in terms of the cross sectional area or elasticity of the tube will give rise to a reflection, this is discussed in more detail in subsequent sections.

For the purposes of this thesis the term wave should be distinguished from the term waveform which will be used to describe the morphology of a measured pressure or flow trace. Aortic pressure and flow waveforms have characteristic pulsatile shapes that depend on the output of the heart and its interaction with the arterial system. These waveforms can be modelled as waves travelling in a one-dimensional system. Wave events in the cardiovascular system have been principally analysed by two approaches, impedance (or Fourier) analysis and wave intensity analysis.

1.5.3 Impedance analysis: Wave analysis in the frequency domain

Impedance analysis of the arterial system resolves some of the shortcomings of the Windkessel. Arterial impedance (Z) (also termed arterial input impedance) is another concept which parallels the synonymous electrical term and is defined as the ratio between pressure (P) and flow (Q).

$Z = P/Q$

Unlike resistance which is calculated from mean pressure and mean flow, impedance is a complex, time (or frequency)-dependent quantity that describes the dynamic relationship between pressure and flow.

If the cardiovascular system is assumed to be in steady state the complex relationship between pressure and flow can be analysed in the frequency domain using Fourier analysis. Fourier analysis is a mathematical technique that enables any complex waveform to be decomposed into a series of sine or cosine waves, each with their own amplitude, phase and frequency as shown in **Figure 1.5**.

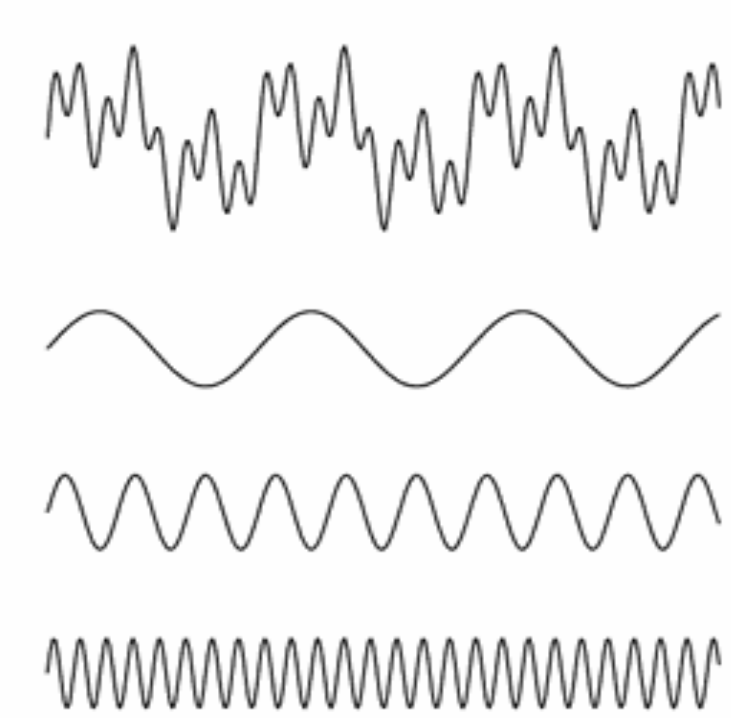

Figure 1.5: An illustration of how Fourier analysis works taken from www.science.org.au. An original (complex) waveform can be reconstructed from the combination of the three simple sinusoidal waveforms shown below.

During the second half of the 20th century digital computers improved vastly in speed and Fourier analysis now finds widespread use in the processing and analysis of many complex

signals. Using Fourier analysis arterial pressure and flow waves can be decomposed into sinusoidal components (harmonics) with the appropriate frequencies, magnitudes and phase shifts.

The fundamental partial differential equations governing flow in an inviscid incompressible fluid were first published in 1775 by a young Swiss mathematician, Leonard Euler. These equations, which are derived from the principles of conservation of mass and momentum, are the basis for all one dimensional models of blood flow in arteries. In 1955 Womersley solved these non–linear equations of flow for an elastic artery and generated linearized forms of the equations which could then be solved using Fourier analysis (Womersley JR. 1955). McDonald was an early proponent of the use of harmonic analysis in arterial haemodynamics (McDonald MG. 1955b). In 1960 McDonald simultaneously measured pressure and velocity at several sites in the aorta and the femoral and saphenous arteries and observed that the amplitude of the pulse wave increases and its upstroke becomes steeper, in contrast the amplitude and upstroke of the flow waveform diminishes as measurements are made more distally (McDonald DA 1960). Taylor expanded upon these observations by developing an analytical model of the whole vascular tree and proposed that the transmission of the pressure pulse was considerably influenced by reflections (Taylor MG. 1966). More recently, Westerhof and colleagues (Westerhof et al. 1972) extended the impedance approach to allow separation of the pressure and flow waveforms into forward and backward components. Investigation into the effects and extent of wave reflections became a popular topic over the following years

Impedance-based analysis has greatly improved our understanding of arterial haemodynamics however, like all techniques it has several limitations: although Fourier analysis can be applied to a waveform of any shape; it assumes that the system is linear, i.e. that waves interact additively. Also, although Fourier transform identifies the amplitude and phases of the various frequencies that contribute to a time series it cannot provide information on their localisation within a time series. Fourier analysis can therefore not be used to study non-periodic or transient flow. Impedance technique therefore assumes both linearity and periodicity; both questionable assumptions in the cardiovascular system.

Varying aspects of the cardiovascular system including the geometry of the blood vessels and the structure of the wall are now known to modulate wave travel (Wang et al. 2004,

Kho et al. 1998). It is reported that at any point in which these mechanical properties of an artery change, a wave will be partially reflected (Khir et al. 2001). Most investigators had previously assumed that reflections from the periphery had a more significant effect than those in the aorta. However Wetterer (Wetterer E. 1956) studied the pressure and flow waves in the ascending aorta and explained that as the pressure pulse is maintained to a high level but the flow decreases rapidly late in systole the aortic reflections clearly affect the contour of the pressure waveform. He also concluded that the reflected wave is the summation of reflection that has arisen from both the heart and the periphery. Remmington (Remmington and O'Brien 1970) confirmed his findings; however these studies were all concerned with the measured pressure and flow waveforms. Numerous efforts were made to separate the pressure and flow pulses into their forward and backward components and in 1972, Nico Westerhof first introduced the separation of pressure and flow into their forward and backward waves. Westerhof dedicated a lot of time to studying the amount of reflection in the arterial system. He found that while the larger arteries contribute a fixed amount to the intensity of reflection (also known as the reflection coefficient of the system) the peripheral contribution is higher, as expected according to Poiseuilles law mentioned in section 1.5.1.

1.6 Wave intensity analysis: Wave analysis in the time domain

1.6.1 Background

In 1988 Parker et al., (Parker et al. 1988) described a new 1-dimensional time-domain-based method for the analysis of arterial waves that was based on the method of characteristics. Unlike impedance analysis the method of characteristics does not assume either linearity or periodicity (Parker and Jones 1990). Fundamentally wave intensity analysis (WIA) views any wave as being composed of small incremental waves or wavefronts and that the intensity of a wave is a measure of energy flux density (i.e. power) carried by the wave. The magnitude of wave intensity is calculated by multiplying the change in pressure by the change in velocity.

$$\mathbf{dI = dPdU} \qquad \textbf{(1.2)}$$

This approach has advantages in a clinical setting as it is a time domain analysis which can be easily related to physiological events. Using terminology derived from gas dynamics waves are considered to be either ‘compression’ waves (associated with an increase in pressure) or 'expansion' waves (associated with a decrease in pressure).

This new approach has led to the discovery that reflected (compression) waves are not the only factors that influence the shape of the waveforms. WIA has revealed that late in systole the reduction in rate of contraction of the LV generates a forward travelling expansion wave (FEW) that contributes to closure of the aortic valve (Parker and Jones 1990, Parker et al. 1988). If linearity of the system is assumed then WIA, like impedance analysis, can be used to separate pressure and flow into forward and backward components using the Water hammer equation. Under uniform conditions the water hammer equation enables one to estimate the pressure dependent wave speed of a wavelet when travel is unidirectional and will be explained in further detail in chapter 2, section 2.2

The method of characteristics is arguably more flexible than impedance analysis; nevertheless it does assume that the 1-D theory is valid: pressure and velocity will vary

along the system but will have a uniform value at each cross-sectional area and that speed of propagation of the wave (wave speed) is greater that the velocity of blood flow.

1.6.2 Wave speed

Measured wave intensity can be directly calculated from the measured blood pressure and blood flow velocity and requires no knowledge of the wave speed, however in order to separate the measured waveforms into their forward and backward components the wave speed must be known (Parker et al. 1990).

Sir Isaac Newton (1687) was the first to develop an analytical description for the speed of sound and described the wave speed of waves propagating in an elastic medium. The speed of wave propagation (often termed pulse wave velocity) depends on both the inertial and elastic properties of the medium. In 1809 Thomas Young expanded Newton's theory and defined the wave speed of given arterial segments as the change in pressure and distensibility (Young 1809). Young estimated that wave transmission is approximately 15.5ft/s (4.7m/s), which corresponds well with modern aortic estimations in both canines (Khir et al. 2004) and humans (Davies et al. 2005). The wave speed in an artery depends on the cross sectional area and elastic characteristics of the vessel and the density of blood. Vessel distensibility is inversely proportional to the square of the wave speed. It is for this reason that wave speed is now commonly used by clinicians as an indicator of cardiovascular disease and arterial stiffening. A decrease in distensibility due to stiffening of the arteries (arteriosclerosis) leads to an increase in wave speed (Aviolo 1990). Vasoconstriction would also have this effect on wave speed. Young's modulus, E, is a measure of the rigidity of a vessel and in 1878 Moens and Korteweg both independently defined the wave speed equation for thin walled tubes with homogenous elastic properties.

$$c = \sqrt{\frac{Eh}{\rho d}} \qquad \textbf{(1.3)}$$

Where h is the wall thickness and d is the internal diameter. This formula also assumes that the wall thickness is small in comparison to the vessel radius.

Wave speed has been evaluated by various methods over the years. The most commonly used method until the last decade is known as the foot-to-foot method.

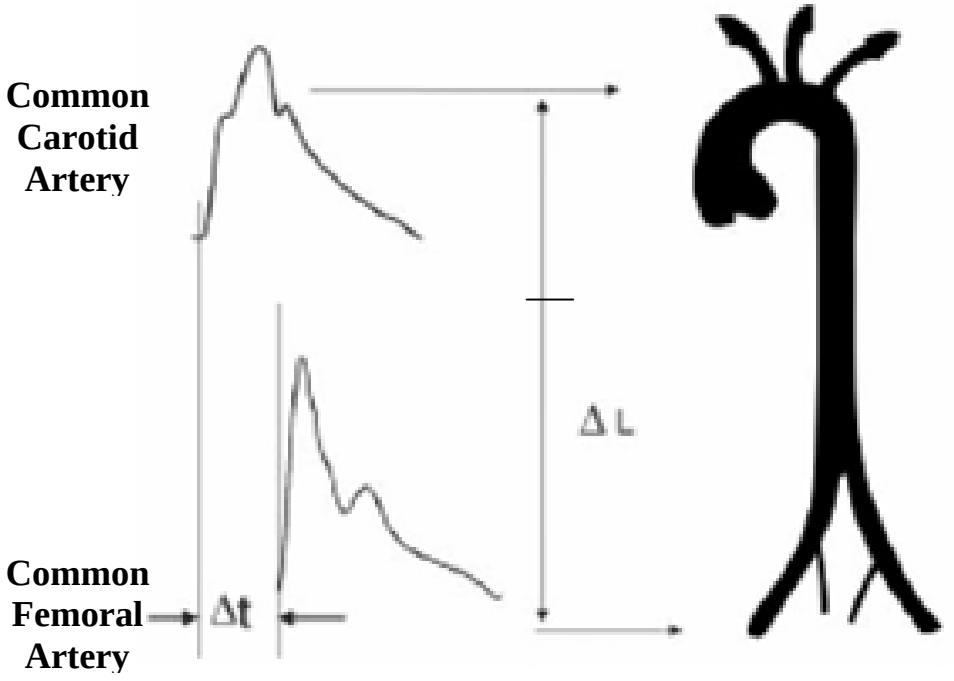

Figure 1.6: The foot-to-foot technique involves measuring the transmission time that it takes for a wave to travel from one site to another. If the distance (L) apart is known then wave speed can be calculated. A reference point on the waveform is required which is the foot of the pressure wave in this example. In this example the first site is the common carotid artery and the second site is the common femoral artery.

The foot-to-foot technique involves measuring the transmission time that it takes for a wave to travel from one site to another a known distance (L) apart. A reference point on the waveform is required which is usually the foot of the pressure wave (Latham 1988) as seen in **Figure 1.6**. Other investigations have used several sites along the rising limb of the pressure waveform (Frank 1905, Kapal et al. 1951) and found the wave speed measured at

these various points was not much changed. Regardless of where the reference point is chosen to be the major limitation to this technique is that the wave speed is time-averaged. The wave speed calculated using this technique would only be accurate if the physical properties of the length of artery measured remained constant, which is not the case over the distances routinely used to measure wave speed using transit time methods. Due to this shortcoming of the foot-to-foot method, the PU-Loop method was developed as a measure of wave speed (Khir et al. 2001). This method requires the simultaneous measurement of both blood pressure and blood flow velocity at one chosen site and the wave speed is calculated on the basis of the Waterhammer equation from a linear segment of the relationship when it is presumed that there are no reflections. Further details of the methodology are provided in chapter 2, section 2.3. The PU-loop method has the advantage of measuring local wave speed. The PU-loop and foot-to-foot methods have been compared (Khir and Parker 2004) and wave speeds calculated by the foot-to-foot method were found to give consistently higher results than those calculated using the PU-loop method. This was not a surprising finding as wave speed increases in more distal arteries and the foot-to-foot method represents a weighted average of all the intervening segments.

Another method that can be used to calculate wave speed is the sum of squares technique (Davies et al. 2006). This method is commonly used when determining coronary wave speed as the PU-loop fails in these vessels due to the lack of a straight line during the beginning of the cycle. This non-linearity is a consequence of reflected waves in the coronaries that arise very early in systole (Davies et al. 2006, Kolyva et al. 2008). The sum of squares uses measured blood pressure and blood velocity waveforms over the whole cardiac cycle.

$$\rho c^2 = \frac{\sum dP^2}{\sum dU^2} \qquad \textbf{(1.4)}$$

Wave speed is calculated by the square root of the ratio of change in blood pressure (dP) and change in blood velocity (dU) divided by blood density (ρ). There is some controversy over the use of this single point method in the coronaries (Kolyva et al. 2008) however aortic results from this method compare well to those using the PU-loop (Figure 6). As the whole cycle is used to calculate the wave speed it is relatively insensitive to misalignment of timings in the blood pressure and blood velocity waveforms.

1.6.3 Assessment of waves during the cardiac cycle using Wave Intensity Analysis

During systole the left ventricle ejects blood into the aorta and a distinctive pattern of wave intensity is observed. This is clearly demonstrated in **Figure 1.7**. During early systole blood is expelled rapidly into the aorta causing aortic flow acceleration. There is an increase in both blood pressure and blood velocity in the aorta, which gives rise to a dominant forward travelling compression wave (FCW). During mid-systole a discrete negative peak of wave intensity is observed which indicates the arrival of a backward compression wave (BCW) due to reflections. These reflected waves cause an increase in aortic pressure that is accompanied by a decrease in aortic flow. Late in systole, during 'protodiastole' (Wiggers 1921) the left ventricle generates another forward wave. This second forward wave is a forward travelling expansion wave (FEW) that is associated with a decline in aortic pressure and deceleration of flow (Parker et al. 1988). It is now established that the forward compression and expansion waves generated by the LV during early and late systole are responsible for both the acceleration and deceleration of aortic blood flow (Parker and Jones 1988). These hemodynamic events arise as a result of the positive and negative pressure gradients associated with the two types of wavefront. These two forward waves dominate systole and it is apparent that propagating forward waves arising from the ventricle are the principal factors accounting for the morphology of the pressure and velocity waveforms throughout systole in the canine aorta.

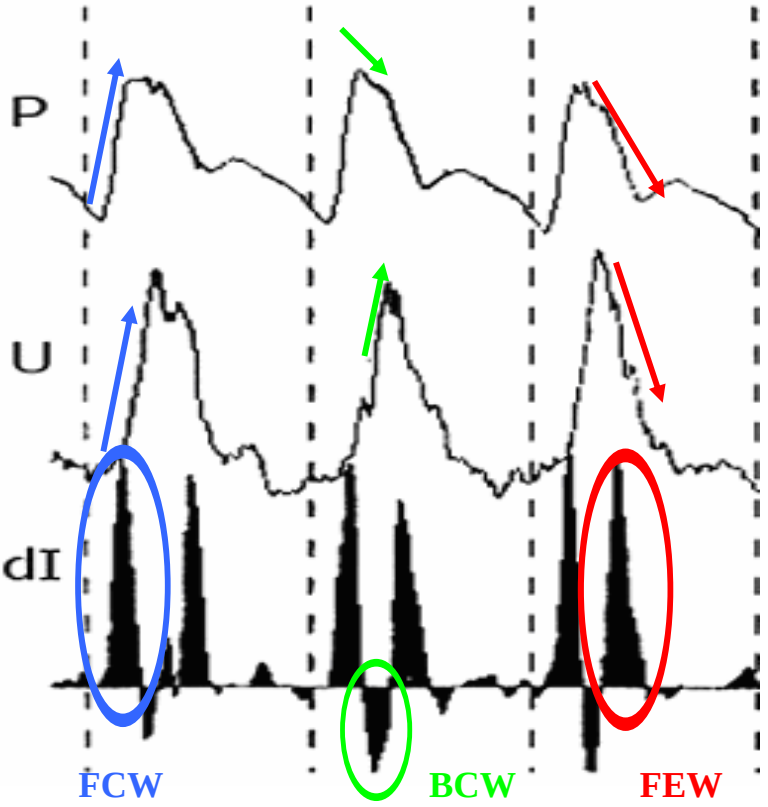

Figure 1.7. A modified diagram plotted using the original human wave intensity data collected by Parker et al 1990. The top trace shows blood pressure (P), the middle trace shows blood velocity (U) and the bottom trace is the calculated wave intensity (dI=dPdU). The figure demonstrates the usual pattern of waves seen in the ascending aorta during the cardiac cycle. During every beat there are three main waves. During early systole a forward compression wave (FCW) is observed as blood pressure and velocity are simultaneously increasing. During mid-systole part of the FCW has been reflected as a backward compression wave (BCW) that returns to the heart bringing about a deceleration in velocity and a further increase in pressure. Near end-systole the LV generates a forward expansion wave (FEW) that causes a decrease in both pressure and velocity. This thesis aims to discover the underlying LV mechanics that generate this FEW.

Most investigations in the field of wave intensity have concentrated on the major waves. The forward compression wave generated by the initial contraction of the LV has been proposed to correspond to Rushmer's 'initial ventricular impulse' (Rushmer RF 1964) and its magnitude is considered an indication of the working state of the LV. Jones and Sugawara (1993) reported that the intensity of the forward compression wave increased and altered in shape (narrowed) as it propagated down the aorta. This was attributed to the non-linear relationship between wave speed and pressure. Several studies have manipulated cardiac and arterial performance with devices or pharmacological interventions and observed the effects on the magnitude of forward travelling aortic waves (Jones et al. 112, Ramsey and Sugawara 1997, Jones and Sugawara 1993, Jones et al. 2002 and Khir et al. 2004). It is reported that even a simple disturbance such as the tilting of ones head has an adverse effect on ventricular contractility and therefore lessens the FCW magnitude (Ramsey and Sugawara 1997). One study imposed total occlusions at 4 sites (thoracic, diaphragmatic, abdominal and iliac) in the dog aorta (Khir et al. 2005). Proximal occlusions were found to induce a large increase in systolic, diastolic and mean aortic pressure and a decrease in mean aortic flow rate. Both the FCW and FEW were significantly reduced and the BCW was increased in magnitude and duration and arrived back at the heart sooner. Another similar experiment in canines involved the placing of an intra-aortic balloon into the ascending aorta (Ramsey and Sugawara 1997). The timing and magnitude of the BCW could be manipulated depending on the site of balloon inflation. A thorough investigation into the link between LV contractility and the degree of wave intensity was made using several pharmacological interventions (Jones and Sugawara 1993, Jones et al. 2002). It was revealed that the magnitude of the FCW is susceptible to external load and inotropic intervention. On the contrary, the FEW is unaffected by changes in inotropic state but is reduced by vasodilators. Perhaps unsurprisingly given that wave intensity is the product of the derivatives of pressure and flow, peak FCW intensity was directly proportional to maximum rate of LV pressure increase (max dp/dt).

1.6.4 The forward expansion wave (FEW)

The detection of the FEW during late systole is a significant finding that was only possible due to the development of wave intensity analysis (Parker and Jones 1990, Parker et al.. 1988). Parker et al. noted that "*the primary determinant of aortic deceleration, and therefore aortic valve closure and end systolic ventricular volume, is an expansion wave generated by the LV, and not wave reflections from the periphery*" (Parker et al. 1988). Previously the results of impedance analysis had been interpreted as indicating that reflected waves were responsible for the deceleration of flow at the end of systole. Wave reflections can be seen in mid-to-end systole using WIA, but it is the FEW that principally accounts for flow deceleration. Wave reflections are most marked at mid-systole, rather then end systole even during complete aortic occlusion (Khir et al. 2005) or during severe vasoconstriction (Jones et al. 2002). It has been proposed that reflected compression waves may have an adverse effect on the cardiac performance (Parker et al. 1988) due to increased load on the ventricle (Jones et al. 2000).

The source of the FEW is not well understood. As it is a positive wave, it is forward travelling and presumed to originate in the LV. What is known is that it is consistently present although its magnitude fluctuates from beat to beat. In healthy adults the expansion wave is only a third of the size of the FCW and unlike the FCW it broadens in shape as the pulse wave propagates distally (Jones et al. 1993). The magnitude of the wave appears to be dependent on a variety of factors including the mechanical properties of the large arteries and the peripheral vascular resistance. Evidence of this is seen during pharmacological interventions with vasoconstrictor and vasodilator drugs (Jones et al. 2002). Vasoconstrictor drugs significantly increase the magnitude of the FEW whereas vasodilators such as nitroglycerine and glyceryl trinitrate significantly decrease the magnitude.

LV function is likely to be a major factor in determining the magnitude and timing of the FEW. Sugawara proposed that "*expansion wave generation by the left ventricle will be a consequence of both a reduced rate of myocardial shortening and myocardial relaxation*" (Sugawara et al. 1997). It is generally recognised that myocardial relaxation begins before closure of the aortic valve. It has been argued that when the rate of LV contraction diminishes there will be a mismatch between contraction of the chamber and blood flowing

into the aorta under its own momentum. The inertial effect of the momentum of blood flow has a long history preceding that of wave intensity analysis: in 1968 Nobel stated, "*The blood once set into motion, will continue in motion because of its inertia until resistance stops it*" (Nobel 1968). This concept of blood momentum was used to explain the existence of a negative pressure gradient between the LV and the aorta near end-systole before the aortic valve had closed (Spencer and Greys 1962) despite continued blood flow into the aorta.

Sugawara et al. therefore modified Nobel's statement to read "*The blood, once set into motion, will continue in motion because of its inertia until it is stopped by the heart, causing a rapid decline in left ventricular pressure*." (Sugawara et al. 1997), thereby emphasizing that the heart itself that possesses the ability to actively decelerate flow and contribute to closure of the aortic valve through generation of an expansion wave. Sugawara et al. developed a means of measuring the degree of inertia force present near end-systole. They defined the inertial force as the product of density, wave speed and rate of deceleration ($\rho c \alpha$) and reported that the inertial force correlated strongly with cardiac index, stroke volume index, ejection fraction, and LV end-diastolic pressure. Inertial force has since been proposed to play a vital role in LV recoil during isovolumic contraction aiding LV relaxation (Yoshidu et al. 2006). Furthermore, inertial force has also been linked to another phenomenon known as apically directed intraventricular flow (Ohte et al. 2002). Apically directed intraventricular flow occurs during isovolumic relaxation and also aids LV filling. However, it is initially observed when flow is still running out of the LV outflow tract. It is said to be a '*mediator of better systolic function*' (Ohte et al. 2002) and absence of this flow is a feature of global LV dysfunction from end-ejection to early relaxation. A strong inertial force produces 'spread flow', which may play an important 'sucking' role in conjunction with FEW from late systole to isovolumic relaxation. (Yanada et al. 2003).

The above-mentioned studies imply that the magnitude of the FEW may be related to both the inertial force and the apically directed flow; however the question still remains as to what exact mechanism generates the FEW. Is it when the LV fibres stop shortening but retain their tension? Is it when the rate of fibre contraction slows, or is there another mechanism? Sugawara el at considered that it may be a consequence of both (Sugawara et

al. 1997), while Jones et al. presumed that it is a consequence of LV volume falling as myocardial shortening diminishes (Jones et al. 2000). It seems likely that both explanations are oversimplified. For instance the rate of fibre contraction in the ventricle is not uniform and slows in different regions of the LV at different times. Secondly, how does the LV compensate for wall and valve abnormalities that can occur during diseased states and how does this in turn affect FEW generation? Niki et al. have shown that the FEW is significantly diminished in patients with mitral regurgitation and that this diminution is immediately reversed after valve replacement surgery (Niki et al. 1999). Currently the mechanisms responsible for the FEW are incompletely understood and there is clearly a need for a thorough investigation into LV wall motion near end-systole. One goal for this thesis is to attempt to establish the detailed mechanisms behind the timing, generation and magnitude of the FEW.

1.7 Recent developments in wave intensity analysis

1.7.1 "Time-corrected" wave intensity

One limitation of wave intensity analysis is that the magnitudes of the waves vary when the sampling rates are altered. The wave's magnitudes are dependent upon the derivatives of pressure and velocity and consequently higher sampling rates result in lower amplitude waves. To allow data collected at different frequencies to be compared it has been proposed that all wave intensity data should be normalized to take account of the sampling rate (Jones et al 1992, Ramsey and Sugawara 1997). Thus

$$dI = \frac{dP}{dt}\frac{dU}{dt} \qquad \textbf{(1.5)}$$

Normalisation for sampling rate has merit but has the disadvantage that the units lose physical meaning (W/m^2s^2) and cannot be directly interpreted as power density (Bleasdale et al. 2003). Consequently many researchers choose not to use this approach.

1.7.2 Wave and reservoir theory

As mentioned in section 1.5.1 the Windkessel model was first solved by Otto Frank in 1899 and relatively successfully describes the shape of the aortic pressure waveform during diastole. However, as a non-dimensional model, the Windkessel is incompatible with wave transmission and in practise it cannot satisfactorily predict the sharp upstroke or the shoulder often observed on the aortic pressure waveform. For this reason, the impedance-based approaches developed by Womersley (1955), McDonald (1955) and Westerhof (1969) have dominated arterial haemodynamics since their formulation. However, impedance analysis and wave separation in particular are not without problems as illustrated in **Figure 1.8**. After the aortic valve closes aortic flow stops almost immediately while the corresponding aortic pressure remains high and slowly decreases. If zero flow were to be a realistic outcome the proximal-to-distal pressure gradient would also be required to be zero which is not the case as shown in **Figure 1.8**. The only explanation to be drawn from one-dimensional wave theory is that equal magnitude, self cancelling forward and backward waves are present (Wang et al. 2004). The source of such 'self cancelling' waves in diastole is unclear. This led Wang et al., (Wang et al. 2003) to propose a compromise between the Windkessel model and the wave model, termed the wave-reservoir model. This model takes account of the distensibility of the aorta, and attributes the quasi-exponential decline in diastolic pressure to this, but also incorporates wave transmission in systole. This attractive, if contentious proposal, remains to be established. Davies et al., (Davies et al. 2007) have argued that neglect of the radial expansion of the aorta and large elastic arteries in systole (potentially accommodating up to 40% of the blood ejected in systole) may lead to misleading results using simple wave analysis and that subtraction of this 'reservoir pressure' should be performed before undertaking wave separation (**Figure 1.8**).

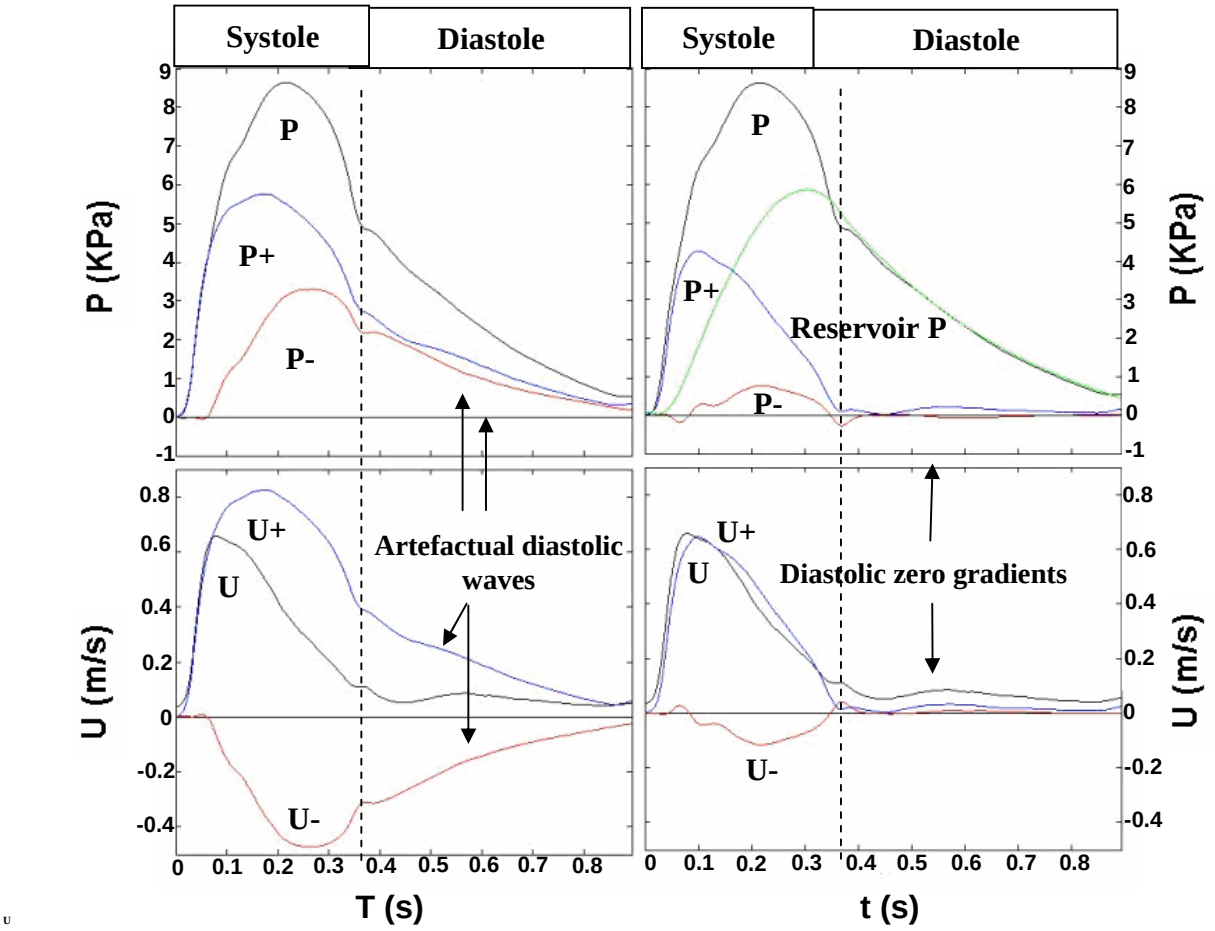

Figure 1.8: A figure modified with kind permission from Professor Kim Parker. The waveforms on the left side of the figure are aortic pressure (P) and velocity (U) traces before aortic reservoir subtraction while those on the right are plotted after subtracting the aortic reservoir. Measured P and U are shown in black, forward waveforms are in blue and backward waveforms are in red. The measured waveforms show that during diastole U becomes zero almost immediately while the corresponding P remains high and slowly decreases. For zero U to be a realistic outcome the proximal-to-distal P gradient would also be required to be zero which it is not the case before aortic reservoir subtraction. The only explanation to be drawn from the original theory is that equal magnitude, self cancelling forward and backward waves are present (Wang et al 2004). However after substituting the aortic reservoir (shown as a green line on the top right plot) and then re-separating the wave-only measures it can be seen that the self-cancelling artefact waves have disappeared and the diastolic P decay can be explained by the slowly emptying reservoir

1.7.3 Non-invasive wave intensity

Diameter Vs Pressure

A major limitation to the initial use of wave intensity as a measure of ventricular and vascular function in an every day clinical setting was that invasive pressure and flow recordings were needed. In 2000 Sugawara and colleagues studied the relationship between intravascular pressure and diameter-change of the carotid artery. Their research revealed that during diastole the pressure-diameter relationship was slightly non-linear; however during systole, when wave intensity is well defined in the carotid artery the waveforms are in fact very similar (Sugawara 2000). Through this discovery a new non-invasive real-time measurement system of wave intensity was developed (Harada et al. 2000). Diameter changes can be measured accurately using an echo-wall tracking (sub)-system, which is installed into an ultrasound system and arterial diameter changes can be used as a surrogate for pressure changes. The blood flow velocity along the vessel can then be measured using range-gated Doppler signals. Both diameter change and velocity measurements along with the ECG are fed into a personal computer that displays all information in real time. Blood pressure is taken using a cuff manometer at the upper arm; this information is also fed into the personal computer. The systolic and diastolic blood pressures are used to convert diameter change into pressure and wave intensity can be calculated.

Another study by Feng and Khir (2007) involved the development an algorithm to separate wave intensity into its forward and backward directions using measured diameter of a flexible tube's wall with measured velocity. This group also found that the results determined using measured diameter were almost identical to those calculated using measured pressure and velocity in the traditional wave intensity way.

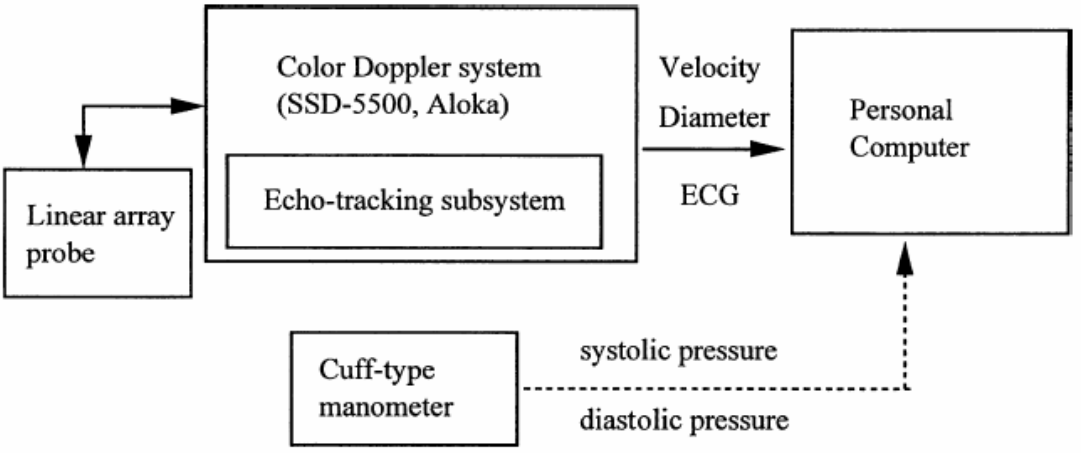

Figure 1.9: A block diagram of the system used to non-invasively acquire wave intensity analysis data, taken from Harada et al. (2000). The Aloka ultrasound machine has an in-built echo-wall tracking function that tracks the posterior and anterior walls of the common carotid artery and then uses the arterial diameter changes can be used as a surrogate for pressure changes.

Applanation tonometry

Applanation tonometry enables local pressure waveforms to be assessed non-invasively using a high fidelity strain gauge-tipped pencil probe. When combined with pulsed-wave Doppler ultrasound to measure arterial velocity it is also possible to calculate wave intensity at peripheral sites. Zambanini et al. (2005) used this technique to look at wave energy patterns in the carotid, brachial and radial arteries.

Data were collected from 21 healthy volunteers and WIA was applied to determine the timings and energies of all waves. This group found that systolic pressure was significantly higher in the carotid artery than the brachial and radial arteries but that wave speed was lower as one would expect. An additional wave (X) was observed during mid-systole which is a forward travelling expansion wave that may be due to re-reflection of backward travelling compression wave from an open-end type reflection at the root of the carotid artery. **Figure 1.10**

Although easy to perform, both non-invasive techniques have limitations. Tonometry and Doppler cannot acquire pressure and velocity simultaneously; this can lead to errors and the echo-tracking system may lose a degree of accuracy during the diameter to pressure conversions. Also, one should not compare tracings measured with varying heart rates; a maximum of 5 beats per minute difference should be adhered to (Swillens and Segers 2008). When studying LV function one must also always consider the time delay it takes for the waves to get from the LV to the carotid. Nonetheless, non-invasive techniques are easily used and it has been suggested that changes in wave intensity parameters could be used as a guide to selecting suitable candidates for surgery and vasodilator therapy (Niki et al 1999, Fujimoto et al 2004).

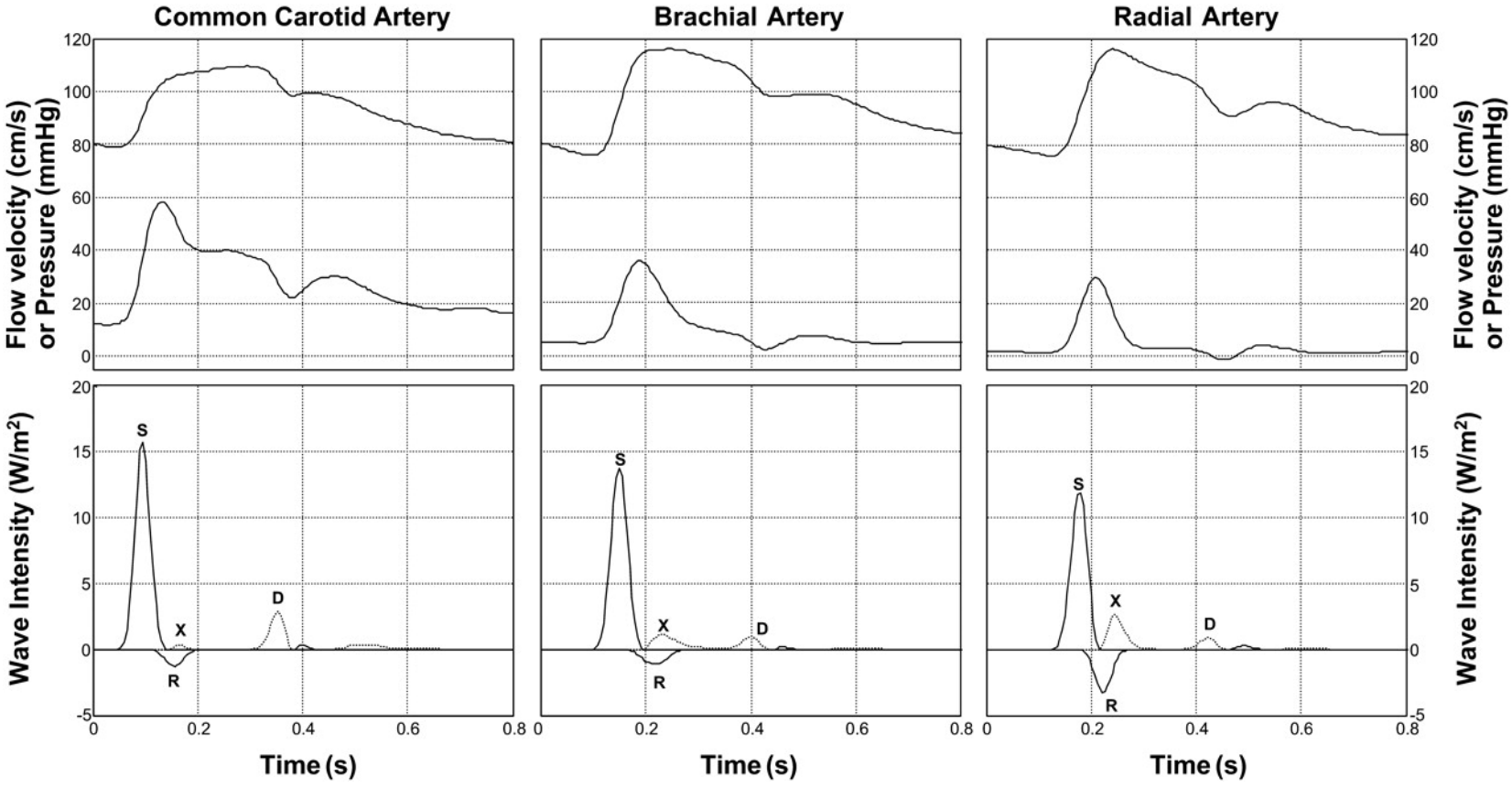

Figure 1.10: Figure taken from Zambanini et al. 2005. Illustrating the relationship between pressure, flow velocity and WIA in the carotid, brachial and radial arteries. An additional wave (X) is observed in these arteries which is a mid-systolic forward expansion wave. The X wave was significantly smaller in the carotid artery.

1.8 Motivation

It is essential to identify the specific, detailed mechanisms that underlie 'normal' left ventricular ejection in order to optimise the treatment of cardiovascular disease. Generation of the FEW by the LV at the end of systole has been previously explored; however the precise LV mechanics that generate the wave remain unknown. The FEW contains important information about the condition of the LV and its interaction with the arterial system. In addition it probably makes an important contribution to aortic valve closure. Once the details of FEW generation are revealed, greater understanding of cardiac physiology and pathophysiology may facilitate the development of new treatments in heart disease.

1.9 Chapter objectives

This literature review describes a variety of techniques that have been developed to quantify human haemodynamics. It highlights the key findings, merits and limitations of each technique. A key issue that was identified was the poor understanding of the events underlying generation of the FEW. The aim of the following chapters is to further our knowledge of this phenomenon and specifically to answer the questions:

1. *How does the LV generate the forward expansion wave at the end of systole?*
2. *What is the effect of antihypertensive therapy with a beta blocker on arterial waves in man*?

The next chapter (chapter 2) contains detailed mathematical explanations for all the theories used throughout this thesis.

The first two experimental chapters (chapters 3 and 4) use data collected invasively from canines to examine the generation of the FEW. Chapters 3 and 4 contain data from the same animals. In chapter 3 the animals are in a control condition. In chapter 4 the results found in chapter 3 are tested using aortic manipulation.

The remaining chapters contain data from human subjects. Chapter 5 contains unique human invasive data and extends the observations made in dogs to humans with normal LV function. Chapters 6 and 7 assess whether non-invasive measurements can be used in man to measure arterial waves. Chapter 7 in particular, aims to show how WIA can be used to better understand the effects of a class of antihypertensive agents, beta blockers on the heart and arteries.

Chapter 2:
Theoretical Analysis

Prologue

In 1775 Leonard Euler introduced a one-dimensional model to describe blood flow in arteries, and wrote the fundamental non-linear equations that are still widely used in fluid dynamics today. Euler's one-dimensional equations of motion for fluid (Euler, 1775, Fruss et al 1962) are intricate, hyperbolic partial differential equations that were so advanced that it was a further 100 years before Bernhard Riemann introduced the general solutions of hyperbolic equations using the "method of characteristics" (Riemann, 1860). The work of Riemann prepared the way for the development of wave intensity analysis, which is described in chapter 1. Throughout this thesis only wave intensity analysis will be performed on all data acquired, and this chapter gives full analytical details for the derivation of wave intensity analysis starting with the conservation laws that each arterial segment must obey.

2.1 General equations

The one-dimensional equations of flow in the arterial system comply with conservation laws of mass and momentum.

Mass law: The Continuity equation expresses the conservation law by equating a net flux over a surface with a loss or gain of mass or volume within the surface. Mass can neither be created nor destroyed thus an equal quantity of incompressible fluid flowing into a system must flow out.

$$S_t + U(S)_x = 0 \qquad \textbf{(2.1)}$$

Where S is the cross-sectional area, t is time, U is spatially averaged velocity and x is the axial distance along the tube.

Momentum law: As momentum is 'mass in motion' Newton's second law:
Force = mass x acceleration (Newton 1687) can be reworked to become Force = rate of change of momentum, which is equal to the resultant acting on the body.

$$U_t + UU_x + \frac{P_x}{\rho} = 0 \qquad \textbf{(2.2)}$$

Where P is the spatially averaged pressure.

Blood vessels are assumed to be impermeable elastic tubes where the effects of viscous dissipation are insignificant and the properties are believed to be uniform and constant. As the cross-sectional area of the tubes differs during systole and diastole as a result of the change in pressure and the elastic properties of the wall, the values rely on the instantaneous pressure only (Parker et al. 1990). Therefore the cross-sectional area can be described as a function of pressure, which itself is a function of distance and time. Equation 2.3 is the Tube Law which describes the relationship between transmural pressure and cross sectional area,

$$S = A(P_{(x,t)}) \quad \textbf{(2.3)}$$

The values can then be expressed as the rate of change of the cross-sectional area (A) at time (t) and distance (x) and the continuity equation (2.1) can be rephrased as an ordinary differential equation in terms of pressure and velocity.

$$\frac{dA}{dP}P_t + \frac{dA}{dP}UP_x + AU_x = 0 \quad \textbf{(2.4)}$$

Which when divided by a measure of the segment's compliance (dA/dP) and rearranged becomes:

$$P_t + UP_x + \frac{A}{dA/dP}U_x = 0 \quad \textbf{(2.5)}$$

Equation 2.5 is a first order hyperbolic partial differential equation, which can be solved using the method of characteristics, using the characteristic directions U ± c (Riemann 1860). U is the tube speed and the waves propagate with a wave speed of c. Equations 2.2 and 2.5 can be written in matrix form:

$$\omega t + \Omega\omega x = \Phi \quad \textbf{(2.6)}$$

where $\omega = \begin{pmatrix} P \\ U \end{pmatrix}$ and $\Omega = \begin{pmatrix} U & \frac{1}{D} \\ \frac{1}{\rho} & U \end{pmatrix}$ and distensibility $D = \frac{1}{A}\frac{dA}{dP}$

Eigenvalues,λ, of the matrix, Ω, are solutions of the characteristic polynomial

$$| \Omega - \lambda I | = 0 \qquad \textbf{(2.7)}$$

Where **I** is the identity matrix and the eigenvalues depict speed of propagation

$$\Omega = \begin{bmatrix} (U-\lambda)\frac{1}{D} \\ \frac{1}{\rho}(U-\lambda) \end{bmatrix} = (U-\lambda)_2 = \frac{1}{\rho D} \qquad \textbf{(2.8)}$$

Wave speed = c = $(\rho D)_{1/2}$ and $D = \frac{1}{A}\frac{dA}{dP}$

Thus, $c^2 = \frac{A}{\rho}\frac{(dP)}{(dA)}$ or $\frac{1}{\rho D}$ or $(U-\lambda)_2$ **(2.9)**

Therefore the eigenvalue of the matrix Ω : $\lambda \pm = U \pm c$ **(2.10)**

Knowledge of the wave speed is essential for the separation of waves into their forward and backward components (Parker et al. 1990) and the eigenvalues signify the transmission speed of disturbance (U + c for forwards and U – c for backwards directions. Characteristic directions are routes utilised to convert partial differential equations (PDE) into systems of ordinary differential equations (ODE) assuming that the waves are in the same space and time (x, t) plane.

The physical value for the characteristic direction is:

$$\lambda \pm \frac{dx}{dt} \text{ thus } \frac{dx}{dt} = U \pm c \qquad \textbf{(2.11)}$$

The PDEs are reduced to ODEs

$$\frac{dU}{dt} \pm \frac{1}{\rho c}\frac{dP}{dt} = 0 \qquad \textbf{(2.12)}$$

If wave speed is a function of local pressure these equations can be written in Riemann function terms, R represents Riemann invariants in the forward (+) and backward (-) directions.

$$R\pm = U \pm \int_{P_0}^{P} \frac{dP}{\rho c} \qquad \textbf{(2.13)}$$

where P_o = arbitrary reference pressure

The integrating factor solves the first order ODEs which can continue to be simplified in differential form which involves Riemann invariants.

$$dU \pm \frac{dP}{\rho c} = 0 \qquad \textbf{(2.14)}$$

2.2 The water hammer equation

Equation 2.14 is employed to obtain the water hammer equation, derived from the conservation laws and best illustrates the straight forward association between the pressure and velocity across waveforms.

$$dP\pm = \pm \rho c dU \qquad \textbf{(2.15)}$$

As mentioned in chapter 1, under uniform conditions the water hammer equation enables one to estimate the pressure dependent wave speed of a wavelet when travel is unidirectional.

The first comprehensive accounts of the water hammer phenomenon were reported by two engineers independently at the turn of the 19th century: Joukowski (1900) and

Allievi (1909). These works have remained the basis of present day pressure wave analysis however their solutions are limited to simple systems. 30 years later Schryder (1932) and Bergeron (1935) developed a graphical method that allowed more complex water hammer calculations to be performed in the era before computers became widely available.

2.3 The pressure-velocity loop method

If P is plotted against U over the whole cardiac cycle a PU-loop is obtained **Figure 2.1**. However if analysis is restricted to the period of early ejection, when it is assumed that only forward waves are present, a straight line with a slope of ρc is observed as predicted by integration of the water hammer equation (2.15).

$P_+ - P_0 = \rho c U_+$ where P_o= pressure at end diastole, t = 0,U = 0. **(2.16)**

Therefore, a PU-loop can be obtained for a particular cycle by plotting measured pressure against measured velocity. The slope of the loop during early systole equals ρc and the wave speed can be calculated assuming blood density =1050Kg/m^3. The wave speed calculated by this method is then used to separate measured pressure and flow into their forward and backward components. The PU-loop method has been shown to be accurate in *in vitro* experiments (Khir et al. 2005) and is the method used throughout this thesis.

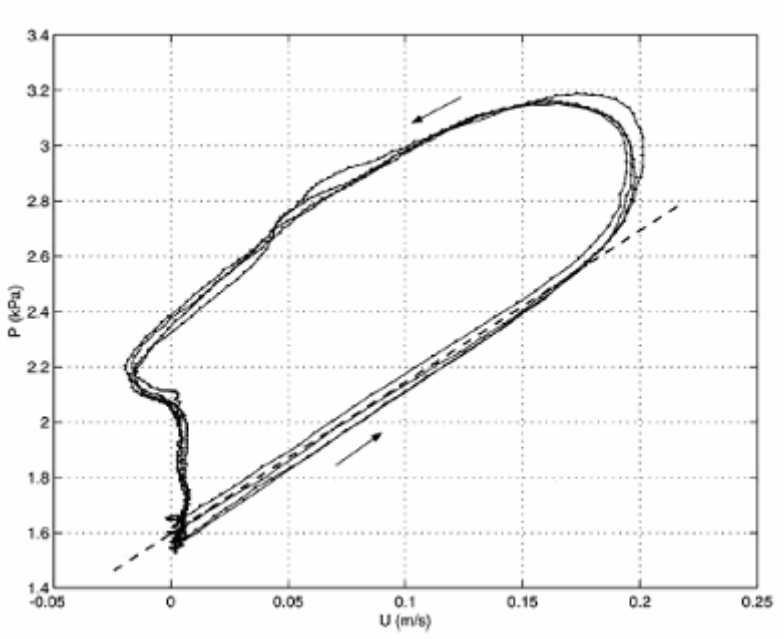

Figure 2.1: An example of a PU-loop, with permission from Khir et al. 2001. During early systole only wave fronts generated from the ventricle are present and so a straight line can be seen. The slope of the straight line can be used to calculate the wave speed if blood density is known.

All measured pressure and velocity values are derived from a forward and backward wavefront that intersect at a precise time and plane. If forward and backwards waves are assumed to interact in an additive manner (i.e. the system is linear) (Parker et al. 1990) then:

$$dP = dP_+ + dP_- \quad \textbf{(2.17)}$$

and

$$dU = dU_+ + dU_- \quad \textbf{(2.18)}$$

The water hammer equation (2.15) can be used to separate the derivatives of measured pressure and velocity into forward and backward components.

$$dP\pm = \frac{1}{2}(dP \pm \rho c dU) \quad \textbf{(2.19)}$$

$$dU\pm = \frac{1}{2}(dU \pm dP/\rho c) \quad \textbf{(2.20)}$$

The forward and backward pressure and velocity waveforms can then be calculated by integration.

$$P_+ = P_d + \sum_{t=0}^{T} dP_+ ,\ P_- = \sum_{t=0}^{T} dP_- \quad \textbf{(2.21)}$$

$$U_+ = \sum_{t=0}^{T} dU_+ ,\quad U_- = \sum_{t=0}^{T} dU_- \quad \textbf{(2.22)}$$

where P_d is an integration factor (diastolic pressure) and T is the duration of one cardiac cycle. At each intersection the calculated wave intensity is the combination of the forward and the backward wave intensities and thus equations 2.21 to 2.22 are used to calculate the intensity, dI for forward (dI+) and backward waves (dI-),

$$dI\pm = \pm \frac{1}{4\rho c}(dP + \rho c dU)^2 \quad \textbf{(2.23)}$$

The wave speed enables the separation of forward and backward waves, which in turn allows the estimation of distances to reflection sites.

2.5 Wave Classification

There are four categories of waves: forward and backward (reflected) compression and expansion waves. Direction is expressed in relation to the normal principal direction of blood flow from the heart and by convention forward wave travel is positive. Compression waves can be thought of as 'pushing' or' blowing' waves, they are associated with an increase in pressure (dP>0). Forward travelling (i.e. positive) compression waves are associated with an increase in velocity, dU>0, while backward compression waves are associated with a decrease in velocity, dU<0. Expansion waves (also termed rarefaction waves in gas dynamics) are the opposite of compression waves; they can be thought of as 'pulling' or 'sucking' waves and are associated with a decrease in pressure (dP<0).

Wave intensity is a measure of the energy flux (power) per unit cross sectional area associated with a wave and is usually measured in W/m^2. It is calculated as the

product of the derivatives of pressure and velocity. Both forward compression and backward expansion waves result in flow acceleration while both backward compression and forward expansion waves bring about flow deceleration.

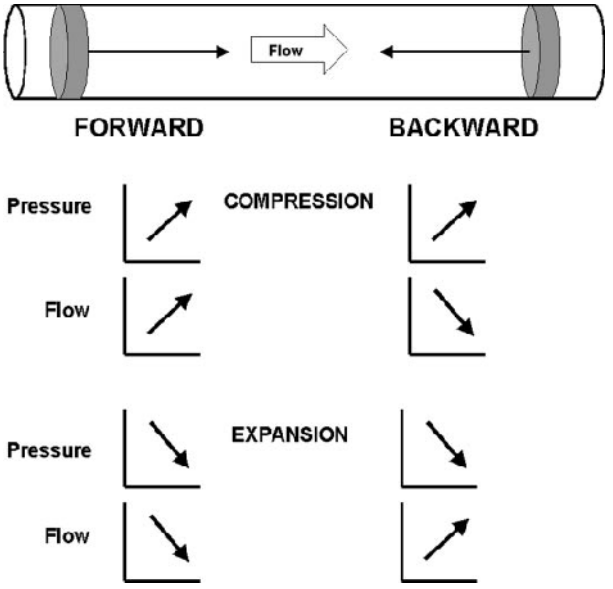

Figure 2.2 A diagram showing the direction of change of the pressure and the flow (velocity) measured at any site in the vascular system, by the passage of each of the four types of wave fronts (forward travelling compression or expansion waves or backward travelling compression or expansion waves). A sketch taken from Bleasdale et al. 2003.

Westerhof et al. (1969) was the first to separate pressure and flow into their forward and backward components using Fourier-based impedance analysis. He proposed that reflected waves caused deceleration of blood flow, but this technique was not capable of detecting the forward expansion wave seen in late systole as in essence it relies on identifying discordance in the pressure and flow waveforms (i.e. a rise in pressure accompanied by a fall in flow due to a backward travelling compression wave). Without the application of WIA the forward expansion wave would have remained undiscovered (Parker et al. 1989). Since WIA is a time-domain based approach it is

also allows timing of waves to be determined. The arrival time of reflected waves and the time of the forward expansion wave onset are of physiological importance. When looking at the timings of the different waves throughout the cycle one must use the separated waveforms. The net wave intensity is easier to calculate as no knowledge of wave speed is required; however the timings of the net intensity can be misleading. (Khir and Parker 2002)

2.6 Wave and reservoir theory

As discussed in chapter 1, section 1.7.2, Parker and Tyberg have advocated a modification of WIA that takes into account the distensibility of the aorta and considers the pressure and flow waveforms as consisting of a wave component and a reservoir component (Wang et al. 2004). The reservoir component has been equated with the Windkessel described by Frank.

According to this proposal, aortic pressure (P_{AO}) is the sum of a time-varying reservoir pressure (P_{wk}) and wave pressure (P_{ex}) that varies with time and distance.

$$P_{AO(x,t)} = P_{wk(t)} + P_{ex(x,t)} \quad \textbf{(2.24)}$$

The reservoir is described using a two-element windkessel model so that:

$$Q = C\left(\frac{dP}{dt}\right) + \frac{P}{R} \quad \textbf{(2.25)}$$

where Q is inflow, C is the compliance (dV/dP), and dP/dt the rate of change of pressure in the reservoir.

The solution of this differential equation is:

$$P(t) = \frac{1}{C} e^{-t/RC}, \int_{o}^{t} Q(t') e^{t'/RC} dt' + P_0 e^{-t/RC} \quad \textbf{(2.26)}$$

where P_0 is the pressure value at t=0.

2.6.1 Reservoir theory:

Following conservation of mass, the blood volume stored in the reservoir is the difference between inflow ($Q_{in(t)}$) and outflow ($Q_{out(t)}$) from the reservoir. While P_{wk} the reservoir pressure is the reservoir volume divided by the compliance, C, which is assumed to be a constant.

$$\frac{dP_{wk(t)}}{dt} = \frac{dP_{wk(t)}}{dPV_{wk}} \frac{dV_{wk(t)}}{dt} = \frac{Q_{in(t)} - Q_{out(t)}}{C} \quad \textbf{(2.27)}$$

Further, if the outflow from the reservoir (Qout(t) is assumed to be governed by a simple 'Ohmic' resistive relationship, with R being the effective resistance to outflow (assumed to equate to the peripheral systemic circulation), and the pressure difference driving outflow is given by P_{wk} minus the pressure at which there is no outflow (P_∞), this is not necessarily 0 but can be estimated from the exponential decline of pressure in diastole, then:

$$\frac{dP_{wk(t)}}{dt} + \frac{dP_{wk(t)} - P_\infty}{RC} = \frac{Q_{in(t)}}{C} \quad \textbf{(2.28)}$$

This equation can be solved by multiplying by the integrating factor, $e^{\frac{t}{\tau}}$ where $\tau = RC$:

$$P_{wk(t)} - P_\infty = (P_0 - P_\infty)e^{\frac{-t}{\tau}} + \frac{e^{\frac{-t}{\tau}}}{C} \int_{t_0}^{t} Q_{in}(t')e^{\frac{t'}{\tau}} dt' \quad \textbf{(2.29)}$$

t_0 and P_0 are the time and pressure at the onset of ejection.

Q_{in}= 0 during diastole as the aortic value is closed, then the equation preduicts that pressure will fall in a simple exponential manner with the time constant (τ). R , C and P_∞ are determined experimentally. As waves are assumed to be minimal during the last two thirds of diastole measured pressure is assumed to equal P_{wk} during that time. The pressure waveform in diastole is fitted using a least squares non-linear regression algorithm (the Matlab routine 'fminsearch' which uses the direct search method

(Nelder-Mead simplex)) as described by Wang et al. (22). Subtracting estimated reservoir P_{wk} from measured pressure allows the calculation of excess wave pressure, P_{ex} throughout the whole cardiac cycle.

2.6.2 Wave theory:

After subtraction of the reservoir pressure wave intensity analysis (section 2.3) can be applied to the excess pressure. The measured pressure differentials are replaced by the differentials of the 'wave only' pressure allowing calculation of reservoir subtracted wave intensity and forward and backward pressures as described above.

$$dI\pm = \pm\frac{1}{4\rho c}(dP_{ex} + \rho c dU)^2 \qquad \textbf{(2.30)}$$

Chapter 3:
Ventricular-Aortic Interaction in Canines: Control

3.1 Introduction:

As mentioned at the end of chapter one, this chapter investigates the relationship between WIA and LV wall movement collected invasively from 11 dogs during control conditions. The primary aim of this investigation is to better understand the mechanical movement of the LV that generates the forward running expansion wave (FEW) in late systole. Previous reports have shown the effects of several LV and aortic manipulations on the magnitudes of waves generated (Jones et al. 2002, Niki et al. 2005, Fujimoto et al. 2004), see chapter 1, sections 1.6.3 and 1.6.4. These studies have provided a great deal of information on the FCW during early systole but have not explained in detail the precise LV mechanics linked to the FEW at end systole. By investigating the haemodynamic events at the aortic root while monitoring LV movement we can provide more information on the global performance of the LV. The experimental design for this thesis was initially based on an experiment performed by Van Den Bos et al. in 1976 and the study was originally carried out for Dr Ashraf Khir's PhD thesis. Both the seventies investigation and the later work by Khir et al. (2000) were primarily designed to investigate the size and effect of reflections in the systemic arterial system. The key difference between the two is that Van Den Bos et al. used the older, frequency domain impedance analysis technique which is explained in chapter 1, whereas Khir et al. used the time domain wave intensity analysis. This study will use both original wave intensity analysis and the new 'wave and reservoir system' analysis explained in chapter 2 to describe systolic LV haemodynamics and movement.

Animal studies:

Animals have played an important role in cardiovascular research for centuries. Animal models allow researchers to investigate the cardiovascular system in ways that would not be easily accessible in humans. They also allow one to perform procedures that require a level of impairment that would not be ethical to inflict on human volunteers. One scientist that was very successful using dog models in the cardiovascular research field is of course William Harvey (Harvey 1628) who was the first scientist to study biology quantitatively. Dog experiments, like Harvey's have advanced our understanding and management of numerous cardiovascular problems including the creation of the heart-lung machine, which enables surgeons to sustain life while performing heart surgery (Gibbon 1937). Dogs have also been central in the

development of angioplasty (Gleason et al. 1989, 1990), in surgical approaches to mitral regurgitation (Tsutsui et al. 1994) and in the investigation of cardiac hypertrophy (Dolber et al. 1994, Koide et al. 1997). The main advantage of using dog models over smaller animals is that they allow much more accurate study of LV function and volumes (Hasenfuss et al. 1998). It has been found that the human cardiac excitation-coupling process is very similar to that of the dog myocardium (Lompre et al. 1981). It is for this reason that dog models are ideal for this project.

3.2 Hypotheses

It seems logical to assume that the deformation of the LV during contraction will play a critical role in determining the onset and magnitude of the FEW. As blood is effectively incompressible, and movement of intraventricular blood will accompany regional wall movement throughout the cardiac cycle;

1) The FEW will be generated when the last LV axis to slow reaches its maximum velocity of contraction.
2) The axial rate of shortening during early and late systole will correlate with the energy carried by the FCW and FEW respectively. Larger waves will be generated by higher rates of shortening.

If these two hypotheses are correct the LV will not only generate both the FCW and FEW but it will control the magnitude of these waves and actively control aortic haemodynamics during both early and late systole.

3.3 Methods

In this investigation haemodynamic data was collected invasively from11 mongrel dogs (4 females and 7 males, average weight 22.09±3.11kg). All experiments were performed at the University of Calgary (Alberta, Canada) by Professor Tyberg's Cardiovascular Research Group. The surgery was performed by dog surgeons Cheryl Meek and Gerry Groves and the data were collected by Ashraf Khir and Greg Nelson. All experiments in this study adhered to the University of Calgary's guiding principles in the care and use of animals and were approved by the appropriate ethics committee.

3.3.1 Instrumentation and preparation

All 11 open chest dogs were anaesthetised using 30mg/kg per body weight of sodium pentobarbital administered intravenously in addition to a maintenance dose of 75mg/h for the length of the experiment. The dogs were endotracheally intubated and mechanically ventilated (constant volume ventilator, model 607, Harvard Apparatus Company, Millis, MA, USA). ECG traces were recorded by connecting leads to both the forelegs and the left back leg of the dogs. The average baseline heart rate of all 11 dogs was 92 beats per minute with a mean R-R interval of 666±56 ms.

Haemodynamic measurements

A circumferential electromagnetic ultrasonic flow probe (model T201, Transonic Systems Inc., Ithaca, NY, USA) was snug-fitted to the ascending aorta, approximately 1cm distal to the aortic valve after a median sternotomy. Pressure was measured in the LV and aortic root (approximately 1cm distal to the aortic valve) using high-fidelity pressure catheters (Milnar Instruments inc., Houston, TX, USA). The aortic catheters were inserted into either the right/left brachial or the carotid arteries. The LV pressure catheter was also inserted into either a brachial artery or into the LV directly through myocardium at the LV apex. Measurements of flow and both aortic and LV pressure were recorded for 30 seconds. Flow was converted into velocity using the post-mortem determination of circumference values of the ascending aorta. Prior to analysis the velocity and pressure waveforms were smoothed using a Savitzky-Goley filter (Savitzky-Goley 1964, 7 point each way filter) and the foot of both waveforms were aligned (as the transducers have different frequency responses). Shifting of no more than 3 sampling intervals was required to adjust for the lag caused by the filter in the

ultrasonic flow meter (Sun et al 2000). A mercury manometer was used to calibrate the pressure catheters before every experiment and all data were recorded at a 200Hz sampling rate

Left ventricle wall movement

The pericardium was removed and two pairs of ultrasound sonomicrometer crystals (5MH, Sonometrics, Ontario, Canada) were embedded in the left ventricle myocardium to measure the movement of the long (base-apex) and minor (septum- free wall) axis. The locations that each of the crystals were sutured are shown in **Figure 3.1**. A third set of crystals were implanted into the LV anterior and posterior walls to measure a third axis (anterior-posterior) in two dogs.

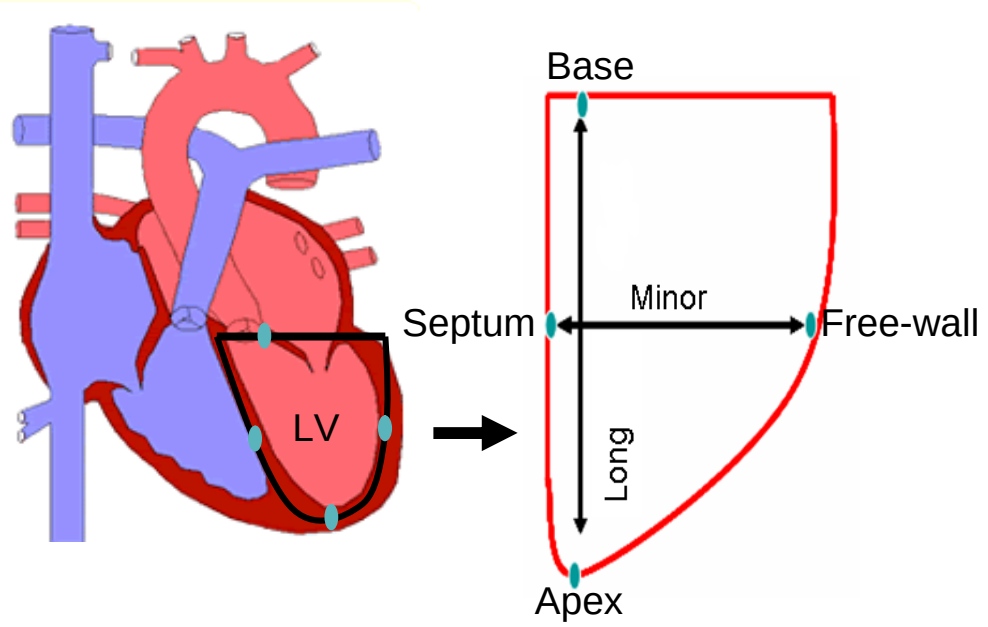

Figure 3.1: The diagram on the left is a longitudinal 4 chamber cross-section of the heart highlighting the left ventricle (LV). The diagram on the right is a sketch of the LV that roughly shows where the ultrasound crystals were embedded in the myocardium. The crystals both transmit and receive sound energy allowing the distance between pairs of crystals to be recorded throughout the cardiac cycle.

The small piezo electric transducer crystals can both transmit and receive sound energy. A specialised digital circuitry continuously measures the distance between the transducers throughout the cycle allowing LV axial dimensions to be measured while the LV is moving. Data from the crystals was obtained using Sonometrics System Software and output to a computer containing LabVIEW software, (National Instruments, Austin, TX, USA). **Figure 3.2** is a diagram that demonstrates how the crystals enable the calculation of moving LV axis dimensions. The change in length of the axes over time can be plotted offline using custom written programs in Matlab (The MathWorks Inc., MA, and USA). This can be seen in Figure 3.3

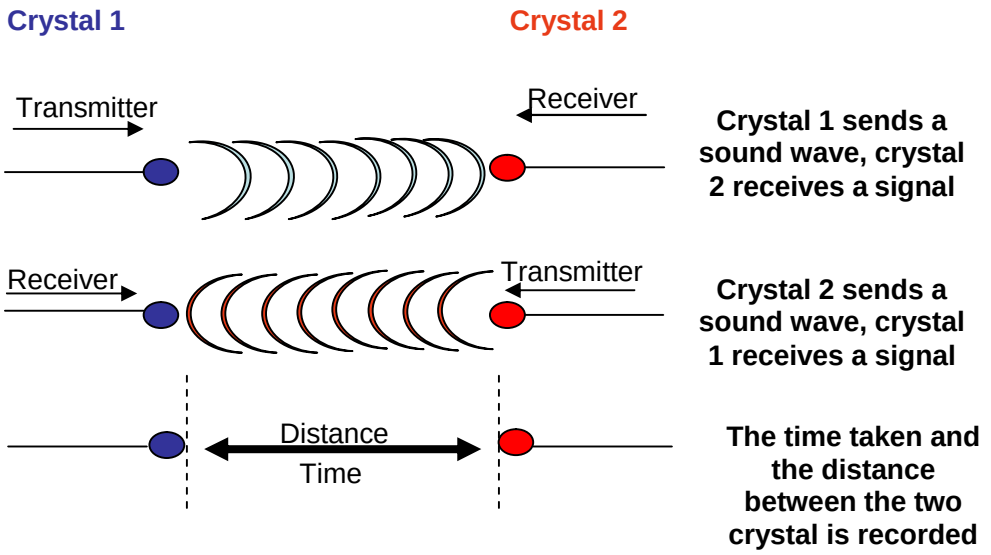

Figure 3.2: A diagram demonstrating how the ultrasound crystals enable the calculation of left ventricle (LV) axis dimensions by acting as both transmitters and receivers. A specialised digital circuitry continuously measures the distance between the transducers throughout the entire cardiac cycle allowing LV axial dimensions to be measured while the LV is moving

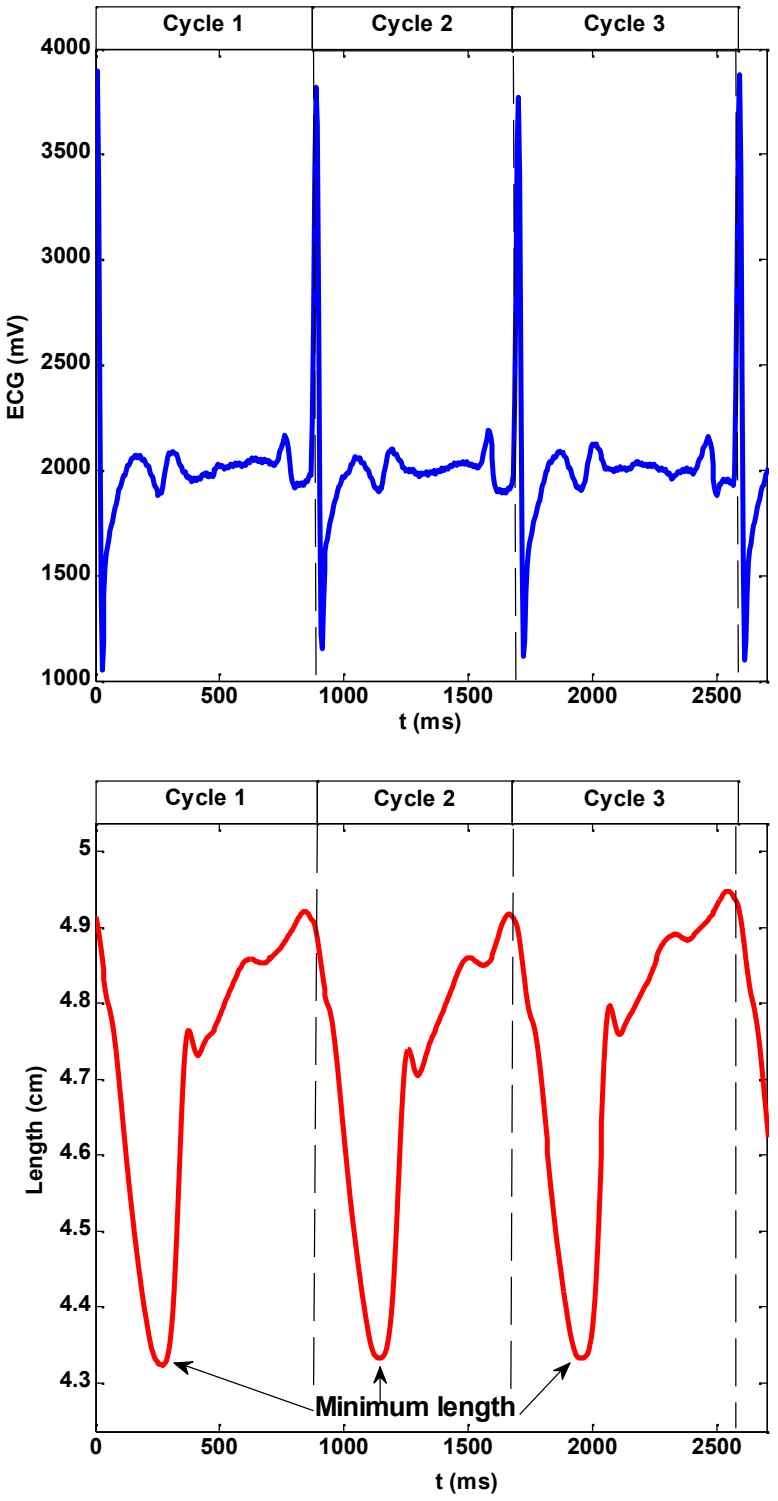

Figure 3.3: 3 representative beats taken from one dog showing how the change in length of an axis can be collected by tracking the ultrasound crystals and plotted against time. In this example the distance between the two crystals in this example decreases from ~4.9cm to ~4.35 cm during each systole.

3.3.2 Data Measurements

Parameters measured

1. **LV pressure**
2. **Aortic pressure** ~ 1cm from the aortic root
3. **Aortic flow**~ 1cm from the aortic root
4. **ECG**
5. **LV minor axis movement** (septum to free wall)
6. **LV long axis movement** (base to apex)
7. **LV minor axis movement** (posterior to anterior wall): dogs 10 and 11
8. **Ascending aorta circumference-** post mortem

Parameters calculated

1. **LV Volume**: Volume $= 0.5((4/3) \times \Pi \times r1r2r3)$. The LV was considered as an ellipsoid, where r represents the LV dimensions: r1= long axis (base-apex). r2 = Septum-free wall and r3 =anterior wall-posterior wall. In the case where the anterior-posterior axis was not measured r3 (anterior-posterior) was considered equal to r2 (Septum-free wall). Volume is measured in cm^3.
2.
3. **Aortic Velocity**: Aortic flow = area × velocity (Q=AU). The aortic velocity can therefore be measured by dividing the aortic flow data measured at the aortic root by the aortic area. Ascending aorta radius was measured post-mortem and the aortic cross- sectional area was considered circular, $A= \pi r^2$

4. **Wave speed**: Calculated using the PU-loop method (Khir et al. 2001). When measured pressure is plotted against measured velocity the slope of the loop during early systole equals ρc, assuming blood density =1050Kg/m^3 . An example of a typical PU-loop is shown in **Figure 2.1 ,** chapter 2, and the full theory behind performing a PU-loop is explained in chapter 2, section 2.3.

5. **Wave Intensity:** Both using the original theory, see Chapter 2: section 2.7 and the new wave-reservoir theory See Chapter 2: section 2.7

6. LV axis velocity of shortening: The time of maximum shortening velocity of both axes was calculated by plotting the first derivative of the distance-time graph of LV axis movement during contraction. This is demonstrated in **Figure 3.4.** Plot a) is an example of LV minor axis shortening during systole acquired using the ultrasound crystals placed in the septum and free wall (the long axis shows a similar pattern of shortening when plotted). To identify the point of maximum velocity of shortening the first derivative of plot a) is calculated and then plotted against time. This is shown in plot b). Lengthening of the axis produces a velocity above the zero crossing while shortening of the axis produces a velocity below the zero crossing.

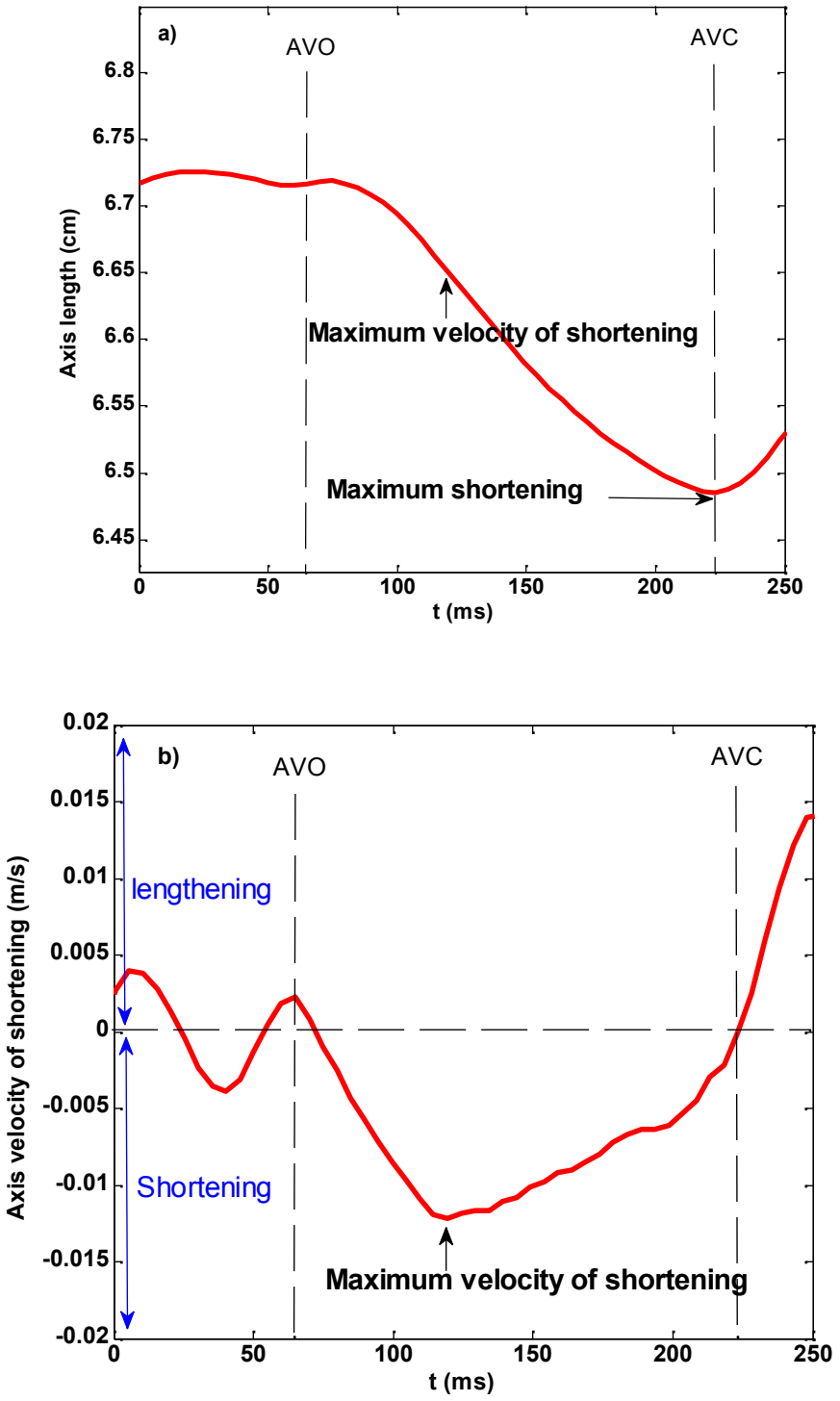

Figure 3.4. Plot a) is a representative example of left ventricle (LV) minor axis shortening from one dog during systole acquired using the ultrasound crystals placed in the septum and free wall. The point of maximum velocity of shortening is found by plotting the first derivative against time. This is shown in plot b). Movement that lengthens the axis has a velocity above the zero line while movement that shortens the axis has a velocity above the zero line. The time of maximum velocity of shortening located in plot b) is pointed out in plot a). AVO= aortic valve opening, AVC=aortic valve closure.

3.3.3 Data collection

Custom written programs in Matlab (The MathWorks Inc., MA, and USA) were used to analyse all data. The R wave of the QRS complex was always taken as t=0 and the following haemodynamic events were identified and their timings recorded: peak measured aortic blood velocity **(U_{max}),** peak aortic forward blood velocity **(U_f)** and an inflection point on the descending limb of the aortic blood velocity **(U_i)** identified by plotting dU/dt against time as shown in **Figure 3.5;** Other haemodynamic events also measured were peak measured aortic blood pressure **(P_{max}),** peak aortic forward blood pressure **(P_f);** Peak LV pressure (**P_{LV})** and its derivative with respect to time (**dP_{LV}).**

Wave Intensity Analysis: The main waves of WIA observed during systole were plotted using the theory explained in chapter 2 and shown in **Figure 3.6**. The times of the following events were recorded: Net FCW onset (**dI+C)**, separated FCW onset **(dI_{+c})**, net BCW onset (**dI-C)**, separated BCW onset **(dI_{-c})**, BCW peak**.** Net FEW onset **(dI+E)**, separated FEW onset **(dI_{+e})**. Looking at **Figure 3.6 b)** it is difficult to determine the onset of the FEW without zooming in. The FEW was noted to consistently have a slow onset followed by a rapid increase; the times of both phases were recorded. FEW onset **dI_{+e1}**, FEW rapid phase **dI_{+e2}**. **Figure 3.7**

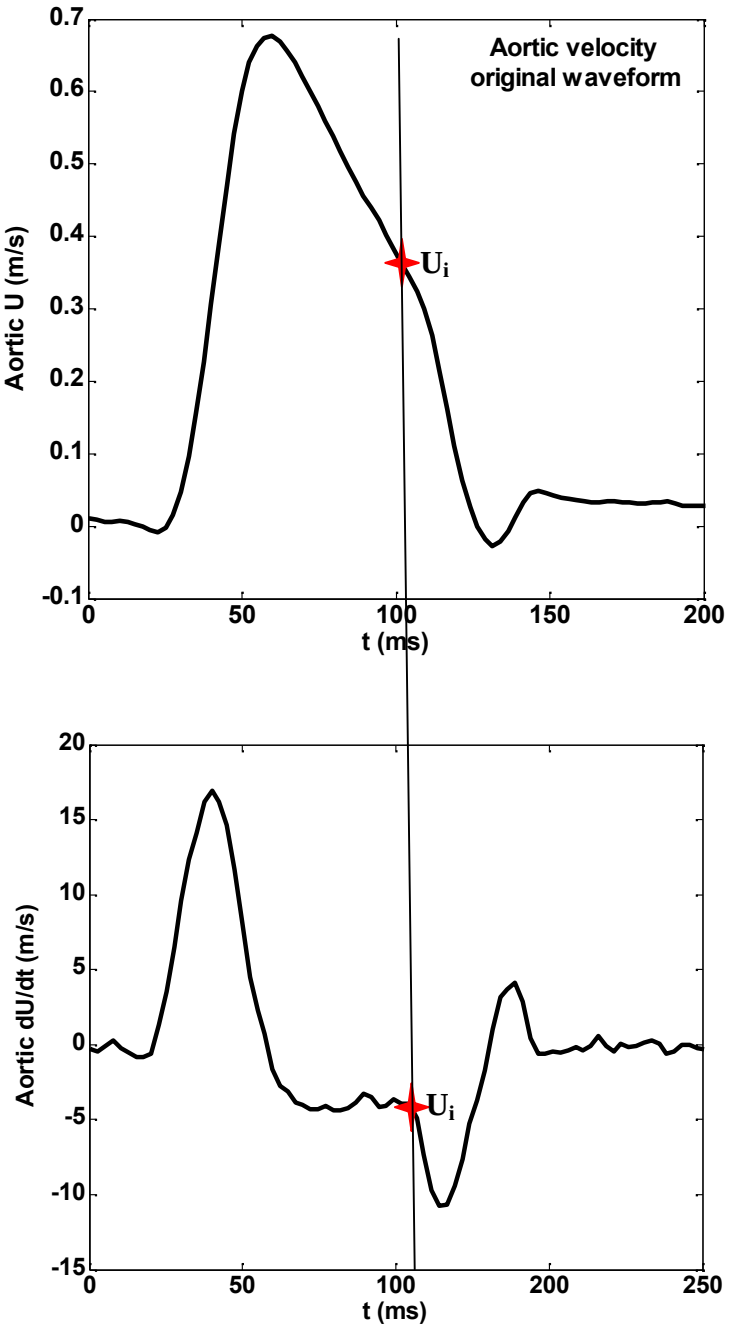

Figure 3.5: This figure shows how the inflection point on the aortic velocity waveform ($\mathbf{U_i}$) was determined. The 1st derivative of aortic velocity with respect to time (dU/dt) was calculated and plotted against time. Aortic velocity reaches a peak in mid-systole and decreases slowly for ~70ms after which the dU/dt rapidly drops. The sudden drop of dU/dt is identified by the red star (✦), which was taken as the time of $\mathbf{U_i}$.

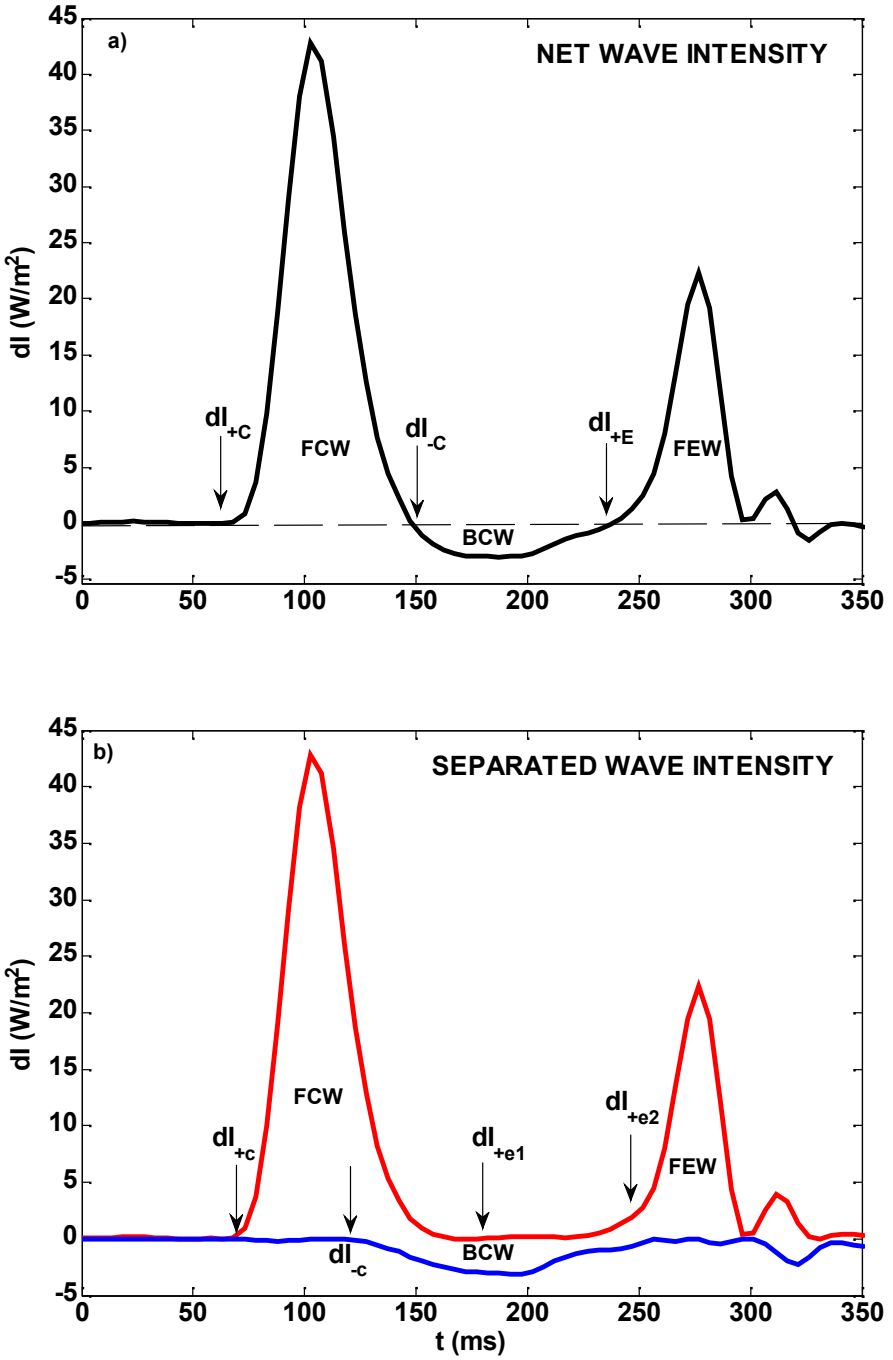

Figure 3.6: A typical example of a) the 3 main net waves of wave intensity analysis (WIA) observed during systole. b) The 3 main waves after separating the net WIA into its forward (red) and backward (blue) waveforms. The times of all the important haemodynamic events highlighted were recorded. $\mathbf{dI_{+C}}$ = Net FCW onset, $\mathbf{dI_{+c}}$ =separated FCW onset. $\mathbf{dI_{-C}}$ = Net FCW onset, $\mathbf{dI_{-c}}$ =separated FCW onset $\mathbf{dI_{-cmax}}$ =FCW peak. $\mathbf{dI_{+E}}$ = Net FCW onset, $\mathbf{dI_{+e1}}$ =separated FEW onset , $\mathbf{dI_{+e2}}$ =FEW rapid increase in energy.

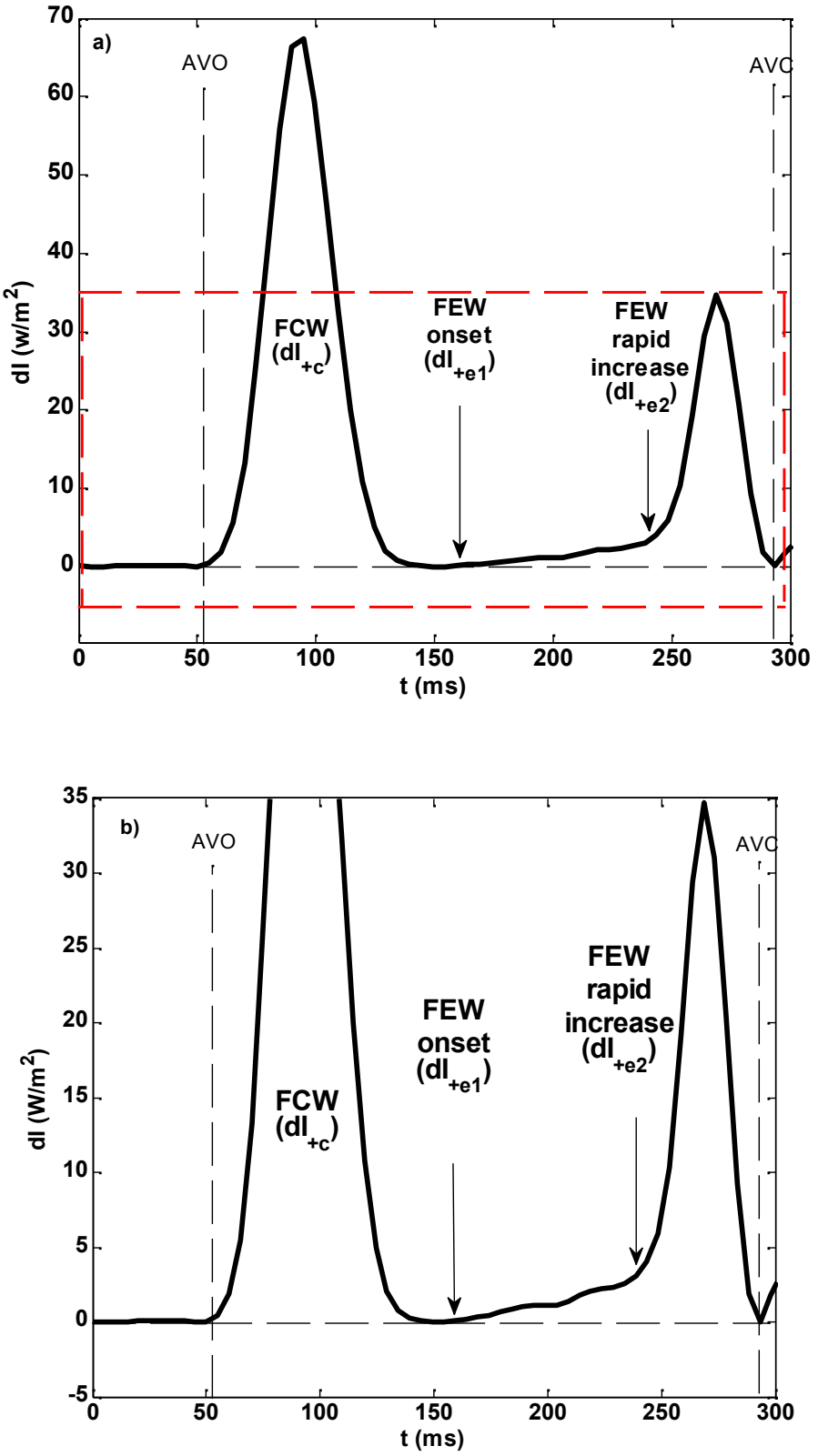

Figure 3.7: Forward wave intensity in (a) and an enlargement of the forward expansion wave (FEW) to show the onset of the slow (**dI$_{+e1}$**) the rapid (**dI$_{+e2}$**) phases in (b). The FEW was consistently observed to have a slow onset followed by a rapid increase in energy. AVO=aortic valve opening, AVC= aortic valve closure.

Left ventricle wall movement

Velocity of the LV long (L) and minor (M) axis (and anterior-posterior (AP) axis when available) wall shortening (contraction) was determined by differentiating the movement with respect to time as seen in **Figure 3.4**. Any velocity above zero represents axis lengthening and is positive while any velocity below the zero line represents axis shortening and is negative. It is noted that each axis was observed to contract in three stages, although all individual stages of each axis do not occur simultaneously. **Figure 3.8**.

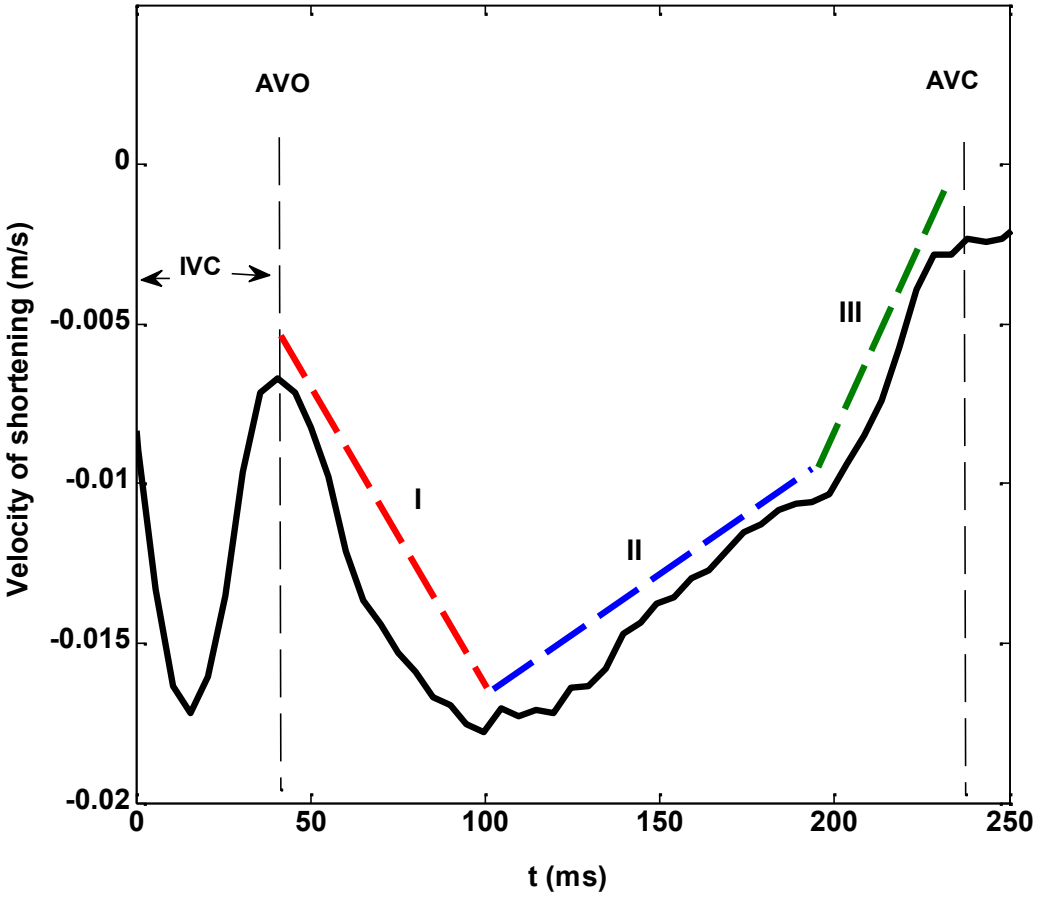

Figure 3.8: An example of a typical plot of minor axis velocity of shortening calculated by ultrasound crystal movement differentiated by time, as explained in **Figure 3.2**. After the aortic valve opens all axes share a similar pattern, which can be split into 3 stages. Stage **1** increasing velocity of shortening, stage **II** decreasing velocity of shortening; stage **III** a further change in the rate of shortening. AVO= aortic valve opening, AVC= aortic valve closure, IVC= isovolumic contraction.

Stage 1: Begins as the aortic valve opens, the axis shorten with increasing velocity until reaching their respective maximum rates of shortening ($\mathbf{L_{maxU}}$, $\mathbf{M_{maxU}}$ and $\mathbf{AP_{maxU}}$ when available).

Stage II: Begins at the point of maximum velocity of shortening, after which the velocity of each axis begins to decline. The axes are still shortening but at a reduced rate until they reach an inflection point in late systole. ($\mathbf{L_i}$, $\mathbf{M_i}$ and $\mathbf{AP_{i)}}$

Stage III : Begins at the onset of the inflection point until the time of aortic valve closure. During this stage the axes are continuing to shorten but their rate of deceleration steepens. The inflection point was identified by plotting the second derivative of minor and long axis movement and observing minima, after which the curve begins to increase. **Figure 3.9**

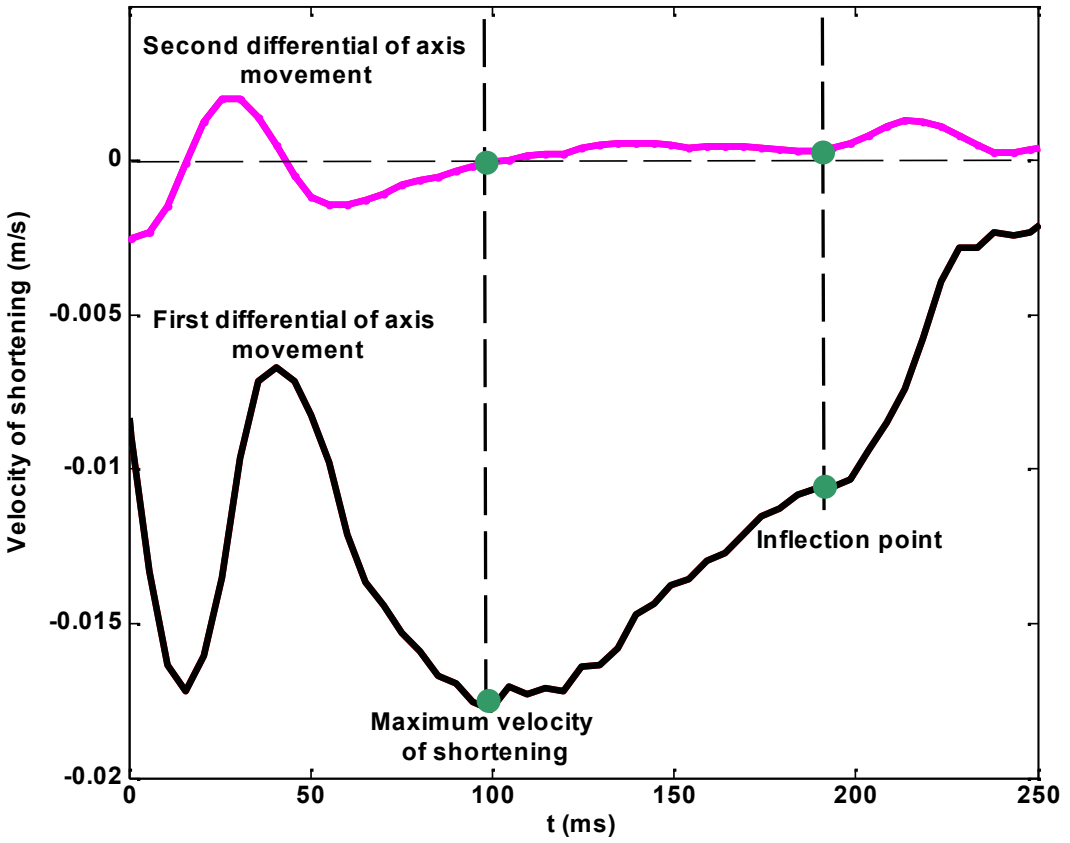

Figure 3.9: A plot to demonstrate how both the peak velocity of shortening and the inflection point can be determined. The second differential of axis movement (pink trace) was plotted against the first differential (black trace). The zero crossing of the second differential represents peak velocity of shortening while a secondary increase in rate of shortening represent the shoulder seen in late systole.

3.3.4: Statistical analysis

A representative cycle was analysed during steady state for each dog. All data are presented as mean ± SD and Concordance correlation coefficients (CCC) were calculated using Lin's concordance method to determine the extent of agreement between variables occurring at similar times. Pearson correlation coefficients were calculated to establish the strength of the relationship between velocity of LV axes shortening and the magnitude of the FCW and FEW

Pearson correlation coefficient *(r):* Pearson product-momentum correlation coefficients are applied to measure the linear dependence (correlation) between the slopes of LV wall velocity (acceleration and deceleration stages) with the magnitude of the forward waves. The coefficient ranges from –1 to 1, with +1 indicating a perfect positive relationship and –1 indicating a perfect negative relationship and zero indicating no relationship.

Concordance coefficient: In 1989 Lawrence Lin first proposed the "concordance correlation coefficient" (CCC) to assess concordance in continuous data. The concordance correlation coefficient allows the agreement (reproducibility and inter-rater reliability) between alternative methods for continuous data.

Lin has the form of the concordance correlation coefficient ρ_c as

$$\rho_c = \frac{2\rho\sigma_x\sigma_y}{\sigma_x^2 + \sigma_y^2 + (\mu_x - \mu_y)^2}, \quad \textbf{(3.1)}$$

where μ_x and μ_y are the means for the two variables and σ_x^2 and σ_y^2 are the corresponding variances ρ is the correlation coefficient between the two variables.

When the concordance correlation coefficient is computed on an N-length data set the form is

$$r_c = \frac{2s_{xy}}{s_x^2 + s_y^2 + (\bar{x} - \bar{y})^2}, \quad \textbf{(3.2)}$$

where the mean is computed as

$$\bar{x} = \frac{1}{N}\sum_{n=1}^{N} x_n \qquad \textbf{(3.3)}$$

and the variance

$$s_x^2 = \frac{1}{N}\sum_{n=1}^{N} (x_n - \bar{x})^2 \qquad \textbf{(3.4)}$$

and the covariance

$$s_{xy} = \frac{1}{N}\sum_{n=1}^{N} (x_n - \bar{x})(y_n - \bar{y}) \qquad \textbf{(3.5)}$$

Concordance coefficients will be calculated to determine the time agreement between various parameters throughout this thesis.

3.3.5 Reproducibility

The time intervals from the R wave of the QRS complex to the peak velocity of shortening of both the minor and long axis as well as to the onset of all three main waves were repeated three times for each beat analysed in each dog. The mean difference±SD to the time of $\mathbf{M_{maxU}}$ was 2±2ms (within subject coefficient of variation = 1.81%). The time to $\mathbf{L_{maxU}}$ was 2±4ms (within subject coefficient of variation = 1.36%). The time to the onset of the FCW was 1±2ms (within subject coefficient of variation = 1.78%), the onset of the BCW was 1±1ms (within subject coefficient of variation = 0.93%), and the onset of the FEW was 2±3ms (within subject coefficient of variation = 1.34%). All beats were plotted individually using the same MatLAB program, with identical smoothing and shifting functions by the same operator who used the zoom function to locate exact times. For these reasons the reproducibility is at a very high standard.

3.4 Results

3.4.1 Left ventricle wall movement

Pre-ejection: This chapter will begin with describing LV wall movement during isovolumic contraction (IVC). LV peak velocities and timings were recorded for both the minor and long axes throughout the IVC period. During IVC the LV long axis lengthens in all dogs 100% of the time reaching an average velocity of 0.024±0.014m/s at 51±15ms after the R wave after the QRS complex. The minor axis shortens in 7 dogs (64%) and lengthens in the remaining 4 (36%). In the 4 dogs that were observed to have a lengthening minor and long axis during IVC it can be assumed that the anterior to posterior axis that was not measured shortens during IVC. Average shortening velocities of the minor axis reach -0.016±0.013 m/s at 38±16ms while lengthening velocities reach 0.013±0.05 m/s. When measured (dog 10 and 11 only) the AP axis shortens in dog 10 and lengthens in dog 11 reaching velocities of 0.005±0.002m/s at 23±10ms and 0.033±0.037m/s at 42±10ms respectively. **Figure 3.10** nicely demonstrates typical long and minor axis behaviour during isovolumic contraction (IVC) in one of the dogs.

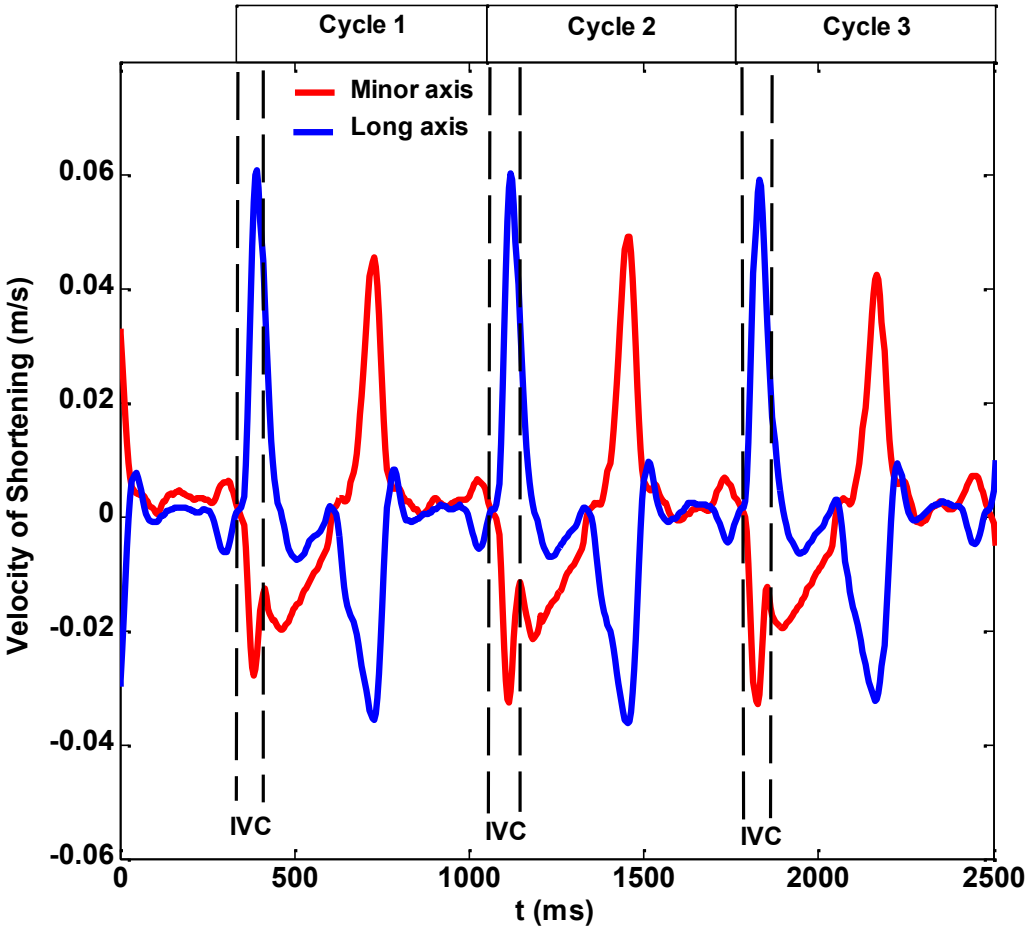

Figure 3.10: Three representative cycles taken from one dog to highlight typical long and minor axis behaviour during isovolumic contraction (IVC). The dashed black lines enclose the period of IVC within each cycle. It can clearly be seen that the left ventricle long axis (blue) increases in length while the minor axis (red) shortens in this example.

Ejection:

Using the aortic flow velocity waveform as a physiological marker, ejection can be divided into three stages: early, mid and late systole. Early systole is taken from the time of zero velocity to the time of peak velocity ($\mathbf{U_{max}}$). Mid systole starts from the time of peak flow velocity until a time later in systole when an inflection point is observed on the velocity waveform ($\mathbf{U_i}$). Late systole starts at the time of $\mathbf{U_i}$ and finishes at the time of aortic valve closure. These time stages are demonstrated in **Figure 3.11.** The movement of both the LV minor and long axes were observed and can be explained in terms of their behaviour during these three stages of ejection.

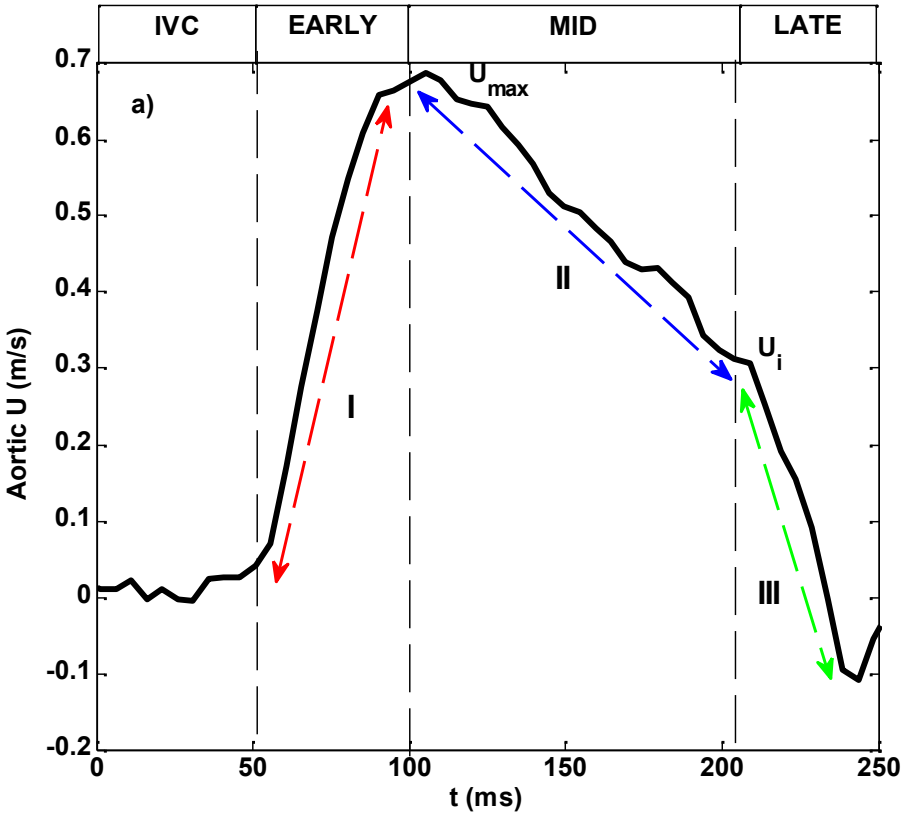

Figure 3.11: A plot of aortic flow velocity demonstrating how ejection can be divided into early, mid and late systole. Early systole (Stage I) is from the time of zero velocity to the time of peak velocity ($\mathbf{U_{max}}$). Mid systole (stage II) starts from the time of peak flow velocity and finishes at a time where an inflection point is observed on the velocity waveform ($\mathbf{U_i}$). Late systole (stage III) starts at the time of $\mathbf{U_i}$ and finishes at the time of aortic valve closure when velocity is zero again.

Early systole

After averaging a representative beat from each dog it is seen that the aortic valve opens 54±22ms after the R wave of the QRS complex. At the opening of the aortic valve the minor axis undergoes a second period of shortening in these animals as seen in **Figure 3.12**. In some cases the minor axis started this second period even before the valve opens, at an average time of 51±23ms after the R wave. In contrast, the long axis initially shows a small increase in length after opening of the aortic valve but subsequently begins to shorten at 85±27ms. The commencement of long axis shortening during early systole therefore lags minor axis shortening by ~30 ms. This can also be seen in **Figure 3.12** (delay 1). Even at this early stage of systole there is a natural asynchrony between the two axes. Both minor and long axes then continue to shorten rapidly during early systole. The end of early systole is marked not only by peak aortic flow but also by peak shortening velocity of the minor axis ($\mathbf{M_{maxU}}$) at 111±26ms. The minor axis reaches an average shortening speed of 0.0015±0.004m/s.

Mid systole

Mid systole begins at the time of $\mathbf{U_{max}}$. During this stage of ejection the velocity of shortening of the LV long axis increases until eventually reaching its peak shortening velocity ($\mathbf{L_{maxU}}$). On average $\mathbf{L_{maxU}}$ occurs 29± 13 ms later than $\mathbf{M_{maxU}}$ at 141±26ms. This is indicated in **Figure 3.12** (delay 2). The long axis therefore reaches its peak velocity of shortening during mid-systole unlike the minor axis that reaches its peak velocity of shortening at the end of the early stage of systole. The long axis reaches an average shortening speed of 0.009±0.005m/s. The long axis does not exceed the shortening velocities of the minor axis with the exception of dog 8, an example of this is shown in **Figure 3.13**.

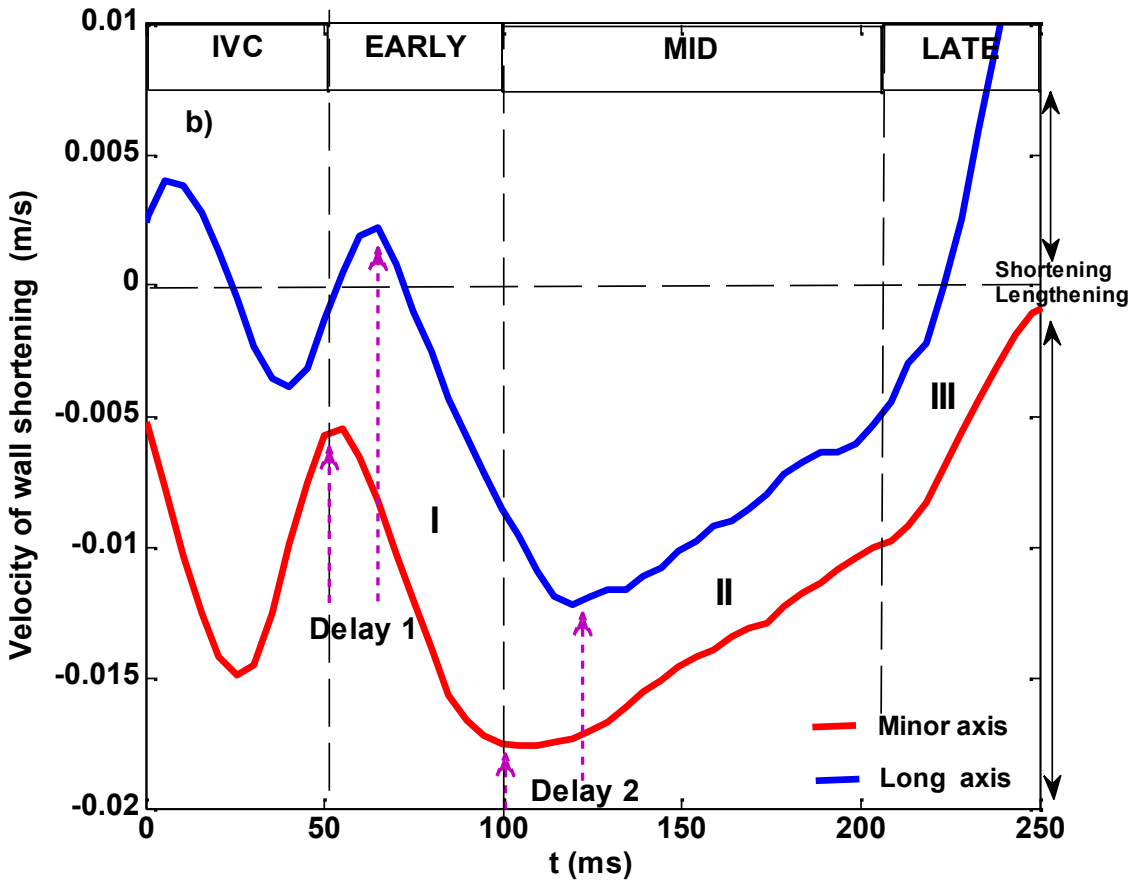

Figure 3.12: Shortening velocity of the long (blue) and minor (red) axes during the early, mid and late stages of systole. The stages of systole were determined by the nature of the aortic velocity plot (See **Figure 3.11**). Notice that during the early stages of isovolumic contraction (IVC) the minor axis is shortening while the long axis is lengthening. During early ejection the long axis begins to shorten ~30ms after the minor axis. (delay 1) and reaches its peak velocity of shortening ~30ms after that of the minor axis (delay 2). In this example the minor axis peak velocity of shortening is ~0.018m/s compared to the long axis which is only 0.012m/s. The minor axis was seen to reach higher velocities in 10 out of the 11 dogs measured.

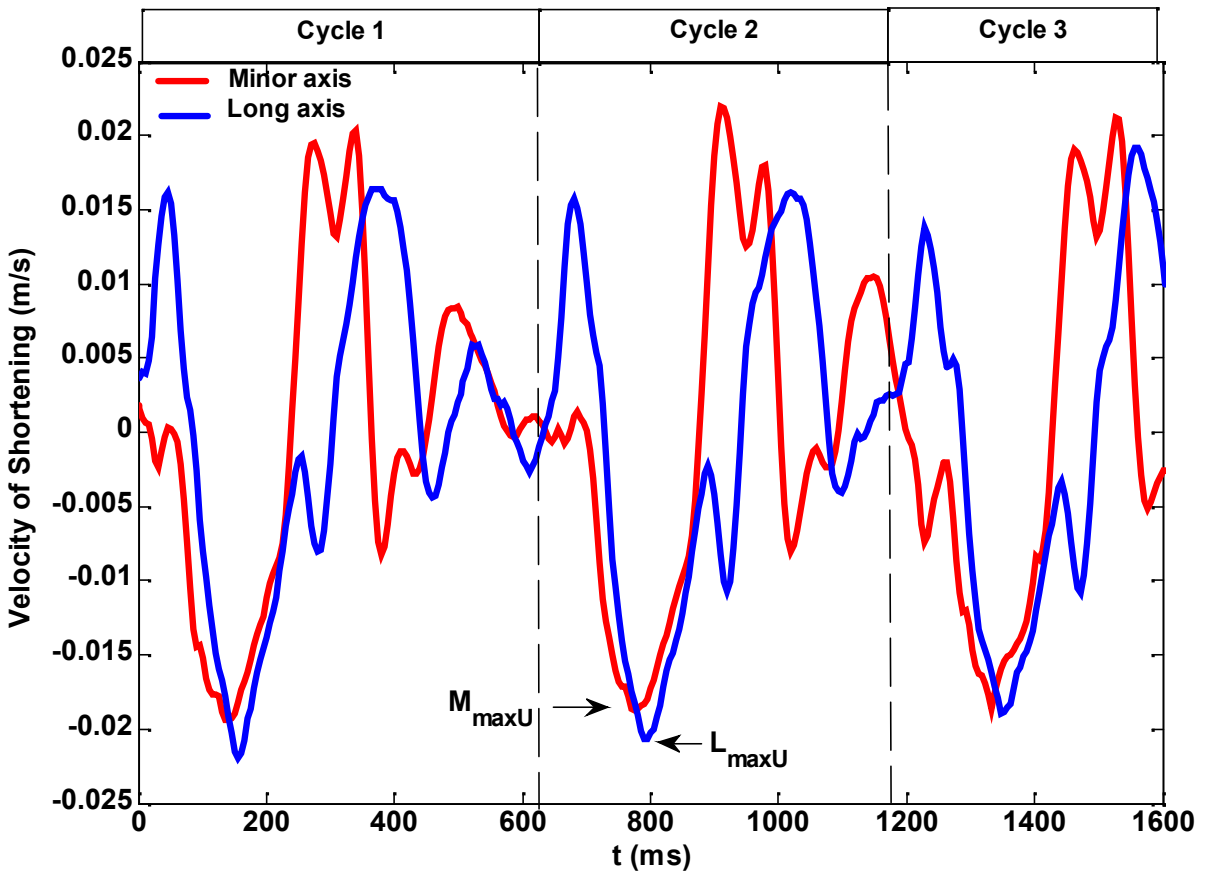

Figure 3.13: 3 consecutive beats of velocity of shortening of the minor (red) and long (blue) axes plotted using data collected from dog 8. Unlike in all the other dogs, maximum shortening velocity of the long axis, $\mathbf{L_{maxU}}$ is faster than that of the minor axis, $\mathbf{M_{maxU}}$ in this dog.

Late systole

Late systole begins at the point of $\mathbf{U_i}$ on the aortic velocity waveform (**Figure 3.11**) During late systole both axes show an increased rate of decline of shortening. The time of this point for both axes occurred ~190± ms after the R-wave. The two inflection points ($\mathbf{L_i}$, $\mathbf{M_i}$) coincide with each other. Average difference 0.00±0.01s, CCC=0.88. The time of the inflection point are identified in **Figure 3.14.**

.

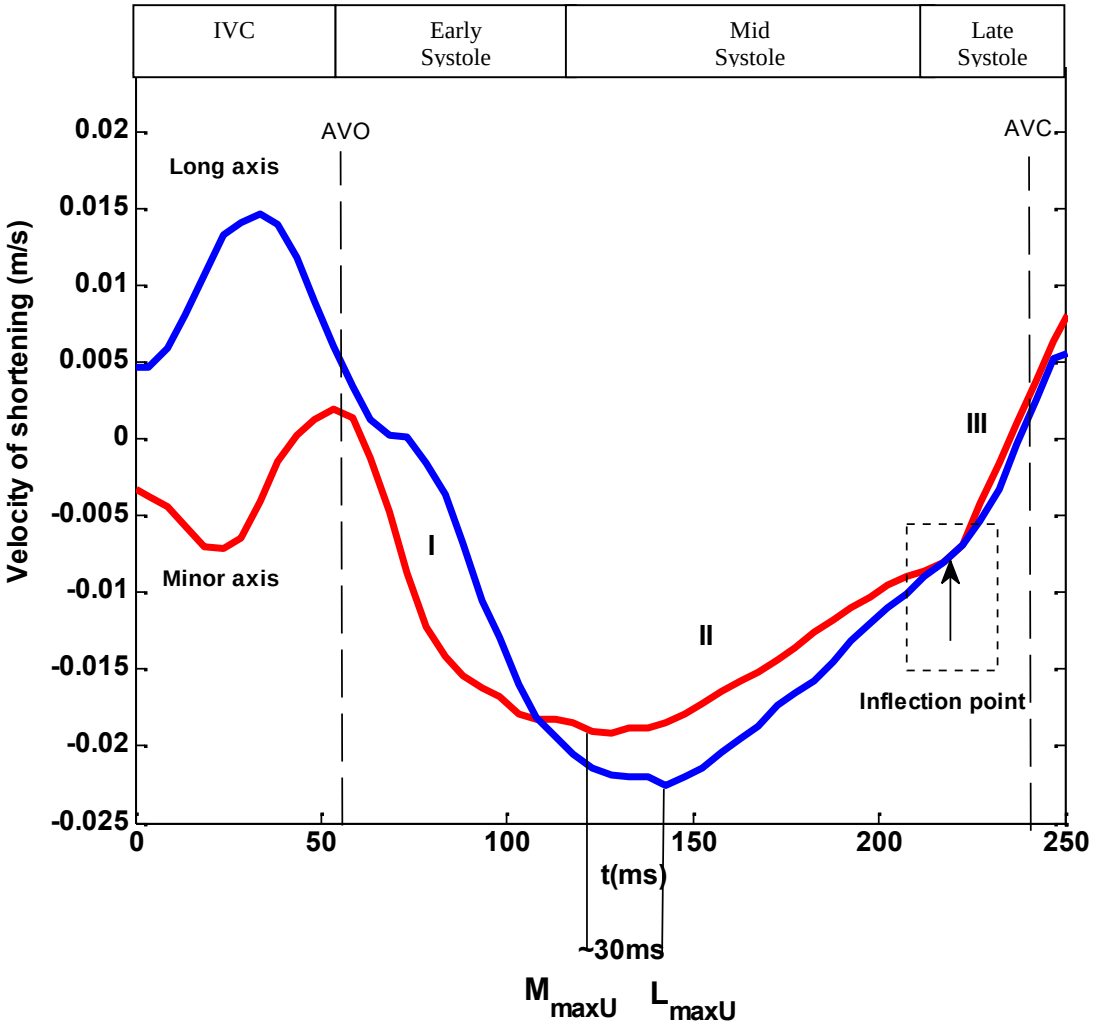

Figure 3.14 A plot of long (blue) and minor (red) axis shortening velocities taken from dog 8 showing the different phases of LV wall shortening. Stage I represents acceleration of shortening velocity; stage II and stage III are both deceleration of shortening velocity phases. The inflection points observed at the start late systole are specifically highlighted.

3.4.2 Original wave intensity analysis (WIA)

The timings of all haemodynamic parameters were calculated throughout the cardiac cycle. The sequence of events during systole can be seen in **Figure 3.15**. The times of all important haemodynamic events were recorded and the events were observed to fall into three groups each within one of the stages of aortic velocity and axis contraction described previously in **Figures 3.11 and 3.12.** Events within each group occur simultaneously. **Table 3.1** shows the average timings from all 11 dogs. Individual results can be seen in **appendix 3.1 and 3.2**

Table 3.1: Average times of events measured from the R wave of the QRS complex. All events fall into three groups labelled group A,B and C. Aside from $\mathbf{U_{max}}$, all events within each group occur almost simultaneously, see **Figure 3.15**. $\mathbf{M_{maxU}}$ = maximum shortening velocity of the minor axis, $\mathbf{U_{max}}$ = peak aortic flow, $\mathbf{L_{maxU=}}$ maximum shortening velocity of the long axis, $\mathbf{dI_{+c}}$ =separated forward compression wave onset**,** $\mathbf{dI_{-c}}$ =separated backward compression wave onset**,** $\mathbf{dI_{+e1}}$ =separated forward expansion wave onset**,** $\mathbf{dI_{+e2}}$ =forward expansion wave rapid increase in energy. $\mathbf{P_{max=}}$ peak aortic pressure, $\mathbf{U_{fd=}}$ peak forward aortic velocity, $\mathbf{P_{fd}}$ **=** peak forward aortic pressure**,** $\mathbf{L_i}$= long axis inflection point, $\mathbf{M_i}$ = minor axis inflection point.

Group A		**Group B**		**Group C**	
$\mathbf{M_{maxU}}$	110±40ms	$\mathbf{L_{maxU}}$	147±20ms	$\mathbf{dI_{+e2}}$	191±18ms
$\mathbf{U_{max}}$	125±39ms	$\mathbf{dI_{+e1}}$	149±23ms	$\mathbf{U_i}$	190±17ms
$\mathbf{dI_{-c}}$	107±41ms	**Pfd**	149±27ms	$\mathbf{P_{max}}$	192±27ms
		Ufd	149±27ms	$\mathbf{M_i}$	189±20ms
				$\mathbf{L_i}$	190±20ms

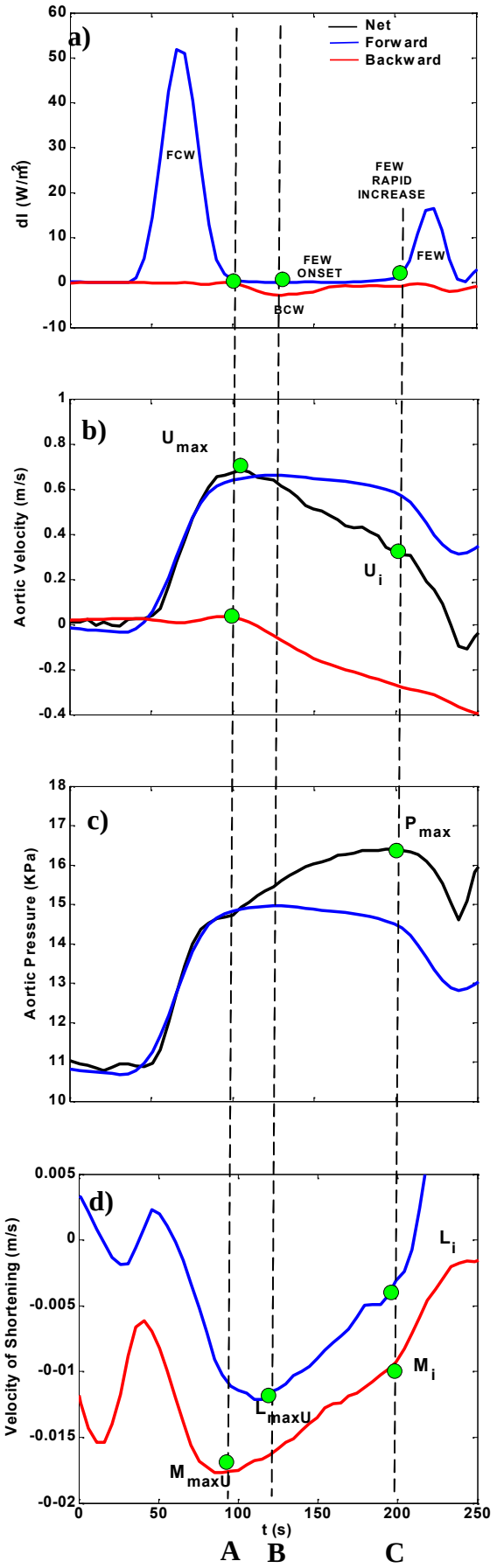

Figure 3.15: A representative cycle taken from dog 9 showing all haemodynamic events and the groups that they fall into. The green dots represent times of important haemodynamic events. The times of these events fall into three time groups. A, B and C. The groups are explained on pages 92 and 93 and relate to **Table 3.1**. FCW= forward compression wave, BCW= backward compression wave, FEW= forward expansion wave, $\mathbf{U_{max}}$ = peak aortic velocity, $\mathbf{U_i}$= aortic velocity inflection point, $\mathbf{P_{max}}$= peak aortic pressure. $\mathbf{M_{maxU}}$= maximum shortening velocity of the minor axis, $\mathbf{L_{maxU}}$= maximum shortening velocity of the long axis $\mathbf{L_i}$= long axis inflection point, $\mathbf{M_i}$=minor axis inflection point. As always, the LV long axis is plotted in blue, while the minor axis is plotted in red (plot **d**).

***Group A:* ~110ms after the R wave of the QRS complex.**

After averaging the representative cycles from each dog it was seen that at this time the minor axis reaches its maximum velocity of shortening, $\mathbf{M_{maxU}}$, but the velocity of shortening of the long axis continues to increase. See **Figure 3.15d**. The time of $\mathbf{M_{maxU}}$ leads to peak aortic velocity **($\mathbf{U_{max}}$)**. This makes physiological sense there is less of a push coming from the LV mid-wall fibres, average difference (0.01±0.02s, CCC= 0.76). During this stage the FCW produced in early systole was found to have propagated down the arterial bed and been reflected as a BCW. The BCW increases pressure and reduces flow (dP>0, dU<0), thus its arrival also brings about $\mathbf{U_{max}}$ as expected. A very interesting finding is that the arrival time of the separated BCW also corresponded closely with $\mathbf{M_{maxU}}$: (average difference 0.01±0.02s, CCC= 0.69). This finding presents a physiologically important question; does the BCW cause the LV minor axis to slow?

***Group B:* ~140ms after the R wave of the QRS complex**

At this time the LV long axis reaches its maximum velocity of shortening, $\mathbf{L_{maxU}}$, approximately 30ms after that of the minor axis, **Figure 3.15d.** The separated FEW always have a slow onset followed by a rapid increase, as seen in **Figure 3.7**. The onset of the separated FEW **($\mathbf{dI_{+e1}}$)** occurred 145±27ms after the onset of ejection and thus coincides with $\mathbf{L_{maxU}}$ **(**average difference 0.01±0.04s, CCC=0.97). **Figure 3.15** line B and **Figure 3.16.** The onset of the FEW therefore actually occurs in mid systole, considerably before the net FEW is seen in late systole. These events also coincide with peak forward pressure and velocity $\mathbf{P_f}$ (average difference 0.00±0.03s, CCC=0.96) and $\mathbf{U_f}$**,** (average difference 0.00±0.03s, CCC=0.96) as expected due to the nature of a FEW.

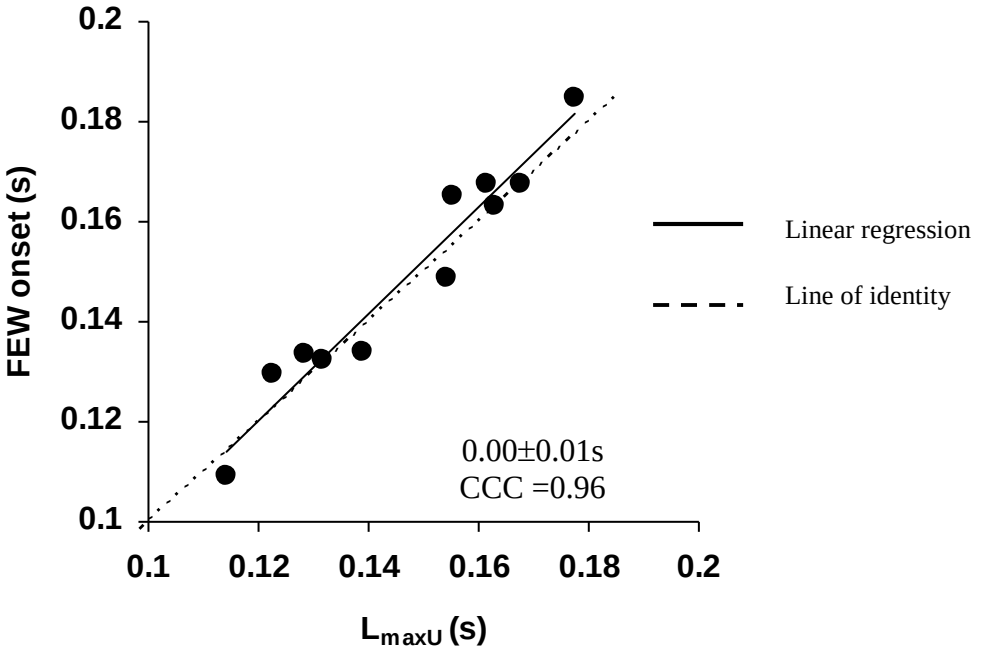

Figure 3.16: Lin's concordances plot using one representative beat from each dog to demonstrate the strong agreement found between the time of forward expansion wave (FEW) onset and the time of maximum velocity of shortening of the left ventricle long axis **(L_{maxU}).** These two events occur together in all beats analysed.

Group C: ~190ms after the R wave of the QRS complex

The rapid increase in energy of the FEW **(dI_{+e2})** occurred on average at 191±18ms after the R wave, (i.e. 40ms after the onset). As the rapid increase begins both LV axes show an inflection point in their velocity curves corresponding to a secondary decline in their rate of shortening, **L_i** , **M_i.** **Figure 3.15 and 3.17 a** and **b.**

At this time the shortening of both axes began to decline at a steeper rate until aortic valve closure. Also at this time peak aortic pressure **(P_{max})** (average difference 0.01±0.02s, CCC=0.82) is reached simultaneously with an inflection point **(U_i)** on the descending limb of the flow waveform (average difference 0.00±0.01s, CCC=0.77). Furthermore, onset of **dI_{+e2}** always coincides with a sharp decline in LV pressure (average difference 0.00±0.01s, CCC=0.97) as shown in **Figure 3.18**.

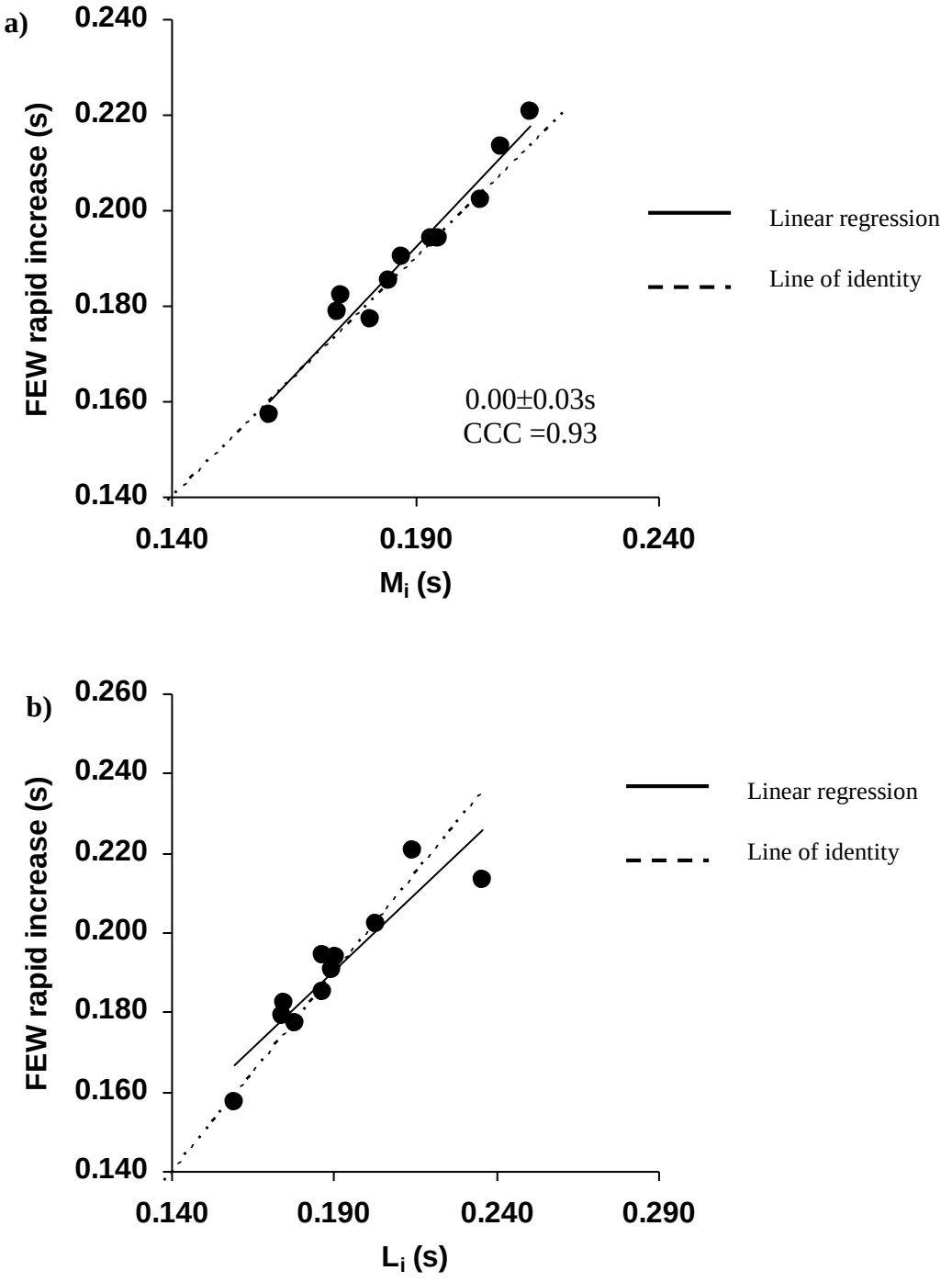

Figure 3.17: Lin's concordance correlation plot showing the excellent agreement between the rapid increase in energy of the forward expansion wave (FEW) and the inflection points seen on both axes velocity of shortening plots. **a) M_i b) L_i** .

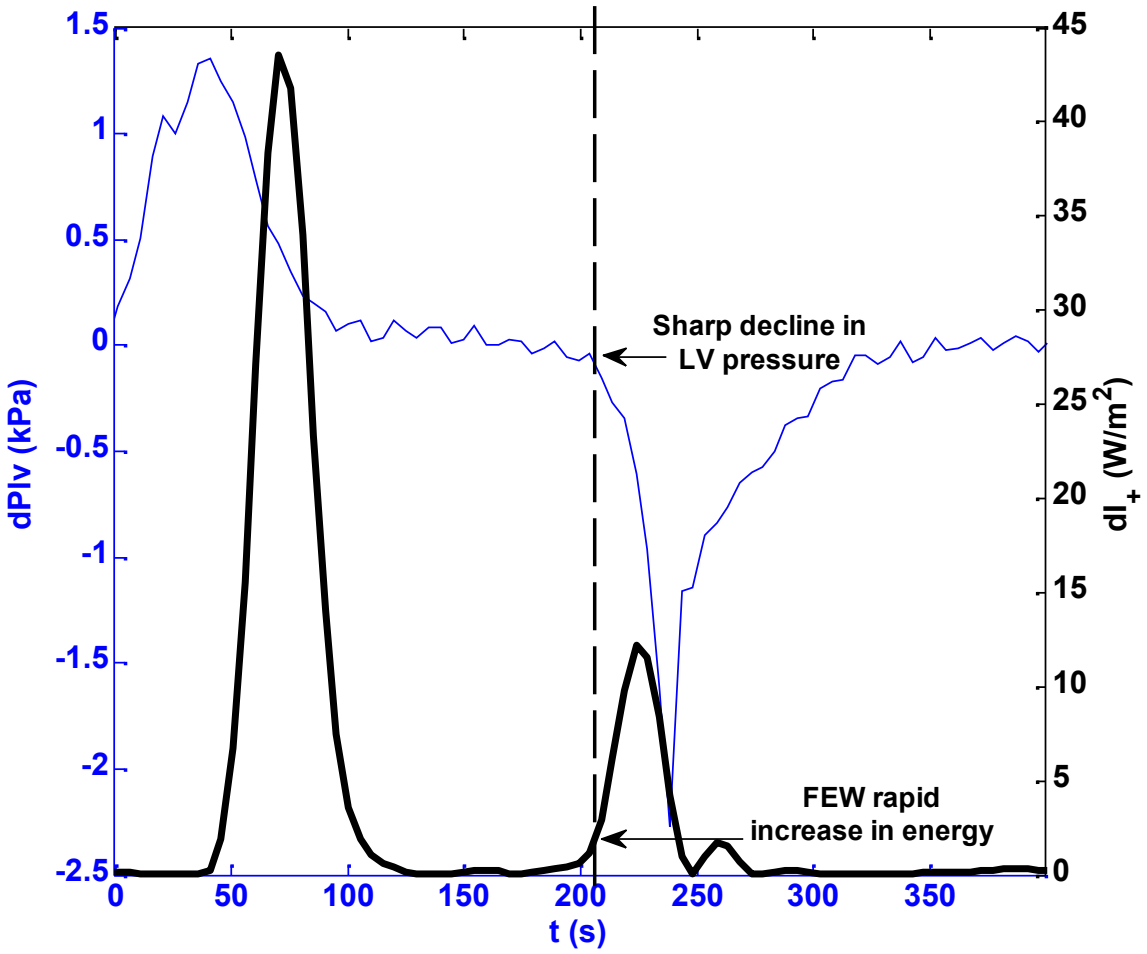

Figure 3.18: Forward wave intensity (black) and differentiated left ventricle pressure of dPLV (blue) plotted from a representative beat taken from dog 3. A sharp decline in left ventricle pressure coincides with the onset of the rapid increase of the forward expansion wave (FEW) as indicated by the vertical dashed line.

The expansion wave ends with aortic valve closure, which coincides with the end of long axis shortening. The minor axis continues to slowly shorten for an average of ~20ms after the long axis has stopped. These results enable us to now link LV mechanical activity to the 3 stages of systole, **Table 3.2**.

Table: 3.2: The left ventricle mechanical activities that accompany wave intensity waves during ejection. + indicates an increase, - indicates a decrease, WIA = wave intensity analysis.

Time	Minor axis stage of Velocity	Long axis stage of Velocity	Aortic Pressure	Aortic velocity	WIA
Early systole	Acceleration	Acceleration	+	+	FCW
Mid systole	Max velocity of shortening	Acceleration	+	-	BCW
Mid systole	Deceleration	Max velocity of shortening	-	-	FEW slow
Late systole	Deceleration	Deceleration	-	-	FEW rapid

3.4.3 Wave energy

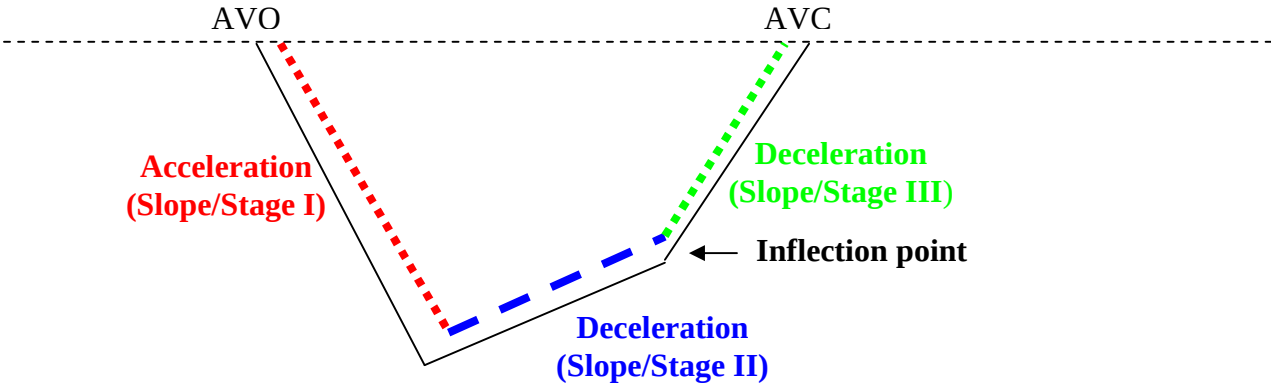

Figure 3.19: A sketch to highlight and explain the three slopes of axis velocity of shortening measured throughout ejection. The slopes match the 3 stages of shortening. See **Figure 3.8**. AVO= aortic valve opening, AVC= aortic valve closure.

The slopes of axes increasing velocity of shortening (acceleration) and decreasing velocity of shortening (deceleration) stages during systole were calculated and compared to the energy carried by the waves.

During early systole the rate of shortening velocity of both the minor and long axis correlates highly with the energy carried by the FCW (minor axis, r=0.-76, p <0.007, long axis, r=-0.82, p<0.002). **Figures 3.20 a/b**.

During late systole the slope of the long axis shortening velocity from the time of the inflection point to the beginning of axis lengthening during IVR (stage 3) correlates well with the energy carried by the forward expansion wave. **(**r=0.74, p=0.009). **Figure 3.21**

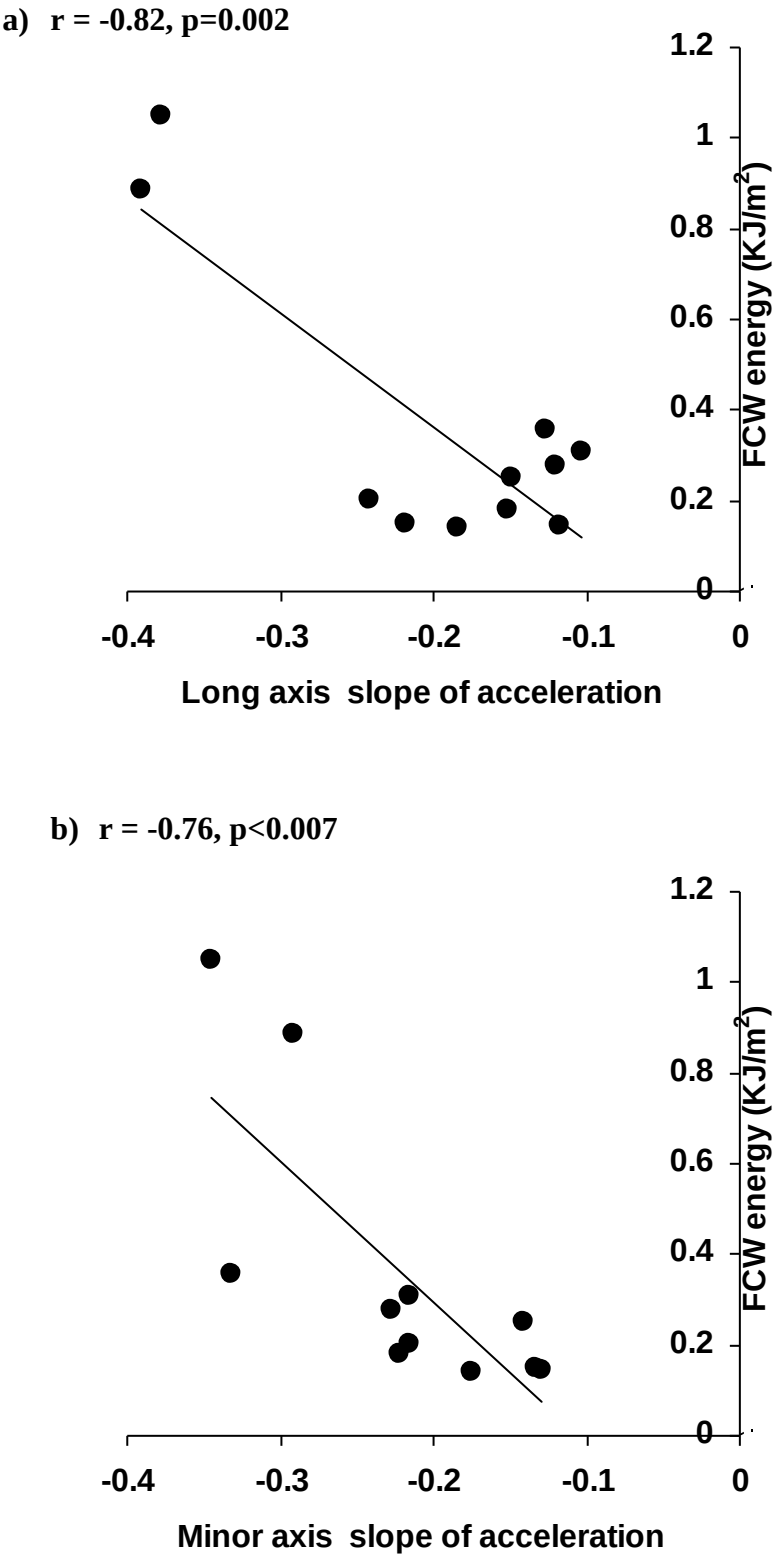

Figure 3.20 Correlation plot showing the strong relationship between the acceleration stage of a) Long axis and b) Minor axis shortening and the energy carried by the forward compression wave (FCW) during early systole.

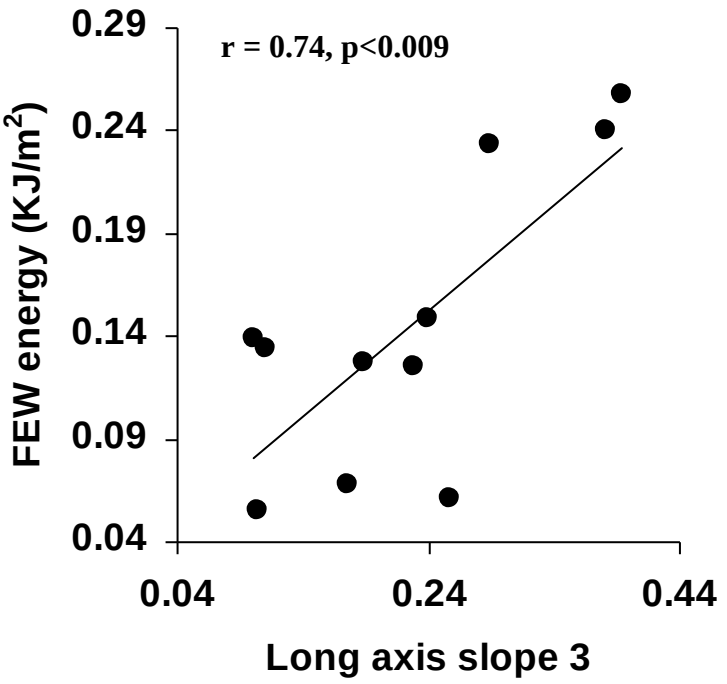

Figure 3.21: Correlation plot showing the strong relationship between the deceleration slope 3 (stage 3) of long axis velocity of shortening described in **Figure 3.19** and the energy carried by the forward expansion wave (FEW) during late systole.

3.4.4 Wave and reservoir theory

Introduction

While studying the timings of these waves it is important to consider that although WIA has been a well-accepted technique for 20years, it neglects the 'Windkessel' or reservoir effect caused by the elastic properties of the aorta (Davies et al 2007). As mentioned in chapter 1 section 1.7.2 and chapter 2, section 2.6 over the past few years a new mathematical version of WIA has been developed that takes into account the 'cushioning' effect of the aorta and splits the arterial system into reservoir and wave-transmitting only functional properties (Wang et al. 2004). This new form of analysis could perhaps enhance understanding of the mechanical relationship between the LV and the arteries further. The aim of this section was to calculate WIA after aortic reservoir subtraction, and compare it to WIA before reservoir subtraction, whilst observing any differences in the timing and magnitudes of the waves. The overall being plan to investigate the underlying relationship between ventricular wall movement in late systole and aortic ejection stages to identify the determinants of aortic flow deceleration.

Analysis: Full details for the calculation of aortic reservoir pressure and wave pressure plus WIA theory can see seen in Chapter 2, section 2.6 explains the mathematical calculation of aortic reservoir pressure.

Aortic pressure: Before and after aortic reservoir subtraction.

As explained in chapter 2, wave only pressure is calculated by substituting the aortic reservoir pressure away from measured aortic pressure. **Figure 3.22** is a representative example of this plotted from one cycle of aortic pressure acquired in dog 5.

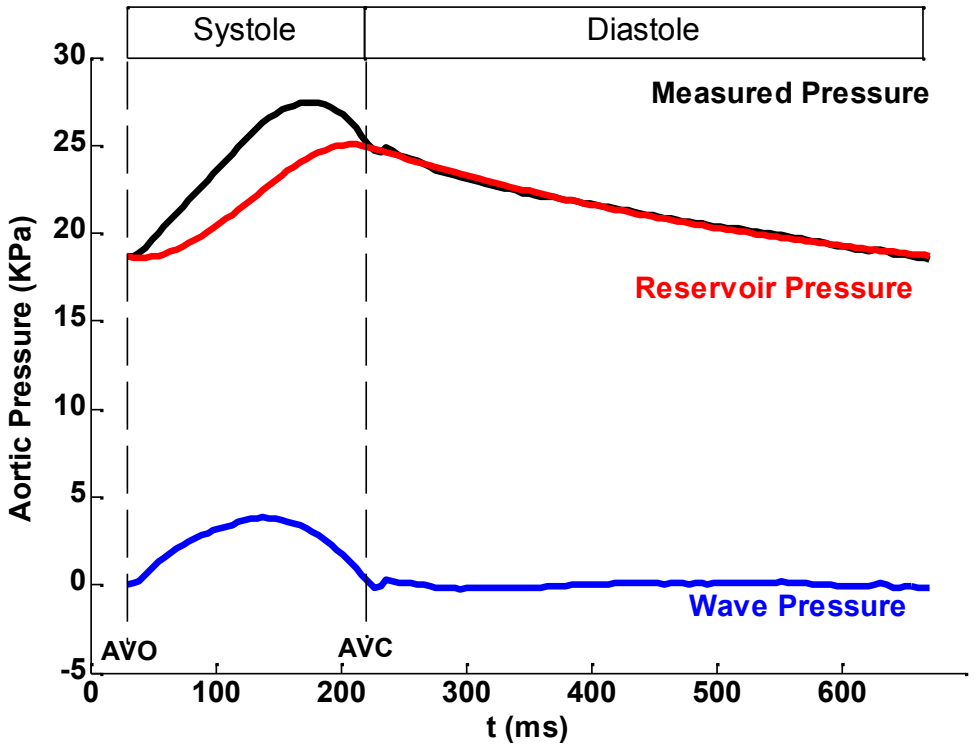

Figure 3.22: A figure demonstrating how aortic measured pressure (black) can be separated into reservoir (red) and wave only (blue) components. Reservoir pressure is first calculated then substituted from the measured pressure to get the wave only pressure. The wave only pressure is then used to calculate the waves using the original wave intensity analysis equations. See chapter 2, section 2.6 for mathematical details.

Wave intensity analysis: Before and after aortic reservoir subtraction

The distinct pattern of wave intensity observed before aortic reservoir subtraction described in **Figure 3.6** remains unchanged. During early systole a FCW is generated, in mid-systole a BCW wave returns to the LV and in late systole a FEW is consistently seen. The magnitudes and some of the timings of the waves however, do alter quite significantly.

Net waves: The timing of the FCW onset and FCW peak is unchanged (CCC=1.0, CCC=0.73) however when the aortic reservoir function is subtracted the net FCW is on average 27% smaller. The net reflected wave is present only 69% of the time after aortic reservoir subtraction. When present the BCW arrives at the heart at the same time before and after reservoir subtraction (0.00±0.01s, CCC=0.95). Reservoir subtraction dramatically decreases the reflected wave magnitude by 93% and the reflected wave reaches its peak a little (0.01±0.03s) earlier. The time of the FEW peak is unchanged (0.00±0.02s, CCC= 0.93) however unlike the other two waves, the timing of the net FEW onset is dramatically changed (0.04±0.05s ,CCC=0.036). The FEW occurs 44±3ms earlier, it is also 11% larger. **Figure 3.23**

Separated waves*:* Net waves can often be misleading before reservoir subtraction, to get more accurate timings one must separate the net waves into their forward and backwards components, as described in Chapter 2, section 2.4. When comparing the separated waveforms both before and after reservoir subtraction there is no difference in timing of the FCW (0.00±0.00 CCC=1.0) but the onsets of the BCW and FEW are altered very slightly. The BCW occurs a few ms later while the FEW occurs ~10ms earlier. However both waves still highly agree with their before reservoir subtraction timings. (BCW average difference 0.00±0.02s, CCC=0.78, FEW average difference 0.01±0.01s, CCC=0.87) **Table 3.3** shows the timing of all the net and separated waves both before and after reservoir subtraction.

Forward expansion wave phases: The FEW consistently has a slow onset followed by a rapid increase in energy. After aortic reservoir subtraction the slow onset is much more prominent, as shown in **Figure 3.24**

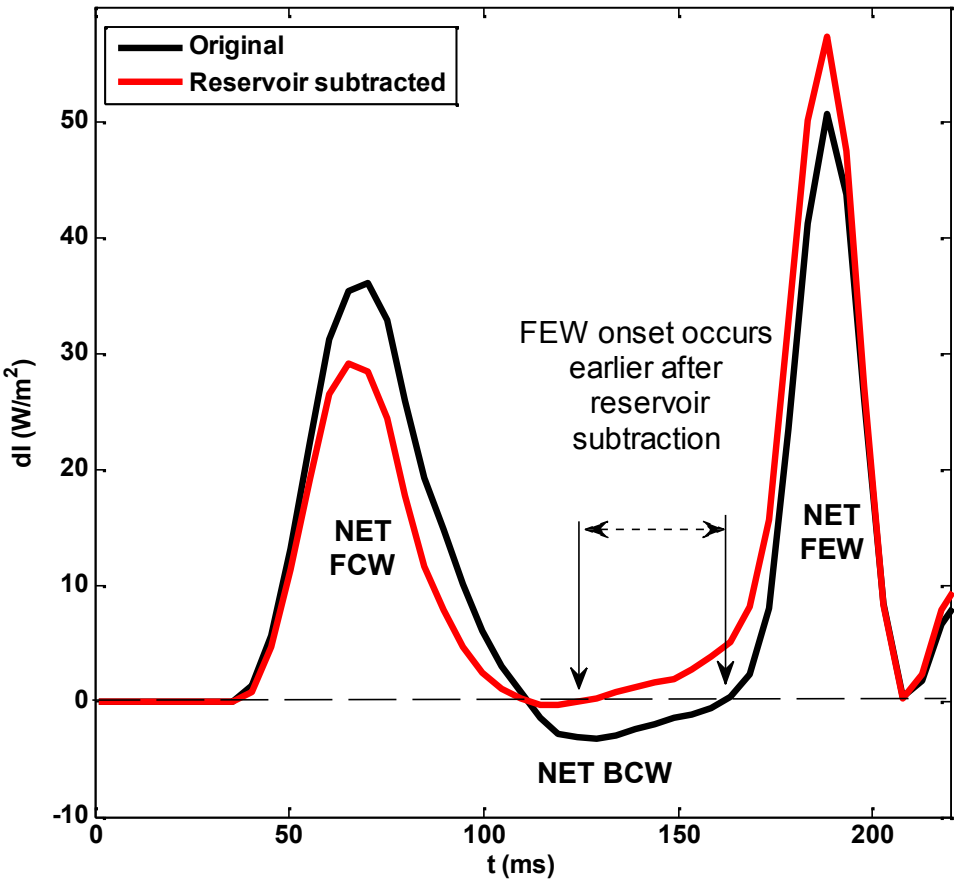

Figure 3.23: Data taken from one representative beat from dog 4. The black line represents the net forward compression wave (FCW), backward compression wave (BCW) and forward expansion wave (FEW) before aortic reservoir subtraction. The red line shows all three waves after aortic reservoir subtraction. The net FCW and BCW are reduced while the FEW energy is increased. This pattern is observed in all 11 dogs. After averaging representative beats from all dogs the net FCW is reduced by 27%, the BCW is reduced by a significant 93%. The FEW is 11% larger and interestingly occurs much earlier after aortic reservoir subtraction shown by the two black arrows in the figure. Net waves, however can be deceiving when looking at the onset of the FEW.

Table 3.3: Average times of all 11 dogs from the R wave of the QRS complex to the onset of the three main net waves and separated waves both before and after aortic reservoir subtraction. The difference observed between the net onset of the forward expansion wave (FEW) before and after reservoir subtraction disappears when the waves are separated, the concordance correlations for agreement are highlighted in yellow**.** The poor agreement between the two net times for FEW onset (CCC=0.36) becomes strong after separating the waves into their forward and backward components (CCC=0.87)**.**

Net waves				
Wave	**Onset before reservoir subtraction**	**Onset after reservoir subtraction**	**Difference**	**Agreement**
FCW	**0.052s**	**0.052s**	**0.00±0.00s**	**CCC= 1.00**
BCW	**0.124s**	**0.129s**	**0.01±0.03s**	**CCC= 0.95**
FEW	**0.181s**	**0.137s**	**0.04±0.05s**	**CCC= 0.36**
SEPERATED WAVES				
Wave	**Onset before reservoir subtraction**	**Onset after reservoir subtraction**	**Difference**	**Agreement**
FCW	**0.052s**	**0.052s**	**0.00±0.00s**	**CCC= 1.00**
BCW	**0.107s**	**0.105s**	**0.02±0.02s**	**CCC= 0.78**
FEW	**0.149s**	**0.139s**	**0.01±0.01s**	**CCC= 0.87**

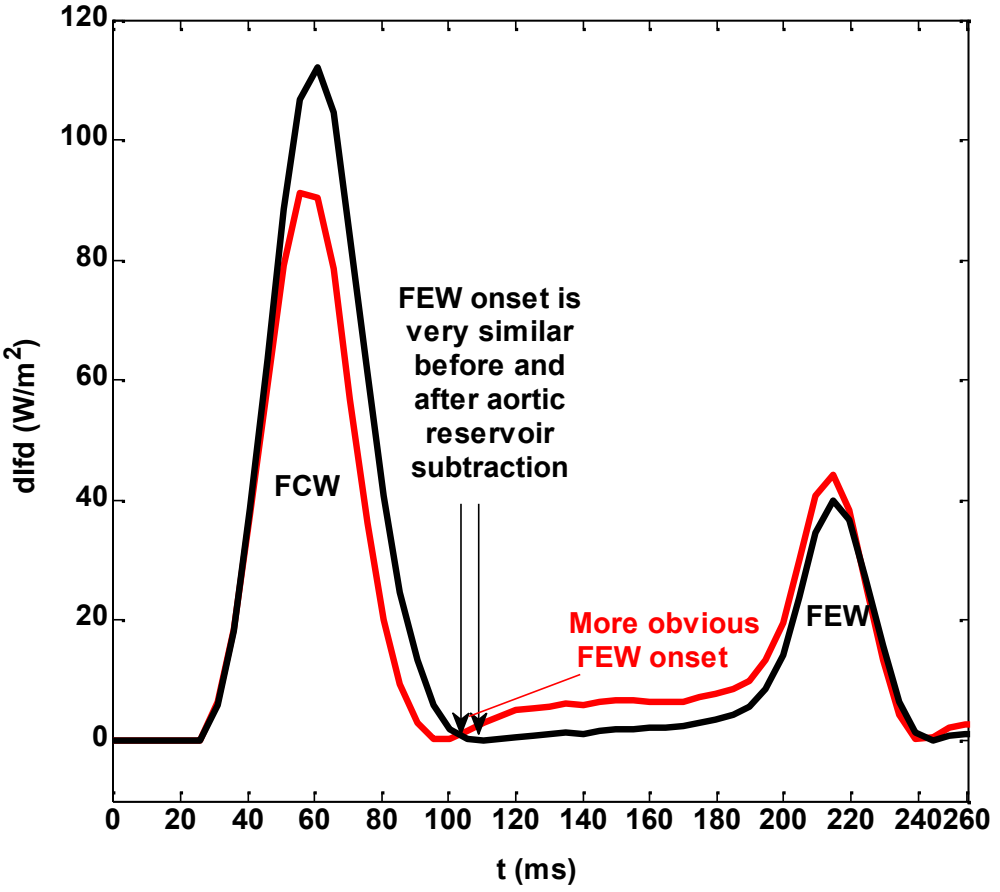

Figure 3.24: A diagram plotting separated forward only wave intensity (dIfd) before (black line) and after aortic reservoir subtraction (red line). The forward expansion wave (FEW) occurs at a vey similar time before and after aortic reservoir subtraction. The slow FEW onset is significantly more prominent after reservoir subtraction.

Haemodynamics and left ventricle wall mechanics: Before and after aortic reservoir subtraction

The sequence of haemodynamic and wall mechanical events during systole can be seen in **Figure 3.25**. Just as before reservoir subtraction (section 3.4.2) the events fall into three groups. Events within each group occur at almost exactly the same time and highly agree with each other. The three groups are first described in **Figure 3.15** and **Table 3.1**.

Early-ejection: Group A

The times to $\mathbf{M_{maxU}}$ and $\mathbf{U_{max}}$ are unaffected by aortic reservoir substitution and still agree, (average difference 0.02±0.04s, CCC=0.70). The arrival time of the separated BCW still corresponded closely with $\mathbf{M_{maxU}}$ (average difference 0.00±0.04s, CCC=0.61).

Mid-ejection: Group B

The separated FEW has a more prominent slow onset after reservoir subtraction, as seen in **Figure 3.24**. The onset of the separated FEW **($\mathbf{dI_{+e1}}$)** still coincides with $\mathbf{L_{maxU}}$ (average difference 0.00±0.01s, CCC=0.91). The strong agreement is observed in **Figure 3.26 b).** The onset of the FEW still occurs during mid-systole, considerably before the net FEW which is seen later, this is demonstrated in **Figure 3.23**.

Late-ejection: Group C

The rapid increase of the FEW **($\mathbf{dI_{+e2}}$)** occurs at identical times before and after reservoir subtraction. This time was 191±15ms after the peak R wave (191±18 before) in these animals. The rapid increase of the FEW still coincides with both LV axes shoulders, $\mathbf{L_i}$, $\mathbf{M_i}$ (0.00±0.01ms CCC=0.90**,** 0.00±0.00ms, CCC=0.96) as well with peak aortic pressure **($\mathbf{P_{max}}$)** (0.00±0.02ms, CCC=0.69) which was reached simultaneously with an inflection point **($\mathbf{U_i}$)** on the descending limb of the flow waveform **(**0.00±0.00ms, CCC=0.95) . The agreements can all be seen in **Figure 3.27a, b, c and d.**

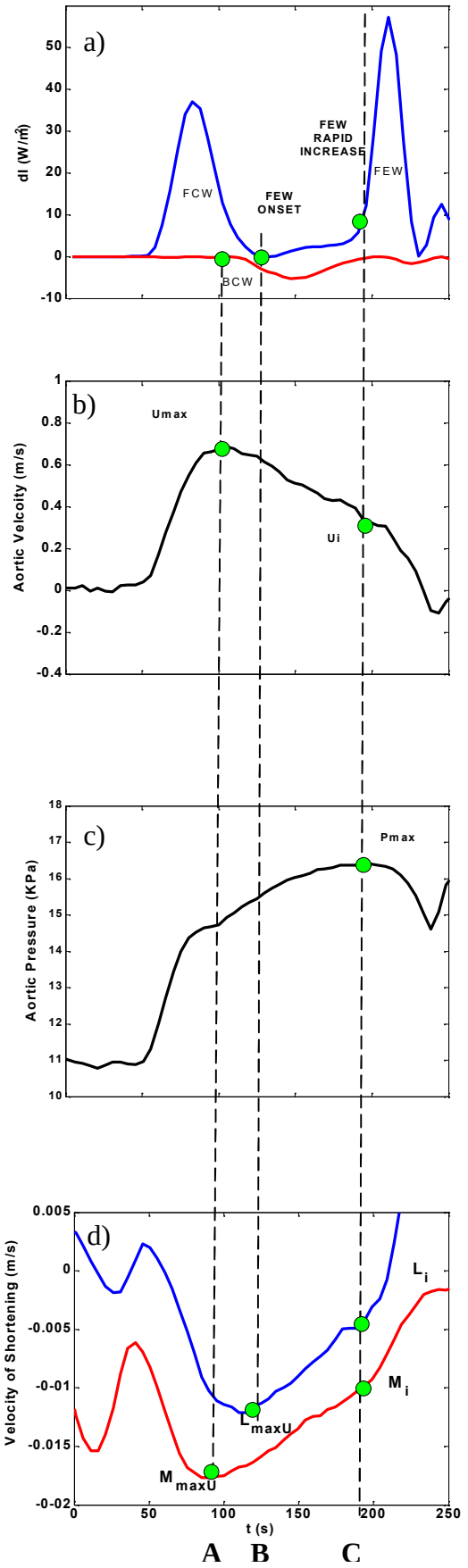

Figure 3.25: A representative cycle taken from dog 9 showing all haemodynamic events and the groups that they fall into even after aortic reservoir subtraction. Plot a) is of forward wave intensity (blue) and backward wave intensity (red). It shows that the FCW magnitude is reduced by reservoir subtraction while the FEW magnitude is increased. b) is a plot of measured flow velocity. c) is a plot of measured aortic blood pressure and d) is a plot of long (blue) and minor (red) LV axes velocity of contraction. The green dots represent times of important haemodynamic events. The times of these events still fall into the three time groups found in **Figure 3.15**. From this figure it can be

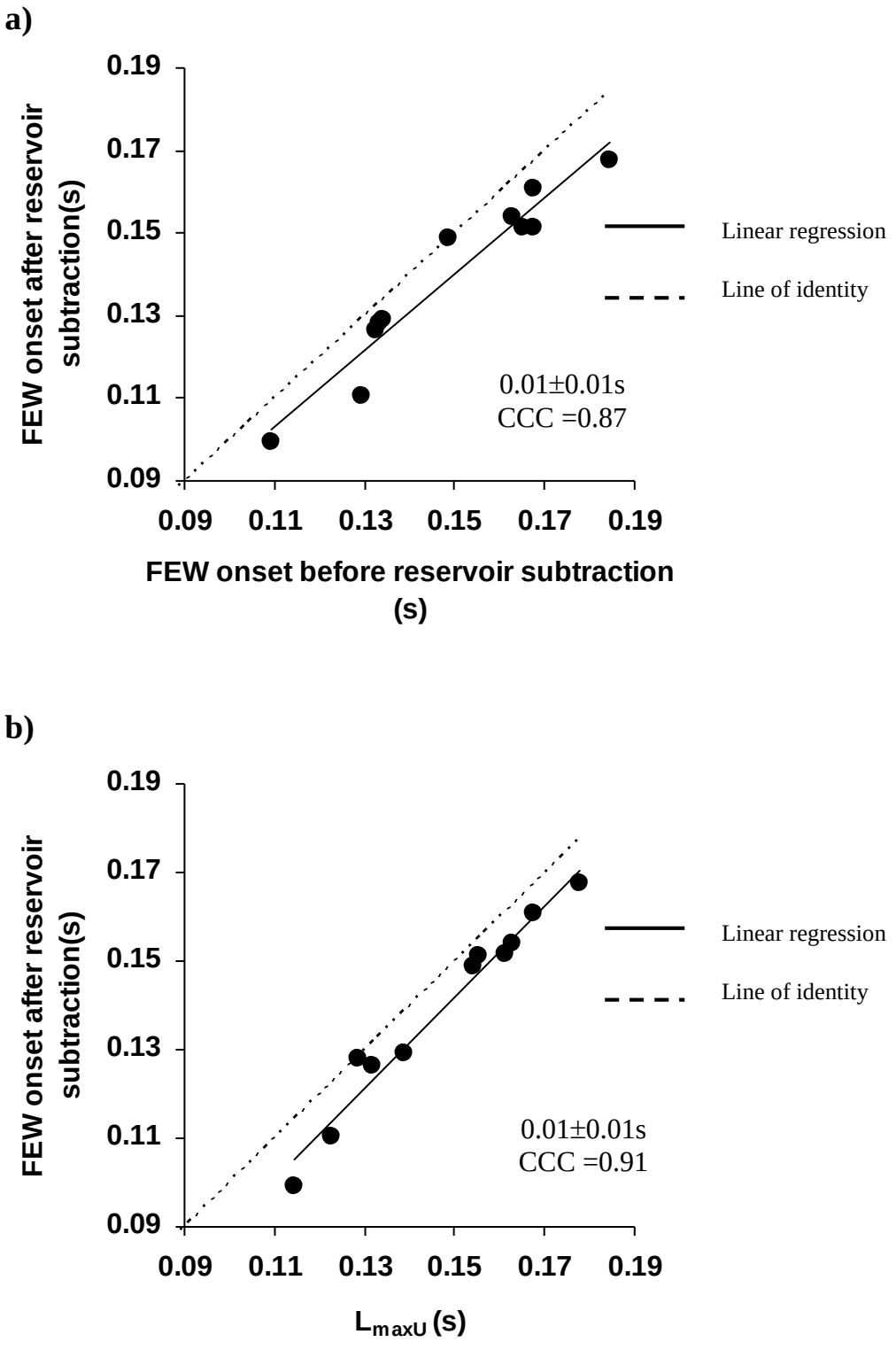

Figure 3.26: Lin's concordance correlation plots using a representative beat from each dog. The graphs show the excellent agreement between **a)** the onset of the forward expansion wave (FEW) both before and after aortic reservoir subtraction in all dogs and **b)** the FEW onset after reservoir subtraction with the time of maximum shortening velocity of the long axis ($\mathbf{L_{maxU}}$) in all dogs. Aortic reservoir subtraction does not alter the timing of the separated FEW and does therefore not affect the mechanism found in this study.

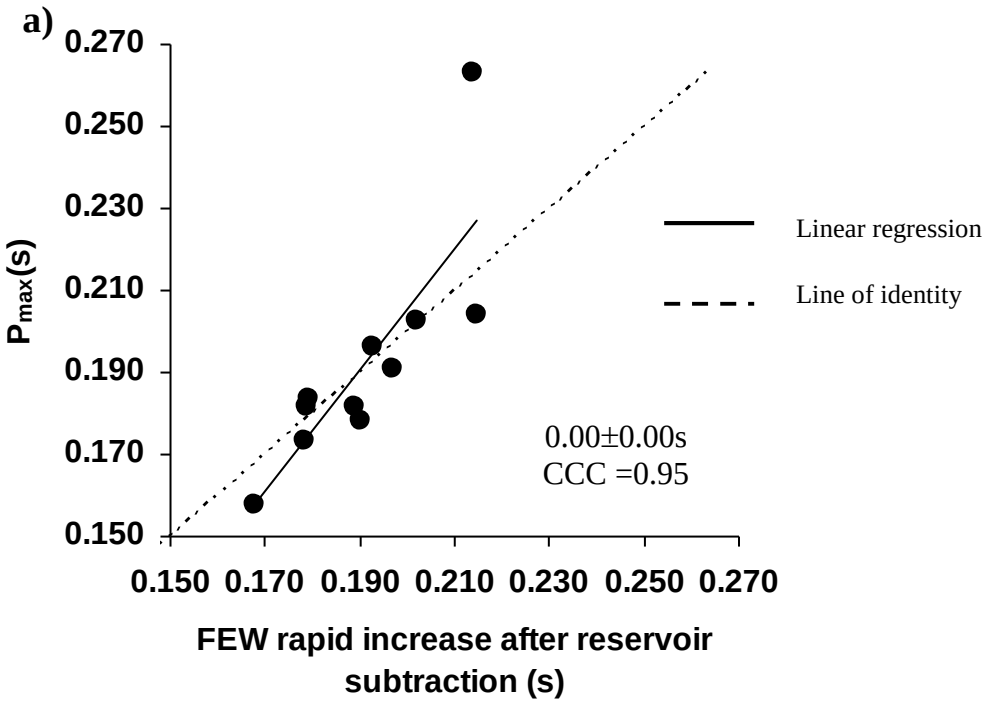
a)
0.270
0.250
0.230
0.210
0.190
0.170
0.150
P_{max}(s)
0.150 0.170 0.190 0.210 0.230 0.250 0.270
FEW rapid increase after reservoir subtraction (s)
Linear regression
Line of identity
0.00±0.00s
CCC =0.95

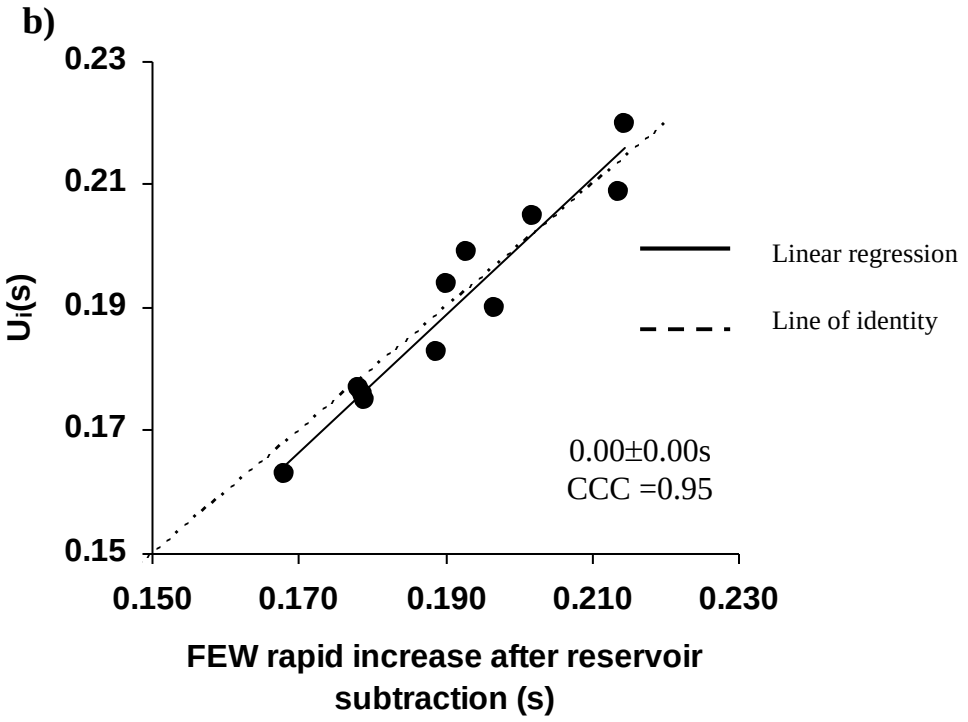
b)
0.23
0.21
0.19
0.17
0.15
U_i(s)
0.150 0.170 0.190 0.210 0.230
FEW rapid increase after reservoir subtraction (s)
Linear regression
Line of identity
0.00±0.00s
CCC =0.95

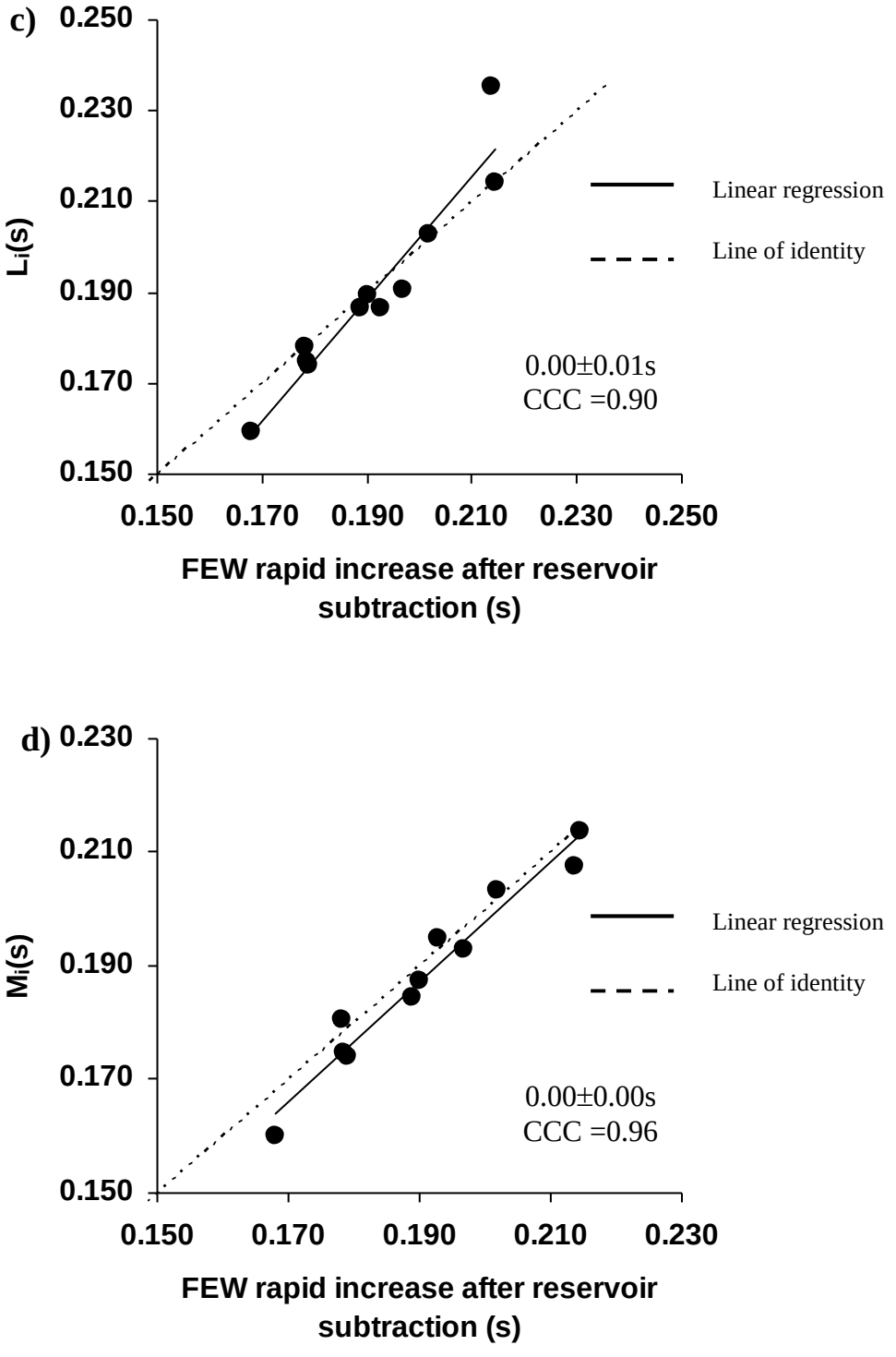

Figure 3.27: Lin's concordance correlation plots showing the excellent agreement between the onset of the rapid increase in energy of the forward expansion wave (FEW) after reservoir subtraction and a) peak aortic pressure $\mathbf{P_{max}}$**, b)** aortic velocity inflection point ($\mathbf{U_i}$) and c),d) both the long **(**$\mathbf{L_i}$**)** and minor axis **(**$\mathbf{M_i}$**)** inflection points during late systole.

Wave energy

As aortic reservoir subtraction alters the magnitudes of all 3 main waves as seen in **Figure 3.23** and **3.24**, the next set of analyses was performed to verify that the energy carried by the FEW is still controlled by the rate of LV deceleration during late systole. After reservoir subtraction the FCW seen in early systole still correlates highly with the rate of shortening velocity of the minor axis ($r=-0.65$, $p>0.007$) and long axis ($r=-0.79$, $p>0.003$). **Figures 3.28**. During Late systole the FEW still highly correlated with the long axis shortening velocity, stage 3. ($r=0.73$, $p>0.001$), this can be seen in **Figure 3.29.**

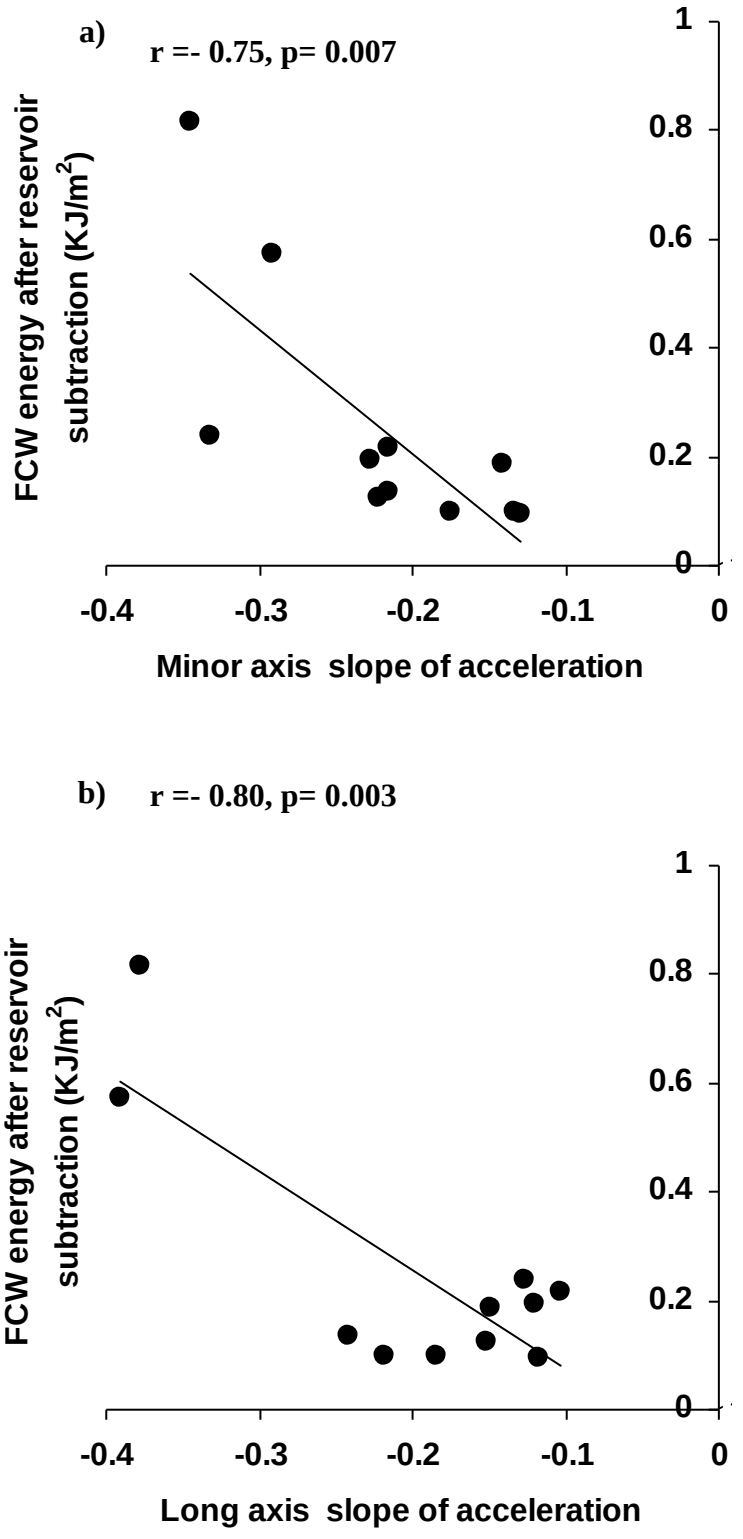

Figure 3.28: Correlation plot showing the strong relationship between the acceleration stage of the a) minor axis and b) long axis shortening and the energy carried by the forward compression wave (FCW) after reservoir subtraction, during early systole.

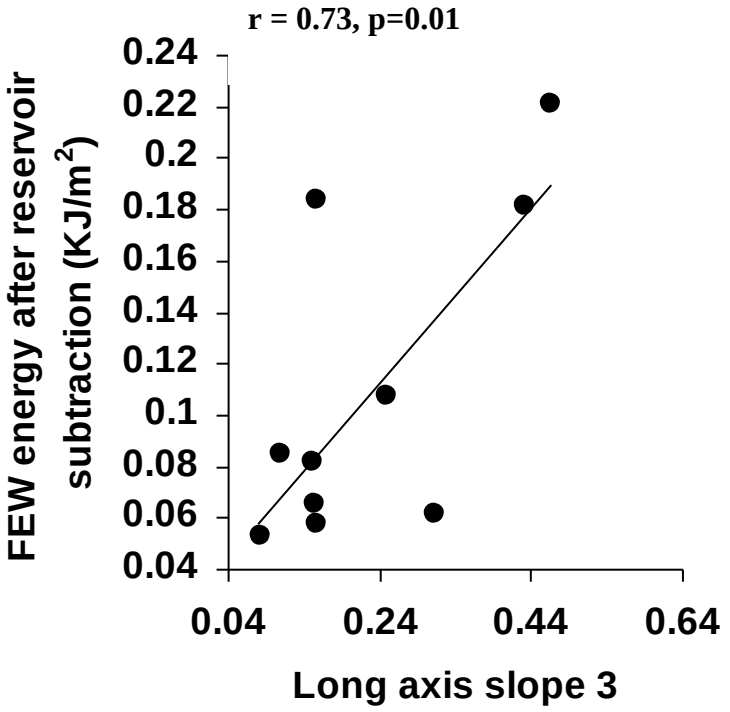

Figure 3.29: Correlation plot showing the strong relationship between the deceleration (stage 3) of long axis shortening and the energy carried by the forward expansion wave (FEW) during late systole after reservoir subtraction.

3.5 Discussion

Left ventricle axes behaviour:

In this study it was found that close time relations exist between left ventricular mechanical function as shown by the shortening of its long and short axes and haemodynamic events of aortic ejection. This experiment demonstrates that ejection events are determined by the normal relationship between the two contracting axes of the left ventricle. During IVC and ejection both long axis shortening onset and peak velocity lagged behind that of the minor axis by ~30 ms respectively representing a degree of physiologically normal asynchrony between the two components of ventricular systolic function as seen in **Figures 3.12** and **3.14.** Early studies of left ventricular synchronous function by Wiggers highlighted evidence for 'fractionate contractions' (Wiggers 1927). This has recently been demonstrated by studying the two components of ventricular function; long and minor axes (Henien et al. 1994). They are complementary contributors to overall systolic function of the ventricle, with the 100% thickening fraction of the posterior wall achieved by the timely shortening of the long axis that results in significant fattening of the segment during systole (Greenbaum et al. 1981). The findings in the current study also remain consistent with the known time relations of shape change during isovolumic contraction (pre-ejection) in similar canine studies (Rankin et al. 1976).

Windkessel effect:

Due to the compliance of the aorta the pressure measured in the aorta is in fact a combination of the wave and reservoir pressure. Some believe that the cardiovascular system (CVS) should now be considered as a wave and Windkessel system (Wang et al. 2003, Davies et al. 2007). The data in this study show that subtracting the reservoir pressure significantly alters the magnitude of all the waves calculated by WIA , as seen in **Figure 3.23** and **Figure 3.24,** but, with the exception of the net FEW, it does not change their timings dramatically. The timings of the separated BCW and FEW still agree well. This is demonstrated in **Figure 3.24** and **Table 3.3**.

Forward expansion wave:

As mentioned in chapter 1 a previous account for the generation of the FEW was suggested by Sugawara et al. (1997) and includes "both the loss of tension bearing ability caused by myocardial relaxation and the deceleration of aortic blood flow caused by the reduced rate of myocardial shortening". The authors reason that as the rate of maximum negative change in LV pressure (-dP/dt) occurs before the time of aortic valve closure there must be another factor acting in union with myocardial relaxation that influences the ejection of

blood. They proposed the "ability of the left ventricle to decelerate blood flow under its own momentum", which was assumed to be analogous to the situation in isolated cardiac tissue, where contraction ceases before tension-bearing ability declines (Brutsaert 1989). As a result, blood would continue to flow into the aorta on account of inertial forces (Nobel 1968) until the aortic valve closed. They propose that the momentum of the blood flowing into the aorta would create a rapid decrease in LV pressure which would in turn generate a FEW. Niki et al. agreed with this explanation for FEW generation and went one step farther to discover how patients without such an inertial effect lacked a large FEW completely (Niki et al. 1999).

This study aimed to expand upon all previous observations by examining LV wall movement and the timing of the FEW in great detail. It was observed that the FEW is generated when the LV long axis velocity of shortening begins to slow, and that its duration can be divided into two distinct phases, **Figure 3.7.** The onset occurs with $\mathbf{L_{maxU}}$, **Figure 3.15** and **Figure 3.16** and as the minor axis is already slowing at this time the slow FEW is associated with the simultaneous slowing of contraction speed of both axes until they reach an inflection point, after which their contraction speed is further reduced. This promotes the onset of the rapid stage of the FEW indicating the wave is carrying higher intensities. The effect of the onset of the rapid stage of FEW on pressure and velocity waveforms is distinct; aortic pressure begins to decline and velocity is further reduced with a slope that is steeper than its previous reduction, marked by an inflection point. **Figures 3.11** and **3.15.**

The results agree with those of Westerhof et al. (1972) that the arrival of reflected waves to the aortic root in mid systole, which are compression in nature, cause the initial deceleration of blood flow. The results are also in line with the proposal of Parker et al. (1998) that the slowing down of LV wall speed generates the FEW, which has a significant role in slowing the ejection of blood in the aorta. Furthermore, Jones et al. (2002) suggested that two temporally distinct processes, such as the slowing of the myocardial shortening and complete cessation of myocardial shortening, might generate the FEW. In our results we also observed that the FEW has two phases**.** The results in this study further show that the onset (first phase) of the FEW does coincide with slowing of myocardial shortening of the long axis. However the rapid increase in energy (second phase) does not correspond to complete cessation of myocardial shortening but coincides with a secondary decline in the velocity of shortening of both the minor and long axis, **Figure 3.15** and **3.17.**

The results presented in this chapter are in agreement with the hypothesis that the generation of the FEW results from the reduction in velocity of shortening of the last left ventricular axes to slow at end systole. The LV minor axis (septum to free wall) reaches its maximum velocity of shortening prior to the onset of the FEW; however as soon as the long axis (base to apex) reaches its maximum velocity of contraction the FEW is produced. It is claimed that the LV minor axis plays a dominant role during systolic ejection compared to that of the long axis (Karliner et al. 1971, Oki et al. 1999). However in this study the FEW is only generated when the long axis reaches its maximum velocity of shortening. Nonetheless the two axes work in union (Greenbaun et al. 1981, Henien and Gibson 1991, Keith 1918); further evidence of which is seen 40ms after the onset of the FEW when both axes simultaneously change their rate of shortening, generating the rapid increase of the expansion wave. The mechanism behind the sudden change in LV axes velocity of deceleration is not known. By comparing the results found in this chapter to a previous MRI study looking into the 3-D deformation of the LV (Rosen et al. 2004) it appears that the time of $\mathbf{L_i}$ and $\mathbf{M_i}$ that leads to the rapid increase in FEW energy could coincide with the release of torsion. Rosen and colleagues saw that LV unfolding is related to radial thinning that is observed ~40ms before aortic valve closure. The release of torsion would bring about a rapid decrease in LV pressure resulting in a larger FEW.

Wave energy:

It has been generally accepted that LV wall movement generates the FCWs found in early systole and the results in this chapter further confirm that the LV also generates the FEW in late systole. The FCW is accepted to be a consequence of the ejecting force created by LV wall contraction (Jones et al. 2002, Ramsey and Sugawara 1997) and in this study the speed of both the minor and long axis during the beginning of systole correlated well with the magnitude of the compression wave (**Figure 3.20 a and b**). A significant correlation also exists between the energy carried by the FEW and the rate of long axis shortening during late systole **Figure 3.21.** It is therefore reasonable to extrapolate that LV wall movement influences both the acceleration and deceleration phases of aortic flow (Jones et al. 1997. Parker and Jones 1988, Ramsey and Sugawara 1997).

Limitations:

One possible limitation to the study was that only two axes were studied in the majority of dogs, base-apex and septum-free wall. It might have been more informative had the anterior-posterior axis also been recorded and studied in all cases. LV geometry is intrinsically complex, particularly during ejection and the timings of the third axis

contraction on the deceleration of flow in the aorta could well support our hypothesis and findings. Further, possible effects of the rotational component of LV ejection on each axis velocity of shortening was not considered in our study. The crystals used for measuring the axes movement were embedded into the myocardium and the relative movement of each axis was therefore taken into consideration, and thus this possible limitation does not invalidate our conclusions. Further research into LV torsion and the inflection points observed on both LV axes would be of great interest.

3.6 Conclusion

In conclusion reflected waves instigate aortic flow deceleration and the LV further actively decelerates aortic flow by generating a FEW towards end of systole. The onset of the FEW occurs when the shortening velocity of the LV long axis begins to decline. The FEW has a slow onset followed by a rapid increase in energy, both of which closely follow LV wall movement. The rapid increase in energy causes a decrease in aortic pressure and an increase in the rate by which flow decreases. As the timing of the separated FEW is not altered dramatically by reservoir subtraction our hypothesis and suggested mechanism for the generation of the FEW is unchanged when our data are studied using the new Windkessel and wave technique.

This chapter has uncovered the mechanism behind the generation of the FEW during control conditions in canines. In order to test this theory the same measurements have also be acquired on the same dogs under stressed haemodynamic conditions. The next chapter reveals whether the mechanism holds true.

Chapter 4
Ventricular-Aortic Interaction in Canines: Occlusion

4.1 Introduction

In chapter 3 LV wall movement and its accompanying hemodynamic events were analysed in 11 dogs under control conditions. In order to scrutinize the relationships observed in chapter 3 identical measurements were recorded in the same 11 dogs during stressed hemodynamic conditions. Total closed-end occlusion sites were introduced along the aorta of each dog at four different levels. In the original experimental design Khir *et al.* used this approach to focus on the effects that aortic clamping have on the magnitude of the BCW during mid-systole. Khir's investigation showed that during proximal occlusions the reflected wave arrived back to the heart significantly earlier, its duration was longer and its magnitude was much greater. They additionally noticed that the forward waves are both reduced (Khir et al. 2000). Using the data collected during the periods of occlusion this chapter examined the effect that these larger reflected waves had on LV performance and FEW generation at the end of systole. In order for the relationships discovered in chapter 3 to remain robust, the same relationships should be seen during these extreme conditions.

4.2 Hypotheses

1) The FEW will continue to be generated when the long axis reaches its maximum velocity of contraction in spite of aortic occlusion.
2) The axial rate of shortening during early and late systole will be affected by larger reflected waves generated by the total occlusions. The rate of axial shortening will correlate with the energy carried by both the FCW and FEW. The FCW and FEW magnitudes will be diminished as a consequence of a reduced rate in axial shortening velocity.

4.3 Methods

In this study the same 11 mongrel dogs (4 females and 7 males, average weight 22.09±3.11kg) were analysed as in the control study, Chapter 3. The experiments were in fact carried out simultaneously. All experiments were performed at the University of Calgary (Alberta, Canada) by Professor Tyberg's Cardiovascular Research Group. The surgery was again performed by dog surgeons Cheryl Meek and Gerry Groves and the data was collected by Ashraf Khir and Greg Nelson. The experiment adhered to the University of Calgary's guiding principles in the care and use of animals and ethical approval was given by the appropriate council.

4.3.1 Instrumentation

Both invasive hemodynamic measurements and LV wall movement measurements are identical to those used in the control experiment, Chapter 3: section: 3.3.1. LV movement was monitored throughout the experiment and compared to the timings of invasively acquired aortic root pressure and velocity events. The acquired pressure and flow velocity were used to calculate aortic waves using wave intensity analysis (WIA).

4.3.2 Occlusions

Closed-end reflection sites were created by snares positioned during the preparation stage at 4 sites, shown in **Figure 4.1:** Site1: Upper descending thoracic aorta at level of aortic valve (thoracic), site 2: Lower thoracic aorta (diaphragm), site 3: between the renal arteries (abdominal) and site 4: Iliac-Left iliac artery, 2cm downstream from the aortic-iliac bifurcation (iliac).

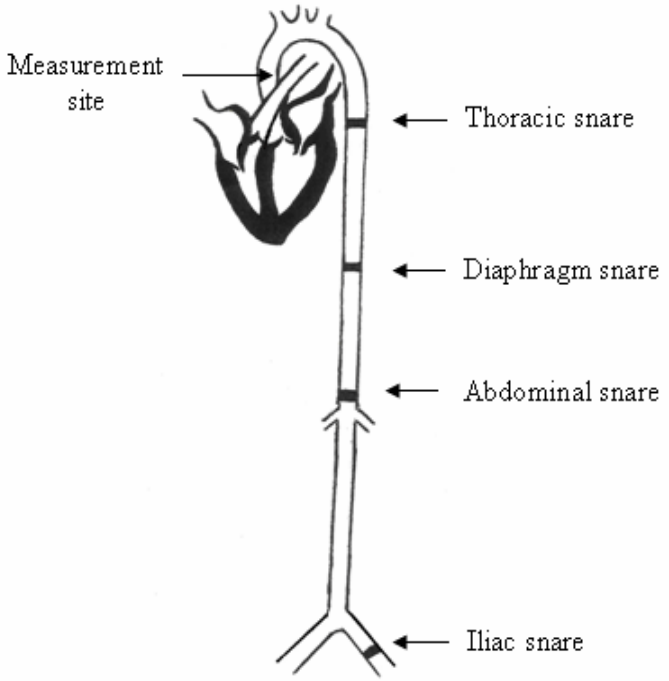

Figure 4.1: Diagram of the heart and aorta showing the site of aortic pressure (P) and velocity (U) measurement ~2cm from the aortic root and the 4 sites of occlusion.

Measurements of flow and pressure were recorded for 30 seconds. Each occlusion lasted for 3 minutes and 15 minute intervals between occlusions were observed to allow for the return to control conditions. A third pressure catheter was inserted into either the left or right femoral or iliac artery in order to measure aortic pressure at the site of clamping to ensure that the clamping created a 100% occlusion. The catheters were marked at the occlusion sites as they were removed post-mortem which enabled the distances between sites to be calculated. As in the Control experiment flow is converted into velocity after post-mortem examinations and prior to analysis the baseline of the velocity and pressure waveforms were aligned.

4.3.3 Protocol

1. Acquire data before clamping
2. Apply the first clamp
3. Wait 3 minutes
4. Acquire data during clamping
5. Move the pressure catheter at the clamp site to the next site of occlusion
6. Wait 15 minutes
7. Repeat steps 1-6 at the second site of occlusion
8. Repeat Steps 1-6 at the third site of occlusion
9. Repeat steps 1-4 at the last site of occlusion

4.3.4 Parameters measured

1. LV pressure- from a catheter inserted into the LV
2. Aortic pressure ~ 1cm from the aortic root during all occlusions
3. Aortic flow~ 1cm from the aortic root during all occlusions
4. Pressure- at the site of each occlusion to ensure total occlusion conditions
5. ECG
6. LV minor axis movement (septum to free wall)-via piezo electric crystal movement, see chapter 3, **Figure 3.2**.
7. LV Long axis movement (base to apex) – via piezo electric crystal movement, see chapter 3, **Figures 3.1** and **3.2**.
8. Post mortem distance to the occlusion site from the measurement site
9. Post mortem ascending aorta circumference

4.3.5 Parameters calculated: (as in Chapter 3, section 3.3.2)

1. Aortic Velocity: Aortic flow = area × velocity (Q=AU). The aortic velocity can therefore be measured by dividing the aortic flow data measured at the aortic root by the aortic area. Ascending aorta radius was measured post-mortem and the area of the aortic cross- sectional area was considered circular, area = πr^2

2. Wave speed: Calculated using the PU-loop method described in chapter one, section 1.6.2 and chapter 2 section 2.3. When measured pressure is plotted against measured velocity the slope of the loop during early systole equals ρc, assuming blood density =1050Kg/m^3 .

3. **LV axis velocity of shortening**: The slope of the distance-time graph of LV axis movement during contraction was used to calculate the wall speed. See chapter 3, **Figure 3.4**.
4. **Wave Intensity**-original analysis- See Chapter 2: sections 2.4, 2.5
5. **Wave Intensity-wave and reservoir theory** See Chapter 2, section 2.6..

4.3.6 Data collection

Custom written programs in Matlab (The MathWorks Inc., MA, USA) were used to analyse the data. The R wave of the QRS complex was taken as t=0. The times to the onsets of all three main waves of WIA (FCW, BCW, FEW) were recorded and compared to wall movement throughout systole during thoracic, diaphragm, abdominal and iliac occlusions. Unfortunately some occlusion data is missing from certain dogs due to the complications of such an invasive procedure. During diaphragm and abdominal occlusions all 11 dogs were successfully measured. During thoracic and iliac occlusion data from dogs 2 And 6 could not be either obtained or used. The data from the remaining 9 dogs was averaged in these cases.

4.3.7 Statistical analysis

A representative cycle was analysed during each occlusion for each dog and compared to the control data in chapter 3. All data are presented as mean ± SD and Concordance correlation coefficients were calculated using Lin's concordance method to determine the extent of agreement between variables occurring at similar times. Pearson correlation coefficients were calculated to establish a relationship between velocity of LV axes shortening during occlusions and the magnitude of both the FCW and FEW. Student Paired t-tests were performed to see if there is a significant difference between wave speed before and during occlusions. The null hypothesis is that the wave speed is not significantly different. To test the significance, the alpha level was set at 0.05.

4.3.8: Reproducibility

As the results to chapter 3 and 4 were analysed simultaneously please refer to chapter 3 section 3.3.5.

4.4 Results

4.4.1: Left ventricle axes velocities during Pre-ejection:

During IVC the LV long axis lengthens in all dogs 100% of the time. The minor axis shortens in 7 dogs (64%) and lengthens in the remaining 4 (36%). This is identical to axes behaviour during control conditions in chapter 3, section 3.4.1. The peak velocity of shortening and lengthening are presented in **Table 4.1**. In this set of data the long axis pre-ejection velocities are relatively unaltered by distal occlusions (abdominal and iliac). Long axis pre-ejection velocities are however, increased by proximal occlusions (thoracic and diaphragm). Minor axis velocities are relatively unchanged throughout.

Table 4.1: Maximum velocity of shortening and lengthening values for the left ventricle axes during the 4 occlusions. Proximal occlusions have a more pronounced effect on the long axis than the minor axis during the isovolumic contraction (IVC) phase. The long axis percentage increase in maximum velocity during proximal occlusions is highlighted below.

Long Axis Lengthening Velocities (All dogs)				
	Thoracic	**Diaphragm**	**Abdominal**	**Iliac**
Before	0.024±0.01m/s	0.024±0.01m/s	0.024±0.01m/s	0.024±0.01m/s
During	0.033±0.03m/s	0.036±0.02m/s	0.025±0.02m/s	0.026±0.01m/s
% Difference	**38% increase**	**50% increase**	**4% increase**	**7% increase**
Minor Axis Lengthening Velocities (7 dogs)				
	Thoracic	**Diaphragm**	**Abdominal**	**Iliac**
Before	0.013±0.005m/s	0.013±0.005m/s	0.013±0.005m/s	0.013±0.005m/s
During	0.011±0.00m/s	0.014±0.01m/s	0.012±0.01m/s	0.015±0.01m/s
%Difference	**15% reduction**	**8% increase**	**8% reduction**	**15% increase**
Long Axis Shortening Velocities (4 dogs)				
	Thoracic	**Diaphragm**	**Abdominal**	**Iliac**
Before	-0.016±0.01m/s	-0.016±0.01m/s	-0.016±0.01m/s	-0.016±0.01m/s
During	-0.018±0.01m/s	-0.013±0.01m/s	-0.018±0.01m/s	-0.018±0.02m/s
%Difference	**13% increase**	**19 % reduction**	**13% increase**	**13% increase**

4.4.2: Left ventricle axes velocities during ejection:

During ejection both the LV long and minor axes shorten. The maximum velocity of shortening of each axes during each occlusion are presented in **Table 4.2.** The opposite happens to that observed during pre-ejection. The minor axis ejection velocities are unaltered by distal occlusions (abdominal and iliac) however reduced by 20% during proximal occlusions (thoracic and diaphragm), while the long axis velocities appear to be less effected throughout (only 11% slower during proximal occlusions). This is also shown in **Figure 4.2**.

Table 4.2: Maximum velocity of shortening values for each left ventricle axis during the 4 occlusions. The minor axis peak velocity of shortening is slower by 20% during proximal occlusions while the long axes maximum velocity of shortening is only reduced by 11%. The increase in afterload generated by the occlusions has a slightly more pronounced effect on minor axis shortening during the ejection phase.

Long axis Shortening				
	Thoracic	**Diaphragm**	**Abdominal**	**Iliac**
Before	-0.009±0.005m/s	-0.009±0.005m/s	-0.009±0.005m/s	-0.009±0.005m/s
During	-0.008±0.001m/s	-0.008±0.002m/s	-0.009±0.01m/s	-0.0085±0.01m/s
% Difference	**11% reduction**	**11% reduction**	**0% change**	**6% reduction**
Minor Axis Shortening				
	Thoracic	**Diaphragm**	**Abdominal**	**Iliac**
Before	-0.015±0.004m/s	-0.015±0.004m/s	-0.015±0.004m/s	-0.015±0.004m/s
During	-0.12±0.01m/s	-0.12±0.02m/s	-0.014±0.01m/s	-0.015±0.002m/s
% Difference	**20% reduction**	**20% reduction**	**7% reduction**	**0% change**

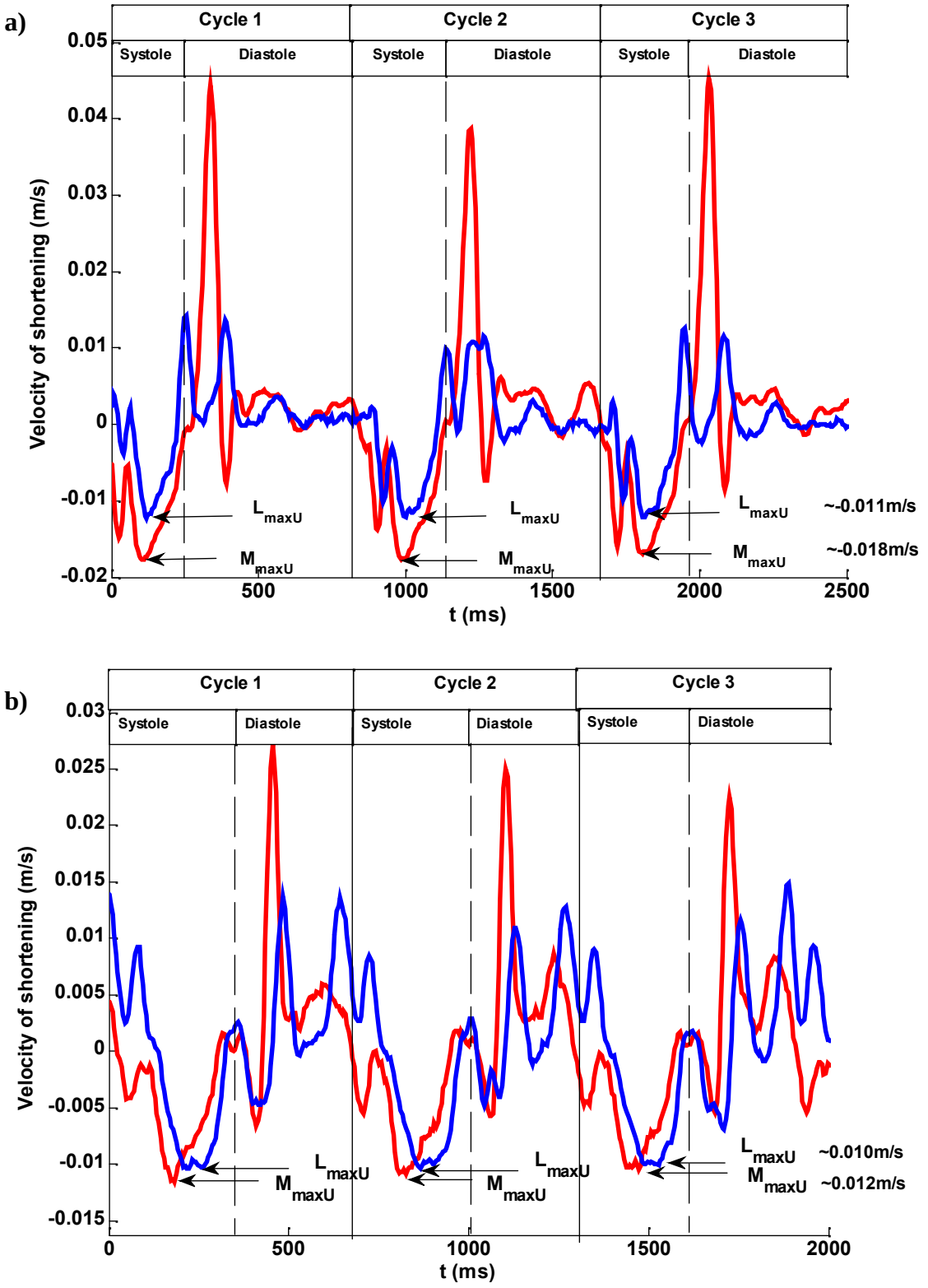

Figure 4.2: Three consecutive beats taken from dog 9 of long and minor axis velocity of shortening a) before and b) during thoracic occlusion. During control conditions the minor axis reaches higher maximum velocities than the long axis (a). During occlusion the long axis maximum velocity of shortening is barely affected while the short axis maximum velocity of ejection is significantly reduced (b).

4.4.3 Aortic haemodynamics during ejection: Original wave intensity analysis

4.4.3.1 Wave speed

Wave speed plays a major role in wave separation as explained in chapter 2, section 2.4. Individual dog changes in wave speed caused by all four occlusions can be seen in appendix 4.1. Wave speed is dramatically affected by thoracic occlusion but less so by more distal occlusions. During thoracic occlusion average wave speed increases from 5.98±5.64m/s to 11.0±7.51m/s. This is a significant increase of 84%. ($p=0.0003$). During diaphragm occlusion there is a minor increase in wave speed from 5.41±93m/s to 6.07 ±1.36m/s, this is a 12% increase but not large enough to be a statistically significant increase ($p=0.1$). Abdominal occlusion actually brought about a small decrease in wave speed (8%) while iliac occlusion created a very small 3% increase both of which are not significant.($p=0.25$, $p=0.36$ respectively).

4.4.3.2 Wave magnitudes

During thoracic Occlusion: the energy carried by the separated FCW was on average found be reduced by 21%, the BCW is 507% greater while the FEW is reduced by 35% **Figure 4.3** demonstrates the change in wave magnitudes caused by thoracic occlusion of the aorta.

During diaphragm occlusion: the energy carried by the separated FCW is reduced by 50% The BCW is 116% greater and the FEW is reduced by 58%.

During abdominal occlusion: the energy carried by all the waves is relatively unchanged. The FCW is 3% smaller, the BCW is only 10% greater and the FEW is reduced by 11%.

During iliac occlusion: the FCW energy is reduced by 8% while the FEW is 6% greater The BCW is actually marginally reduced by 10%.

Average values for wave magnitudes before and during all occlusion can be found in appendix 4.2. During proximal occlusions the energy carried by the forward waves is reduced while the reflected wave is markedly greater. During the distal occlusions the magnitudes of all three main waves are not significantly affected.

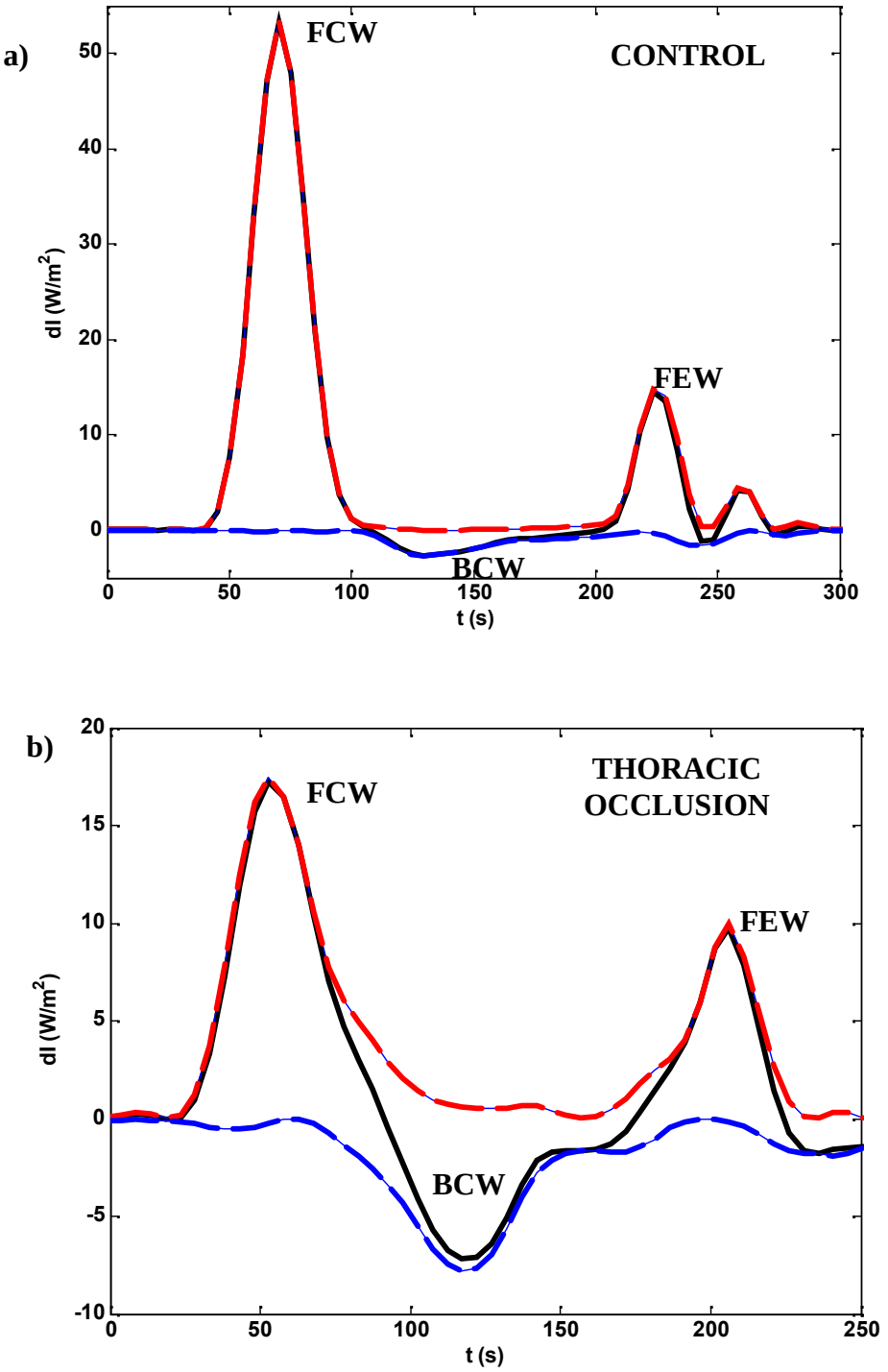

Figure 4.3 Invasive data collected from a representative dog to demonstrate how the magnitudes of waves are affected by proximal occlusions. The black lines represent net wave intensity, the red lines represent forward only wave intensity while the blue lines represent backward wave intensity. Plot a) shows the magnitude of the waves during control conditions. Plot b) demonstrates how the magnitudes of all three waves are altered during thoracic occlusion. This figure nicely demonstrates how the forward waves (FCW and FEW) are smaller while the reflected wave (BCW) is larger during thoracic occlusion.

The backward compression wave arrival

During all occlusions the BCW arrives at the heart at a similar time to that of the control experiment. Control = 103±23ms, thoracic occlusion = 103±20ms diaphragm occlusion = 121±20ms (which is a little later), abdominal occlusion = 97±20ms and iliac occlusion = 102±20ms. In the control data this time coincided with $\mathbf{M_{maxU}}$ (average difference 0.01±0.02s, CCC =0.69). Throughout all occlusions the relationship between the two events remains strong as shown in **Figures 4.4** and **4.5**

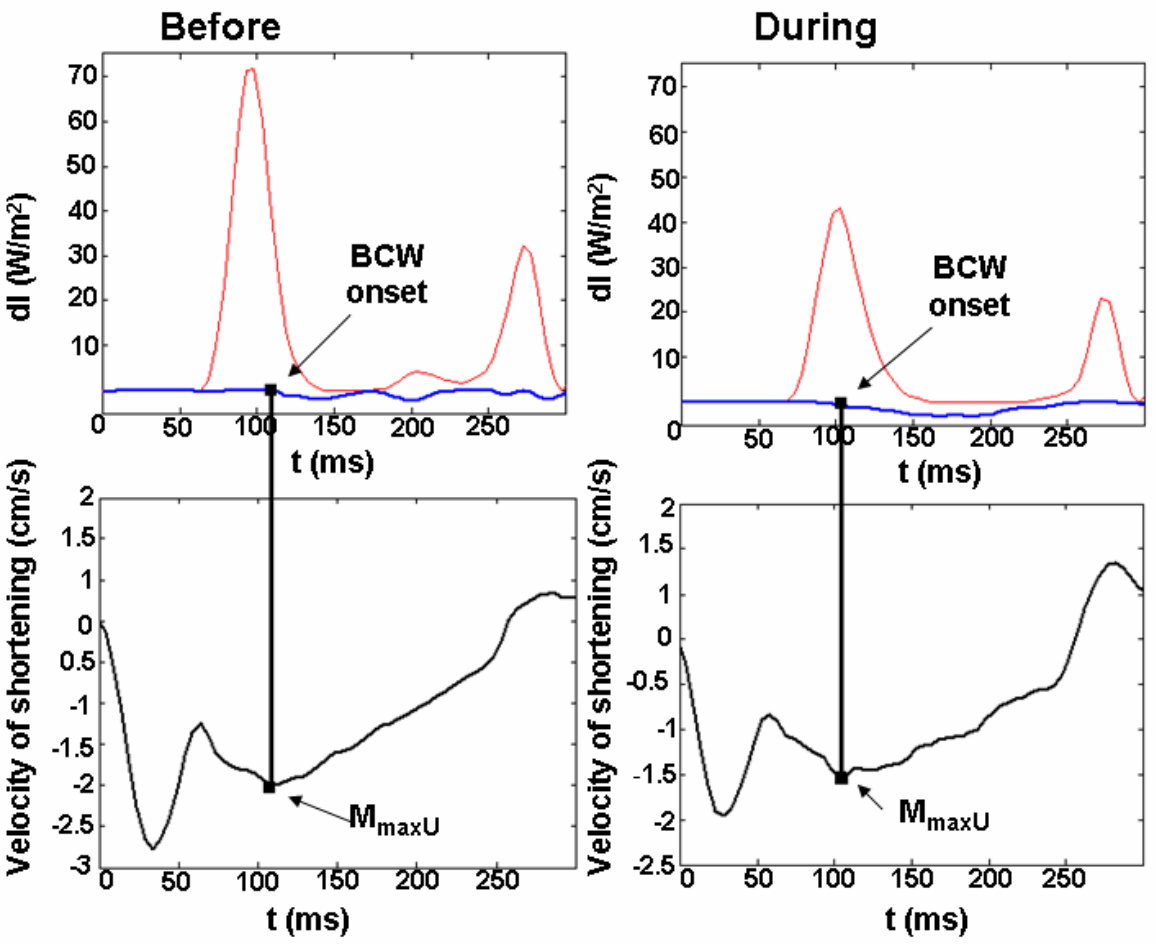

Figure 4.4: Data collected from a single dog showing that the time that the backward compression wave (BCW) arrives at the heart still coincides with the time of maximum velocity of shortening of the minor axis ($\mathbf{M_{maxU}}$); even during thoracic occlusion. The forward compression wave (FCW) and forward expansion wave (FEW) magnitudes are reduced during occlusion, especially the FCW that is reduced from ~70W/m^2 to ~50W/m^2 in this example. The BCW is again enlarged.

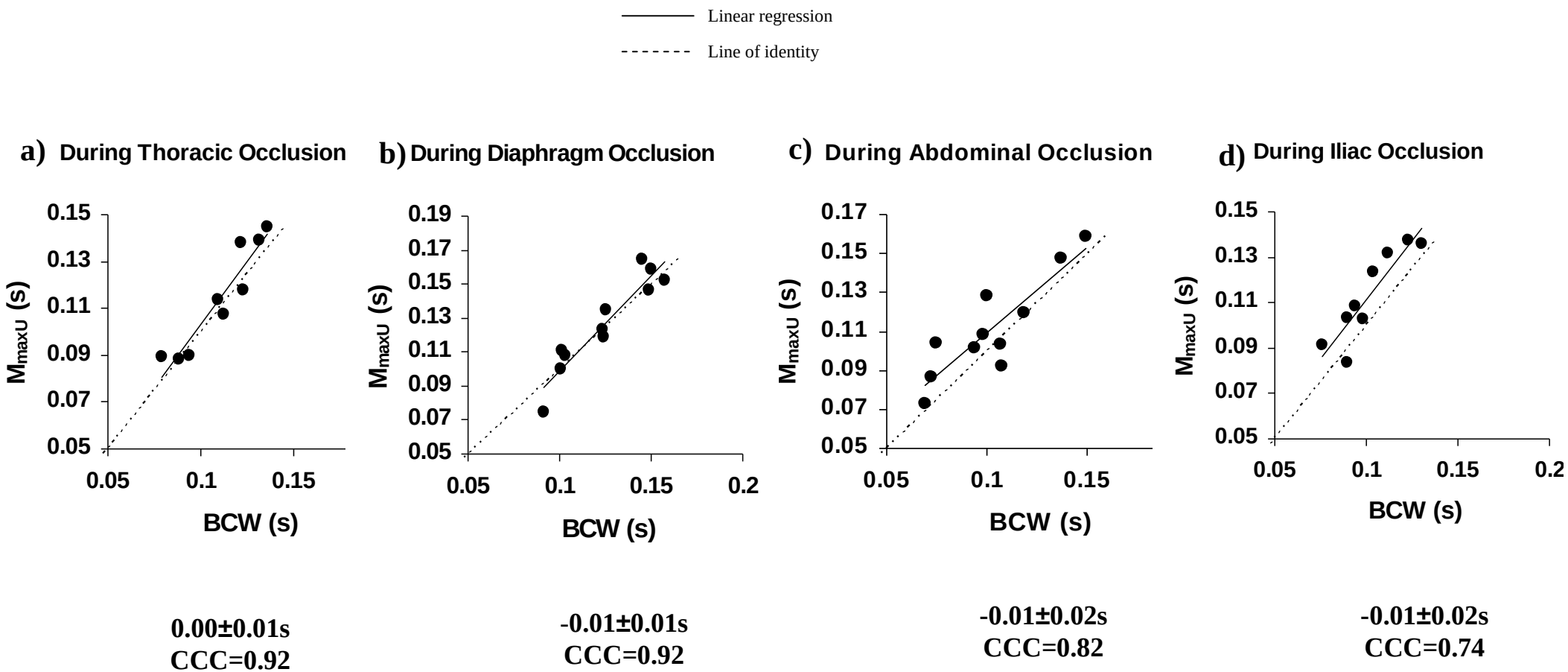

Figure 4.5: Lin's concordance correlation plots showing that the relationship between the time of backward compression wave (BCW) arrival at the heart and the time of maximum shortening velocity of the minor axis ($\mathbf{M_{maxU}}$) is still strong during a) thoracic, b) diaphragm, c) abdominal and d) iliac occlusion. During thoracic and iliac occlusion the data from dogs 2 and 6 could not be acquired, therefore only 9 dots can be seen in these plots, see section 4.2.6.

The onset of the forward expansion wave

On average the onset of the FEW occurs at 153±30ms after the R wave of the QRS complex during thoracic occlusion and 163±30ms during diaphragm occlusion. These times are slightly later than during control conditions in chapter 3, **Table 3.1**, (149±26ms). During the more distal occlusions the timing of the wave is very slightly earlier than that of before occlusion (abdominal 140±40ms, iliac 134±20ms). In the control study (chapter 3) the onset of the FEW always coincides with LV $\mathbf{L_{maxU}}$ (average difference 0.00±0.01s, CCC=0.96). If the mechanism holds true during occlusions $\mathbf{L_{maxU}}$ should always coincide with the FEW onset irrespective of whether the FEW is seen earlier or later. The results shown in **Table 4.3** and **figures 4.6** and **4.7** show that during all occlusions the FEW is indeed still generated when the LV long axis reaches its maximum velocity of shortening.

Table 4.3: Average times from the R wave of the QRS complex to the forward expansion wave (FEW) onset and maximum shortening velocity of the left ventricle (LV) long axis ($\mathbf{L_{maxU}}$) during all four occlusions. The FEW is always generated when the LV long axis begins to slow. Strong agreements are seen during all occlusions

.

Occlusion	FEW onset	L_{maxU}	Average difference	CCC
Thoracic	0.153±0.3s	0.158±0.2s	0.01±0.02s	0.68
Diaphragm	0.163±0.3s	0.158±0.2s	0.02±0.02s	0.88
Abdominal	0.140±0.4s	0.139±0.2s	0.02±0.03s	0.68
Iliac	0.134±0.2s	0.140±0.2s	0.01±0.02s	0.57

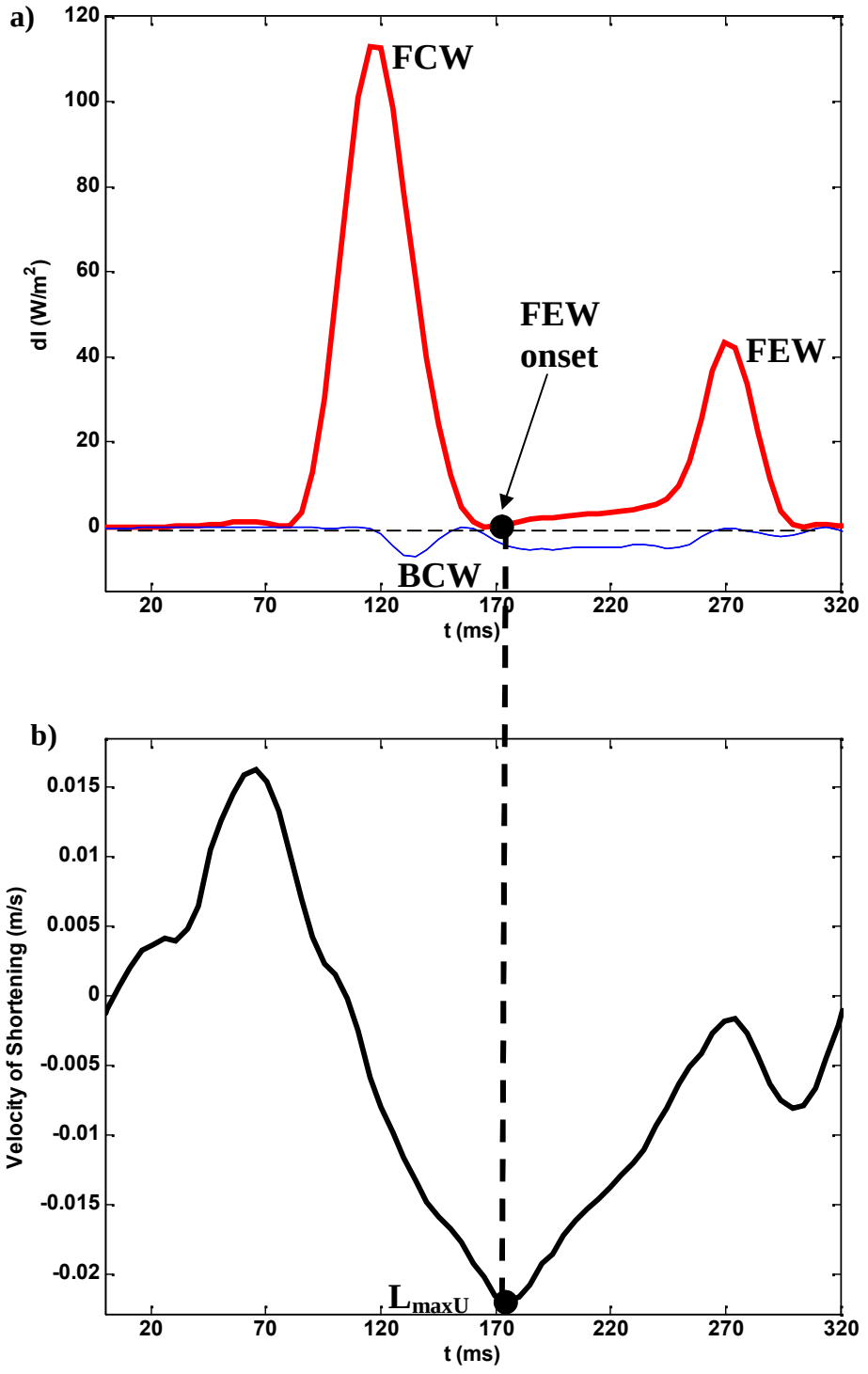

Figure 4.6: Data taken from one representative beat of dog 10 during thoracic occlusion showing wave intensity in plot a) and long axis velocity of shortening in plot b). Thoracic occlusion does not effect the excellent agreement between the forward expansion wave (FEW) onset and maximum shortening velocity of the long axis (**L_{maxU}**). The mechanism of FEW generation remains the same even when the time is altered slightly.

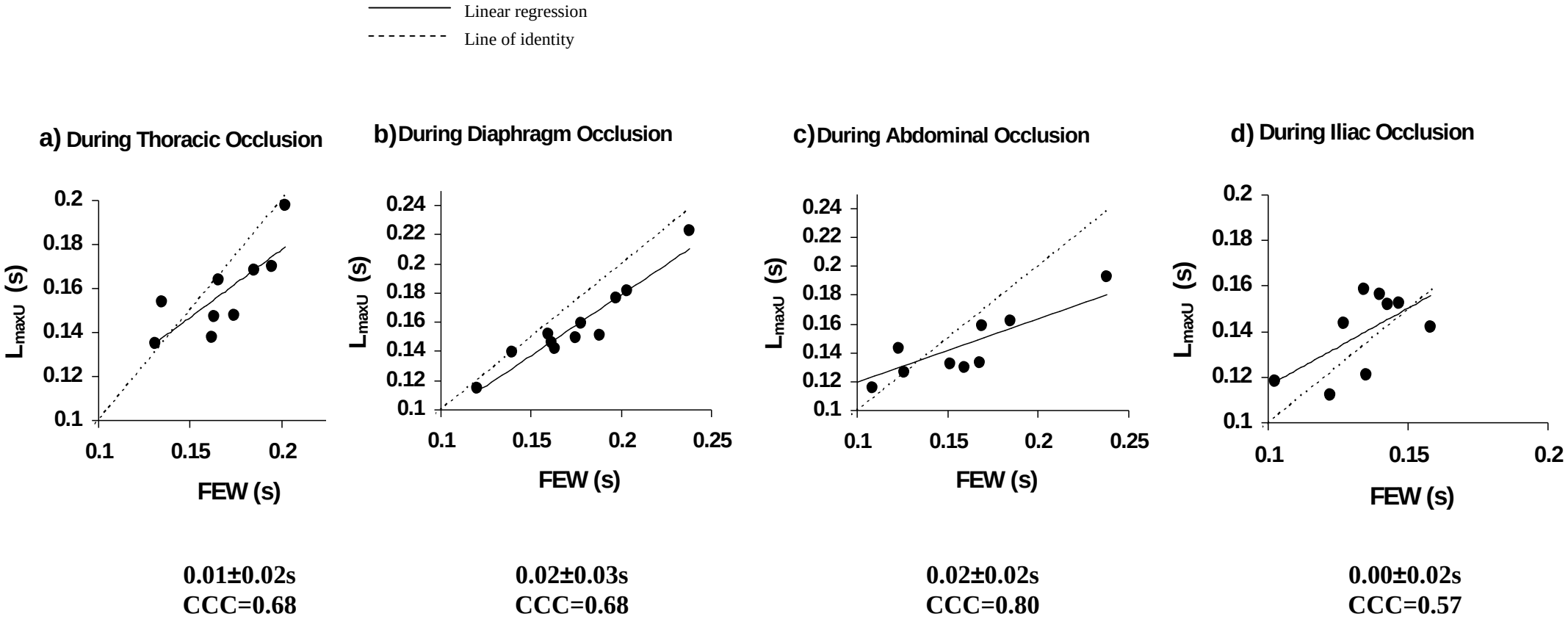

Figure 4.7: Lin's concordance correlation plots showing that the relationship between forward expansion wave (**FEW)** onset and maximum shortening velocity of the long axis (**L_{maxU})** remains strong during thoracic, diaphragm, abdominal and iliac occlusion. Each dot is a representative time taken for each dog; data is again missing for dogs 2 and 6 during thoracic and iliac occlusion.

The rapid stage of the forward expansion wave

In Chapter 3 the three phases of LV wall velocity of shortening were described **Figures 3.8** and **3.14**. It was found that in late systole both the minor and long axis undergo a simultaneous change in velocity ($\mathbf{L_i}$ and $\mathbf{M_i}$) which generates the rapid increase of the FEW. This is shown in **Figure 3.17**. Under control conditions described in chapter 3 this time occurred ~190ms after the R wave of the QRS complex (**Table 3.1**). This also corresponds with the times to both peak aortic pressure ($\mathbf{P_{max}}$) and an inflection point in the aortic flow waveform **(Ui)**. During proximal occlusions the time interval from the R wave of the QRS complex to the FEW rapid increase in energy is delayed by an average of 5-10ms (See appendix 4.3). However, the onset of the FEW rapid stage still highly agrees with $\mathbf{L_i}$, $\mathbf{M_i}$, $\mathbf{P_{max}}$ and **Ui** as they are all also delayed by 5-10ms. This is shown in **Figure 4.8. Table 4.4** displays the average times and concordance values calculated between the rapid increase of the FEW and the other 4 events mentioned above, all times agree well**.** Individual dog timings for all events can be found in **Appendix 4.3**.

Table 4.4: Time intervals (average± standard deviation) during all four occlusions from the peak R wave of the QRS complex to the time of the forward expansion wave rapid increase ($\mathbf{dI_{+e2}}$), long ($\mathbf{L_i}$) and minor ($\mathbf{M_i}$) axis velocity of shortening inflection point, peak aortic pressure ($\mathbf{P_{max}}$) and an infection point on the aortic velocity wave form ($\mathbf{U_i}$). During all occlusions these 5 events coincide with each other. The CCC values represent the level of agreement found between the time of $\mathbf{dI_{+e2}}$ with all other events during each occlusion

Occlusion	**dI_{+e2}**	**L_i**	**M_i**	**P_{max}**	**U_i**
Thoracic	**0.201±0.022s**	**0.196±0.028s** **CCC=0.90**	**0.194±0.025s** **CCC=0.89**	**0.204±0.021s** **CCC=0.90**	**0.196±0.027s** **CCC=0.92**
Diaphragm	**0.211±0.035s**	**0.205±0.033s** **CCC=0.96**	**0.202±0.034s** **CCC=0.96**	**0.212±0.033s** **CCC=1.00**	**0.211±0.036s** **CCC=0.96**
Abdominal	**0.181±0.030s**	**0.182±0.030s** **CCC=0.99**	**0.179±0.029s** **CCC=0.97**	**0.180±0.031s** **CCC=0.98**	**0.181±0.029s** **CCC=1.00**
Iliac	**0.197±0.020s**	**0.195±0.021** **CCC=0.83**	**0.191±0.022** **CCC=0.84**	**0.190±0.016s** **CCC=0.84**	**0.192±0.018s** **CCC=0.90**

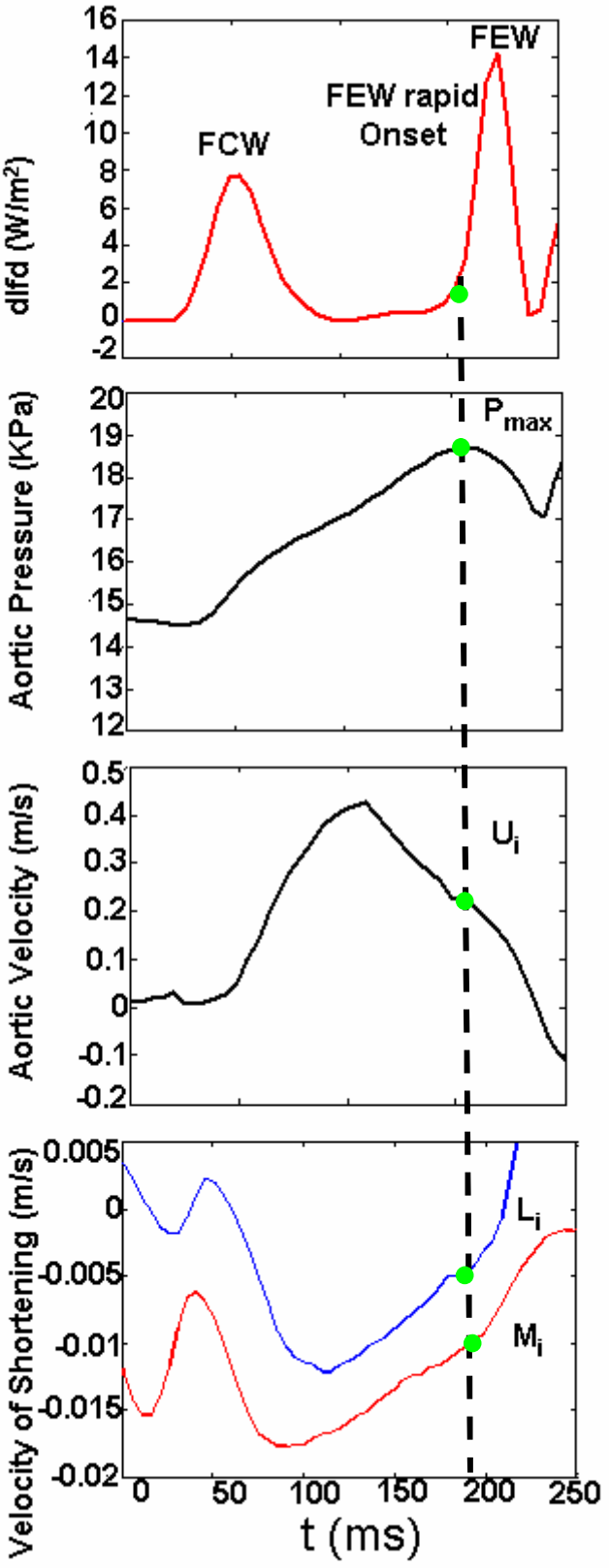

Figure 4.8: A composite showing that during thoracic occlusion the rapid increase in energy of the forward expansion wave (FEW) still coincides with $\mathbf{L_i}$, $\mathbf{M_i}$, $\mathbf{P_{max}}$ and **Ui**. The vertical line shows the coincidence of the inflection points with aortic U as well as the onset of the rapid FEW which are represented by the green dot (●). The bottom plot is of long (blue) and minor (red) axis velocity of shortening.

4.4.4 Wave energy

During control conditions the slopes of LV axes movement during the respective stages of ejection were found to influence the energy carried by both the FCW and FEW (**Figure 3.20** and **Figure 3.21**). During all occlusions the energy carried by the FCW and FEW correlate with the axes stages of acceleration and deceleration. The FCW correlates with both axes acceleration of shortening as seen in **Figures 4.9** and **4.10.** The FEW also still correlates with the long axis rate of deceleration in late systole **Figure 4.11.**

Acceleration

During proximal occlusions the rate of both minor axis and long axis acceleration decreases. During thoracic occlusion the slope of minor axis acceleration decreases from -0.22±0.08 m/s to -0.15±0.07 m/s. The slope of long axis acceleration also decreases from -0.20±0.08 m/s to -0.14±0.07 m/s. The resulting magnitude of the FCW is reduced due to the slower axial rates during early systole.

Deceleration

During proximal occlusions the slope of long axis deceleration during end systole (stage III) is less steep during proximal occlusions compared to control. During thoracic occlusion the slope of long axis deceleration is only 0.17±0.05 m/s compared to the 0.23±0.07 m/s seen during control conditions. The magnitude of the FEW is also diminished suggesting that the rate of axial shortening of the long axis during this late stage controls the energy carried by the FEW.

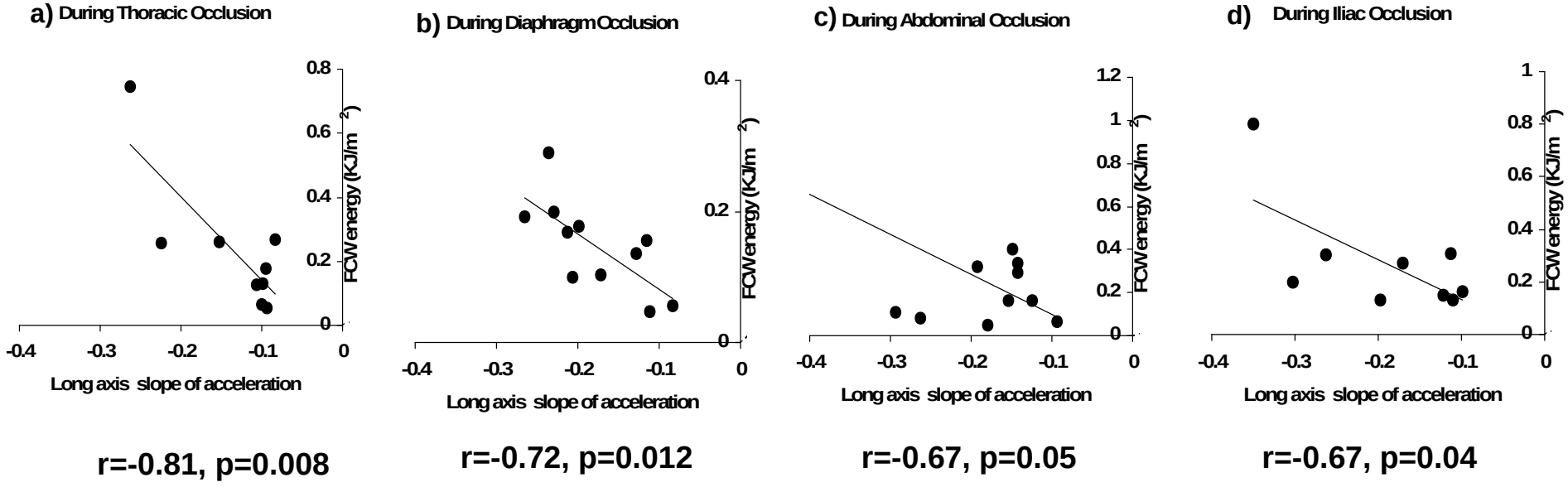

Figure 4.9: Correlations plots during all four occlusions showing the strong negative correlation seen between the energy carried by the forward compression wave (FCW) and the rate of acceleration of the long axis during early systole. The slower the rate of acceleration the smaller the FCW.

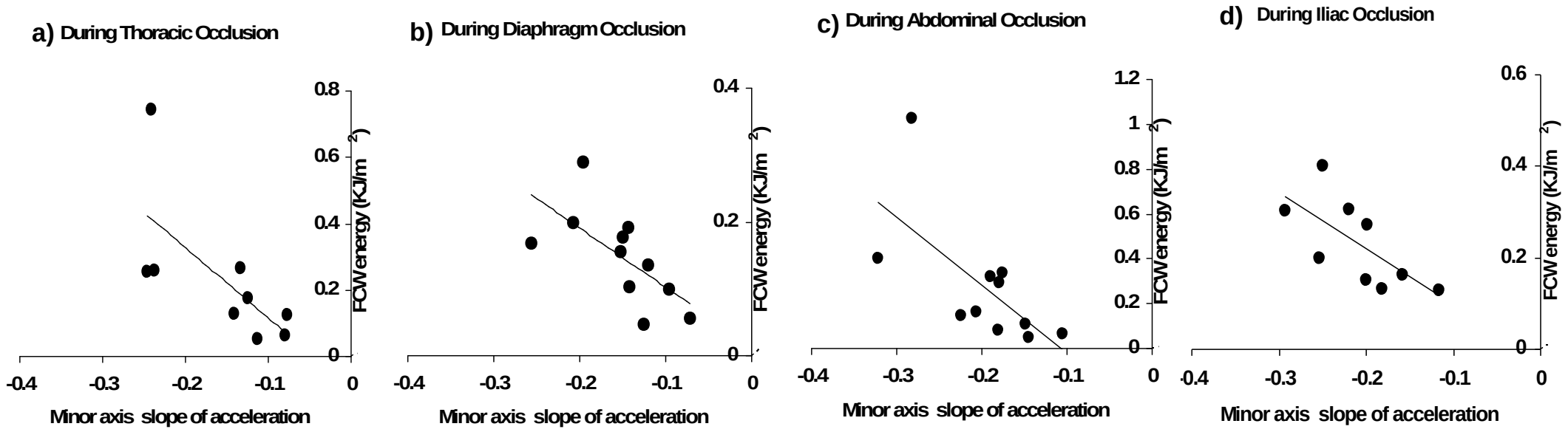

Figure 4.10: Correlations plots during all occlusions showing the strong negative correlation seen between the energy carried by the forward compression wave (FCW) and the rate of acceleration of the minor axis during early systole.

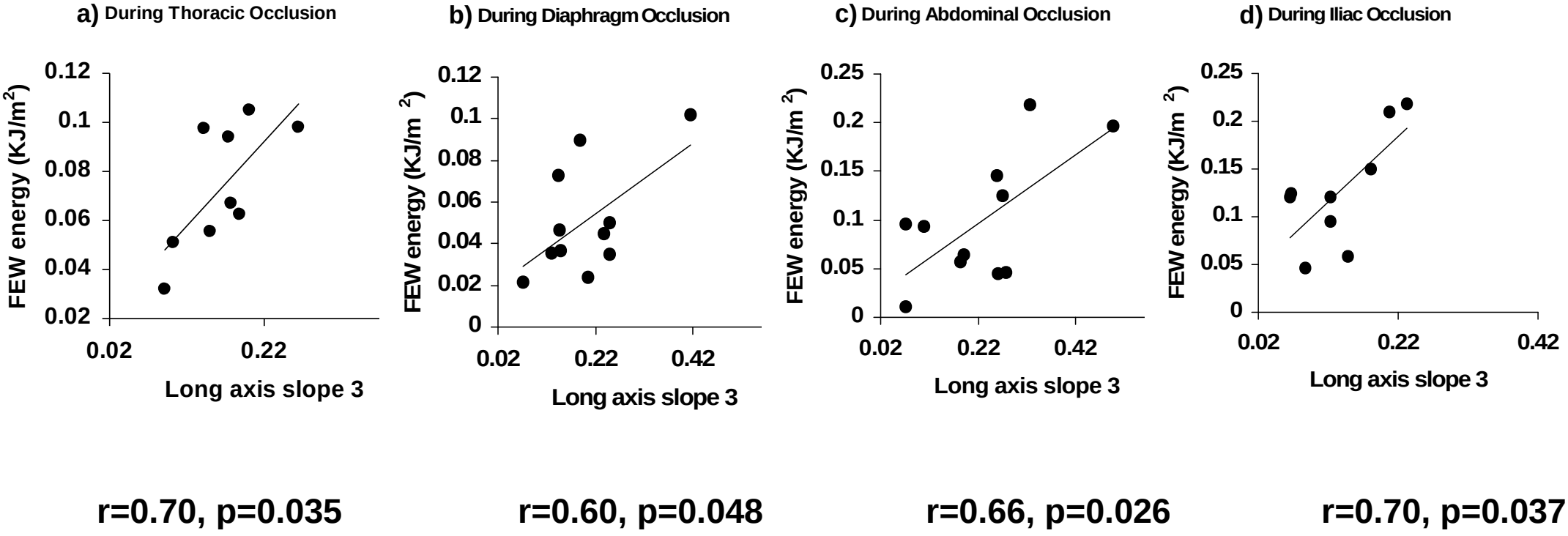

Figure 4.11: Correlation plots during each of the four occlusion demonstrating the positive correlation observed between long axis rate of deceleration at end systole and the energy carried by the forward expansion wave (FEW).

4.4.5 Reservoir and wave theory

Wave speed

Appendix 4.4 shows individual dog wave speeds before and during all four occlusions both before and after aortic reservoir subtraction.

In summary, after aortic reservoir subtraction wave speed is reduced by 11% (5.87±1.62m/s vs. 5.21±1.66m/s) before thoracic occlusion compared to a significantly larger reduction of 39% (10.61±3.51m/s vs. 6.46±2.35m/s) during thoracic occlusion. Diaphragm occlusion follows a similar pattern; the wave speed is reduced by 14% (5.65±1.32m/s vs. 4.85±1.37m/s) before occlusion and by 35% (6.07±1.36m/s vs. 3.93±0.75m/s) during diaphragm occlusion. The two distal occlusions have less of an effect on wave speed both before and after aortic reservoir subtraction. Wave speed is reduced by 11% before and 10% during abdominal occlusion and by 13% both before and during iliac occlusion.

Wave magnitudes

Appendix 4.2 shows average wave magnitudes before and during all four occlusions both before and after aortic reservoir subtraction.

During thoracic occlusion the FCW is reduced by 21%, however after aortic reservoir subtraction the energy carried by FCW is further reduced from 232±209J/m^2 to 159±132 J/m^2. The BCW is reduced dramatically after aortic reservoir subtraction from -213±40J/m^2 to just -14±10 J/m^2 during thoracic occlusion. The FEW energy is increased from 78±64J/m^2 during thoracic occlusion to 98±28 J/m^2 after aortic reservoir subtraction during thoracic occlusion. A similar pattern is seen during all occlusions; the FCW and BCW are smaller after reservoir subtraction while the FEW is slightly larger.

Wave timings during thoracic occlusion

The backward compression wave:

After reservoir subtraction the BCW occurs within 0.01±0.01s, this time agrees highly with the before occlusion time, CCC=0.82 as shown by **Figure 4.12 a.**

The time of BCW arrival back to the heart is not altered significantly by aortic reservoir subtraction even during thoracic occlusion, the relationship between BCW and $\mathbf{M_{maxU}}$ is still robust, CCC= 0.79, this is seen in **Figure 4.12 b.**

The forward expansion wave:

After reservoir subtraction the FEW occurs on average 0.01±0.02s before that of original WIA, this time still agrees closely with the before occlusion time during thoracic occlusion, CCC=0.75 as shown by **Figure 4.13 a.** Again, as the timing of the FEW onset is not altered dramatically there is still a remarkable agreement seen between the onset of the FEW and $\mathbf{L_{maxU}}$. CCC= 0.71. This can be seen in **Figure 4.13 b.**

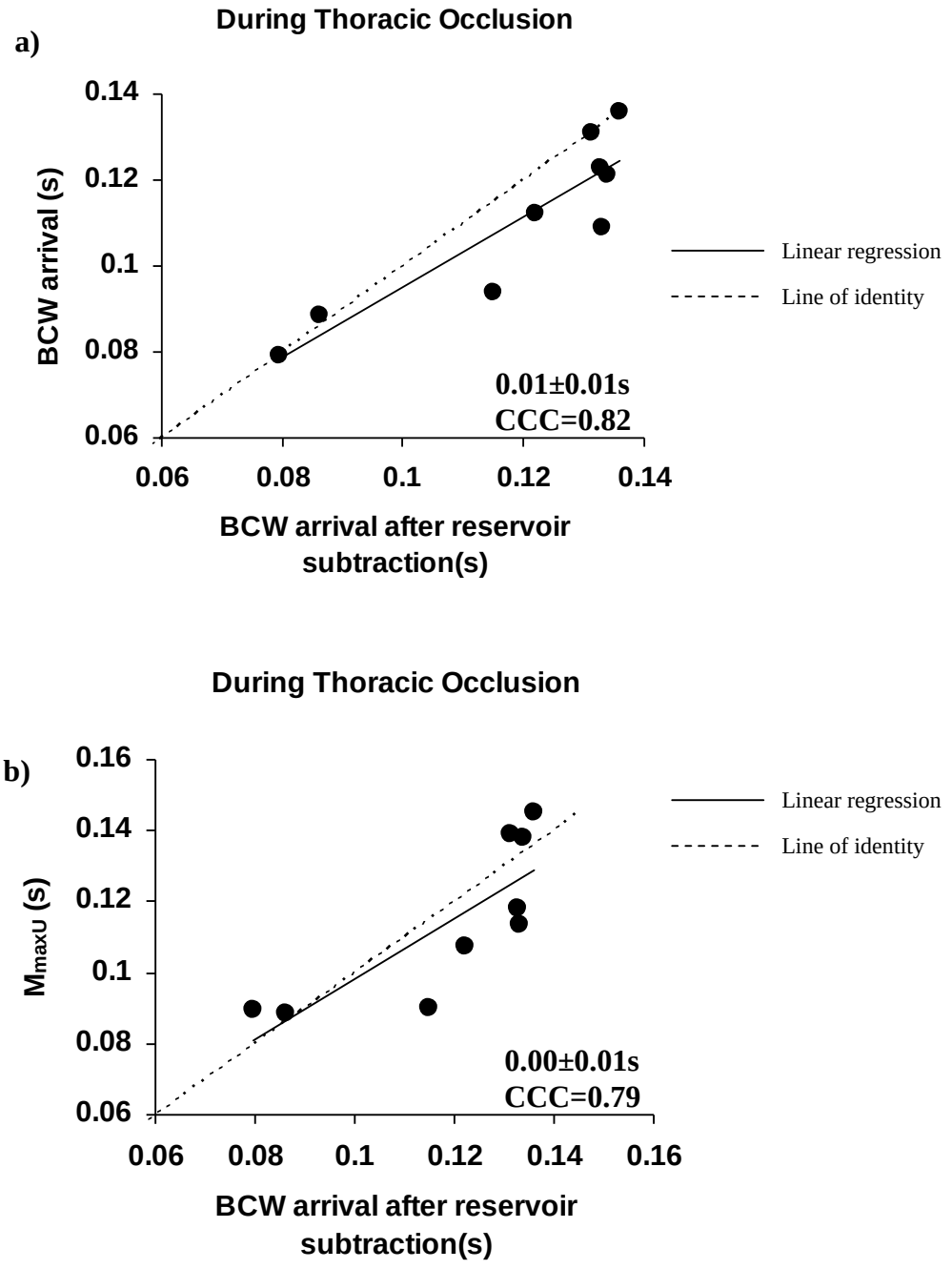

Figure 4.12: Lin's concordance correlation graphs showing that the time from the R wave of the QRS complex to the time of the backward compression wave (BCW) arrival at the heart is not altered by aortic reservoir subtraction in a). This time always coincides with the time of maximum shortening velocity of the minor axis ($\mathbf{M_{maxU}}$) as shown in b).

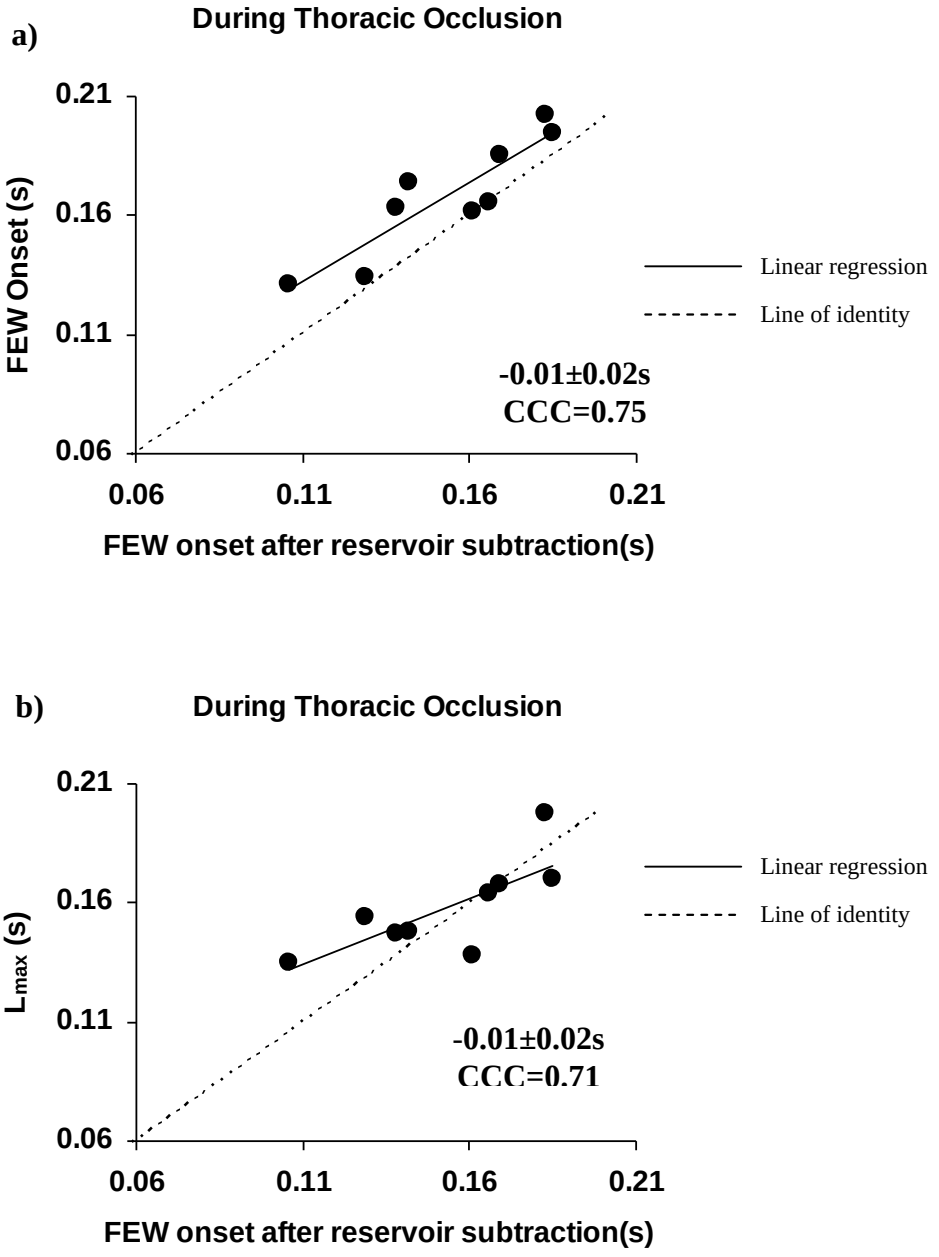

Figure 4.13: Lin's concordance correlation graphs showing that the time from the R wave of the QRS complex to the time of forward expansion wave (FEW) generation is not altered by aortic reservoir subtraction in a). This time still coincides highly with the time to maximum shortening velocity of the long axis ($\mathbf{L_{maxU}}$) as shown in b).

The forward expansion wave rapid increase in energy: The FCW always coincides with $\mathbf{M_{maxU}}$; the FEW onset always coincides with $\mathbf{L_{maxU}}$. **Figure 4.14** shows that the rapid increase of the FEW always coincides with a change in velocity of both long and minor LV axes irrelevant of any occlusion or aortic reservoir subtraction. The results for diaphragm, abdominal and iliac occlusion are presented in **Table 4.5**.

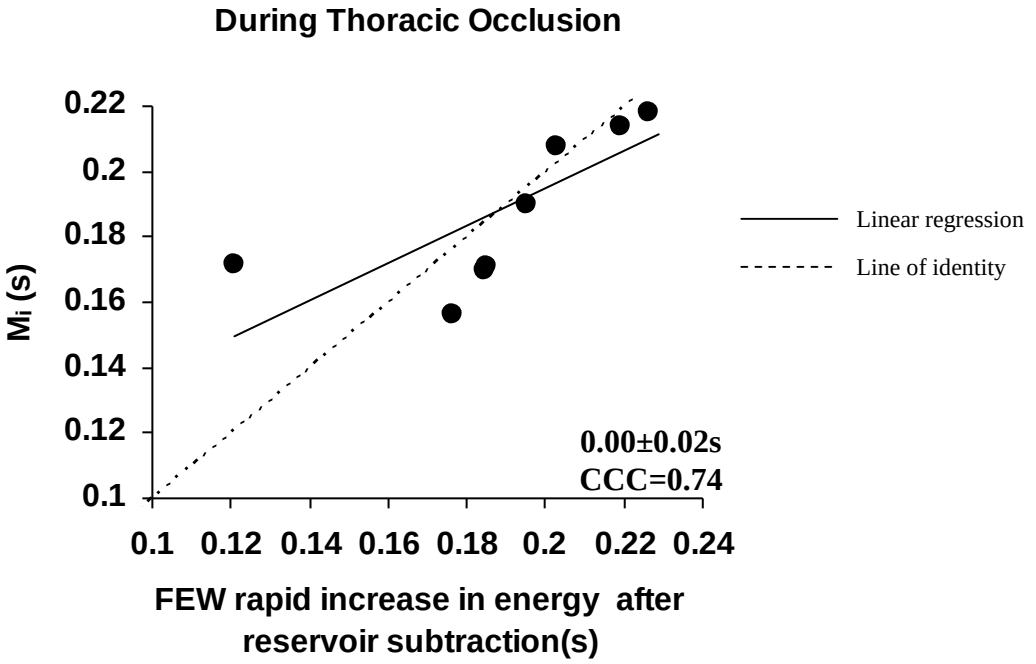

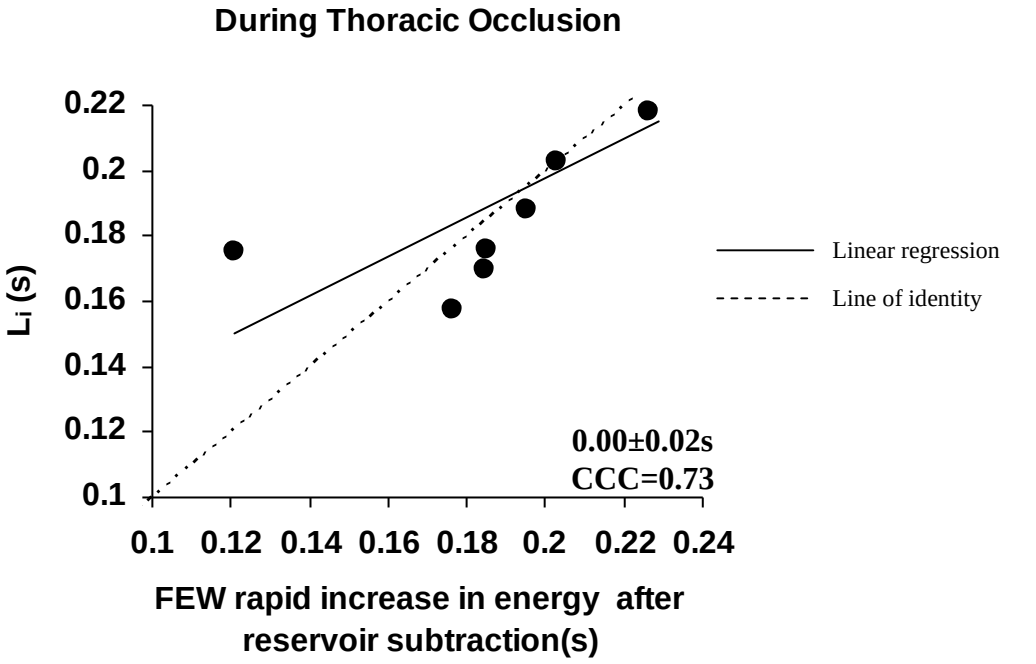

Figure 4.14: The rapid increase in energy of the forward expansion wave (FEW) still corresponds to the time that both the minor ($\mathbf{M_i}$) axis in a) and long ($\mathbf{L_i}$) axes in b) change velocity in late systole, even during thoracic occlusion.

Table 4.5: A table to show the average differences and Lin's concordance results after aortic reservoir subtraction between the mechanical relationships already formed. The backward compression wave (**dI_{-c}**) arrival still coincides with maximum velocity of shortening of the minor axis (**M_{maxU}**). The forward expansion wave onset (**dI_{e+1}**) still coincides with maximum velocity of shortening of the long axis (**L_{maxU}**). The forward expansion wave rapid increase in energy (**dI_{e+2}**) is still generated when both the minor and long axis change their rate of shortening during late systole (**M_i, L_i**).

	Thoracic Occlusion	**Diaphragm Occlusion**	**Abdominal Occlusion**	**Iliac Occlusion**
dI_{-c}: M_{maxU}	0.00±0.01s **CCC=0.79**	0.00±0.00s **CCC=0.91**	0.00±0.02s **CCC=0.85**	0.00±0.00s **CCC=0.95**
dI_{e+1}: L_{maxU}	0.00±0.02s **CCC=0.71**	0.00±0.01s **CCC=0.92**	0.01±0.02s **CCC=0.75**	0.00±0.02s **CCC=0.60**
dI_{e+2}: M_i	0.00±0.02s **CCC=0.74**	0.01±0.01s **CCC=0.98**	0.00±0.01s **CCC=0.98**	0.00±0.01s **CCC=0.84**
dI_{e+2}: L_i	0.00±0.02s **CCC=0.73**	0.01±0.01s **CCC=0.97**	0.00±0.01s **CCC=0.97**	0.00±0.01s **CCC=0.83**

Wave energies: The magnitudes of the waves are altered by aortic reservoir subtraction. The new energies carried by the wave calculated after aortic reservoir subtracted were correlated with their corresponding LV slopes**. Table 4.6.**

Table 4.6: A table to present the Pearson's correlation coefficients calculated between the energy of both the forward compression wave (FCW) and forward expansion wave (FEW) after aortic reservoir subtraction with left ventricle (LV) axial rates of acceleration and deceleration. Although the magnitudes of the waves are altered by aortic reservoir subtraction the correlations observed during all occlusions remain respectable.

	FCW energy and LV minor axis acceleration slope	**FCW energy and LV long axis acceleration slope**	**FEW energy and LV long axis deceleration (slope III)**
Thoracic Occlusion	r=-0.69, p=0.039	r=-0.79, p=0.014	r=0.70, p=0.03
Diaphragm Occlusion	r=-0.71, p=0.015	r=-0.71, p=0.048	r=0.58, p=0.045
Abdominal Occlusion	r=-0.69, p=0.018	r=-0.62, p=0.025	r=0.66, p=0.026
Iliac Occlusion	r=-0.59, p=0.052	r=-0.64, p=0.06	r=0.70, p=0.037

4.5 Discussion

The introduction of snares along the aorta and in the iliac artery brings about acute changes in blood pressure and flow. Previous studies have used such occlusions to create closed end reflection sites in order to study aortic pressure, velocity and the reflected wave seen in mid-systole (Khir and Parker 2004, 2005, Van Den Bos et al. 1976, Ramsey and Sugawara 1997). The size of the reflected waves produced has previously been explored by Khir et al. (2005). The Khir et al. investigation observed that during proximal occlusions the reflected wave arrive at the heart significantly earlier (thoracic occlusion=45% and diaphragm occlusion=15%), their duration is longer and their magnitude is much greater, with peak intensity increasing by 257% and 125% compared to control conditions. The effects of more distal occlusions were found to be negligible. Others that agree with these conclusions are Ramsey and Sugawara (1997) who performed a similar experiment and noticed that the large reflected wave seen during thoracic occlusion became smaller and was more delayed as the occlusion site moved distally. The forward waves were also seen to be effected by proximal occlusions in the Khir at al. study. The FCW peak was reduced by 41% during thoracic occlusion while the FEW peak was reduced by 42%. This chapter aimed to determine whether LV wall movement still controlled the onset and magnitude of the FEW during times of increased load created by the larger reflected waves.

Left ventricle wall movement and the forward expansion wave

During the control experiment (chapter 3) a mechanism for FEW generation emerged. The FEW was seen to have two phases: a slow onset followed by a rapid increase in energy. The slow onset is generated when the long axis reaches its maximum velocity of shortening ($\mathbf{L_{maxU}}$) while the rapid increase is generated later in systole when both axes show an inflection in their velocity of shortening and begin to decelerate at a steeper rate ($\mathbf{M_i,L_i}$). For this mechanism to be accurate the story must hold true regardless of any aortic manipulation such as occlusions. This is indeed what was found after looking at the timings of these events during occlusion. Throughout all occlusions the time of FEW onset always corresponded to $\mathbf{L_{maxU}}$. The close agreement can be seen in **Table 4.3** and Figures **4.6** and **4.7**.

The rapid increase in energy of the FEW also still begins with the inflection points in both LV axes velocity of shortening plots as seen in **Figure 4.8**. This time still also

agrees with peak aortic pressure ($\mathbf{P_{max}}$) and an inflection point on the aortic velocity wave form ($\mathbf{U_i}$) as seen in **Table 4.4**.

Left ventricle wall movement and the backward compression wave

Under control conditions it was seen that the BCW always coincides with the time of maximum velocity of shortening of the LV minor axis ($\mathbf{M_{maxU}}$). Throughout all occlusions the time of BCW arrival at the heart continues to agree with the time of $\mathbf{M_{maxU,}}$ this is seen in **Figures 4.4** and **4.5**. The separated BCW was found to be 507% larger during thoracic occlusion, 116% larger during diaphragm occlusion, 10% larger during abdominal occlusion and 10% smaller during iliac occlusion. These results are consistent with those seen by previous groups (Khir et al. 2000).

Wave energy

During thoracic occlusion the rate of minor axis acceleration of shortening decreases from -0.22±0.08m/s m/s to -0.15±0.07m/s. The long axis acceleration also decreases from -0.20±0.08m/s to -0.14±0.07m/s. In addition, peak minor and long axis velocities are 20% slower. These reductions result in a FCW that is 21% smaller than during control conditions. During diaphragm occlusion similar results are seen and the FCW is again reduced, this time by 50%. Wall movement appears to be relatively unaffected by the distal occlusions. The rate of both minor and long axis acceleration correlates well with the energy carried by the FCW during all occlusions. **Figures 4.9** and **4.10**

Before occlusion the slope of long axis deceleration in late systole (stage III) controlled the energy carried by the FEW. During all occlusions there is still a good correlation between rate of deceleration and FEW magnitude as seen in **Figure 4.11**. The magnitude of the FEW is diminished during proximal occlusion while the rate of deceleration is not as steep. This provides further evidence that the rate of axial shortening of the long axis during this late stage controls the energy carried by the FEW.

Aortic reservoir subtraction

As the cardiovascular system is now thought of as a wave and windkessel (reservoir) system by many (Wang et al. 2003, Davies et al. 2007) aortic reservoir subtracted wave intensity analysis was additionally performed on the data during all occlusions. During control conditions aortic reservoir subtraction does not dramatically alter the time of the three main wave onsets and the same was found during each occlusion

experiment. The onset of each wave still agrees well with its original wave intensity time. The data are presented in **Table 4.5**. The times to onset thus still correlate well with their respective axis peak velocities. The BCW still coincides with $\mathbf{M_{maxU}}$ shown in **Figure 4.12**. The FEW still coincides with $\mathbf{L_{maxU}}$ as seen in **Figure 4.13**, and the rapid increase in FEW energy additionally still coincides with $\mathbf{M_i}$ and $\mathbf{L_i}$, **Figure 4.14**.

It is now established that the magnitudes of all waves are altered by reservoir subtraction. During thoracic occlusion the FCW is reduced by 21% before and 50% after reservoir subtraction. The BCW is 507% larger before aortic reservoir subtraction however it is actually 66% smaller after reservoir subtraction. The FEW on the other hand increases after reservoir subtraction from 35% smaller to only 10% smaller. These changes in magnitude made it necessary to compare the new magnitudes of the forward waves to LV axes acceleration and deceleration stages during early and late ejection. The results show that a strong negative correlation is still found between both minor and long axes acceleration during early systole and the energy carried by the FCW. A strong positive correlation is again found between the energy carried by the FEW and the rate of deceleration of the long axis in late systole FCW. The results can be found in **Table 4.6.**

Wave speed

Previous studies also looked at the effect of occlusion on local wave speed (Khir et al. 2004) and saw that during proximal occlusions the wave speed is significantly larger. This makes physiological sense as arteries become less compliant under such increased pressure. This study took these data a step further by investigating the effects of aortic root wave speed not only before and during occlusion but additionally before and after aortic reservoir subtraction. Wave speed is used as a surrogate marker of cardiovascular disease therefore it is important to determine the wave only effect on wave speed. In control conditions the wave speed is reduced by 11% (5.65±1.32m/s vs. 5.21±1.66m/s) after reservoir subtraction as seen in appendix **4.4**. Before accounting for the aortic reservoir this study found that there is a marked increase from control conditions and proximal occlusions. Thoracic occlusion increases the wave speed by 84%. However after reservoir subtraction the wave speed value is decreased by 39% from 10.61±3.51 m/s to 6.46±2.35 m/s, which is actually not very different to the value seen before occlusion (5.21±1.66 m/s). It appears that

during the times of proximal occlusion the aortic reservoir plays a big role in determining the wave speed.

4.6 Conclusion

The aim of this occlusion study was to determine whether the mechanism for FEW generation found in chapter 3 remains correct during aortic manipulation. The results demonstrate that this is true. Proximal occlusion has a much greater effect on haemodynamics than distal occlusions however the FEW is always generated when the LV long axis reaches its maximum velocity of shortening in mid-systole. The FEW has a slow onset followed by a rapid increase in energy which is consistently seen. The energy carried by the FEW is controlled by the long axis rate of deceleration during late systole. Another interesting finding is that during times of increased reflected waves the arrival of the BCW at the heart always coincides with maximum shortening velocity of the minor axis. Further investigation is required to determine the exact effect that this increased load has on LV minor axis function.

The last two chapters have used canine data to provide substantial and convincing evidence that the FEW is generated by the LV when the long axis begins to slow and also that the BCW could bring about a reduction in the shortening velocity of the LV minor axis during mid-systole. The following two chapters will aim to discover whether these mechanisms occur in human hearts.

Chapter 5
Ventricular-Aortic Interaction in Humans: The Left Ventricle Long Axis and Wave Intensity Analysis

5.1 Introduction

Animal studies have various advantages as described in the introduction to chapter 3, however in order for the mechanisms found in this thesis so far to be considered useful in clinical practise human data are a necessity. The next two chapters concentrate on the relationships found between LV movement and WIA in human volunteers. Three associations have been observed in the dog studies:

1) ***The FEW onset coincides with the time of maximum shortening velocity of the LV long axis.***
2) ***A rapid increase of the FEW is consistently present and corresponds to a time during late systole when both the minor and long axes change their rate of shortening.***
3) *There is a strong association between the arrival of the BCW at the heart during mid-systole and the slowing of the minor axis velocity of shortening.*

This chapter will concentrate on points 1 and 2 while chapter 6 concentrates on point 3. The results from chapters 3 and 4 have shown that these time relationships are preserved even when the aorta and iliac arteries are manipulated by snares. In the next chapter the timing and magnitude of the FEW have been studied in 11 individuals with normal LV function and compared to LV wall velocities to validate the mechanisms found in previous chapters in human hearts.

5.2 Hypothesis:

In humans the FEW will have a slow onset followed by a rapid increase in energy later in systole. The FEW will be generated when the LV long axis reaches its peak velocity of contraction. The FEW rapid increase in energy will be the consequence of changes in axial velocity during late systole.

5.3 Methods

5.3.1 Subjects: 11 individuals (age 54±10years, 7 female) with normal LV function, classified as having an ejection fraction over 50%, were studied. Baseline characteristics for all individuals can be seen in **Table 5.1**. All subjects were patients at St Mary's Hospital, Paddington who had been admitted for a coronary angiogram after experiencing atypical chest pain. All patients received an echocardiography examination immediately before their procedure. The echocardiograms found no abnormal LV function, while the angiograms also revealed no signs of significant coronary disease. Subjects were excluded if they had any previous coronary intervention, valvular pathology, regional wall motion abnormality or rhythm other than sinus. The protocol was approved by St Mary's Ethics committee and met with the requirements of the Research Governance Framework (RGF). Written informed consent was obtained from all participants. See appendix 5.1 and 5.2 for patient consent form and further information.

Table 5.1 Individual baseline characteristics for every subject. LV=left ventricle, LVH= left ventricular hypertrophy, EF=ejection fraction. All patients are appropriately medicated.

Subject	Sex	Age (yrs)	Weight (kg)	Echocardiography comment	Medication
N1	M	49.56	86	Good LV, LVH, EF>50%	Asprin, Lansoprazole
N2	F	45.46	82	Good LV, EF> 50%	nil
N3	F	59.34	82	Good LV, LVH, EF> 50%	Amlodipine, Atenolol, Asprin g, Simvastatin
N4	F	46.60	88.9	Good LV, EF> 50%	nil
N5	M	45.46	82	Good LV,LVH, EF> 50%	Asprin 75mg, Simvastatin 40m
N6	F	55.96	90	Good LV, LVH, EF> 50%	Atenolol,Citalopram mg, Lansoprozole , Tibolone
N7	F	50.79	68.9	Good LV, EF> 50%	Paracetamol, Vioxx
N8	F	54.89	54	Good LV, EF> 50%	Asprin 75, Fluvastating, Flixatide, Salbutamol, Serevent
N9	F	71.55	75	Good LV, EF> 50%	nil
N10	M	45.36	69	Good LV, EF> 50%	asprin 75mg, atorvastatin 20mg
N11	M	72.95	67	Good LV, EF> 50%	Atorvastatin, asprin
Average		**54.36**	**76.8**		
±SD		**10.02**	**11.09**		

5.3.2 Invasive hemodynamic measurements:

The calculation of wave intensity requires the measurement of blood pressure and velocity, as described in chapter 2 sections 2.2-2.4.

Instantaneous aortic blood velocity

Aortic velocity was recorded using a single-use J-tip Doppler Flowire (Volcano Therapeutic Corp, Rancho Cordova, and CA.USA). The wire is 0.014" in diameter with a Doppler transducer tip placed at the distal end of the wire. The transducer was guided up into the aortic root to measure peak flow velocity using pulse wave Doppler focused 5mm ahead of the tip of the wire. Recordings were taken for 60 seconds. The raw data are sampled at 100Hz and passed from the tip into a flowmap console where the analogue signal is converted into a digital instantaneous Doppler velocity waveform.

Instantaneous aortic blood pressure

Aortic pressure was recorded using a single-use J-tip Doppler Wavewire (Volcano Therapeutic Corp, Rancho Cordova, CA.USA) diameter 0.014". Unlike the Doppler transducer tip the pressure transducer is located 30mm from the tip of the wire. An instantaneous pressure measurement can be acquired wherever the wire is placed. The raw data are passed from the transducer into a Wavemap console where the analogue signal is converted into a digital signal by a 12 bit analogue to digital converter. The signal is sampled at 200Hz to form a pressure waveform

Three ECG leads were positioned and attached to the patient's chest to record a signal in all subjects during all recordings.

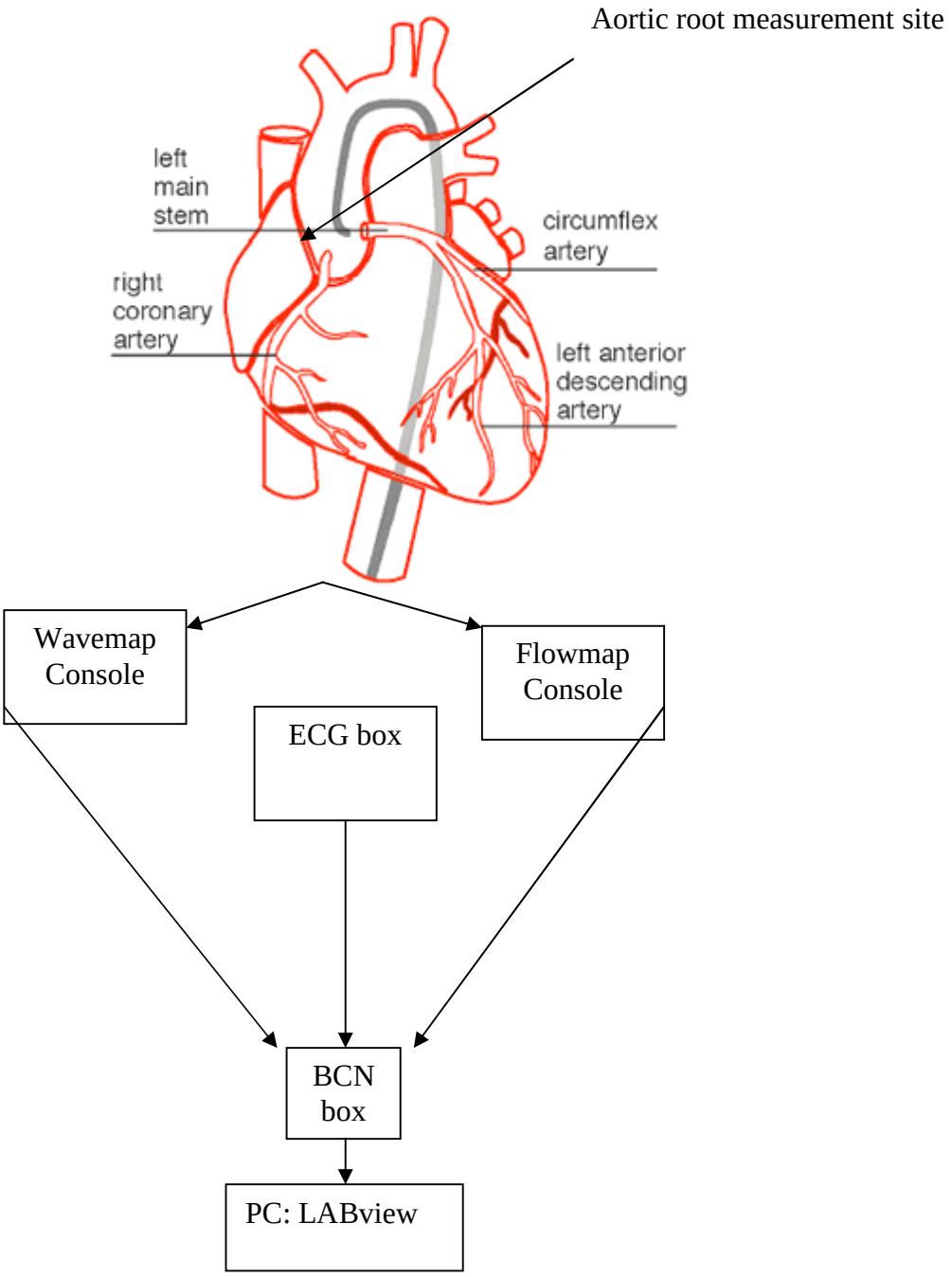

Figure 5.1: A sketch to represent the arrangement of data acquisition. The catheter is inserted into the aorta via one of the femoral arteries. The flow and wave wires are advanced into the catheter allowing measurements of aortic root pressure and flow to be recorded invasively. The data is fed back to a PC containing LABview software, which presents and records the information.

5.3.3 Protocol

1. Insert appropriate coronary catheter: For these aortic measurements a Judkins right diagnostic coronary catheter was inserted into the femoral artery and advanced into the right coronary artery. This catheter was selected, as it is large enough for both wires to be held free from the vessel wall.

2. Calibration of wires: The wires were calibrated prior to each use by sending a test signal through both wires. The calibration plots can be seen in **Figure 5.2** During each test the wires both transmit and receive. They adjust their transmission to maintain uniform amplitudes.

3. Alignment of wires: It is essential that pressure and velocity be recorded at exactly the same level within the aortic root. The wires are aligned using fluoroscopy to guide them ensuring that the transducers are level. Each wire has a radiolucent and radio opaque portion. As the radiolucent-radiopaque interface of the pressure wire is the site of the sensor this site was aligned with the tip of the velocity wire.

3. Optimise the velocity signal. The wire was rotated slowly to achieve the best quality Doppler envelope and a maximal velocity recording. Once this was achieved setting the flowmap console to the correct velocity of scaling (optimal –0-80cm/s, 0-200cm/s in weaker velocity conditions) and direction optimised the tracking. Blood was tracked in an anterograde mode at this position in the aorta. The signal intensity can also be improved by altering the velocity Doppler signal intensity but one must be careful to not increase the threshold above the optimum as the signal can become noisy.

4: Record signals: The signals were recorded in 60s periods

Wavemap

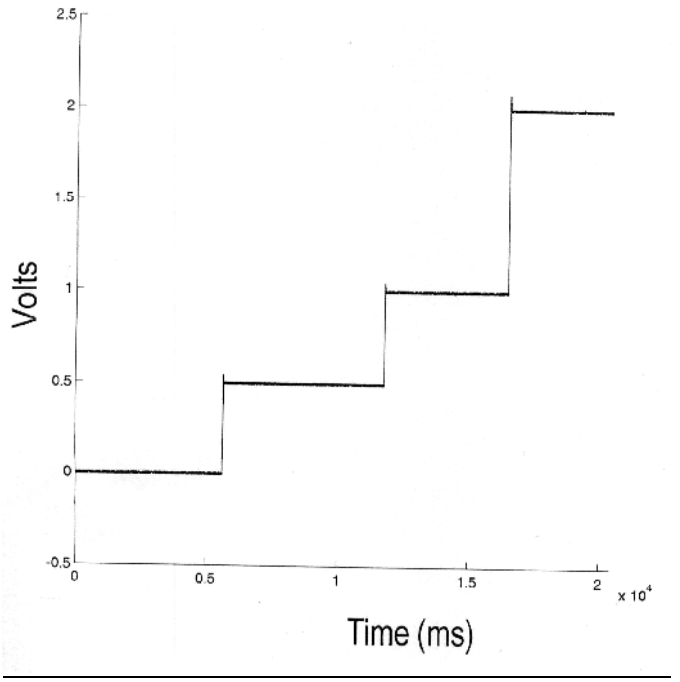

Flowmap

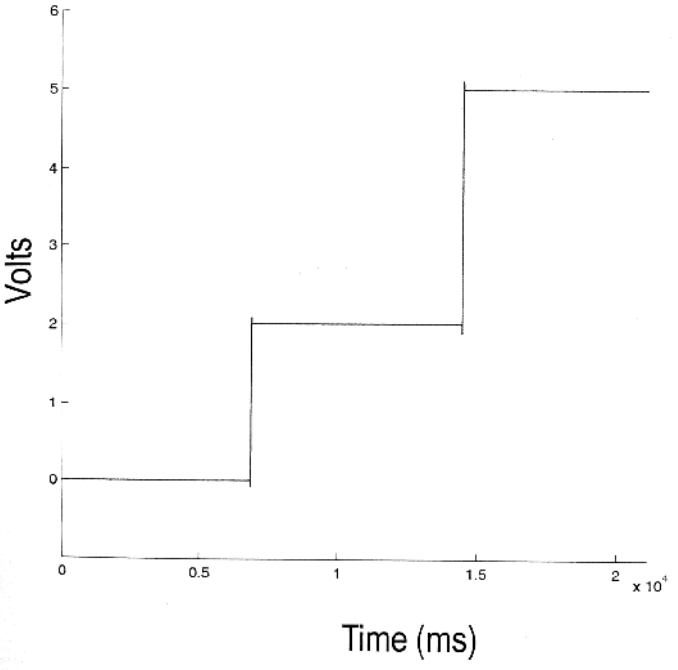

Figure 5.2: Calibration plots for both the wave wire and flow wire taken with kind permission from Davies J 2007: The wires both transmit and receive, a test signal is sent down them prior to each use.

5.3.4 Data Collection

The analogue output from both the flowmap and wavemap consoles plus an ECG signal from a separate ECG box are fed into a BNC connector box (BCN-2010, National Instruments) which leads into a PC containing customised acquisition software developed in LABview (National Instruments). Aortic velocity, pressure and the ECG signal are recorded as individual text files that can be loaded into matlab. Custom written programs in Matlab (The MathWorks Inc., MA, USA) were used to analyse the data.

5.3.5 Smoothing and Aligning

Prior to analysis the velocity and pressure waveforms were smoothed using a Savitzky-Goley filter (Savitzky-Goley 1964). Due to the close proximity of the transducers to the aortic valve opening the traces show strong quantization. A 30 point each way filter was applied to the data. **Figure 5.3** demonstrates how effective this method is. The foot of both waveforms were also aligned. This is required as instantaneous processing of both Flowmap and Wavemap is not possible and both consoles introduce a delay. Shifting of up to 5ms was required to adjust for the lag caused by the filter in the ultrasonic flow meter

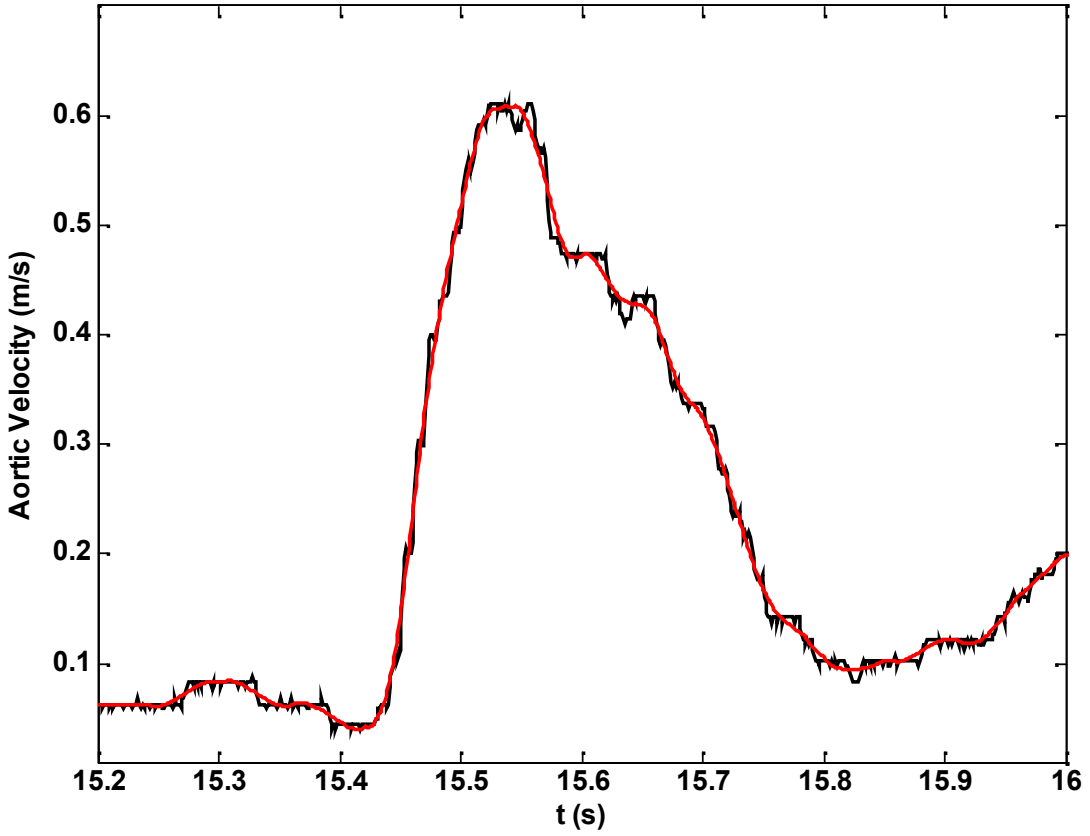

Figure 5.3: An example of an aortic root flow velocity plot collected by the flow-wire. After the acquisition in LABview (National Instruments) the raw data can be loaded and plotted in Matlab (The MathWorks Inc., MA, USA). In the aortic root flow is quite noisy. A custom made program written into Matlab can smooth the data to ignore the underlying noise making analysing the trace easier. The black trace above is aortic root velocity pre-smoothing and is rather noisy. The red trace represents the smoothed velocity plot. Time (t) is measured from an arbitrary time of acquisition.

.

5.3.6 Wave intensity analysis:

Both original wave intensity analysis theory and aortic reservoir and wave theory analysis were performed on the data. (See Chapter 2 for theoretical details).

5.3.7 Invasive data analysis

3-5 representative beats from each subject were plotted and analysed in Matlab (The MathWorks Inc., MA, USA). The times of all R-R intervals were recorded. The R wave of the QRS complex was taken as t=0. Wave speed was calculated using the PU-loop method described in chapter 2, section 2.3 and the results were used to separate the waves calculated using WIA into their forward and backward components as described in chapter 2 section 2.4. In chapters 3 and 4 it was observed that the FEW onset ($\mathbf{dI_{+e1}}$) is followed by a rapid increase in energy ($\mathbf{dI_{+e2}}$). The times to both of these stages were also calculated before and after aortic reservoir subtraction, described in chapter 2.6.

5.3.8 Haemodynamic analysis reproducibility

The time interval from the R wave of the QRS complex to the onset and rapid increase in energy of the FEW were repeated three times for each subject. The mean difference±SD to the onset of the FCW was 2±7ms (within subject coefficient of variation = <1%), the rapid increase of the FEW was 1±9ms (within subject coefficient of variation = <1%),

5.3.9 Non-invasive left ventricle tissue Doppler imaging

Velocity measurements*:* All subjects underwent an echocardiographic examination. This not only ensured that they had normal LV function but it allowed the measurement of regional LV long axis wall motion. A commercially available ultrasound system (Philips ATL HDI 5000, Andover, MA, USA) was used to perform the examinations. LV mitral annular wall velocities were acquired using pulsed-wave tissue Doppler imaging (TDI) at 5 different LV segments. In the apical four chamber view septal and lateral wall velocities were recorded, the transducer was then turned anticlockwise to achieve an apical two chamber view allowing the collection of inferior and anterior wall velocities. An apical three-chamber view was also obtained to recorded posterior wall velocity. All 5 segments can be seen in **Figure 5.4**. All recordings were made with a simultaneous superimposed ECG. Recordings were made at a sweep speed of 50mm/s. Pulsed-wave TDI provides high temporal resolution to record peak velocities. A 5mm sample volume is placed at the mitral annulus on the wall of interest and the low Doppler shift frequencies are recorded due to the heart moving through the sample volume throughout the cycle. Approximately 5-10 consecutive beats were recorded for each LV wall.

a)

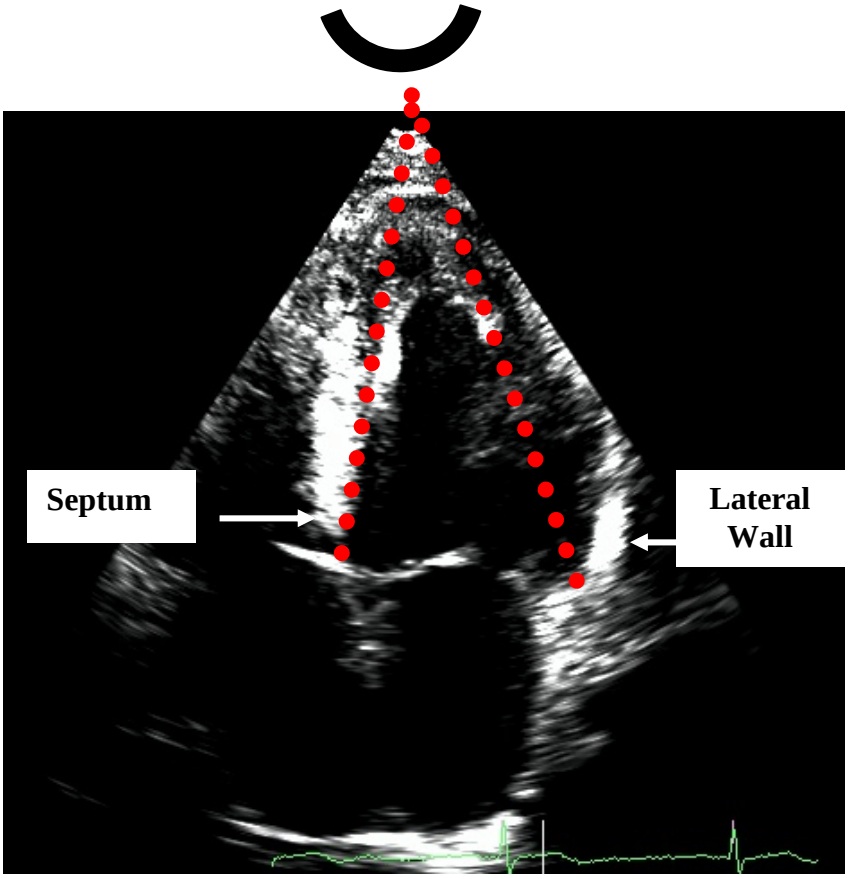

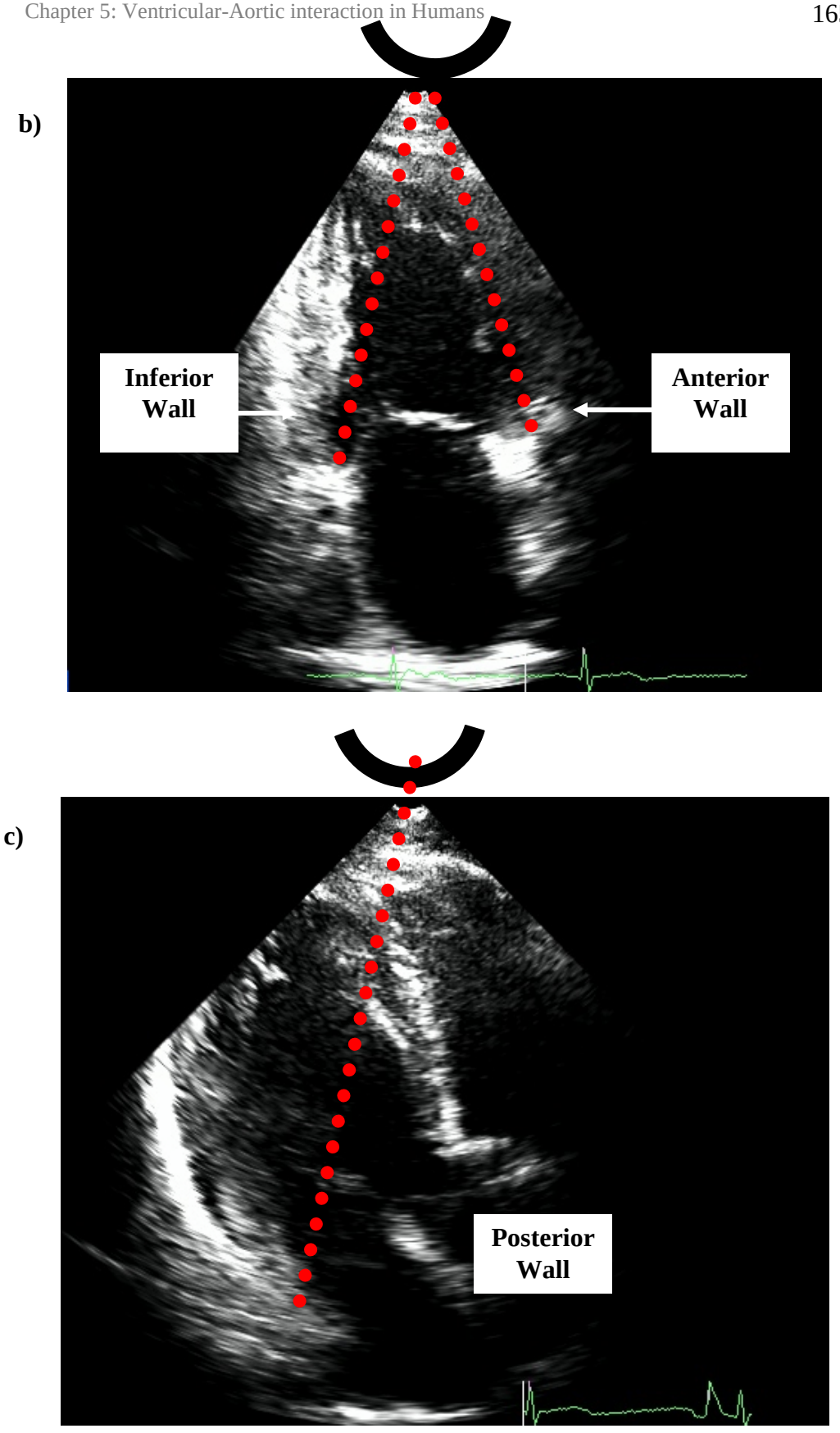

Figure 5.4: An example of an a) apical four-chamber view, b) apical two-chamber view and c) apical three-chamber view of the heart. The lines represents where the sample volume is placed to measure septal, lateral, anterior, inferior mitral annular wall velocities respectively**.**

5.3.10 Non-invasive tissue Doppler data analysis

3-5 representative cycles were analysed for each segment. R-R intervals were collected for each beat analysed. The R of the QRS represented t=0. TDI can be divided into a systolic and diastolic phase as shown in **Figure 5.5.** The systolic phase starts with an often multi-phasic narrow peak representing isovolumic contraction (IVC) (S1) which is followed by a positive systolic wave (S-wave) during ejection (S2). The diastolic phase consists of two negative waves representing rapid filling as the annulus descends away from the apex (E wave) and active atrial contraction (A-wave) that assists LV filling. The time interval from the R wave to the peak systolic S-wave (S2) wave was recorded.

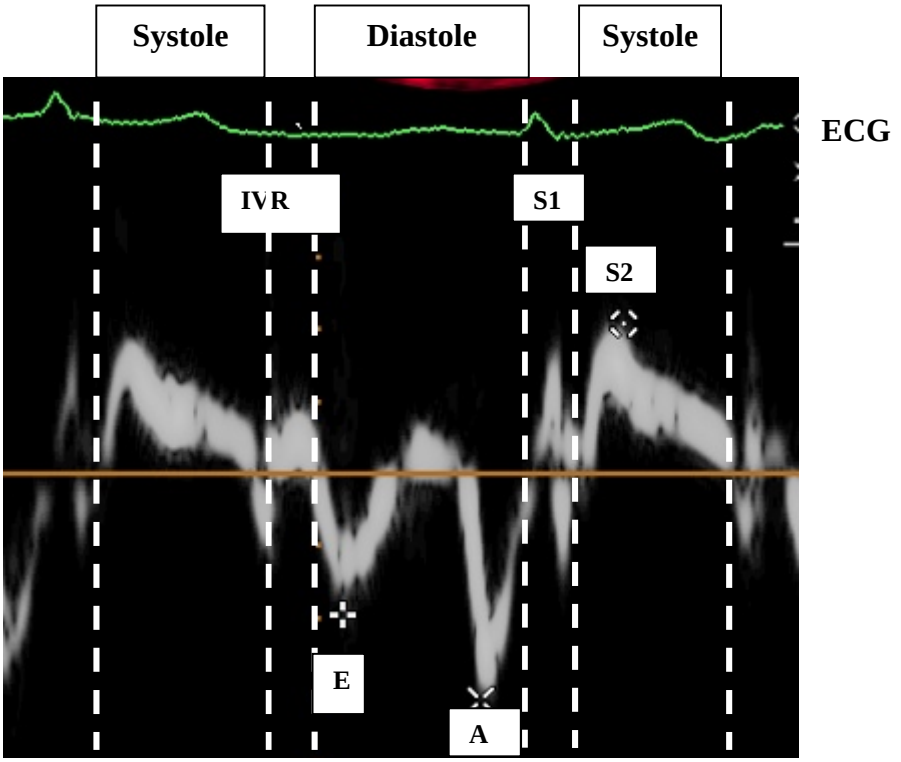

Figure 5.5: Longitudinal pulsed wave Doppler of the myocardium: S2= peak systolic wave, A= atrial contraction, E= Rapid filling, S1=isovolumic contraction (IVC), IVR=Isovolumic relaxation.

5.3.11: Tissue Doppler reproducibility

Each TDI S2 wave peak velocity amplitude and time to peak velocity measurement from the R wave of the QRS complex were repeated 3 times. Results were analysed by the same operator. The mean difference±SD for the time interval to peak S2 of all 5 LV segments are as follows. Septum 1±5ms (within subject coefficient of variation = 0.42%), lateral wall segment 0.7±4ms (within subject coefficient of variation = 0.41%), inferior wall segment 2±4ms (within subject coefficient of variation =1.45 %), anterior wall segment 4±11ms (within subject coefficient of variation = 1.7%) and posterior wall segment 2±5ms (within subject coefficient of variation = 0.95%).

Reproducibility data for peak velocity values for each segment are: Septum 0.075±0.13m/s (within subject coefficient of variation = 0.98%), lateral wall segment 0.003±0.072m/s (within subject coefficient of variation = 0.39%), inferior wall segment 0.055±0.18m/s (within subject coefficient of variation = 0.73%), anterior wall segment 0.038±0.17m/s (within subject coefficient of variation = 0.56%) and posterior wall segment 0.77±0.18m/s (within subject coefficient of variation = 0.91%)

5.3.12 Comparison of invasive data with tissue Doppler image data

The objective of this study was to compare non-invasively measured LV wall motion to the onset of the FEW calculated using WIA on invasively acquired pressure and flow velocity data. Previous results in this thesis have shown that the FEW is generated when the velocity of LV long axis shortening begins to slow. To see if a similar relationship exists in human hearts the time at which all LV segments had begun to show a reduction in S wave velocity was calculated from each subject and compared to the time of the FEW onset. This time was chosen as it was considered to be the time when the long axis has achieved its maximum velocity of contraction; from this time onwards all segments are decelerating.

In an ideal situation invasive and non-invasive data would be collected simultaneously in the catheterisation laboratory. Unfortunately this was not possible in practise (unlike the data collected in chapters 3 and 4). Instead, LV wall movement data was acquired by echocardiography performed immediately before the patient was prepared for the invasive angiogram procedure. To minimize one source of variability in this sequational mode of data acquisition, beats collected

both invasively and non-invasively were matched for R-R interval (i.e. heart rate). This allowed the timing of events in each cycle to be matched reasonably accurately.

5.3.13 Statistical analysis

All data are presented as mean ± SD. Concordance correlation coefficients (CCC) were calculated using Lin's method to determine the extent of agreement between variables occurring at similar times. As mentioned before, the time from the R wave of the QRS complex to the both the slow onset of FEW (**dI_{+e1}**) and rapid increase in energy of the FEW (**dI_{+e2})** were calculated both before and after aortic reservoir subtraction. The FEW slow onset was compared to the time of peak S2 of the last LV segment to slow while the time to the sudden rapid FEW increase in energy was compared to the rate of decline of wall velocity seen in late systole. Both comparisons are in keeping with the findings from the dogs. The dog results guided the direction of this human analysis.

5.4 Results

5.4.1 Time to peak systolic wave (S2)

The time intervals from the R wave of the QRS complex to the peak systolic wave (S2) were measured in all 5 LV segments (septum, lateral, inferior, anterior and posterior segments). **Figure 5.6** is an example of LV inferior wall mitral annular TDI. The time of the R waves are represented by the dashed yellow line and peak S2 is shown using red crosses ✦. The time interval between these two events was recorded and the average time to S2 peak was averaged over 3-5 R-R interval matched beats for each segment.

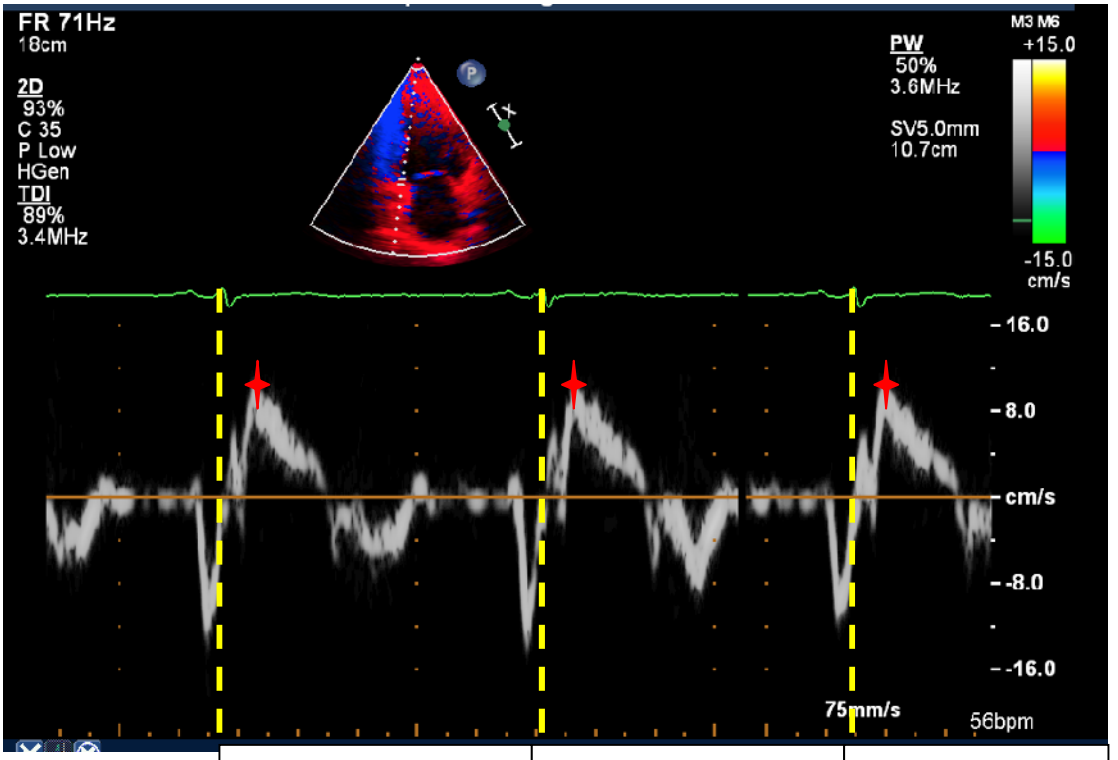

Figure 5.6: Offline analysis allows the calculation of the time interval between the R of the QRS complex (represented as the dashed yellow line) and the peak systolic wave (S2), shown by the red crosses. Each measurement was repeated 3 times for repeatability and the times measured from 3-5 beats were averaged.

The individual results are displayed in **Table 5.2** while average results are shown in **Figure 5.7**. It can be seen that the septum reaches its peak velocity of contraction first (201±38ms after the R wave), followed by the inferior wall (206±32ms after the R wave), then the posterior wall (210±40ms after the R wave). The lateral and anterior walls begin to slow last in all subjects (241±38ms and 240±37ms after the R wave respectively). The average standard deviation of peak contraction time was 25±7ms. The last segment to reach peak S2 and slow for each subject is highlighted in **Table 5.2**. The table demonstrates that the lateral and anterior mitral annular segments are always the last to slow. Averaging the times to peak for all segments in **Figure 5.7** provides conformation of this point.

Table 5.2: Shows the individual times to the peak systolic (S2) wave for each segment for every subject. The lateral and anterior walls seem to be the last to reach their maximum shortening velocity. The numbers highlighted represent the last LV segment to decelerate for each subject.

	Septum (ms)	Lateral (ms)	Inferior (ms)	Anterior (ms)	Posterior (ms)	Average (ms)	±SD (ms)
N1	177	240	178	183	178	**191**	**27**
N2	176	230	177	227	194	**201**	**26**
N3	174	212	188	200	162	**190**	**23**
N4	153	193	182	206	174	**182**	**20**
N5	210	261	191	252	192	**221**	**33**
N6	174	251	202	261	210	**220**	**36**
N7	203	171	188	222	174	**192**	**21**
N8	212	253	242	242	243	**238**	**15**
N9	239	265	269	281	264	**264**	**15**
N10	210	274	203	261	232	**236**	**31**
N11	288	302	248	306	282	**285**	**23**
Average	**201**	**241**	**206**	**240**	**210**	**220**	**25**
±SD	**38**	**38**	**32**	**37**	**40**	**33**	**7**

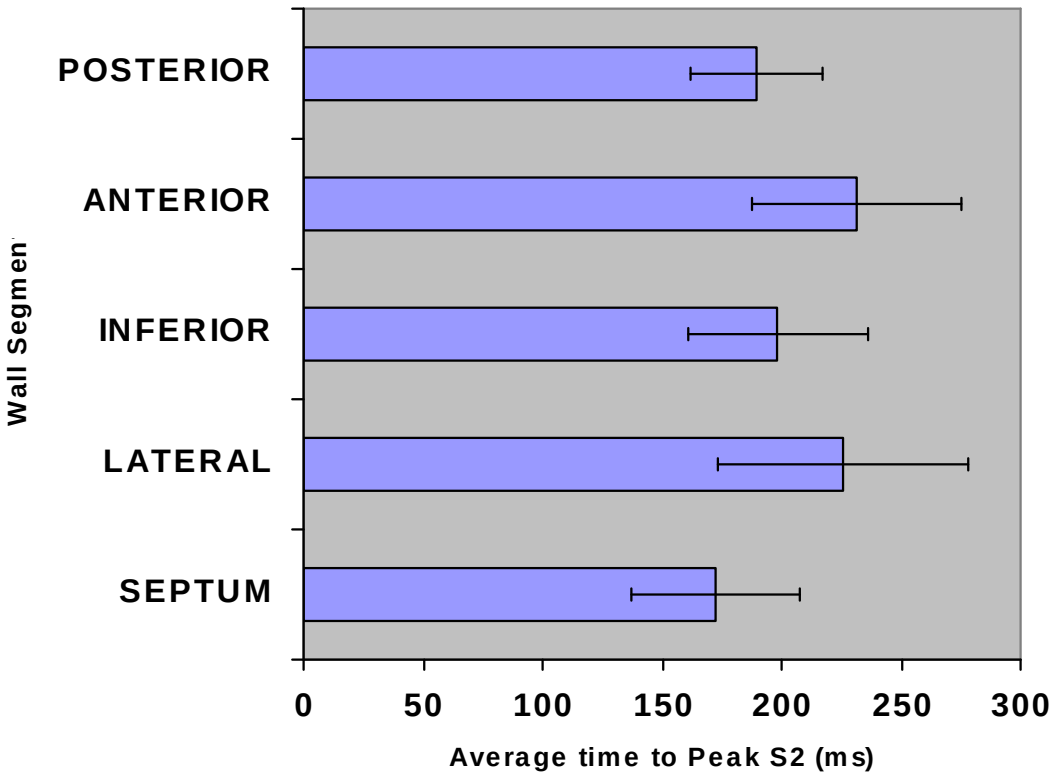

Figure 5.7: A Bar graph showing the average time it takes each mitral annular segment to reach peak velocity of contraction (S2). The lateral and anterior segments begin to slow latest just after 240ms.

5.4.2 Peak systolic wave velocities

The peak velocities of annular movement within each segment were also recorded. The individual peak velocity values of each LV segment for every subject can be seen in appendix 5.3. Average results are presented in **Figure 5.8** where it can been seen that septal, lateral and inferior wall velocities are relatively uniform throughout, while the posterior wall reaches the highest velocities and the anterior wall is always seen to have the smallest peak S value.

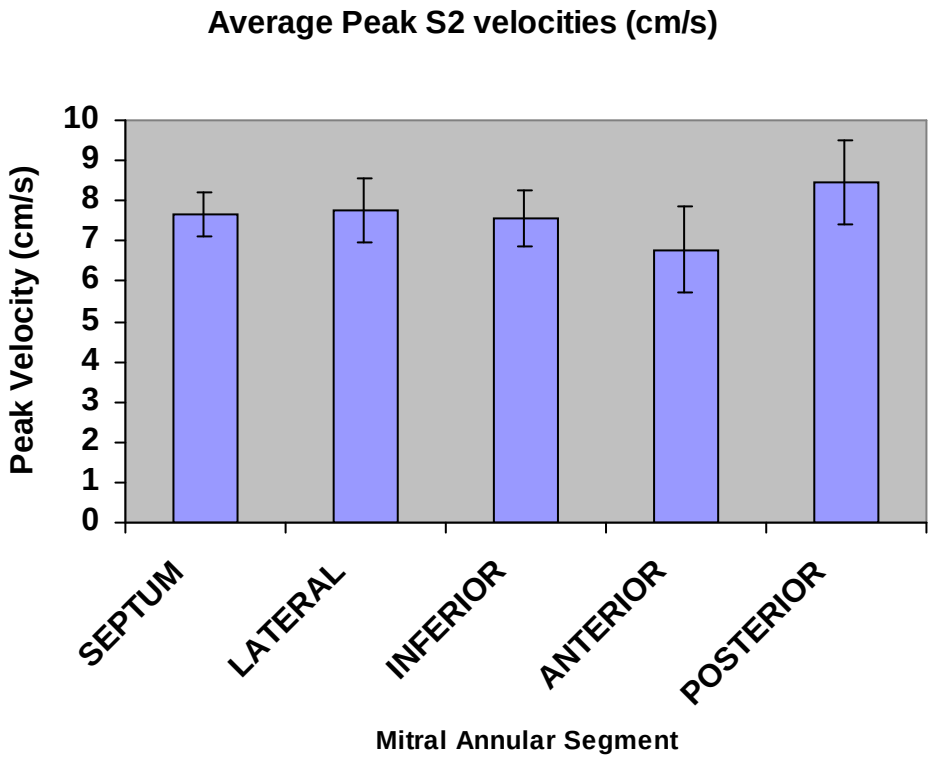

Figure 5.8: A bar graph displaying the average peak velocity values of the systolic wave (S2) in the 5 left ventricle mitral annular segments measured. The graph shows that the posterior wall reaches the highest velocities and the anterior wall reaches the lowest velocities in this set of patients. S2 values for the septum, lateral and inferior walls are similar.

5.4.3 Tissue Doppler measured peak systolic (S2) wave and the onset of the forward expansion wave

The time from the R wave of the QRS complex to the time that the last LV segment reached peak S2 was compared to the time of FEW onset in all subjects**.** The average times of these two measurements were found to coincide extremely well. The average results are presented in **Table 5.3.** The average difference between these events is only 6ms. By performing a concordance correlation on the two data sets it was found that they have a strong agreement (CCC=0.81). **Figure 5.9** is a concordance plot of the results. **Figure 5.10** illustrates that these times are very similar in all individuals.

Table 5.3: Average time intervals from the R wave of the QRS complex to the forward expansion wave (FEW) onset and the peak systolic wave (S2) of the last left ventricle segment to slow. There is only an average difference of 6ms between the two events. Individual time intervals can be seen in appendix 5.3.

	FEW Onset (ms)	Peak S2 (ms)	Difference (ms)
Average time	253	250	6
±SD	35	30	22

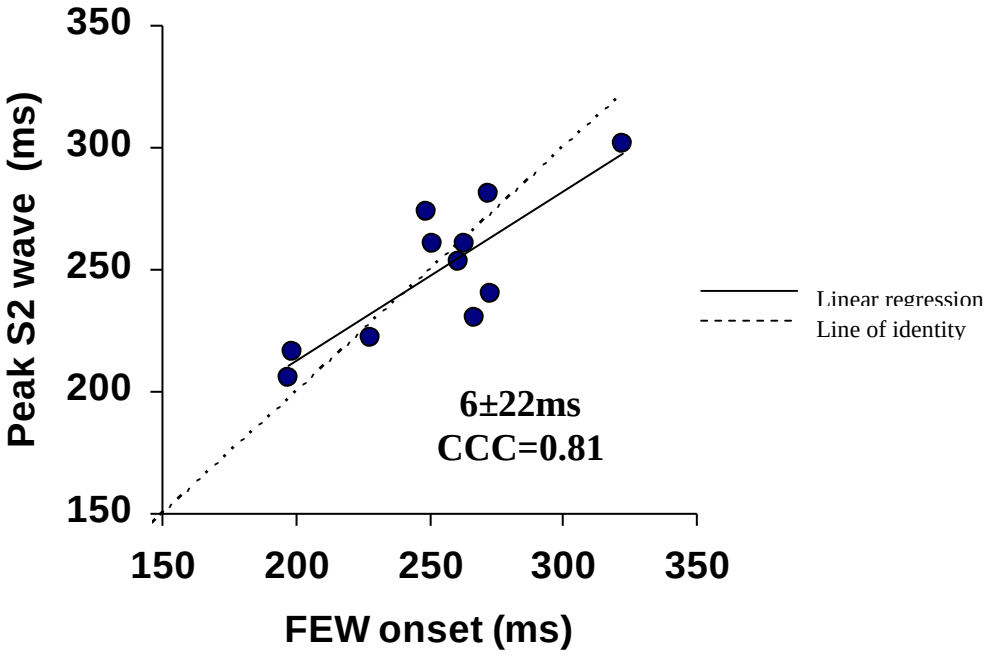

Figure 5.9: Lin's Concordance correlation plot showing the strong agreement between the time of the forward expansion wave (FEW) onsets in 11 individuals and the time of their latest mitral annular segment to slow (peak S2). A reduction in left ventricle (LV) speed of shortening appears to coincide with FEW generation.

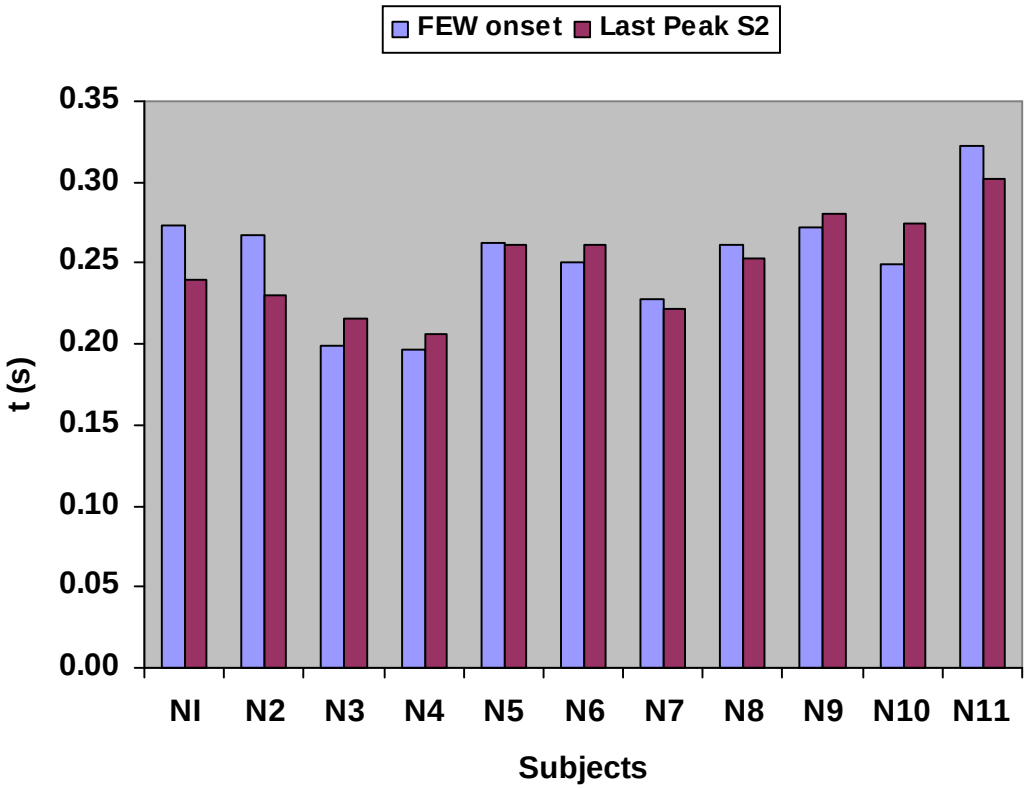

Figure 5.10: A bar graph to demonstrate the strong agreement between the times from the R wave of the QRS complex to the onset of the forward expansion wave (FEW) shown as blue bars, and the time that the last left ventricle mitral annular segment begins to slow in each subject.

5.4.4 Slopes

When studying the shape of TDI systolic waves it can be seen that the acceleration phase is normally a little steeper than the deceleration phase. Further extrapolation of the deceleration slope provides evidence that the slope can be divided into two components. A sketch to demonstrate this is provided in **Figure 5.11.** Slope 1 represents acceleration; it begins at the onset of the systolic wave and ends at the peak systolic wave. Slope 2 begins at the peak of the systolic wave until ~40ms from the end of the wave (deceleration). At this time the rate of deceleration changes and Slope 3 marks the time from this change in rate until the end of the systolic wave. A similar pattern of wall velocities is observed in the dog studies; refer to chapter 3 **Figure 3.8** and **3.19.**

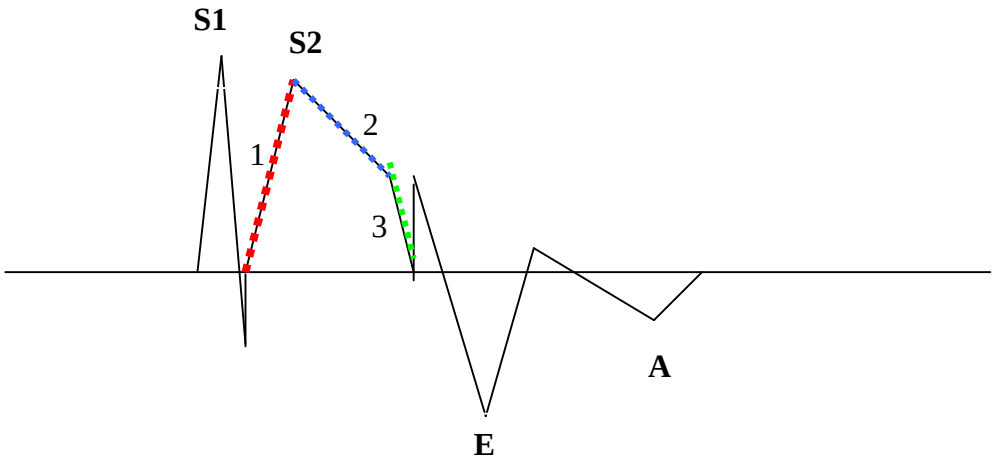

Figure 5.11: A sketch demonstrating how a tissue Doppler derived systolic wave can be divided into three slopes. Slope 1 begins at the onset of the systolic wave and ends at the Peak S2 wave (acceleration). Slope 2 begins at the peak of the systolic wave until ~40ms from the end of the wave (deceleration). At this time the rate of deceleration changes and Slope 3 marks the time from this change in rate until the end of the systolic wave. S1 = isovolumic contraction, S2 = systolic wave, E = rapid filling, A = atrial contraction.

5.4.5 Tissue Doppler systolic wave (S2) deceleration and the rapid increase of the forward expansion wave

A further objective to this experiment was to explore whether the FEW rapid increase in energy occurred in humans. The FEW rapid increase is present in all individuals studied. This finding is consistent with the results of chapters 3 and 4. The time from the R wave of the QRS complex to the onset of slope 3 (**Figure 5.11**) was recorded in all LV mitral annular segments. The time of slope 3 onset was found to be very similar in all LV segments. Therefore, an average time to slope 3 was calculated and compared to the time of the rapid increase of the FEW. The results are displayed in **Table 5.4**.

Table 5.4: The average time intervals from the R wave of the QRS complex to both the forward expansion wave (FEW) rapid increase in energy and the time of the systolic wave (S2) slope 3 onset. The results show that these events occur within 10ms of each other.

	FEW rapid increase (ms)	Slope 3 onset (ms)	Difference (ms)
Average time	359	364	-5
±SD	32	27	15

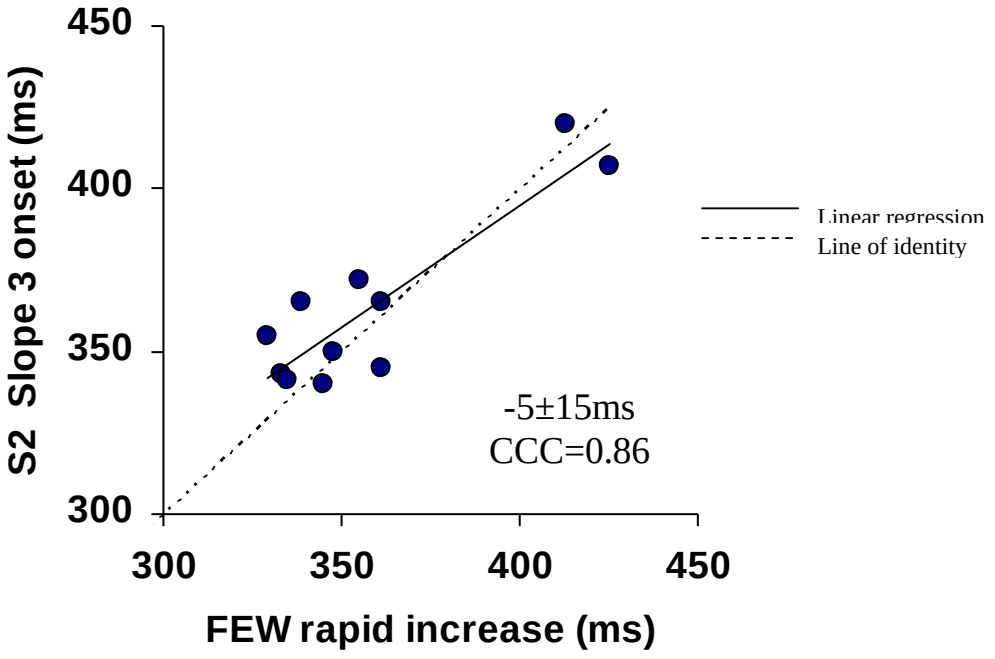

Figure 5.12 Lin's concordance correlation plot showing that the time of the forward expansion wave (FEW) rapid increase in energy strongly agrees with the average time at which slope 3 on the tissue Doppler image systolic wave (S2 wave) begins. Average <10ms and CCC=0.86

5.4.6 After aortic reservoir subtraction

As explained in chapter 1, section 1.7.2 several investigators believe that the cardiovascular system should be treated as a hybrid Windkessel-wave system. In chapter 3 section 3.4.4 and chapter 4 section 4.4.5, it was observed that aortic reservoir subtraction has a significant effect on aortic wave speed and the magnitude of the three main waves, although the timing of the waves did not significantly alter. A similar analysis was performed on this set of human data. **Figure 5.13** is an example of separated aortic pressure before and after reservoir subtraction from one of the individuals. The red line in plot b) represents the calculated reservoir pressure. It is calculated using the method described in chapter 2, section 2.6. Equal, self-cancelling artefact waves in plot a) are generated during diastole using original WIA theory. After reservoir subtraction there is a zero diastolic gradient during diastole as seen in plot b). The exponential decline in pressure during diastole is wholly attributable to the aortic reservoir.

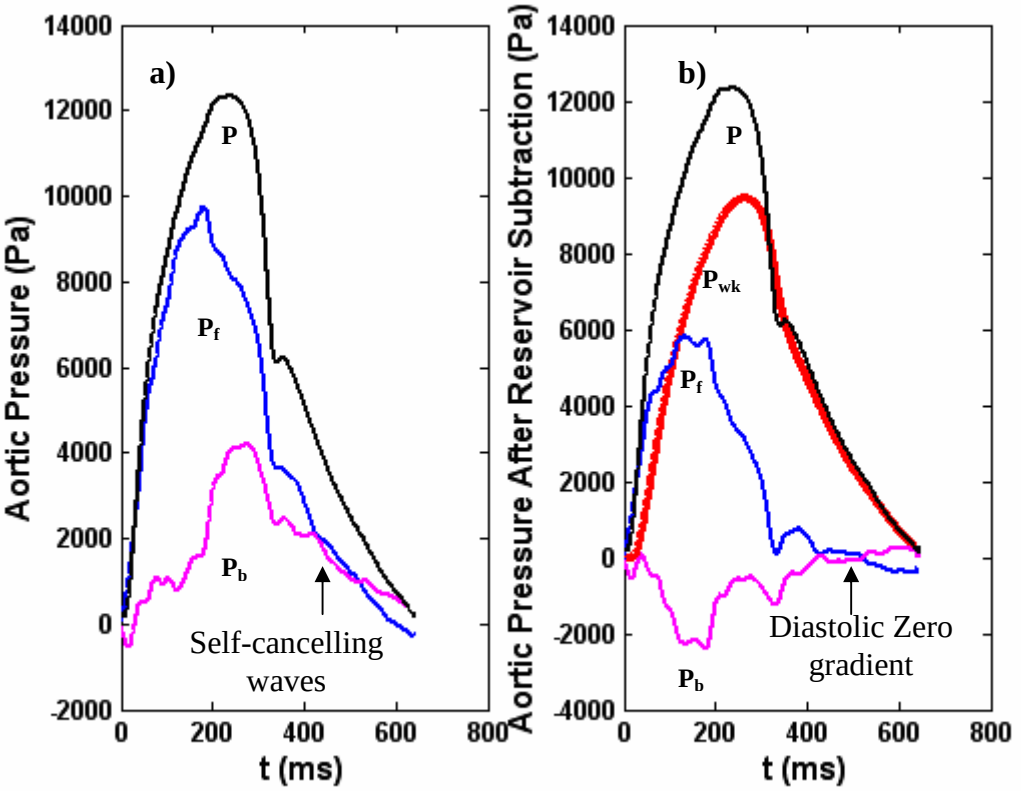

Figure 5.13: Aortic measured pressure (P) separated into its forward (P_f) and backward (P_b) components before (a) and after windkessel separation (b). The red trace represents the windkessel pressure (P_{wk}). Wave pressure is the calculated difference between the measured and windkessel pressure traces. After aortic reservoir subtraction a zero gradient is observed during diastole.

Wave speed

Wave speed was calculated using the PU-loop method (described in chapter 2, section 2.3) at the aortic root before (using measured pressure) and after aortic reservoir subtraction (using wave only pressure). The wave speed was found to be reduced by an average of 27±6% (from 7.4±2.3m/s to 5.4±1.7m/s) by reservoir subtraction. Individual results are seen in appendix 5.4

Wave magnitude

Net waves: After reservoir subtraction the magnitudes of all waves were altered. The energy of the FCW decreased by 1.6%, the BCW decreases by 42% while the FEW increases by 15%

Separated Waves: After aortic reservoir subtraction the separated FCW was reduced by 9%, the BCW is decreased by 74% and the FEW is 25% larger. The values are presented in **Table 5.5** and **Figure 5.14** is an example of separated wave intensity before (red) and after reservoir subtraction (blue).

The FCW and BCW are always reduced after aortic reservoir subtraction while the magnitude of the FEW is increased. This pattern is identical to that seen in the dogs in chapters 3 and 4.

Table 5.5: Values for the energy carried by each of the three main waves of wave intensity analysis before and after aortic reservoir subtraction. The forward compression wave (FCW) decreases in magnitude by 9% and the backward compression wave (BCW) decreases by a significant 74%. The forward expansion wave (FEW) actually increases in magnitude by 25%.

	Before (J/m^2)	After (J/m^2)	Difference (%)
FCW	**480±35**	**267±20**	**-9**
BCW	**-176±51**	**-14±38**	**-74**
FEW	**147±80**	**192±48**	**+25**

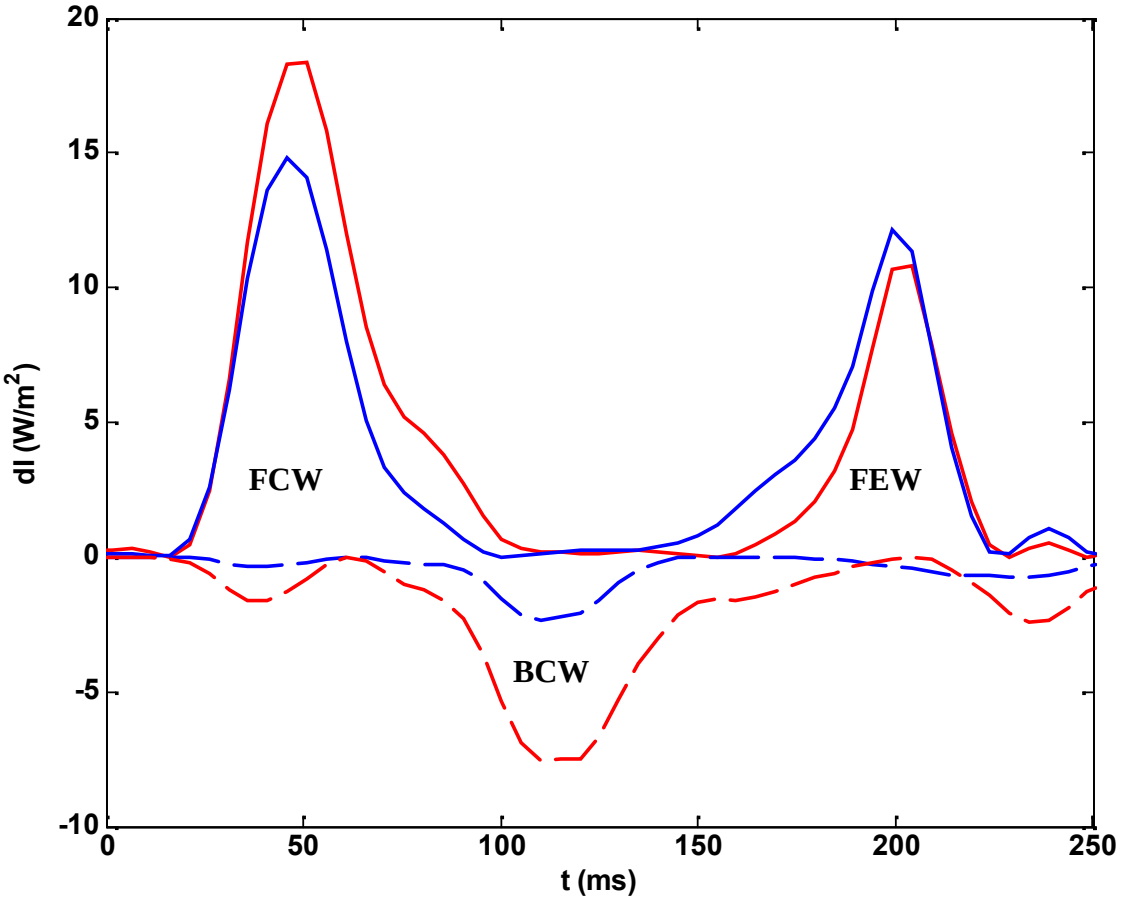

Figure 5.14 Separated forward and backward wave intensity before (red) and after (blue) aortic reservoir subtraction. After reservoir subtraction the forward compression wave (FCW) magnitude is reduced by 9%, the backward compression wave (BCW) is diminished by 74% while the forward expansion wave (FEW) is 25% larger. This pattern is consistent with that found in chapters 3 and 4 after reservoir subtraction.

Timings

Average wave timings

The timings of all the 3 main waves were relatively unaltered by aortic reservoir substitution. These results agree with the results of chapters 3 and 4. **Table 5.6** displays the average timings from the R of the QRS complex to the onset of the three major waves before and after aortic reservoir subtraction.

Table 5.6 Average times to the onset of the three main waves before and after reservoir subtraction. All times were not altered significantly. FCW= forward compression wave, BCW= backward compression wave and FEW= forward expansion wave.

	Before (ms)	After (ms)	Difference (ms)	CCC
FCW	78±30	78±30	0±0	1.0
BCW	153±20	143±40	10±37	0.59
FEW	253±35	247±40	8±14	0.93

Forward expansion wave timings

The individual average times to the onset of the FEW both before and after aortic reservoir subtraction are presented in appendix 5.5 along with the time after the R of the QRS complex that the last LV wall segment begins to fall. The FEW onset always coincides with peak systolic contraction, in all subjects. **Figure 5.17** is a Lin's concordance analysis plot demonstrating that the time to FEW onset still coincides with the time to peak S2 of the last LV wall segment to slow, even after aortic reservoir subtraction.

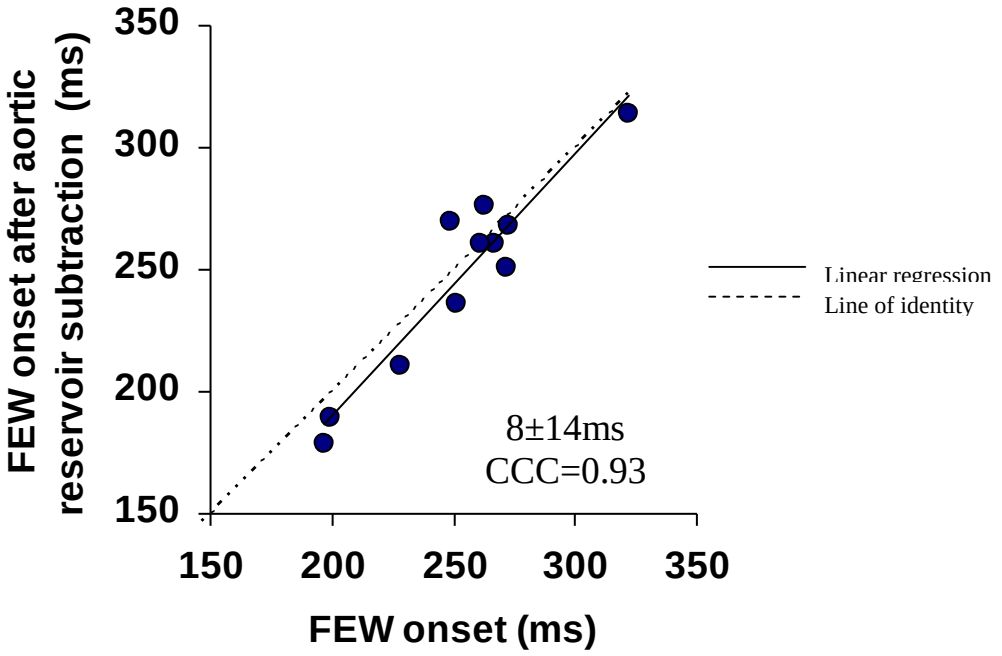

-

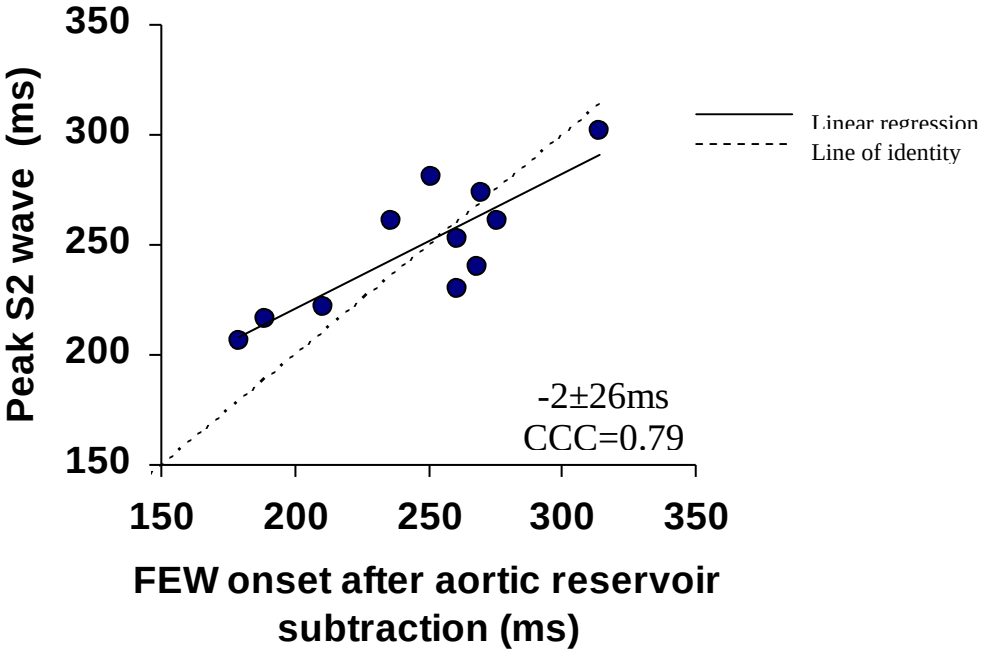

Figure 5.15: Lin's concordance correlation plots showing that the time of forward expansion wave (FEW) onset is not altered significantly after aortic reservoir subtraction, average difference <10ms CCC=0.93 and that it's time still strongly agrees with the time at which the last left ventricle mitral annular segment begins to slow. Average difference -2±26ms CCC=0.79

5.5 Discussion

Tissue Doppler imaging data

Over the past decade Tissue Doppler Imaging (TDI) has emerged as a valuable non-invasive technique to assess cardiac function. Mitral annular descent is now regarded as a substitute measure of LV longitudinal movement (Gulati et al. 1996, Nikitin and Witte 2004). Pulsed wave TDI is particularly effective for measuring LV longitudinal shortening velocities as it allows the calculation of peak velocities, rather than average velocities. Mitral annular velocities are the chosen regions of interest as the magnitudes of velocities decrease from the annulus towards the apex (Pai and Gill 1998). The most popular sites of mitral annular motion measurements are the lateral wall and free wall regions. This is no doubt due to the prevalence of longitudinal fibres in these regions (Nikitin and Witte 2004). Velocities measured at the septal and anteriorseptal regions of the mitral annulus are often lower than those of the lateral and posterior walls (Price et al. 2000). Peak velocities at the LV posterior and lateral walls have even been correlated with ejection fraction and peak dp/dt (Yu et al. 2007). It is for this reason that most studies use these regions in their experiments. In this study all regions of LV mitral annular motion were studied: septal, inferior, lateral, anterior and posterior segments. In this group of subjects the septal, lateral and inferior peak systolic wall velocities were found to be relatively uniform throughout while the posterior wall reached the highest velocities (average 8.448±1.057 cm/s) and the anterior wall was always seen to have the smallest peak S2 value (average 6.795±1.072). The average values are shown in **Figure 5.8**.

Although velocities of annular movement provide interesting insights into LV function TDI can also examine the time interval between LV electrical activation (R wave of the QRS complex) and mechanical activation (peak S2 systolic wave of each segment). It was observed that that the first segment to reach its maximum velocity of shortening in these patients was the septum (201±38ms) closely followed by the posterior (206.±32ms) and inferior (210±40ms) walls. The lateral (241±38ms) and anterior (240±37ms) walls consistently reached their peak velocity of shortening last. This is shown in **Table 5.2 and Figure 5.7.** The standard deviation of the time to peak contraction for all 5 mitral annular segments

was found to be 25±7ms. This represents a measure of overall ventricular synchrony (Ho et al. 2006). TDI is a widely applied technique for assessing LV dyssynchrony (Bleeker et al 2006) and is used in the selection of patients for cardiac resynchronisation therapy (CRT). Yu et al. 2004 reported that in normal subjects the mean +2 standard deviations of the time to peak contraction was 32.6ms suggesting that the individuals in this study did not have severely dysynchronous LV systolic function.

Velocities in this chapter are lower those reported elsewhere. Reference values for the normal longitudinal shortening have been reported as 7.5±1.3 to 9.5±1.4cm/s for the anterior septum and 10.3±1.9 cm/s for the lateral wall (Gulati et al. 1996 and Alam et al. 1999). Although these reference values are higher than those collected in this group of subjects there is much evidence to support the finding that peak systolic velocities lower with increasing age (Tanimoto et al. 1996, Nikitin et al. 2002). Age could also perhaps provide an explanation for the standard deviation of 25ms found in these individuals. It is conceivable that regional differences that naturally occur in the normal LV could increase with age before manifesting as disease.

Invasive data

The FEW was calculated by applying WIA to invasively acquired pressure and flow velocity measurements. In these human subjects it was observed that the FEW has a slow onset and a rapid increase in energy identical to that seen in canines (chapter 3, **Figure 3.7**). In the canine study it was found that the FEW is generated when the LV long axis begins to decelerate. Therefore the timing of deceleration of long axis shortening was compared to the time of FEW onset in these individuals. The results confirm that the FEW is generated at the time when the long axis reaches its peak velocity of contraction. This is shown in **Table 5.3**, **Figure 5.9 and Figure 5.10**. By performing Lin's concordance analysis on the two sets of times it was seen that there is a strong agreement between the two events. The FEW occurs 253±35ms after the R wave of the QRS complex and slowing of the LV long axis begins at 250±30ms, there is only an average time difference of 6±22ms and the measure of agreement is very strong, CCC=0.81.

The rapid increase of the FEW was seen ~100ms after that of the onset. When observing the tissue Doppler velocity traces it is clear that the acceleration slope

(slope 1) of the systolic wave is much steeper than that of the deceleration slope. The deceleration slope appears to be composed of two distinct components with different slopes (slopes 2 and 3 in **Figure 5.11**). The stages of the systolic wave are very similar to those of the velocity of shortening plots described in chapter 3 **Figures 3.8** and **3.19**. The onset of slope 3 occurs at a very similar time in all 5 regions. Slope 3 occurs on average 364±27ms after the R of the QRS complex. This time corresponds well with that of the onset of the rapid increase of the FEW, average 359±32ms (average difference in timing = -5±15 ms, CCC 0.86). The results suggest both stages of the FEW are related to LV long axis motion.

Wave intensity was also calculated after aortic reservoir subtraction. The onset of the FEW occurred marginally earlier (by 8±14ms) after reservoir subtraction but this difference was not statistically significant (p=0.7) and the FEW onset still coincided closely with the time of deceleration of long axis shortening (CCC=0.79). As shown in **Table 5.6, Figure 5.16** and **Figure 5.17**.

Limitations

Although TDI is a well-established, safe, non-invasive diagnostic modality there are several shortcomings of the method that could produce potential errors. The principal shortcoming to this technique is its angle dependency. The velocities recorded are highly dependent on where the sample volume is placed. If the beam is not parallel to the wall being measured large errors can occur. Although pulsed wave (PW) TDI is often the preferred method of choice (as it allows the calculation of peak velocities instead of average velocities) it has several disadvantages to colour TDI. Colour TDI allows offline analysis of multiple segments in one heart beat. Potential errors can occur when using PW TDI to look at several LV segments as each segment analysed is from a different heart beat. Differences in heart rate therefore affect the results and it is for this reason that R-R intervals were matched in this experiment.

Mitral annular excursion as measured by PW-TDI is also affected by the anatomy of the left atrium and is influenced by adjacent myocardial segments. Colour TDI can also be used to generate strain-rate images which can differentiate between passive and active myocardial movement. However colour TDI cannot take the LV rotational component into account and newer techniques that are not angle

dependent such as speckle tracking are becoming more popular modalities to assess LV synchronicity.

The final limitation to PW-TDI occurs when analysing the data. The online trace lines can be quite thick and often blurry; it is therefore very easy to make tiny errors, especially when looking at time intervals. One method to overcome this user-error in the future is to apply tissue synchronization imaging (TSI) to data collected. This technique can be used in combination with a 3D cardiac probe and provides colour-coded maps without the need to process the TDI curves manually (Yu et al 2005).

5.6 Conclusion

In humans, as in dogs, the FEW is generated when the LV long axis reaches its peak velocity of contraction. The FEW has a slow onset and rapid increase in energy both of which are related to LV wall motion as measured by TDI.

Chapter 6
Left Ventricle Minor and Long Axis Asynchrony in Humans

6.1 Introduction

The introduction to Chapter 5 describes three associations that were observed between LV wall movement and WIA in the dog studies: Chapter 5 concentrated on the FEW and confirmed the first two associations in the human LV. The following chapter will concentrate on the third association highlighted below.

1) *The FEW onset coincides with the time of maximum shortening velocity of the LV long axis.*
2) *A rapid increase of the FEW is consistently present and corresponds to a time during late systole when both the minor and long axes change their rate of shortening.*
3) ***There is a strong association between the return of the BCW to the heart during mid-systole and the slowing of the minor axis velocity of shortening***

Reflected waves*:* In the previous chapters (3 and 4) the minor axis peak velocity of shortening always coincided with the arrival of the reflected compression wave (BCW) at the heart. In the dog data this relationship remains true even during proximal aortic occlusion as seen in chapter 4, **Figures 4.4** and **4.5**. Preceding literature has proposed that reflected waves are detrimental to the working condition of the LV (Laskey al. 1987, Papaioannou et al. 2008). This study investigated this concept further using peak aortic flow as a surrogate marker for BWC arrival at the aortic root.

Left ventricle asynchrony: Peripheral tissue perfusion which determines exercise activities as well as all pan organ physiology depends on the cardiac output which itself depends on the stroke volume (Melbin et al. 1982). With a fixed LV outflow tract cross sectional area the stroke volume is determined by efficiency of LV contraction as well as optimum ejection times. In chapters 3 and 4, the dog studies, it was demonstrated that ejection events were determined by the normal relationship between the two contracting axes of the LV, long and minor. As already seen throughout this thesis so far the LV long axis peak shortening velocity consistently lags behind that of the minor axis by ~30 ms (as shown in **Figures 3.12** and **3.14**) representing a degree of physiologically normal asynchrony between the two

components of LV systolic function. It is proposed that this is not a faulty design of the heart, but that delayed peak long axis shortening maintains the LV pressure for a further 30 ms, after which it starts to decline. In this chapter the times of LV minor and long axis peak velocity of shortening during systole in human volunteers were compared to reveal whether normal LV asynchrony was species specific to dogs, or whether 'normal' asynchrony is a common occurrence in human ventricles.

6.2 Hypothesis

In this investigation a normal asynchrony will exist between LV minor and long axis velocity of shortening during systole in human volunteers. The minor axis will begin to slow first and this time will coincide with the arrival of the BCW to the heart, taken to be the time of peak aortic flow. Reflective waves will be shown to have a detrimental effect on LV function.

6.3 Methods

6.3.1 Subjects: 11 male volunteers (average age 65±9 years) were evaluated. 6 individuals had no reported cardiovascular disease; the remaining 5 were patients with hypertension (BP > 140/90mmHg). All subjects were recruited at St Mary's hospital, Paddington and were volunteers for a research study named PICCOLA. Full details for the PICCOLA study are shown in appendix 6.1; PICCOLA is an ongoing study that is investigating the effects of pioglitazone (an insulin-sensitizing agent) on cardiac function. This chapter uses only a small percentage of the baseline data (visit 1) collected from the first 11 subjects that came into the clinic with normal LV function as assessed by echocardiography, with ejection fractions above 50%. The protocol for PICCOLA was approved by St Mary's Ethics committee and written informed consent was obtained from all participants. The consent form can be viewed in appendix 6.2. LV minor axis and apical long axis views were recorded with transthoracic echocardiography, obtained using a commercially available ultrasound machine (Philips IE33, Andover, MA, USA). All recordings were made with a simultaneous superimposed ECG. Recordings were made at a sweep speed of 50mm/s. A 5mm sample volume is placed at the region of interest. Baseline characteristics are given in appendix 6.3.

6.3.2. Tissue Doppler imaging measurements:

As mentioned in chapter 1, section 1.4, tissue Doppler imaging (TDI) measures high amplitude, low-velocity signals reflected from myocardial tissue motion and permits the calculation of radial and longitudinal, systolic function

Longitudinal systolic function: LV mitral annular wall velocities were acquired using pulsed-wave TDI at 3 different LV segments: In the apical four chamber view septal and lateral wall velocities were recorded, the transducer was then turned anticlockwise to achieve an apical two chamber view allowing the collection of the LV inferior wall velocity. See chapter 5 **Figures 5.4a** and **5.4b** to see where the ultrasound beam is placed to achieve septal, lateral and inferior wall velocities in the four and two chamber long axis apical views respectively.

Radial systolic function: LV wall velocities were measured in the parasternal short axis view at the mid-level in two segments, the mid-anterioseptal =**MA1** and mid-inferiolateral=**MA2** segments. **Figure 6.1** demonstrates how this can be achieved.

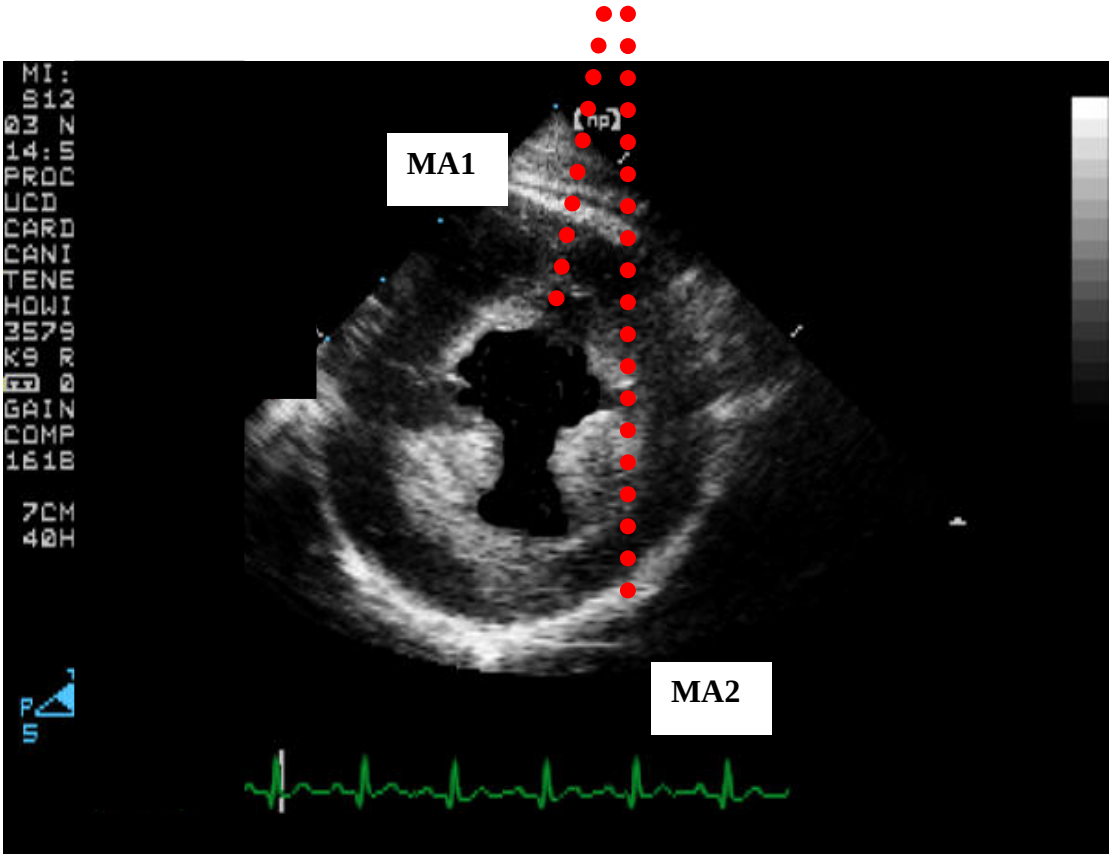

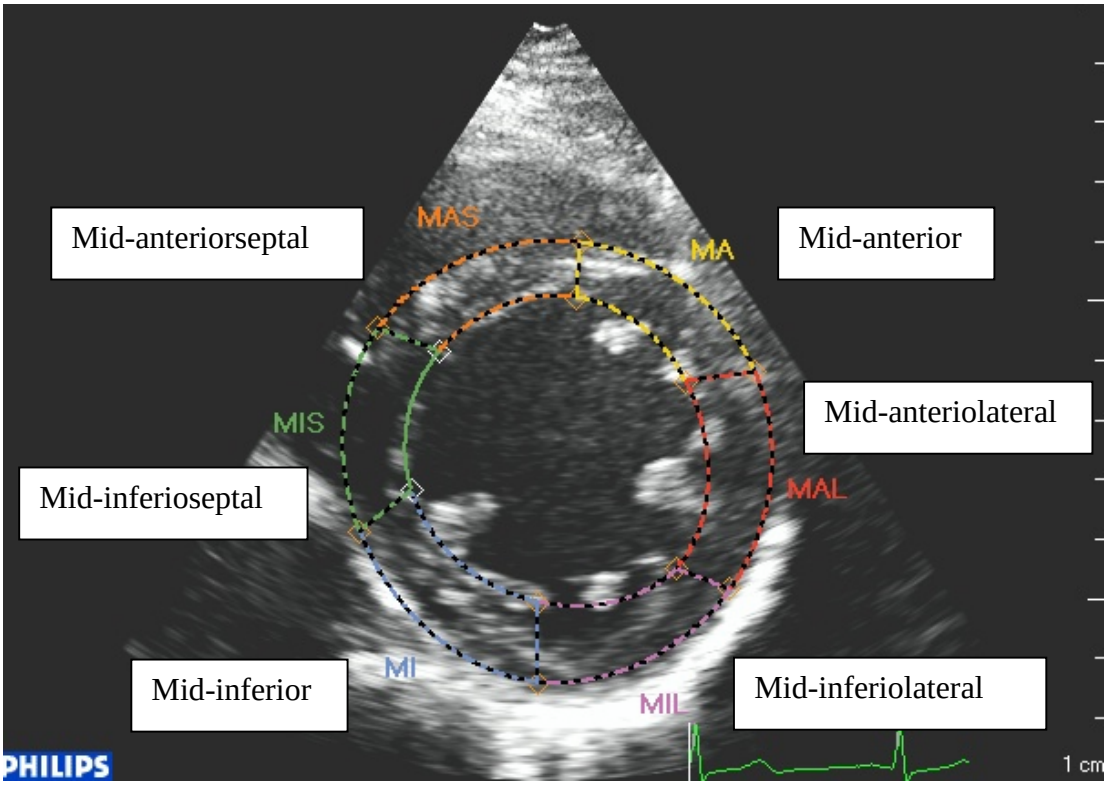

Figure 6.1: An example of the left ventricle myocardium taken from the parasternal short axis view at mid-level. The pulse-wave Doppler beam is placed over the anterioseptal and inferiolateral walls. Velocity of radial wall movement towards the centre of the ventricular cavity is measured and presented as a typical tissue Doppler trace.

6.3.3 Peak Aortic flow measurements: A substitute for reflected wave arrival

Peak Aortic flow can be measured accurately using continuous wave (CW) Doppler applied across the aorta from an apical 5-chamber view. It is now acknowledged that reflected waves instigate deceleration of aortic flow velocity. The time to peak aortic flow can therefore be used as a surrogate marker for the arrival of the reflected wave (BCW). This time was measured, recorded and compared to the time of peak velocity of shortening (peak S2) of the LV minor axis. **Figure 6.2**

a)

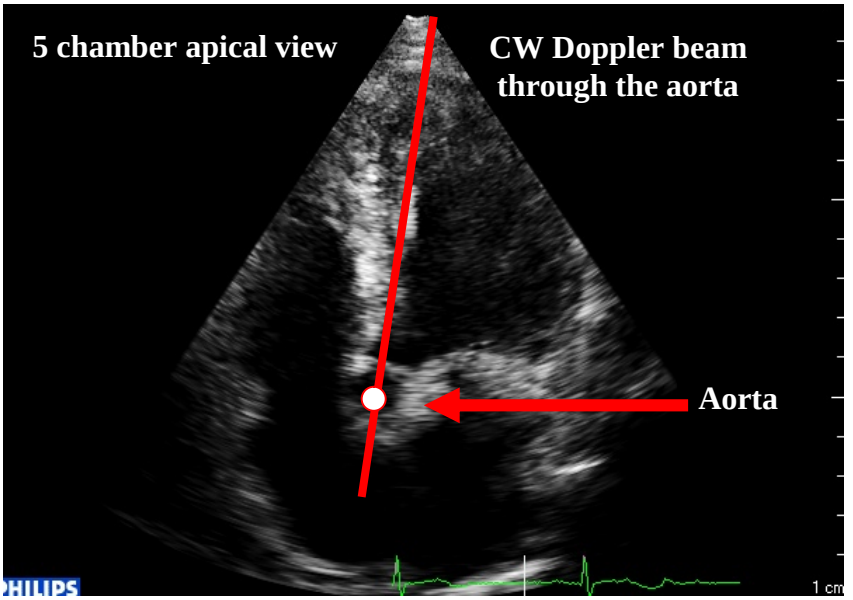

b)

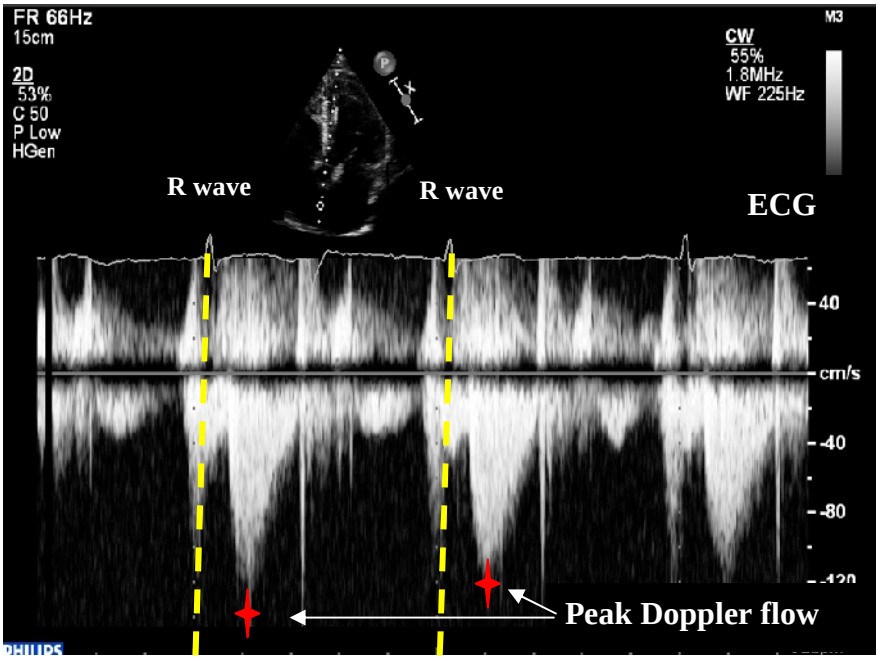

Figure 6.2: An example of aortic flow measurement using continuous wave Doppler in the 5 chamber apical view shown in **a)**. The aortic flow trace recorded is shown underneath in **b)**. The time interval was measured between the R of the QRS complex (represented as the dashed yellow line) and peak aortic flow, (shown by the red crosses (✦)). Peak Aortic flow was used as a surrogate marker for reflected wave arrival.

6.3.4 Data collection

Myocardial velocities during systole consist of a dominant and usually biphasic wave during IVC (S1) followed by a second dominant positive wave during ejection (S2), see chapter 5 **Figure 5.5.** The peak velocities of both S1 and S2 in all 5 segments (2 minor, 3 mitral annular long axes segments) were recorded. The Peak R wave of the QRS complex was always considered as t=0. The time interval from the R wave of the QRS complex to the times of peak S2 for all long and minor axis segments were also recorded. Results from all segments were compared to each other to see if regional differences occur and to determine whether there is a natural asynchrony between peak velocity of contraction along the LV long and minor axes

The time that aortic flow reaches peak velocity was also recorded with respect to the R wave of the QRS complex. The time of peak aortic flow was used as a surrogate marker for the arrival of the BCW at the heart. The average time to peak velocity was compared to the time of the peak S2 wave in all segments to determine whether reflected waves have a detrimental effect on LV function. To supplement this concept the group was further divided into those subjects with normal blood pressure (BP<140/80mmHg) and subjects with hypertension (BP>140/80mmHg). Hypertension is now accepted to cause an increase in LV afterload, which can have adverse effects on LV function. This chapter was interested in looking at the effect of increased afterload on LV axes function.

In an ideal situation all TDI segmental data would be collected simultaneously. This is of course not possible when collecting data from different LV views. To minimize the variability in this sequational mode of data acquisition, beats collected were matched for R-R interval allowing the timing of events in each cycle to be matched reasonably accurately.

.

6.3.5 Statistical analysis

All data are presented as mean ± SD and students paired t test were used to compare peak velocities. Concordance correlation coefficients (CCC) were calculated using Lin's concordance method to determine the extent of agreement between variables occurring at similar times. See Chapter 3 section 3.3.4 for details on concordance coefficients.

6.3.6 Reproducibility

Each TDI S2 wave peak velocity amplitude and time to peak velocity measurement from the R wave of the QRS complex were repeated 3 times and averages were taken for each beat. Results were analysed by the same operator. The mean difference±SD for the time interval to peak S2 along with the peak velocity values of all 5 LV segments are shown in **Table 6.1** along with their within subject coefficient of variation.

Table 6.1: Reproducibility data for the time to peak velocity and peak velocity amplitude of each left ventricle segment. Data are presented as the mean difference±SD and the within subject coefficient of variation.

	TIME TO PEAK VELOCITY		**PEAK VELOCITY AMPLITUDE**	
Left ventricle segment	Difference±SD (ms)	Coefficient of variation (%)	Difference±SD (ms)	Coefficient of variation (%)
MA1	3±7	2.5	0.1±0.7	2
MA2	1±6	0.8	0.1±0.5	1.8
Septum	3±13	1.9	0.2±0.4	2.86
Lateral	4±10	2.6	0.5±0.8	5.8
Inferior	4±10	2.3	0.3±0.8m	4.3

6.4 Results

6.4.1: Myocardial velocities

Pre-ejection velocities: The peak velocity value of S1 during IVC was recorded for each minor and long axis segment. The average values presented in **Table 6.1** show that the two minor axis segments reach very similar peak velocities during IVC (average difference = -0.11±0.96cm/s, p = 0.534). The long axis mitral annular velocities reach higher values than the minor axis mid-wall velocities however the inferior wall mitral annular velocities are not significantly higher (MA1 average difference = -0.59±1.48cm/s, p = 0.09, MA2 average difference = -0.48±0.92cm/s, p = 0.280). The mitral annular lateral segment reaches the highest velocities during IVC and both lateral and septum velocities are significantly higher than all other walls in this set of men.

Ejection velocities: The peak velocity of S2 during ejection was recorded for each minor and long axis segment. The results again show that the minor axis segments reach very similar peak velocities during ejection (the average difference was -0.69±1.78cm/s, p = 0.101). All long axis segment velocities are significantly higher than those reached by the two minor axis segments, especially that of the mitral annular lateral segment.

Pre-ejection verses ejection peak velocities: Individual velocities of peak S1 and S2 were found to be quite similar in this group of subjects. The mitral annular long axis velocities are always higher than those of the mid-myocardial minor axis velocities as one would expect.

Table 6.2: Average peak velocity values of the minor axis (MA1, MA2) and long axis segments measured (Septum, Lateral, Inferior) during both the isovolumic contraction (IVC) phase (S1) and during ejection (S2). Average differences in peak velocities during IVC and ejection are presented. Individual results are shown in appendix 6.3, 6.4 and 6.5)

	IVC Peak velocity of S1 (cm/s)	**Ejection** Peak velocity of S2 (cm/s)	Difference between S1 and S2 velocities
MA1	5.51	4.8	0.65
MA2	5.77	5.72	0.05
Septum	7.23	7	0.05
Lateral	9.01	8.7	0.31
Inferior	6.65	6.95	-0.61

6.4.2 Left ventricle asynchrony

Table 6.3 displays the average times from the R wave of the QRS complex to peak velocity of shortening during ejection (S2) for each LV segment measured. There is asynchrony seen between the times to peak S2 in the LV long and minor axes segments. The radial movement measured in the two short-axis segments reaches peak S2 at least 30ms before that of any long axis segment.

Table 6.3: Average time intervals from the R wave of the QRS complex to the time of peak aortic flow are shown in **black**. This time is taken to be the average time of backward compression wave (BCW) arrival at the heart during mid-systole. Average time intervals from the R wave of the QRS complex to the time of peak S2 of the two minor axis segments measured are presented in **red**. Average times from the R wave of the QRS complex to the time of peak systolic (S2) velocity of the three long axis segments measured are presented in **blue**.

Subject	Peak Aortic Flow (ms)	MA1 (ms)	MA2 (ms)	Septum (ms)	Lateral wall (ms)	Inferior wall (ms)
Average	**122**	**120**	**124**	**156**	**155**	**177**
±SD	**16**	**12**	**10**	**27**	**19**	**22**

P-values were calculated between the times to long and minor axis peak S2 velocities and peak aortic flow. The results are shown in **Table 6.4**. A significant difference is found between long and minor axis time to peak S2 during systole. There is no significant difference between the times to peak S2 of MA1 or MA2 with the time of peak aortic flow. Minor axis segments reach S2 at similar times in these subjects which occur ~30ms before long axis segments.

Table 6.4: P values calculated between the time of peak systolic wave (S2) in the long and minor axes segments and peak aortic flow. There is a significant difference between both minor axis segments and all long axis segments. There is no significant difference observed between the time to aortic peak velocity and both minor axis segments time to peak S2.

	Septal Peak S2 wave	Lateral peak S2 wave	Inferior peak S2 wave	Time to peak aortic velocity
MA1 Peak S2 wave	0.003	0.0002	0.00003	0.26
MA2 Peak S2 wave	0.006	0.0003	0.00004	0.45

Findings: From **Tables 6.3 and 6.4** it can be seen that there is a significant asynchrony seen between the time to peak velocity in the LV long and minor axes.

6.4.3 Flow deceleration:

As reflected waves are known to instigate flow deceleration (Parker et al. 1990) the time of aortic peak flow was taken as the time of arrival of the reflected wave at the heart. **Figures 6.3 and 6.4** show that the time to peak aortic flow always coincides with both minor axis segments peak velocity of shortening (S2). Peak aortic velocity and MA1 average difference=-1±6, CCC=0.91, Peak aortic velocity and MA2 average difference=-5± 10, CCC=0.78.

Findings: The time from the R wave of the QRS complex to the time of peak aortic flow velocity coincides with the time to peak S2 of both minor axis segments. This suggests that the arrival of the BCW at the heart coincides with deceleration of the LV minor axis.

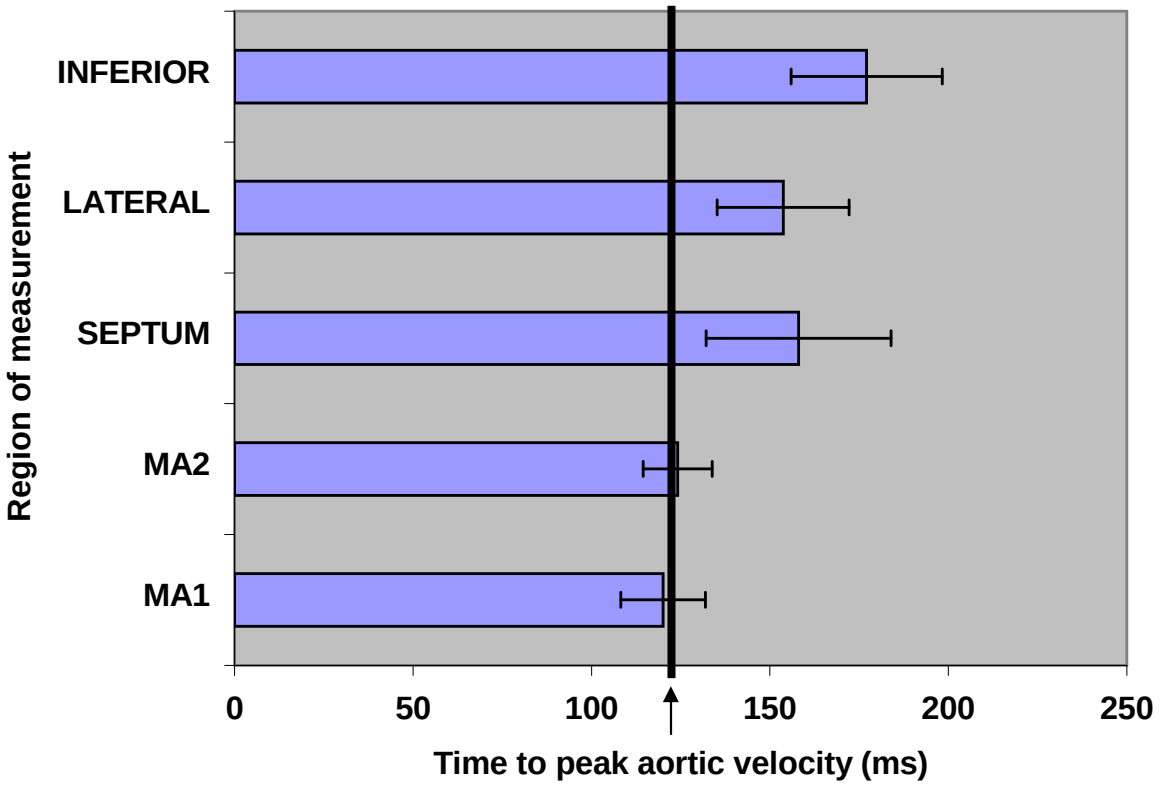

Figure 6.3: A Bar graph showing the average time it takes each left ventricle segment to reach its peak velocity of contraction during ejection (peak S2).The time of peak aortic velocity is shown by the vertical black line. The time to peak S2 of both minor axis segments coincides well with peak aortic velocity.

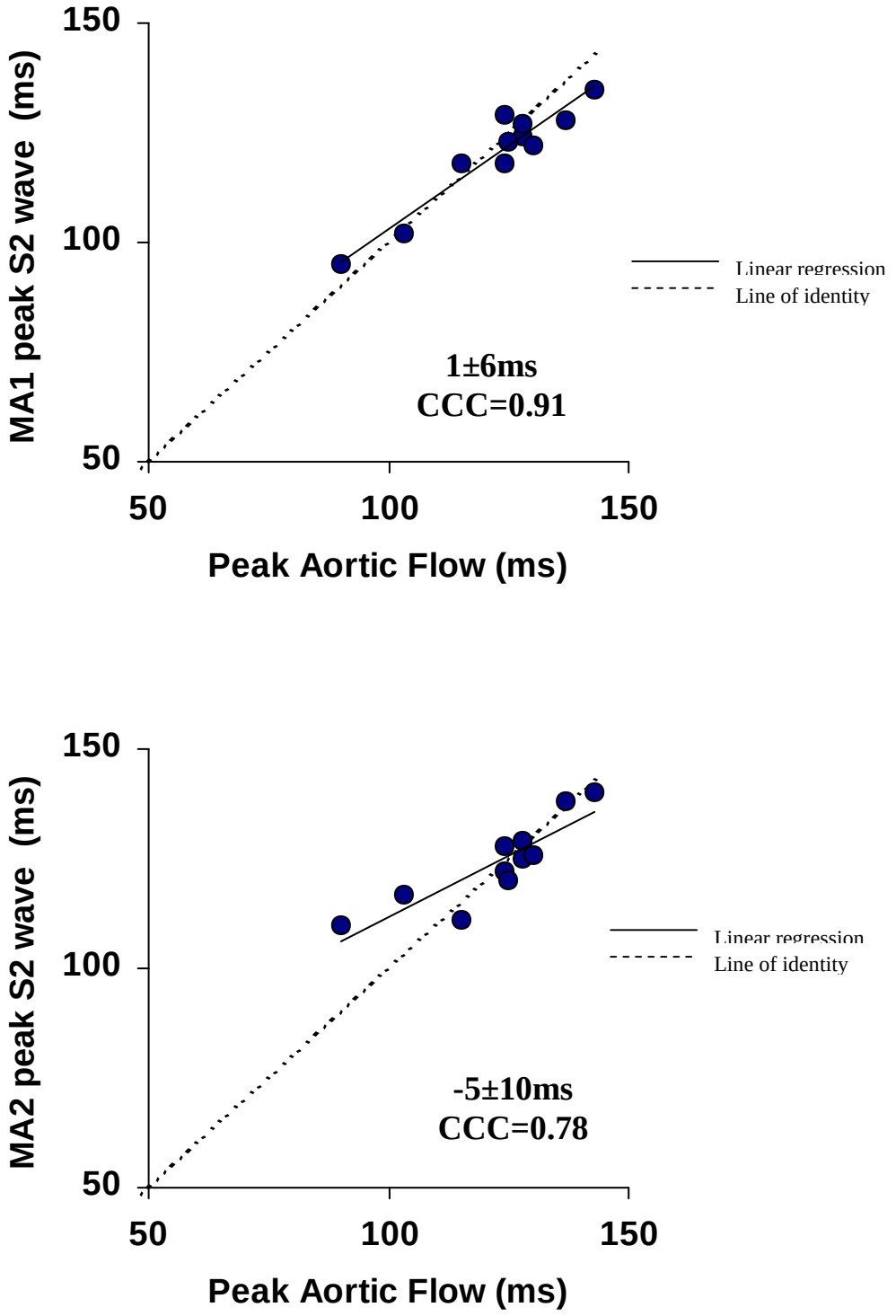

Figure 6.4: Lin's concordance correlation plots showing that the time of peak aortic flow strongly agrees with the time at which both the anterioseptal (MA1) and the inferiolateral (MA2) segment begins to slow. The average difference between peak aortic flow and MA1 is 1±6ms CCC=0.91. The difference between peak aortic flow and MA2 is -5±10ms CCC=0.78

6.3.6 Comparison of normotensive and hypertensive subjects

6.3.6.1 Velocities

6.4.4 Do Reflected waves have a detrimental effect on the left ventricle?

To further investigate the effect of reflected waves on LV function the 11 subjects were separated into those with normal blood pressure (n=6) and those that suffer from hypertension (n=5). Previous literature implies that people with hypertension have larger reflected waves that augment LV afterload. The peak velocities of shortening both during IVC and ejection are presented in **Table 6.5**. During IVC all segments peak shortening velocities were consistently lower in the hypertensive group. The mitral annular lateral segment was most affected by hypertension; its average peak velocity of shortening was reduced by 19%. During ejection however, it was a slightly different story. The minor axis velocities (MA1 and MA2) were both reduced in the hypertensive group (as during pre-ejection) however the mitral annular long axis velocities were not significantly affected by hypertension.

Table 6.5: Left ventricle long and minor segments peak velocities of shortening were split into two sub-groups: normotension (n=6) and hypertension (n=5), during both pre-ejection (S1) and ejection (S2). By looking at the average minor and long axes velocities highlighted in yellow it can by observed that all peak velocity values are effected by hypertension during isovolumic contraction (IVC) however only the minor axis segments peak velocities are effected during ejection.

	Pre-ejection (S1)			Ejection (S2)		
	Normotension (cm/s)	Hypertension (cm/s)	Difference (cm/s)	Normotension (cm/s)	Hypertension (cm/s)	Difference (cm/s)
Minor axis						
MA1	6.15	4.75	1.4	5.55	4.25	1.31
MA2	6	5.5	0.49	6.3	5.19	1.11
Average			**0.95**			**1.21**
±SD			**0.64**			**0.14**
Long axis						
Septum	7.92	6.4	1.53	7.16	6.86	0.3
Lateral	9.88	7.97	1.92	8.66	8.85	-0.19
Inferior	7.03	6.18	0.85	6.93	7.08	-0.15
Average			**1.43**			**-0.01**
±SD			**0.54**			**0.27**

Time to Peak Systolic (S2) wave

The time interval from the R of the QRS complex to the times of peak S2 of all segments plus peak aortic flow were also divided into people with normotention and hypertension. The time to peak S2 was found to occur slightly earlier in the hypertensive subgroup compared to that of the normals; however the time to peak S2 of both minor axis LV segments still coincides with peak aortic flow as shown in **Table 6.6** and **Figure 6.5 and Figure 6.6.** This suggests that larger reflected waves arrive at the heart sooner in people with hypertension, and that BCWs slow the active shortening of the LV minor axis.

Table 6.6: Average time intervals from the R of the QRS complex to peak aortic flow and to all minor and long axis segments peak systolic velocities (S2) in people with normotension and hypertension. All time intervals are reduced in the hypertensive group. Peak Aortic flow velocity still coincides with the time to S2 peak in both minor axis segments irrespective of when time is.

	Normotension	**Hypertension**	**Difference**
	(ms)	**(ms)**	**(ms)**
Peak Aortic Velocity	130	114	**16**
Minor axis segments			
MA1 S2 peak	124	115	**9**
MA2 S2 peak	128	120	**8**
Long axis segments			
Septum S2 peak	168	146	**22**
Lateral S2 peak	158	149	**8**
Inferior S2 peak	188	174	**14**

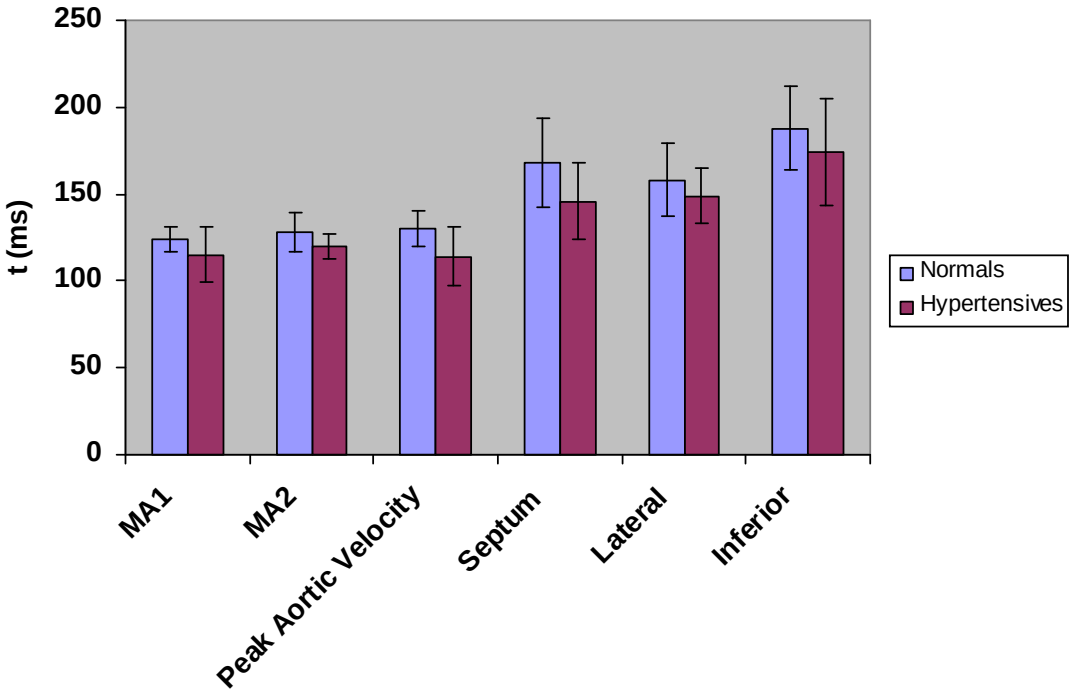

Figure 6.5: A bar chart demonstrating how the average time interval from the R wave of the QRS complex to peak aortic flow and peak systolic wave (S2) in all in segments is lower patients with hypertension (purple bars) compared to those without (blue bars).

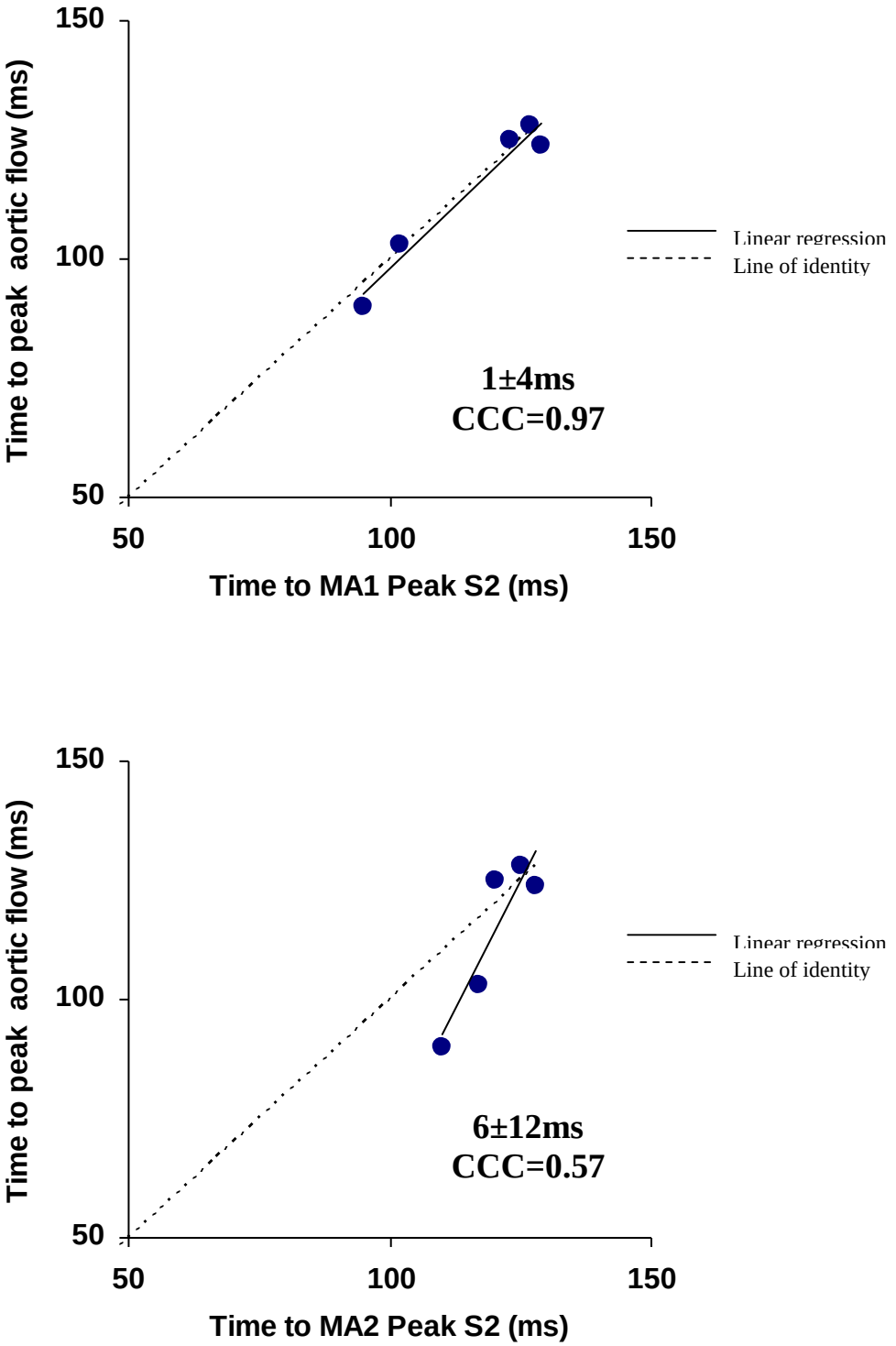

Figure 6.6: Lin's concordance correlation plot showing that the time of peak aortic flow in people with hypertension strongly agrees with the time at which both the anterioseptal (MA1) the inferiolateral (MA2) segment begin to decelerate.

6.5 Discussion

LV systolic function is the amalgamation of long and minor axis shortening. This chapter aimed to further understand the time relationships between the two LV components. The velocities of both the long and minor axes at several regions were studied during both IVC and ejection. The results show that mitral annulus long axis velocities are consistently higher than those of the mid-myocardial minor axis during both IVC (peak S1) and ejection (peak S2). These results agree with previous studies in which LV velocities have been shown to be highest at the mitral annulus and decrease from the base towards the apex (Pai et al. 1998). In this group of patients the velocities of peak S1 and S2 were actually found to be quite similar with S1 being on average higher than S2 in all segments except at the inferior segment of the mitral annulus as seen in **Table 6.2**. S1 has previously been observed to reach higher velocities than S2 (Oki et al. 1999). IVC velocities are implied to be load independent by some groups and S1 is considered to be a very sensitive marker of global contractility (Lindquist et al. 2007, Vogel et al. 2002).

Left ventricle asynchrony:

Coherent LV function has a significant implication on the energy transfer from the myocardium to the circulation. The time interval from the R wave of the QRS complex to the peak systolic wave (S2) was recorded in two minor axis and three long axis segments. Long and minor axis segment timings were compared not only to each other but also to the time of peak aortic flow. Our study elaborates on the pattern of the asynchronous function of the two axes, by demonstrating a normal time delay between the shortening velocities of the two axes in all subjects. In these subjects a difference of ~30ms was seen between the two axes average time to peak velocity of shortening. This matches the asynchrony observed between the long and minor axis in the dogs in chapters 3 and 4 as seen in **Figures 3.12** and **3.14**. This principle of asynchrony has been recently used in assessing patient suitability for cardiac resynchronisation therapy (Yu et al. 2005). However the main difference is the number of segments used (up to 16 in some studies) (Kapetanakis et al. 2005) rather than our simple model of 5 segments.

The reflected wave:

We have seen in the previous chapters that the arrival of BCWs at the heart is associated with a decline in LV minor axis shortening rate in dogs. The findings in this human study are in agreement with the previous data when using peak aortic flow

as a surrogate for BCW wave arrival. The BCW can be postulated to have an effect on the LV wall speed itself, perhaps by affecting the circumferential fibres rate of shortening specifically. The BCW appears to stop the mid-wall fibres that make up the minor axis from generating any more force. The axis continues to shorten but at a much slower rate, probably due in some part to momentum. The explanation for this is a little more difficult to explain but probably lies in the exact stage of mid-wall fibre cross-bridge formation when the BCW arrives. BCWs have been previously shown to have a significantly negative effect on subendocardial function in patients with peripheral arteriopathy during arterial clamping (Henein et al. 1996) and the close relationship between the extent of abbreviated ejection and filling time and clinical response to cardiac resynchronization therapy recently reported supports our current findings (Duncan et al. 2006).

Possible detrimental effect of the reflected wave:

To test the proposition that reflected waves decelerate LV minor axis rate of shortening the subjects were split into two subgroups: Those with normal blood pressure (BP<140/90 and those with hypertension (BP>140/90). In hypertensive subjects the S1 velocities during IVC were reduced in all regions of interest as shown in **Table 6.4**. This data agrees well with that of Oki et al. 1999 in which S1 IVC velocities in both the long and minor axes were observed to decrease during an angiotensin II induced increase in LV afterload. In the same paper, during ejection the increase in afterload only reduced S2 peak velocity in minor axis segments; the long axis mitral annular velocities were unaffected. A similar occurrence was seen in the hypertensive sub-group, shown in **Table 6.5**. This information implies that although the minor axis essentially plays a major role in ejection, during hypertension when the reflected wave magnitude is larger (leading to an increase in LV afterload) the role of longitudinal fibres become more prominent. This conclusion is in contrast with previous studies that have seen that in states of decrease LV function radial axis shortening increases to compensate for a decrease in long axis function (Przewlocka-Kosmala et al. 2006).

When the time of the S2 wave was compared to the time of peak aortic flow it was seen that the time of peak aortic flow consistently coincided with the peak velocity of S2 of both minor axis segments in normal and hypertensive subjects **Figures 6.4** and **6.6** These data also agree with the canine data in previous chapters. Peak S2 was always seen to occur slightly earlier in the hypertensive sub-group compared to that

of the normotensive sub-group, as shown in **Table 6.6**. As flow deceleration is known to occur due to the arrival of the reflected compression wave this would imply that the BCW arrives at the heart earlier in these hypertensive patients, which would be in agreement with previous studies (Nichols WW and Edwards DG 2001, Curtis et al. 2007).

Clinical implications: With LV disease, prolonged early systolic shortening results in delayed onset of tension development and hence onset of ejection (Duncan et al. 2006). Despite the impaired rate of pressure rise, the resulting transvalvular gradient opens the aortic valve and hence ejection follows. However, the end result is abbreviated aortic ejection time despite a prolonged isovolumic contraction period (since timing of aortic closure remains unchanged), impingement of early diastolic filling due to post-systolic tension, and ultimately compromised stroke volume. This study highlights the fundamental basis of LV asynchrony and its effect on ejection. There is evidence to suggest that long axis function becomes more crucial during disease. The results are supported by recently published data in dogs which showed optimised global LV systolic function over broad regions of the lateral wall irrespective of the pacing lead position, (Helm et al. 2007) and hence independent of the regional function of the 16 segment model.

Limitations:

There are three major limitations to this study one being the small number of patients investigated. Nonetheless the findings are extremely insightful and encourage enthusiasm for a larger investigation into this area. All of the individuals recruited for this chapter also have ‘normal’ LV function; applying the same techniques in asynchronous models of cardiomyopathy should provide more insight into the concept of LV asynchrony.

The second major limitation to this investigation is the use of TDI instead of newer more recent techniques such as speckle tracking imaging. All of the limitations to PW TDI have been discussed in the limitations section of chapter 5.

The third and biggest limitation is the lack of directly measured reflected waves. Although reflected waves are known to instigate flow deceleration, peak aortic flow measured non-invasively by continuous wave Doppler through the aortic valve is not a surrogate marker that has ever been used for this purpose before.

6.6 Conclusion:

Close relationships occur between velocities of the two axes and the timing of LV aortic flow events. Normal long and minor axis asynchrony is implicit in supporting aortic pressure timing and hence stroke volume. These timings of normal asynchrony at rest between the minor and long axes and their relations to flow events demonstrate that global function of the ventricle is likely to determine the overall stroke volume. Acquiring these data in patients using available echocardiographic techniques should assist in identifying the most accurate measurements required for optimising ventricular synchronous function, as means of obtaining optimum stroke volume. There is strong evidence to suggest that the LV long axis becomes significantly more important during states of increased LV afterload and that the minor axis velocity of shortening beings to slow with reflected wave arrival at the heart.

Chapter 7: Use of wave Intensity Analysis in a Clinical Setting:

Effect of Pharmacological Intervention on Arterial Waves

7.1 Introduction

Chapters 3-6 have shown how applying wave intensity analysis (WIA) can provide physiologically meaningful results. Although WIA has been around for 20 years it is still only applied in research institutions. The lack of its use in clinical settings could initially be explained by the need for invasively acquired pressure and velocity measurements. However recent developments in equipment to acquire measurements non-invasively (as mentioned in chapter 1, section 1.4.3) should have aided in its integration into every day clinical use. In spite of this WIA is not implemented into routine check ups and precious information is being lost. This chapter aims to show how WIA can provide valuable information that would otherwise be missed in one quick, painless examination. Non-invasive wave intensity analysis (WIA) was applied to the left common carotid artery to examine which of two beta-blocking agents had more favourable haemodynamic affects

7.1.1 Hypertension:

Hypertension is a significant contributor to cardiovascular disease (CVD) and the leading instigator of ischemic myocardial infarction and stroke (Lewington et al. 2002). According to most guidelines adults are considered hypertensive if they have a systolic blood pressure ≥140mmHg and/or diastolic pressure of ≥90mmHg. CVD risk is said to double for every 20/10 mmHg increment starting with a systolic pressure of 115mmHg and diastolic pressure of 75mmHg (Chobanian et al. 2007). It is estimated that over 1 billion people worldwide suffer from hypertension (Chobanian et al. 2007) and the prevalence of hypertension increases with age (Burt et al. 1995) such that the lifetime risk of developing hypertension in people over the age of 65 is about 90% . Mean blood pressure rises with age over the lifecourse (Health Survey for England) but over the age of ~50 years elevated systolic blood pressure becomes more prominent and diastolic pressure stabilizes or declines (Staessen et al. 2003.) as the arteries become stiffer. This increased stiffness is believed to be mainly due to the disruption and remodelling of the elastic elements of the arterial wall (O'Rourke 1976, Wilkinson and McEniery 2003). Arterial stiffening causes increased pulse pressure, which is recognized as an independent risk factor for cardiovascular events (Franklin et al. 2001) and isolated systolic hypertension is the commonest cause of hypertension in people over 60 yrs (Franklin et al. 2001). For this reason older patients are prone to suffer from hypertension related cardiovascular complications.

In primary (essential) hypertension the increase in mean blood pressure is the consequence of high peripheral vascular resistance (Folkow 1982). In older subjects with isolated systolic hypertension, as previously mentioned the major determinant of hypertension is large artery stiffness (Franklin et al. 2001) probably with some contribution from an increased magnitude of reflected waves (Nichols and O'Rourke 1998).

Numerous medications are prescribed for the treatment of hypertension including diuretics, vasodilators, calcium-channel blockers, angiotensin converting enzyme (ACE) inhibitors, angiotensin (AT_1) receptor blockers and beta-blockers. In order to achieve adequate blood pressure control over 60% of patients require more than one anti-hypertensive agent (Cushman et al. 2004). All drugs have both advantageous and adverse effects, it is therefore imperative that the appropriate therapy is given depending on the patient's age, sex ethnicity and concomitant disease.

7.1.2 Beta-Blockers: Until recently (**www.nice.org.uk/CG034**), beta-blockers have been a preferred first-line therapy for hypertension for over 40 years. The mechanism of their antihypertensive action has been hotly debated over the years, but simply put they slow the heart rate and decrease cardiac output. They achieve this by blocking the action of the sympathetic nervous system on β adrenergic receptors located on cardiac myocytes. There are three known subtypes of β receptors in the body, β1 are largely located in the heart and kidneys, β2 are mostly located in the lungs, gastrointestinal tract, vascular smooth muscle and skeletal muscle and β3 are located in fat cells and stimulate lipolysis. Noradrenaline (released from sympathetic nerves) and adrenaline (released from the adrenal medulla) act on β1 receptors to increase heart rate (positive chronotropy) and the force of cardiac contraction (positive isotropy). Both non-selective (e.g. propranolol) and β1 selective receptor antagonists (e.g. atenolol) will prevent these effects and reduce cardiac output. It is possible that effects of β-adrenergic receptor antagonists on renin release and sympathetic nerve activity also contribute to the antihypertensive effects of these agents (Page et al. 1997), however the lack of decrease in peripheral vascular resistance seen with conventional beta-blocker therapy suggests that a reduction in cardiac output is the major mechanism of action (Lund-Johansen 1992). Beta-blockers are alleged to possess anti-ischemic, anti-heart failure and anti-hypertensive properties (Cruickshank 2007). However in more recent times the anti-hypertensive

properties of these agents has been under scrutiny and beta-blockers have lost favour to newer anti-hypertensive agents (Williams 2006, NICE clinical guidelines 2006). Despite this recent shift away from beta–blocker therapy new agents have been developed that possess very different pharmacological properties (Kendall et al. 1997, Toda et al. 2003).

Atenolol was introduced in 1976 as a β1-cardioselective anti-hypertensive agent. It has been extensively prescribed to treat hypertension for 30 years however it is now alleged that Atenolol and other traditional selective β-blockers are inferior to some other antihypertensive drug classes and should not be used as first line agents (Lindholm et al. 2005). While this is not universally accepted (Khan et al. 2008) conventional beta blockers are not effective at improving vascular compliance (Cruickshank 2007); can impair glucose tolerance leading to new-onset diabetes (Opie and Schall 2004); and are unable to reverse LV hypertrophy and other cardiovascular events in the elderly (Messerli 2003).

Nebivolol is a cardioselective third generation β-blocker with mild vasodilating properties. It is believed to cause vasodilatation, improving vascular compliance without markedly inhibiting LV function (Cruickshank et al. 2007) and does not evoke the metabolic disturbances associated with Atenolol (Gress et al. 2000, Jacob et al. 1998). Nebivolol has in actual fact been reported to improve glycemic control and insulin sensitivity (Giugliano et al. 1997, Celik et al. 2006). It may achieve this by increasing peripheral blood flow, aiding insulin delivery (Gress et al. 2000). Nebivolol induces vasodilatation of peripheral arteries by stimulating nitric oxide (NO) release in endothelial cells (Mason et al. 2005, Maffei et al. 2006). The exact pathway that Nebivolol achieves this is still being investigated but it is believed to involve the mimicking shear stress (Mason 2006) and the reduction of reactive oxygen species (ROS) (Mason et al. 2005).

7.1.3 Aim

The aim of this study was to prove how efficient and informative WIA can be in every day clinical settings. Non-invasive WIA was applied to the carotid artery to examine whether a newer beta-blocking agent with vasodilator properties, nebivolol, had more favourable haemodynamic effects compared to the most widely used conventional agent in hypertension, atenolol. This was part of a larger study with the

overall intension of helping to establish whether nebivolol might not share some of the pharmacological disadvantages associated with conventional beta blockers such as atenolol. The full protocol for the larger study can be viewed in appendix 7.1.

7.2: Hypothesis

Atenolol treatment will bring about a decrease in cardiac contractility manifesting in smaller forward waves generated by the LV compared to nebivolol. The reflected waves that return to the heart in mid-systole will however be larger during atenolol treatment compared to nebivolol due to an increase in arterial resistance caused by atenolol.

7.3 Methods

7.3.1 Subjects

A total of 50 people were originally recruited from the Peart-Rose Cardiovascular Disease prevention clinic at Imperial College Healthcare NHS Trust, London, UK to take part in this study but the current analysis in this thesis is restricted to only 38 subjects (age 63±11yrs, 21 female) who attended for all visits. The remaining 12 subjects failed to attend all four visits and so were discounted from this set of analyses. All subjects gave written informed consent in accordance with the local ethics committee. Further information on the extended study can be seen in appendix 7.1. Subjects were included if they presented with either a systolic blood pressure $\geq$ 160mmHg and diastolic blood pressure $\geq$ 90mmHg on one anti-hypertensive drug, a systolic blood pressure $\geq$ 150mmHg and diastolic blood pressure $\geq$ 90mmHg on two anti hypertensive drugs or a systolic blood pressure between >140 and $\geq$ 170 mmHg and diastolic blood pressure $\geq$ 90mmHg on no anti-hypertensive drugs. Any subjects with diabetes mellitus, heart failure, bradycardia, atrial fibrillation, currently taking verapamil/diltizem or any previous intolerance to beta blocker treatment were excluded.

7.3.2 Study design:

This study was a randomised double-blind crossover trial comparing the effects of beta-blockers nebivolol against atenolol. The trial consisted of four stages. Stage 1 was an open label run-in phase which involved taking a low dose thiazide-like diuretic (Bendroflumethiazide 2.5mg) for four weeks. Thiazide-like diuretics are often prescribed as a primary therapy for hypertension as they remove excess water from the body and also vasodilate the blood vessels. After the fourth week the subjects visited the clinical investigation unit at St Mary's Campus where they underwent their first 'baseline' carotid scan. This was followed by 8 week study treatment phase in which patients were randomised double blind and received either nebivolol 2.5mg or atenolol 50mg in addition to the low dose thiazide-like diuretic. After 8 weeks the patients returned for their second carotid scan. Stage 3 consisted of a second 4 week open label washout phase on a low dose thiazide-like diuretic only, again followed by a carotid scan. The final stage was a second 8 week study treatment

phase in which subjects received whichever drug they did not take during stage 2. After 2 weeks of active nebivolol or atenolol treatment during stages 2 and 4 the dose of nebivolol was increased to 5mg and atenolol to 100mg if the systolic blood pressure was ≥ 140mmHg or the diastolic blood pressure was ≥ 90mmHg. A carotid scan was also performed at the end of stage 4.

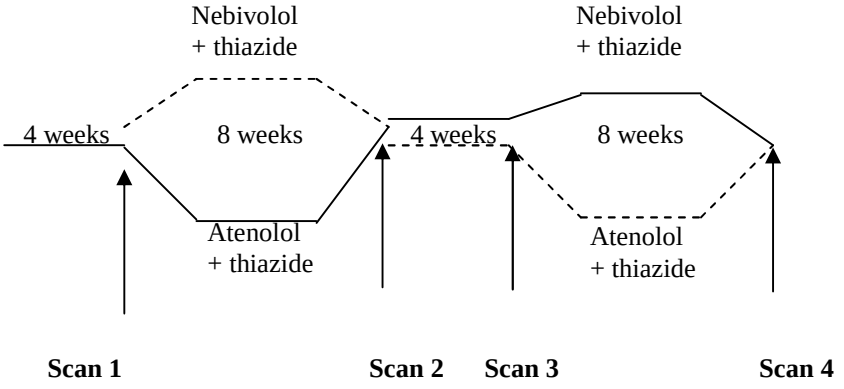

Figure 7.1: Diagram illustrating the study design

Treatment Plan

1) Randomise patient

2) Low dose thiazide-like diuretic only for 4 weeks

3) Scan 1-baseline

4) Either nebivolol 2.5mg or atenolol 50mg (+thiazide-like diuretic)

5) Increase dose of nebivolol to 5mg or atenolol to 100mg after 2 weeks if systolic blood pressure ≥ 140mmHg or the diastolic blood pressure is ≥ 90mmHg C then continue treatment for 6 weeks

6) Scan 2-drug A

7) Low dose thiazide-like diuretic only for 4 weeks

8) Scan 3-washout

9) Either nebivolol 2.5mg or atenolol 50mg (+ thiazide-like diuretic)

10) Increase dose of nebivolol to 5mg or atenolol to 100mg after 2 weeks if systolic blood pressure ≥ 140mmHg or the diastolic blood pressure is ≥ 90mmHg C then continue treatment for 6 weeks

11) *Scan 4-drug B*

7.3.3 Wave intensity measurement protocol

All participants rested in the supine position in a quiet, dark room for at least 10 minutes prior to measurements. Blood pressure was measured in the left arm using a semi-automated, validated oscillometric blood pressure monitor (Omron HEM-705 CP). The left common carotid artery was insonated in the long axis using an Aloka SSD 5500 ultrasound system (ALOKA, Japan) equipped with a 7.5MHz linear array vascular probe at the region of the left common carotid artery approximately 2 cm proximal to the bifurcation and the orientation of the vessel was angled to ~10 degrees. The image was optimised by ensuring that the depth was as shallow as possible, and that the vessel walls were well delineated to permit satisfactory Echo tracking at the interfaces. The gates were positioned manually between the intima and media of the anterior and posterior walls. The range gate for Doppler velocity measurements was automatically positioned at the centre of the vessel using the echo-tracking gates and the velocity scale was adjusted, so that the colour Doppler image filled the vessel and to ensure that no aliasing was occurring. The sample volume size was then adjusted to ensure the whole vessel was interrogated (**Figure 7.2**). A 3- lead ECG trace was recorded concurrently.

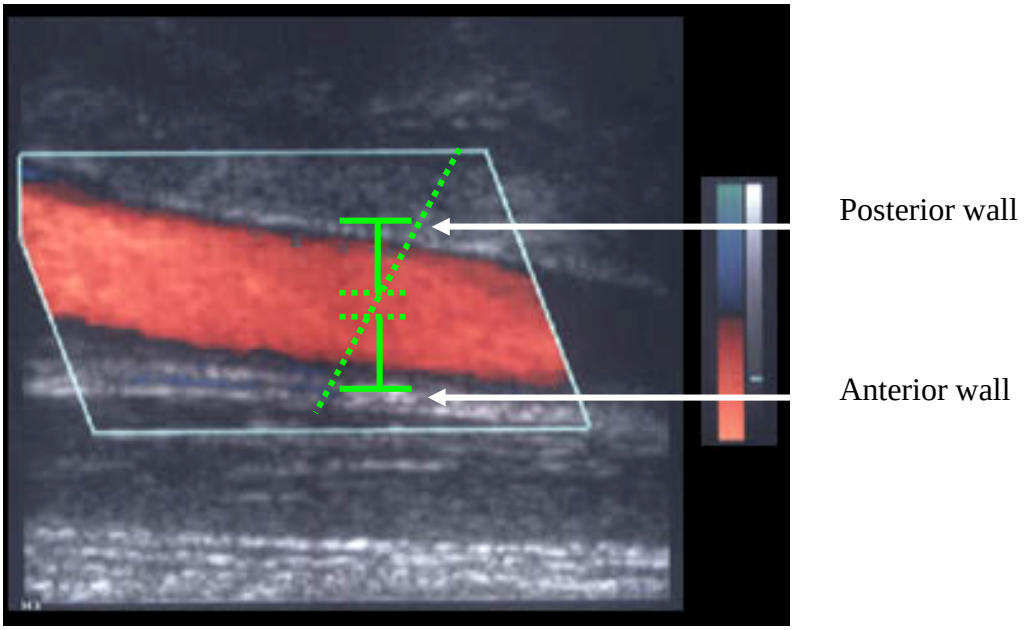

Figure 7.2: The echo-tracking subsystem allows the user to place the lines between the media and adventitia on the posterior and anterior walls of the vessel. The range

gate for velocity measurements are automatically positioned at the centre of the diameter by using echo-tracking gates

7.3.4 Data Analysis

The ultrasound echo-tracking subsystem can measure carotid diameter changes to within one-sixteenth of the ultrasound wavelength (0.013mm) at a sampling rate of 1000Hz. Diameter (D) was calculated as the distance between the common carotid anterior and posterior walls and change in diameter (dD) has been reported to have a linear relationship with change in invasively measured carotid artery pressure (Sugawara et al 2000). The ultrasound machine can use the calculated diameter change and Doppler flow recording to plot wave shapes with the following equation: (dU/dt)/dD/dt/D). Changes in diameter are calibrated to pressure on the basis of the brachial blood pressure enabling wave intensity to then be calculated. Offline, all carotid U and P (D) measurements and ECG data were analysed using custom written programs in Matlab (The MathWorks Inc., MA, USA). Both P and U were smoothed using a 15 point each way Savitzky-Golay filter (Savitzky-Golay 1964). Five of the cleanest P and U waveforms for each patient were then selected using the peak R wave of each ECG complex as the beginning and end of each cycle, as shown in **Figure 7.3.** The waveforms were ensemble averaged to generate single carotid P and U waveforms. No more than 5 beats were ensembled to ensure that the traces are not artifactualy smoothed. Beat were selected based on the quality of their pressure and flow velocity traces. The ensembled traces were then used to calculate wave intensity using the original equation dI=dPdU. The magnitudes and timings of the forward compression wave (FCW), backward compression wave (BCW) and forward expansion wave (FEW) were all recorded.

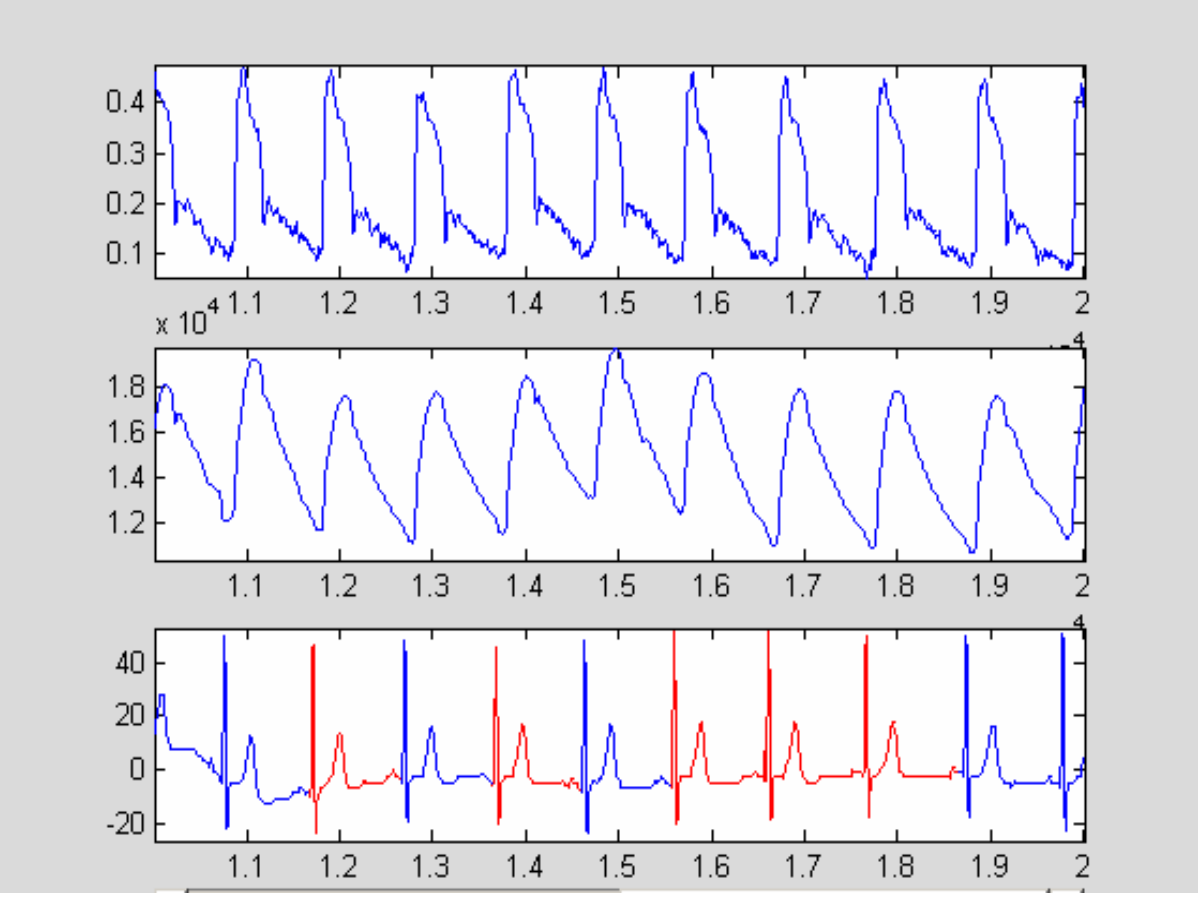

Figure 7.3: ~10s of recorded carotid pressure (P), velocity (U) and electrocardiogram (ECG), the best quality 5 beats (those with the ECG highlighted in red) are ensemble averaged. The wave forms that closely resemble 'perfect' textbook pressure and flow wave forms were selected.

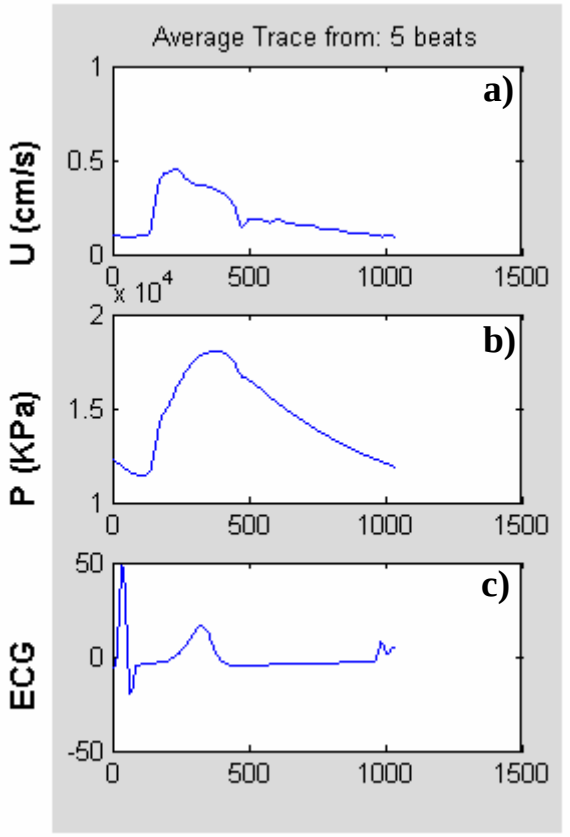

Figure 7.4: An example of ensemble averaged traces a) Velocity (U), b) Pressure (P) and c) ECG trace calculated from the most suitable 5 beats.

7.3.5 Statistical Analysis

As this study is a crossover trial a specific series of statistical tests were required to be performed before performing statistical comparison tests. The first set of analysis assesses whether there is a carry-over of treatment effect. Paired t tests were performed between the baseline (scan 1) and washout (scan 3) data. If no carry-over effect is seen one must then check for two other types of possible problems:

1) **A period effect**: To ensure that there is no systematic difference between one period and the other, two sample t-tests were performed on the differences (Δ) of the two drug periods ($\Delta_1$and Δ_2). If no period effect exists the mean differences between the treatment groups should be the same but have opposite signs.

2) **Order effect**: To ensure that the order in which treatments are given has no effect. This is assessed by calculating the average (a) of each group and comparing them using a two-sample t test (a_1-a_2).

If all statistical tests are favourable then paired t tests can be performed to investigate the differences in wave behaviour measured between nebivolol and atenolol treatment arms. For all statistical comparisons two-way tests were used and $p < 0.05$ was considered significant.

7.3.6 Reproducibility

Reproducibility of wave intensity analysis was studied in 8 subjects. The mean difference (SD) for the energy carried by the FCW was -44 (56) kJm^{-2} (within subject coefficient of variation = 5.8%), for the BCW was -5 (16) kJm^{-2}(within subject coefficient of variation = 9.5%) and for the FEW wave was 8 (20) kJm^{-2} (within subject coefficient of variation = 14.9%).

7.4 Results

The baseline characteristics of the 38 individuals that completed all visits are displayed in appendix 7.3. **Table 7.1** shows the summary details. Drug sequence was randomised and of this group 17 of the 38 subjects received Nebivolol first. Average BP was 133/84mmHg, the majority of subjects were Caucasian and the age ranges from 35 years to 79 years.

Table 7.1: Summary data of baseline characteristics. n= number of participants.

Baseline Characteristics	
n	38
Age (years)	63 (11)
Race (% Caucasian)	71
Systolic blood pressure (mmHg)	133 (13)
Diastolic blood pressure (mmHg)	84 (8)

7.4.1 Statistical checks:

Paired t tests were performed between all baseline (scan 1) and washout (scan 3) parameters and no carry-over treatment effect was observed: the results obtained during the second treatment were not affected by the the first treatment. The p values all show no statistically significant difference and are presented in **Table 7.2** in the column titled 1+3. Two sample t-tests were then performed on the difference (Δ) of the two groups (Δ1=scan 2-1, and Δ2=scan 4-3) to test for a period effect. No period effect was found. The average (a) of each group was additionally calculated (a1=scan 2-1, and a2=scan 4-3) and no treatment effect was evident; therefore a patient's response was not affected by the order of the treatment received.

7.4.2 Haemodynamic measurements:

As all the preliminary statistical tests were favourable for a crossover study, paired t tests were performed to compare drug treatments. **Table 7.2** shows the average±SD values for each parameter during each visit. The results showed that both β-blockers significantly decreased heart rate (HR) and blood pressure (BP) as expected (**Table 7.2)**. When comparing the two drugs directly reductions in systolic and diastolic BP

are similar, however atenolol induced a significantly larger decrease in HR (-14±7 beats per minute) than nebivolol (-7±6 beats per minute) (**Table 7.3)**.

	Control (1)		Nebivolol (2)		Washout (3)		Atenolol (4)		P values			
	Mean	SD	Mean	SD	Mean	SD	Mean	SD	1+2	1+4	2+4	1+3
Wavespeed (m/s))	8.59	3.52	7.48	2.71	8.739	3.43	7.287	2.93	**0.01**	**<0.01**	0.22	0.88
Heart Rate (bpm)	67	8	60	7	68	8	55	6	**<0.01**	**<0.01**	**<0.01**	0.21
Systolic BP (mmHg)	133	13	124	12	133	14	120	12	**<0.01**	**<0.01**	**0.01**	0.99
Diastolic BP (mmHg)	84	8	78	7	84	8	76	8	**<0.01**	**<0.01**	**0.02**	0.52
dIC+ (J/m^2)	28348	11378	26567	10549	29897	11452	24920	11547	0.35	**<0.01**	**0.01**	0.68
dIE+ net(J/m^2)	8892	4605	7670	2335	8488	4184	5902	2504	0.28	**<0.01**	**<0.01**	0.51
dIC- net (J/m^2)	-4124	-2266	-3872	-1968	-4796	-3095	-3911	-2410	0.57	0.3	0.61	0.17
FCW (dIc+)												
dIc+energy (J/m^2)	30029	11859	28132	11689	26145	31162	26534	12045	0.36	**<0.01**	**0.02**	0.61
dIc+max (W/m^2)	929	391	817	346	963	455	765	398	0.11	**<0.01**	**0.01**	0.9
Peak time (ms)	151.7	14	156.5	15	155.3	17	160.2	13	**0.03**	**<0.01**	0.08	0.08
Start time (ms)	105.7	18	112.7	16	108.2	18	113.2	16	**0.02**	**0.01**	0.86	0.33
BCW (dIc-)												
dIc- energy (J/m^2)	-5845	-3281	-6152	-3110	-6935	-169	-5703	-3756	0.7	0.39	0.27	0.79
dIc-max (W/m^2)	-146	-88	-132	-78	-169	-121	-126	-90	0.21	0.06	0.54	0.22
Peak time (ms)	208.63	23	217.66	27	210.82	4.47	220.63	22	**0.03**	**<0.01**	0.11	0.31
Start time (ms)	156.74	15.6	161.08	15	156.21	3	165.18	15	**0.02**	**<0.01**	0.48	0.37
FEW (dIe+)												
dIe+ energy (J/m^2)	7216	3955	5841	2344	6751	3318	4512	2116	0.06	**<0.01**	**<0.01**	0.46
dIe+max (W/m^2)	292	154	234	85	272	143	180	96	0.06	**<0.01**	**<0.01**	0.36
Peak time (ms)	420.2	23	435.7	26	417.13	24	452.4	22	**<0.01**	**<0.01**	**<0.01**	0.4
Start time (ms)	345.3	28	369.6	28	342.95	28	383.6	32	**<0.01**	**<0.01**	0.07	0.62

Table 7.2: Average values for each parameter during each phase of the study. Paired t-test were performed to compare the effect of the different β-blockers. p = 0.05 was considered significant, significant p values are in **bold** text. dIC+ = Net forward compression wave, dIC+ = Net forward expansion wave, dIC+ = Net backward compression wave. dIc-+ = separated forward compression wave, dIe+ = separated forward expansion wave, dIc- = separated backward compression wave.

7.3: Δ Nebivolol compared to Δ Atenolol, P=0.05 was considered significant. HR= heart rate, BP= blood pressure, FCW=forward compression wave, BCW= backward compression wave, FEW= forward expansion wave.

	Δ Nebivolol (scan 2-1)		**Δ Atenolol Scan (4-3)**		**Difference (Nebivolol - Atenolol)**		
	average	±SD	average	±SD	average	±SD	**p-value**
c (m/s)	-0.12	0.29	-0.19	0.31	0.07	0.40	0.30
HR (bpm)	-7.42	5.82	-13.79	6.90	6.37	8.12	**<0.01**
Systolic BP(mmHg**)**	-5.15	6.15	-6.13	7.40	0.97	8.65	0.49
Diastolic BP (mmHg)	-4.81	4.22	-4.39	5.49	-0.42	5.82	0.66
Net FCW (W/m^2)	-0.05	0.34	-0.24	0.43	0.19	0.53	**0.04**
FCW energy (W/m^2)	-0.05	0.34	-0.23	0.44	0.18	0.53	0.05
FCW peak (W/m^2)	-0.09	0.35	-0.28	0.51	0.19	0.58	0.05
Net BCW (W/m^2)	-0.06	0.85	-0.24	0.67	0.19	1.01	0.26
BCW energy (W/m^2)	-0.04	0.57	-0.22	0.50	0.25	0.76	**0.05**
BCW peak (W/m^2)	-0.11	0.55	-0.29	0.64	0.17	0.86	0.22
Net FEW (W/m^2)	-0.08	0.45	-0.32	0.53	0.24	0.67	**0.03**
FEW energy (W/m^2)	-0.14	0.45	-0.38	0.51	0.23	0.65	**0.03**
FEW peak (W/m^2)	-0.16	0.50	-0.40	0.57	0.24	0.71	**0.04**

7.4.3 Wave Patterns

The size and timings of the three main waves observed during ejection were recorded and calculated during the various stages of the trial. **Figure 7.5** plot a) shows a typical carotid wave intensity pattern observed. Plots b, c and d show the associated carotid pressure and velocity changes that accompany the wave pattern. The pattern is very similar to that observed at the aortic root seen in Chapters 3,4 and 5. During early systole a FCW is observed as pressure and velocity both increase in carotid arteries having propagated forward from the aorta. During mid-systole a BCW is observed, however in the carotid artery this arises mainly from a reflection from the head not the body (a reflection from the body would be seen as a forward travelling wave in the carotid as a consequence of its anatomical relationship to the aorta). Reflections from the body are sometimes seen in the carotid arteries during mid systole as small forward travelling waves (Curtis et al. 2007). Near end-systole a FEW generated by the decelerating LV is observed in the carotid artery as was described earlier in the aorta (Chapters 3, 4 and 5).

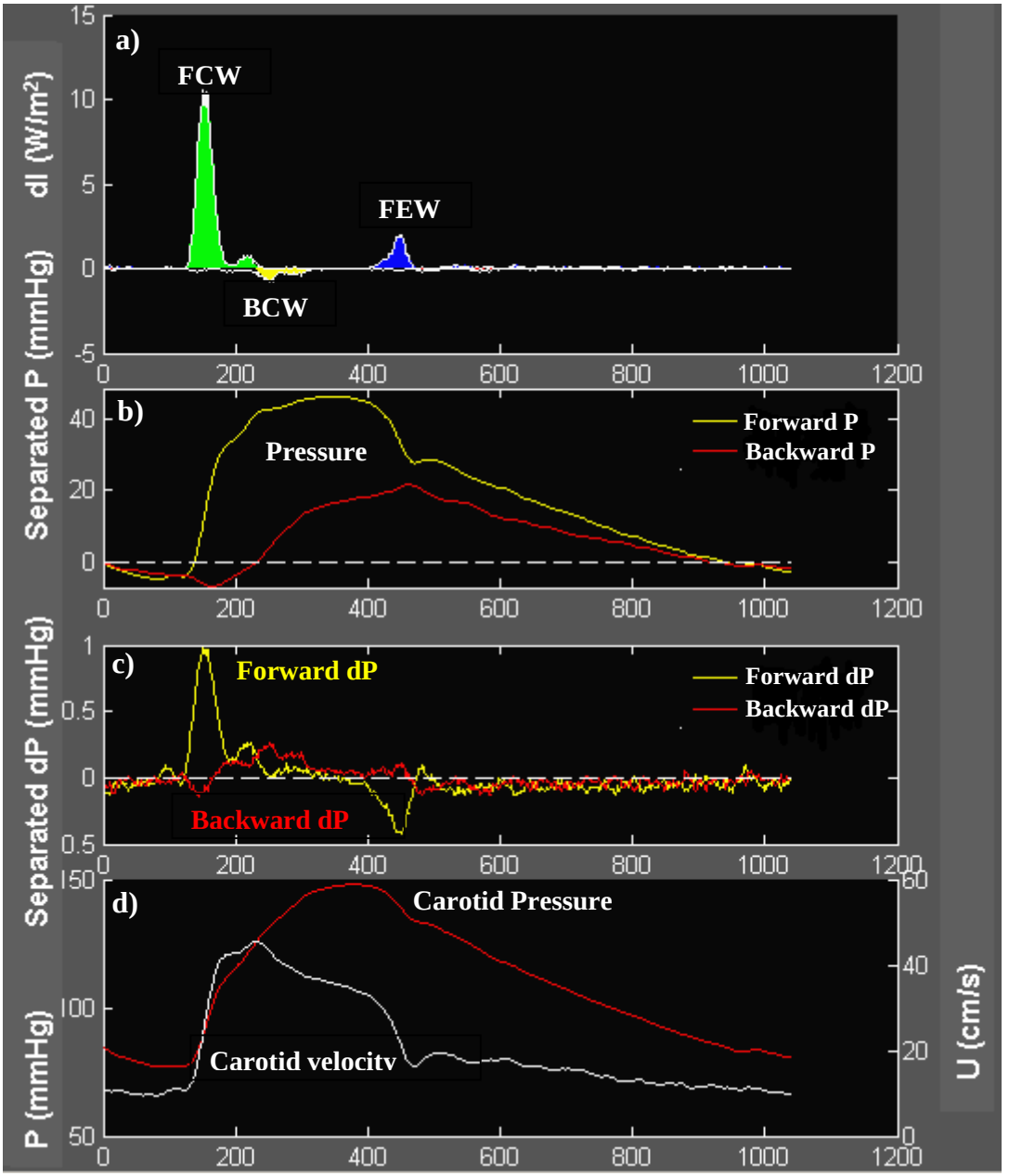

a)

Figure 7.5: A composite demonstrating the pressure and velocity changes that occur in the carotid artery during the cardiac cycle. **Plot a)** is the calculated carotid wave intensity. The three main waves are labelled, FCW = forward compression wave, BCW = backward compression wave and FEW = forward expansion wave. **Plot b)** is forward (yellow) and backward (red) carotid pressure wave forms. **Plot c)** is the calculated first derivatives of forward (yellow) and backward (red) carotid pressure. **Plot d)** contains plots of measured carotid pressure and flow velocity.

7.4.4 The forward compression wave:

During atenolol treatment the net FCW was 12% (28348±11378J/m^2 vs. 24920±11547J/m^2) smaller than during baseline measurements , the separated FCW energy was reduced by 12% (30029±11859J/m^2 vs. 26534±12045J/m^2) and the peak value was 18% (929±391W/m^2 vs. 765±398W/m^2) smaller. All FCW measurements were significantly smaller than those measured at baseline ($p<0.05$) as seen in **Table 7.2**. During nebivolol treatment the net FCW was only 6% (28348±11378J/m^2 vs. 26567±10549J/m^2) smaller than that at baseline, the separated FCW energy was reduced by 6% (30029±11859J/m^2 vs. 28132±11689J/m^2) and the peak value was 12% (929±391W/m^2 vs. 817±346 W/m^2) smaller. Although the FCW was smaller these results are not significantly different from those seen at baseline ($p>0.05$). Atenolol significantly reduces the magnitude and peak of the FCW compared to nebivolol. Atenolol therefore reduces the output from the LV.

7.4.5 The backward compression wave:

During atenolol treatment the net BCW was 5% (-4124±-2266 J/m^2 vs. -3911±-2410J/m^2) smaller than baseline measurements, the separated BCW energy was reduced by 2% (-5845±-3281J/m^2 vs. -5703±-3756 J/m^2) and the peak value was 13% (-146±-88W/m^2 verses -126±-90 W/m^2) smaller. Although the waves are reduced during atenolol treatment the results are not statistically significant from the baseline data ($p>0.05$). During nebivolol treatment the net BCW was only 6% (-4124±-2266 J/m^2 vs. -3872±-1968 J/m^2) smaller than baseline, the separated BCW energy was 5% larger (-5845±-3281J/m^2 vs. -6152±-3110 J/m^2) and the peak value was 9% (-146±-88 W/m^2 vs. -132±-78 W/m^2) smaller. Again, these reductions are not significantly different from the baseline data ($p>0.05$). There was no significant difference seen between the energy carried by the BCW when both β-blockers are directly compared. As the FCW was significantly reduced by atenolol this implies that a higher percentage of the FCW was reflected. The percentage of FCW energy reflected from the head was calculated during baseline, atenolol and Nebivolol treatment. The results are displayed in **Table 7.4** and **Figure 7.6**. As the figure shows the percentage of the FCW reflected is always higher while taking atenolol than when taking nebivolol, but the difference was not statistically significant.

Table 7.4: Percentage of forward compression wave (FCW) generated form the left ventricle that is reflected back towards the carotid artery.

	Baseline		**Nebivolol**		**Difference**		
	Average	±SD	average	±SD	Average	±SD	**P value**
Net energy%	15.1	7.9	14.6	6.7	0.4	7.2	0.7192
Sep energy%	19.8	8.7	21.6	8.7	-1.8	9.3	0.2411
Peak %	16.5	9.7	16	8.8	0.5	7.8	0.7115
	Baseline		**Atenolol**		**Difference**		
Net energy%	15.1	7.9	16.9	8.1	-1.9	7.4	0.1281
Sep energy%	19.8	8.7	22.9	10.2	-3.1	8.1	**0.0232**
Peak %	16.5	9.7	18.9	14.3	-2.4	10.4	0.1691
	Nebivolol		**Atenolol**		**Difference**		
Net energy%	14.6	6.7	16.9	8.1	-2.3	7.6	0.0712
Sep energy%	21.6	8.7	22.9	10.2	-1.3	10.6	0.4479
Peak %	16	8.8	18.9	14.3	-2.8	11.7	0.1414

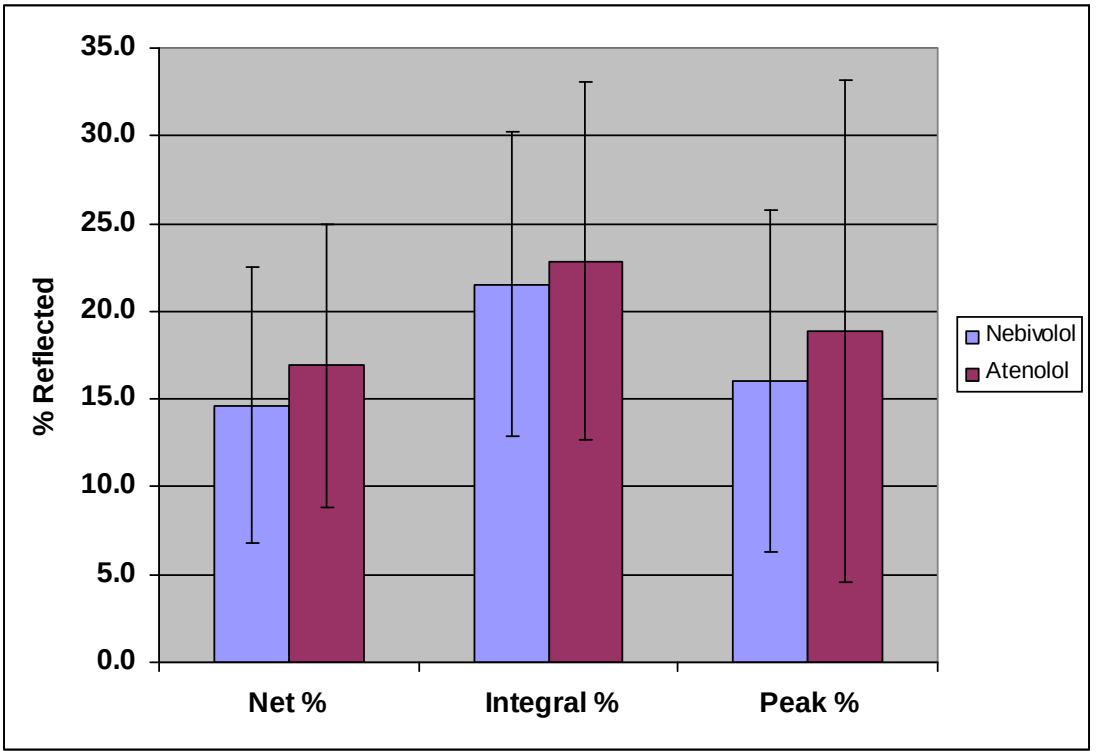

Figure 7.6: A bar graph showing the percentage of the forward compression wave (FCW) reflected during mid-systole with β-blockers nebivolol (blue) and atenolol (purple). Integral represents the energy carried by the separated waves.

7.4.6 The forward expansion wave: The FEW in the carotid artery was consistently seen to have a slow onset and a rapid increase in energy as seen in **Figure 7.7**. This observation is consistent with the two phases found in the aortic root data of both humans (chapter 5) and canines (chapters 3 and 4).

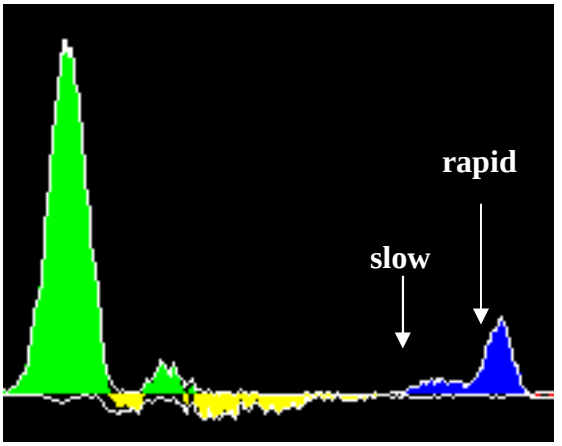

Figure 7.7: A typical wave intensity plot highlighting the slow and rapid stage of the forward expansion wave (FEW).

During atenolol treatment all FEW measurements were significantly smaller than those measured at baseline ($p<0.05$) as seen in Table 7.2. The net FEW was 34% (8892±4605J/m^2 vs. 5902±2504J/m^2) smaller than during baseline, the separated FEW energy was reduced by 38% (7216±3955J/m^2 vs. 4512±2116 J/m^2) and the peak value was 38% (292±154W/m^2 vs. 180±96W/m^2) smaller. During nebivolol treatment the net FEW was only 14% (8892±4605J/m^2 vs. 5902±2504J/m^2) smaller than baseline, the separated FEW energy was reduced by 19% (7216±3955J/m^2 vs. 5841±2344J/m^2) and the peak value was only 20% (292±154W/m^2 vs. 234±85W/m^2) smaller than baseline. All FEW measurements were not significantly smaller after Nebivolol treatment compared than those measured at baseline (**Table 7.2**). When comparing the effects of atenolol with nebivolol a significant difference is seen between FEW energy and peak (**Table 7.3**). From these results we can conclude that Nebivolol does not have any statistically significant effect on the generation of the FCW and FEW or significantly augment the BCW. While atenolol causes a significant reduction in the size of both forward waves and increases the percentage of reflection. These results are shown for representative traces from an individual in **Figure 7.8**. The backward compression wave (BCW) is not dimished after atenolol

treatment even though the forward compression wave (FCW) and forward expansion wave (FEW) are reduced.

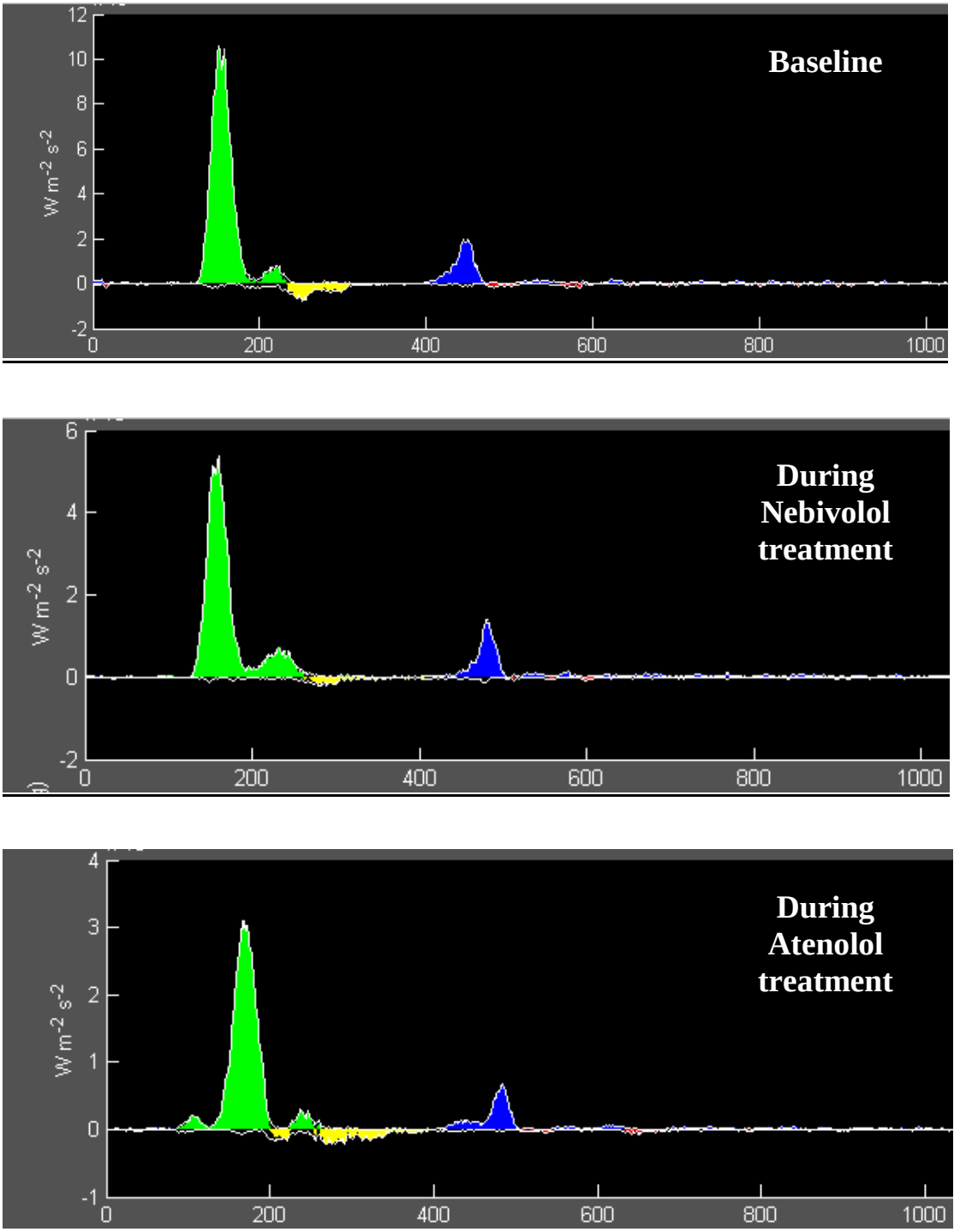

Figure 7.8: Carotid Wave Intensity plots at baseline and after both Nebivolol and Atenolol treatment. During Atenolol the forward waves diminish while the reflected wave remains the same size. Note the different scale of the Y-axis.

7.4.7 Wave timings

The times from the peak R wave of the QRS complex to the onset and peak of the three main waves were calculated after each scan. There was no significant difference observed in the FCW and BCW time to onset or peak between Nebivolol and Atenolol treatment. There is however a significant difference seen between the onset of the FEW: the FEW occurs an average of 16ms later after Atenolol.

Table 7.5 Average mean timings, plus standard deviation (SD) from the R of the QRS complex to the onset and peak times of each wave were calculated. **dIc+** = separated forward compression wave, **dIc- =**separated backward compression wave, **dIe+ =**separated forward expansion wave. **dIC+=** Net forward compression wave**,** **dIC-=** Net forward compression wave**, dIE+=** Net forward compression wave**,**

		Baseline (1)		**Nebivolol (2)**		**Atenolol (4)**			**P value**	
		mean	±SD	mean	±SD	mean	±SD	**1 vs 2**	**1 vs 4**	**2 vs 4**
dIc+ onset (ms)		106	18	113	16	113	16	**0.02**	**<0.01**	0.86
dIc+max (ms)		152	14	157	15	160	13	**0.02**	**<0.01**	0.08
dIc- onset (ms)		157	16	161	15	165	15	**0.02**	**<0.01**	0.48
dIc-max (ms)		209	23	218	27	221	22	**0.03**	**<0.01**	0.11
dIe+ onset (ms)		345	28	370	28	384	32	**<0.01**	**<0.01**	0.07
dIe+max (ms)		420	23	436	26	452	22	**<0.01**	**<0.01**	**<0.01**

7.5 Discussion:

Beta blockers are prescribed to decrease heart rate and cardiac output, leading to a reduction in blood pressure. In this investigation Atenolol and Nebivolol both successfully lowered blood pressure by similar magnitudes, however Atenolol reduced heart rate by two-fold compared to Nebivolol (7bpm Versus 14bpm). This may indicate that atenolol is causing more β-blockade than Nebivolol and closer analysis using wave intensity analysis shows that it carries some possibly disadvantageous effects compared with Nebivolol. Atenolol reduces the magnitudes of both the FCW and FEW. The FCW is linked to contractile function, while the FEW causes aortic flow deceleration, which aids aortic valve closure (Parker et al. 1988). The FEW is generated near end-systole when the LV long axis reaches its peak velocity of shortening (chapters 3,4 and 5) and its magnitude correlates with the rate of LV long axis deceleration. A reduction in the magnitude of this wave could have an adverse effect on flow deceleration at end-systole and could also have adverse implications for early diastolic function (Ohte et al. 2002). Additionally, and perhaps more importantly, Atenolol does not reduce the BCW magnitude despite significantly reducing the FCW magnitude. This indicates that a higher percentage of the FCW is reflected back towards the heart as shown in **Table 7.4** and **Figure 7.6**. The percentage of FCW reflected back is an important indicator of the state of the vasculature, and increased reflection is an indicator of downstream impedance mismatching resulting in reduced forward wave propagation and an increased backward load on the heart. This increased load results in the LV actually having to work harder at end-systole which may be detrimental to LV function. During chronic heart failure there is also a marked reduction in forward wave generation by the heart and an increased magnitude of reflected waves (Curtis et al. 2007). Impairing LV function to achieve lower blood pressure, while augmenting central pressure via large reflected waves is obviously not an ideal situation. In the Conduit Artery Function Evaluation (CAFE) substudy of ASCOT, the combination of atenolol and bendroflumethiazide was observed to be associated with higher central systolic and pulse pressure than the combination of amlodipine and perindopril despite similar brachial blood pressures (Williams et al. 2006). This is probably due to higher wave reflection in the atenolol/bendroflumethiazide group (Manisty et al. 2006) and has

been suggested to contribute to the adverse outcomes in those randomized to atenolol and bendroflumethiazide (Wilkinson et al. 2006).

It is interesting that Nebivolol had no significant effect on forward wave generation by the heart or wave reflection even though it was just as effective at reducing BP as Atenolol. This may be attributable to its vasodilator ability and/or its effects on arterial compliance resulting in better downstream impedance matching. Intra-arterial nebivolol causes forearm vasodilation in man by a mechanism that is blocked by NG-monomethyl L-arginine (LNMMA) an inhibitor of nitric oxide synthase (Cockcroft 1995). Nebivolol has also been reported to decrease pulse wave velocity (a measure of arterial stiffness) in vivo in sheep iliac artery (McEniery 2004) through a mechanism involving nitric oxide, an effect not shared by atenolol.

The vasodilator properties of nebivolol have caused some debate. Nebivolol is not classified as possessing intrinsic sympathomimetric activity (ISA) (Janssens et al. 1989, Brixius et al. 2001), but it has been suggested that Nebivolol may activate β3 adrenoceptors in endothelial cells (Gosgnach 2001). Agents with ISA can induced endothelial NO release (Kokoki et al. 1999) through activation of β2 adrenoceptors (Broeders et al. 2000) and/or ß-3 receptors (Ignaro 2004). Increased NO is generally thought to be beneficial in terms of cardiovascular disease, although this view has been questioned, (Schulman et al. 2006), but ISA agents have been found to be less effective at reducing morbidity and mortality (Cruickshank et al. 2007, Yusuf et al. 1985) and consequently the importance of vasodilation by beta blockers to cardiovascular outcomes remains uncertain.

Limitations:

Milligram for milligram nebivolol resulted in a lesser reduction of heart rate than atenolol. However the two drugs produced equivalent reductions in blood pressure (noticeable by equivalent reductions in 24 hour ambulatory blood pressure [data not shown]). The differential effects on heart rate are attributable to the combined method of action of nebivolol- part beta-blocker, part vasodilator. Although brachial blood pressure reductions are equivalent, the greater heart rate reduction by atenolol might confer a lesser reduction in central aortic blood pressure.

7.6 Conclusion

Non-invasive wave intensity analysis is a practical and valuable tool for evaluating the condition of both the LV and vasculature. Atenolol reduces blood pressure but is associated with diminishing LV function; unlike Nebivolol that appears to improve LV function while resulting in the same blood pressure drop. The new class of ß-blockers that do not induce vascular metabolic disturbances could be used as first-line therapy agents for patients with hypertension.

Chapter 8:
Final Discussion

8.1 Introduction

Ultrasound techniques have revolutionized our understanding of cardiac physiology in health and disease. The ability to provide detailed information on events during various phases of the cardiac cycle has enabled optimum management strategies for many different cardiac conditions over the past decade. Furthermore, studying cardiac physiology in the light of its anatomical basis is of immense importance in this respect. Efficient function of the LV is achieved by coherent behaviour of the two axes. Although time relations of the onset of long and minor axis shortening have been studied before (Jones et al. 1990) further details about their velocity relations was lacking. Little was known about the direct, detailed association between the long and minor axes and the product of overall ventricular systolic function i.e. aortic pressure and velocity events. Finally, potential relationships between mechanical ventricular function of the two axes and aortic waves studied by wave intensity analysis have not yet been reported. The aim of this thesis was to unite LV mechanics at end systole with the elemental forces of arterial flow.

8.2 The Left ventricle axes

The dynamic geometry of the LV has been explored since the 17th Century, (Woods 1892, Henderson 1906, Patterson et al., 1914 Wiggers and Katz 1921, Harvey 1928). During the second half of the last century the pattern of LV dimensional change throughout the cardiac cycle received much attention (Sandler 1974, Rankin et al. 1976) and the contribution of the LV long axis was recognised (Henein and Gibson, 1999). In this thesis it was seen that there is a degree of physiologically normal asynchrony between the two components of LV systolic function starting from the isovolumic contraction (IVC) stage. In the past the pattern of LV dimensional change during IVC has been a topic of debate but in human subjects it is now accepted that the long axis shortens as the minor axis lengthens creating a more spherical LV cavity (Rushmer 1956, Rankin et al. 1976, Jones et al. 1990, Oki et al. 1999). The canine results in chapters 3 and 4 do not agree with these findings. The results presented in this thesis show that during IVC the minor axis shortens 64% of the time and that the long axis lengthens 100% of the time. Several other investigators have reported a similar pattern (Peiper 1966, McDonald 1970, Rankin et al. 1976). Explanations for this discrepancy include inconsistent methodologies; the sequence of events are altered by both anaesthetised, open-chest experiments and varies depending on the precise animal preparation used (Rankin et al. 1976, Jones et al. 1999). There is

however no discrepancy that during IVC the term ‘isometric contraction’ could be exchanged with ‘asynchronous contraction’ as suggested by Rushmer (Rushmer 1955). The explanation behind this asynchronous activity lies in the evidence that myocardial fibres are excited in sequence.

Wall velocities are observed to be higher in the long axis than the minor axis during the isovolumic period. Suggesting that longitudinal fibres dominate over circumferential fibres in this early stage of systole (Oki et al. 1999). The results of the canine data in chapters 3 and 4 agree with this finding, even during proximal aortic occlusions. During ejection both axes undergo three stages of contraction: *acceleration* leading to a peak velocity of shortening followed by *steady deceleration* until a point in late ejection when the rate of *deceleration* further increases, identified by an inflection point in the velocity plot **Figures 3.8, 3.9** and **3.11.** The data presented in chapters 3, 4 and 6 shows that the times of minor and long axis peak velocity of shortening are not synchronous. The minor axis begins to slow ~30ms before the long axis in the dogs and up to ~30-50ms in humans. Minor axis peak velocity of shortening leads to aortic flow deceleration while long axis deceleration leads to aortic pressure decline. Normal long and minor axis asynchrony is implicit in supporting aortic pressure timings.

The peak velocity of shortening along the minor axes has previously been reported to be higher than that of the long axis; this is a scenario where the results of this thesis do comply. In 10 of 11 dogs the minor axis was seen to reach higher velocities during ejection. On the contrary the long axis was observed to reach higher velocities in the human Doppler data presented in chapter 6 however this is to be expected as annular velocities are higher than myocardial velocities (Pai et al. 1998). Due to the previous detection of higher velocities occurring in the minor axis combined with the abundance of larger circumferential fibres within the myocardial wall the minor axis has been understood to dominate during the ejection phase of systole (Streeter et al. 1969, Simone et al. 1997, Oki et al. 1999). The data in this thesis corroborates with the velocity of shortening findings and supports the concept of the minor axis controlling flow generation during ejection, as shown by the close correlation seen between peak aortic flow and peak velocity of minor axis shortening during both control and aortic occlusion conditions. Ejection events are determined by the normal relationship between the two contracting axes of the LV, long and minor axes that work concurrently. The minor axis has a pivotal role during ejection

however adequate ejection fraction is only achieved due to the combined action of both axes (Keith 1918, Henein and Gibson 1999). The long axis plays a rather vital role both during disease states such as hypertension and at end ejection as seen by using wave intensity analysis.

8.3 Wave intensity

8.3.1 The forward expansion wave and left ventricle long axis

Over the past 20 years wave intensity analysis has both introduced and explained numerous hemodynamic unknowns. One of the first and most important insights gained by using WIA was the observation of an unexpected large positive wave at the end of systole. This wave was seen to accompany a decrease in both aortic pressure and flow indicating that it is a forward expansion or 'decompression' wave (FEW). All previous investigations into the generation of this wave have suggested that it is the consequence of a reduced rate in myocardial shortening (Parker and Jones 1989, Sugawara 1997, Jones et al. 2002). This would make perfect mechanical sense; however like all aspects of LV function, LV shortening velocities are not straightforward. This thesis highlights some of the complexities of LV systolic velocities during IVC and ejection and leads one to believe that this description of FEW generation appears to be rather vague.

The findings in chapters 3, 4 and 6 show that a normal asynchrony exists between LV long and minor axes peak velocity of shortening. As the axes begin to slow at different periods of systole the FEW cannot be generated by the simultaneous onset of a reduced rate of shortening of both. During control conditions, in chapter 3, it was seen that the FEW has a slow onset followed by a rapid increase in energy as shown in **Figure 3.7**. The slow onset of the FEW corresponded with the maximum shortening velocity of the long axis in all beats of all dogs. The rapid increase in energy coincided with the minor and long axes inflection points that do occur simultaneously later in systole **Figure 3.15 and 3.17**. During thoracic, diaphragm, abdominal and iliac occlusions the relationships between the FEW stages and LV wall velocities remained robust as seen in chapter 4. In chapter 5 these relationships were investigated in human subjects. The slow onset of the FEW was detected as the last mitral annular segment begins to slow. The rapid increase coincided again, with a sudden change in the rate of wall deceleration in late systole generating a higher energy FEW. In chapter 3 the sudden change in LV deceleration in end-systole that

generates the rapid increase in FEW energy was suggested to be related to torsion mechanics of the LV during systole. During systole the LV apex and base rotate in opposite directions creating a twisting motion which is now known to play an integral part in normal cardiac function. (Burns et al 2008). Untwisting of the LV occurs before aortic valve closure during late systole in normal human hearts (Notomi 2006 and Borg et al. 2008.). This release of torsion in addition to the momentum of blood flowing out of the heart at this stage would create a rapid decrease in LV pressure which would result in the generation of a higher energy FEW. The rate of this release of torsion would also be predicted to correlate well with the magnitude of the FEW generated. In chapters 3 and 4, it was found that the rate of deceleration of the LV long axis during late systole (please refer to slope 3 in **Figure 3.19**) did influence the energy carried by the FEW. The strong correlations are seen during both control conditions, **Figure 3.21** and during all 4 occlusions as seen in **Figure 4.11**. The data in this thesis cannot prove that the inflection points observed on both LV axes are brought about by the release of torsion but it provides very strong evidence that the FEW rapid increase in energy is created by this sudden change in LV axes rate of shortening.

As mentioned in chapter 1, section 1.6.4 Sugawara et al. (1997) proposed that the FEW is generated due to the momentum of blood that causes blood to flow from the LV into the aorta while the LV remains contracted without actively forcing blood out. The data in this thesis show that the FEW is generated when the LV long axes begins to slow down, at this time the minor axis has already reached it's maximum velocity of shortening and has been decelerating for ~30ms. In a later paper by this group (Sugawara et al. 2009) they explain how the magnitude of the FEW is significantly reduced in patients with hypertrophic cardiomyopathy (HCM) (Sugawara et al. 2009). Niki et al. interestingly found that patients suffering with chronic mitral regurgitation (MR) also have absent or greatly reduced FEWs that actually appear again after valve replacement (Niki et al. 1999). This finding suggests that the LV somehow regains the ability to actively decelerate the flow after value replacement. As discussed above, in normal volunteers the LV begins to untwist during late systole, before aortic valve closure however in patients that suffer from the above conditions (MR and HCM) LV untwisting is delayed and does not occur until after aortic valve closure (Borg et al. 2008, Van Dalen et al. 2009). This knowledge in combination with the data in this thesis leads to the speculation that the FEW is always generated in

patients with both MR and HCM however the rapid increase in energy is inhibited due to the lack of a sudden decrease in LV pressure in late systole caused by LV untwisting. From the results in this thesis it is confirmed that previous assumptions regarding the generation of the FEW were essentially accurate: the FEW is indeed generated by a reduced rate in myocardial shortening. This study elaborates on this idea by providing evidence that a reduced rate in long axis myocardial shortening generates the wave, and that a further reduction late in systole induces a higher energy-carrying wave.

8.3.2 The backward compression wave and left ventricle minor axis

In the canine studies during control conditions (chapter 3) the arrival of the BCW at the LV in mid-systole coincided with the time that the LV minor axis reached its peak velocity of shortening. This could be a major coincidence however it could be suggested that the reflected wave's arrival may have an adverse effect on minor axis velocity of contraction. Further evidence for this mechanism was provided by the aortic occlusion data (chapter 4). During proximal occlusions the reflected wave was significantly larger, its time of arrival at the heart often changed and yet it still always coincided with time of minor axis maximum velocity of shortening. During thoracic occlusion the peak velocity of minor axis shorting was reduced by 20%. The minor axis is believed to play the major role during ejection; however increasing the load that the LV has to push against appears to slow the rate of radial shortening in canines. The long axis was relatively unaffected by the larger reflected waves generated during proximal occlusion as its peak velocity of shortening was only reduced by 11%. LV longitudinal myocardial fibres appear to have the ability to continue to generate force and shorten when opposed by mid-systolic reflections. In the human study described in chapter 6 minor and long axis wall velocities were compared between a normotensive group and hypertensive group. During ejection minor axis velocities were reduced by over 1cm/s in the hypertensive group (~20-30%) as shown in **Table 6.6,** while long axis velocities were unaffected (reduced by less than 3%). This data agrees favourably with that found in both the dog study and previous work (de Simone et al. 1997). In previous work it has been discovered that the minor axis is principally responsible for the majority of blood ejected during systole with the long axis responsible for 7% of the ejection fraction in normotensives. In a hypertensive group this percentage increases to a significantly

higher amount, 18% (de Simone et al. 1997). This increase in the long axis role could be attributed to the adverse effects of larger reflected waves on the minor axis during ejection. The augmented cardiac load slows the shortening velocity of the minor axis; the long axis has to overcompensate for this lack of minor axis work to retain an optimal ejection fraction. Reflected waves are clearly not desirable for optimal LV function as previously mentioned by Bleasale et al.: *"Systolic ventricular loading by early and accentuated wave reflections can result in LV hypertrophy and LV failure"* (Bleasdale et al. 2003).

8.4 Wave and reservoir hypothesis:

As mentioned in chapter 1, using original wave intensity theory creates several obstacles, one drawback of using the original analysis to separate pressure and flow is that during diastole self-cancelling waves are observed. This is explained in **Figure 1.8.** In recent years a newer analysis has been developed that first substitutes the aortic reservoir function before calculating the waves. By substituting the aortic reservoir pressure previous investigation have observed a marked reduction in the magnitude of the backward travelling pressure wave (Davies et al 2008). The results in this thesis agree that the BCW is markedly reduced after aortic reservoir subtraction; In control conditions the BCW measured in the canines was reduced by 93% (chapter 3, **Figure 3.23**), while that of the human data was very similar (74%, chapter 5, **Figure 5.14**). The BCW has previously been reported to disappear after subtracting the aortic reservoir however all analyses in this thesis found that although the BCW was indeed significantly reduced it was still always present especially during the canine proximal aortic occlusion study (chapter 4). This new hybrid reservoir-wave analysis could indeed enhance the mechanical relationship between the LV and the arteries even further in the future; however, substituting the aortic reservoir appears to have absolutely no effect on the mechanisms and relationships formed throughout this thesis in both canine and human hearts. Although the magnitude of the waves are altered by aortic reservoir subtraction the timing of the separated waves are not altered significantly and strong agreements are still found between the FEW and peak velocity of the long axis and the BCW and peak velocity of the minor axis.

8.5 Non-invasive wave intensity analysis, pharmacological manipulation and clinical relevance

Arterial stiffness and reflected waves are associated with numerous causes of morbidity and mortality. Not only do reflected waves increase the total load on the LV, increasing myocardial oxygen demand but the associated increase in central systolic pressure also increases the risk of subendocardial ischemia and stroke (Laurent et al. 2007). Better understanding of the pathophysiology of reflected waves is essential as they carry predictive values for these cardiovascular events. Although wave intensity is not yet habitually used in the non-research clinical environment the development of new non-invasive methods to analyse wave intensity will hopefully open the door to widespread use of this technique. One of the aims of this thesis was to use WIA to look into the effects of antihypertensive therapy with a beta blocker on arterial waves in man. In chapter 7 non-invasive wave intensity in the common carotid artery has been shown to be an easy and highly informative process. The results show that the effects of different beta-blockers noticeably vary and that it is imperative that therapies are specifically matched for each individuals needs. Nebivolol was shown to have less of an adverse effect on LV function compared to atenolol while producing the same blood pressure drop. Non-invasive wave intensity can not only inform one about the working state of the LV from the forward waves magnitudes in both early (FCW) and late systole (FEW), but also the state of the vasculature from the reflected waves magnitude (BCW). This method may also aid clinicians in diagnosis to ensure that each patient is receiving the appropriate therapy.

Recently Sugawara and colleagues have produced an enlightening review on the clinical usefulness of wave intensity (Sugawara et al. 2009). They give numerous examples of how non-invasive carotid wave-intensity measures can provide valuable quantitative information. The group have unpublished results on a reasonably large scale comparing non-invasively acquired carotid wave intensity values in 170 normal volunteers to patients with both dilated and hypertrophic cardiomyopathy. The data collected shows that patients with dilated hearts have significantly smaller FCWs when compared to normal volunteers. This is suggestive of a reduction in contractile function, most probably associated with thinning of the LV wall resulting in a reduction of Rushmers ‘initial ventricular impulse’. On the other hand, patients with hypertrophied hearts have significantly smaller FEWs. This signifies a reduction in the rapid LV pressure drop during late systole and the inability of the LV to actively

decelerate blood flow as effectively. This could perhaps be due to fibre disarray inducing delays in LV untwisting that could in turn reduce the rapid increase in energy of the FEW. Regardless of the mechanism behind FCW and FEW reduction, the studies show a need for the condition of the arterial system to regularly be evaluated in conjunction with cardiac function in the future. The expanding use of WIA in the future to study ventricular-aortic interactions is a very appealing thought.

Chapter 9:
Final Conclusions and Future Work

9.1 Conclusions:

This thesis has aimed to unravel the complicated relationship between LV function and the arterial system using wave intensity analysis as a hemodynamic index; there are 5 main findings:

1) During systole the LV long and minor axes reach peak velocities of shortening at different times. This normal long and minor axis asynchrony is implicit in supporting aortic pressure timing and hence stroke volume.

2) The FEW carries information about LV wall efficiency during late systole. This study highlights that the FEW has a slow onset followed by a rapid increase in energy. The slow onset is generated when the LV long axis begins to slow in both canines and humans. The rapid stage is generated later in systole when both LV axes alter their rate of shortening.

3) The BCW could have an adverse effect on LV ejection by increasing the load exerted on the LV and slowing the rate of contraction of the LV minor axis. In cases of enlarged reflections long axis shortening compensates for the lack of minor axis shortening to maintain an optimal ejection fraction.

4) The forward waves generated by the heart are significantly smaller in individuals receiving Beta-blocker Atenolol compared to Nebivolol. This suggests that Nebivolol has a more positive effect on cardiac performance while inducing a comparable blood pressure drop.

5) Non-invasive wave intensity analysis has real prognostic significance, widespread use of this technique in clinical settings could aid in the ideal, patient specific treatment.

9.2 Limitations

At the end of each chapter there are several detailed limitations to each study. Overall and in an ideal world the following measurements would have been ideal:

1) ***Canine study-Chapters 3 and 4*:** More than two pairs of ultrasound crystals would have been embedded into the myocardium. All dogs would have ideally had a third pairs of crystals added to measure the radial axis of the LV.

2) ***Human study-Chapter 5*:** LV minor axis TDI would have been measured along side long axis mitral annular measurements.

3) ***Non-invasive studies-Chapters 6 and 7:*** Chapter 6 lacks wave intensity measurements while chapter 7 lacks LV function measurements. Ideally both of these chapters would have contained both LV and carotid wave intensity measurements so that direct relationships could be seen between non-invasively measured LV minor axis shortening and the BCW and long axis shortening and the FEW during control and pharmacological intervention conditions.

4) All studies in this thesis had small study numbers and all patients also had 'normal' LV function: applying the same techniques to subjects with a variety of LV problems could test the robustness of the mechanisms found all the more.

5) Finally, TDI has limitations in both collecting and analysing the data. TDI is angle dependent and the velocities recorded are dependent on where the sample volume is placed. Mitral annular excursion is also influenced by adjacent myocardial segments. The software used in this thesis to measure the timings is not as accurate as more recent software found on newer ultrasound machines.

9.3 Future work

1) The ideal way to test the robustness of the mechanisms found in this thesis is the use of non-invasively or invasively acquired wave intensity measured simultaneously with LV function during both control and a variety of pharmacological interventions. Paying particular attention to the relationship between the arrival of the reflected wave and minor axis reduced rate of shortening.

2) New ultrasound machines allow LV function to be evaluated using more than just TDI measurements. Myocardial deformation can be calculated in 2-D obtained from B-mode speckle tracking images. Speckle tracking allows accurate assessment of tissue velocity, strain rate and strain in 2 orthogonal dimensions. Comparing myocardial deformation with the onset of the FEW would provide a significant advance in ultrasound assessment of cardiac structure and function. Speckle tracking can also measure LV rotation at the apex and base of the heart allowing the calculation of torsion. This new technology could reveal the true LV wall mechanics behind the rapid phase of the forward expansion wave mentioned in the final discussion.

3) More recently 3-D echocardiography been introduced which can provide new insights into the structure and function of the heart, especially at a regional level. The use of real-time 3-D echocardiography is the next step forward and will solve the shortcomings of all previous methods. 3-D echocardiography generates fast, reliable and reproducible results. Used in conjunction with real time 3-D imaging, speckle tracking could provide a comprehensive visualisation of both regional and global LV function in more than two axes in the future.

4) Exercise testing could be another alternative study: the simultaneous evaluation of LV function and arterial waves could provide additional information on ventricular-arterial interaction.

Abbreviation	Meaning
A	Tissue Doppler imaging acquired wave during atrial contraction
A	Abdominal occlusion
AP_i	Inflection point on the left ventricle anterior-posterior wall axis velocity of shortening plot
AP_{maxU}	Maximum shortening velocity of the left ventricle anterior-posterior axis
AVC	Aortic valve closure
AVO	Aortic valve opening
BCW	Backward compression wave
BP	Blood pressure
C	Arterial compliance
c	Wave speed
CCC	Lin's concordance correlation coefficient
CVD	Cardiovascular disease
CW	Continuous wave Doppler
d	Diameter
D	Diaphragm occlusion
dI	Wave intensity
dI+C	Net forward compression wave
dI_{+c}	Separated forward compression wave
dI+E	Net forward expansion wave
dI_{+e}	Separated forward expansion wave
dI_{+e1}	Slow onset of forward expansion wave
dI_{+e2}	Rapid increase in energy of the forward expansion wave
dI-C	Net backward compression wave
dI_{-c}	Separated backward compression wave
dP	The 1st derivative of pressure
dP/dt	The 1st derivative of aortic pressure with respect to time
dP_{LV}	Left ventricle pressure derivative with respect to time
dt	The 1st derivative of time
dU	The 1st derivative of velocity
dU/dt	The 1st derivative of aortic velocity with respect to time
E	Young's modulus
E wave	Tissue Doppler imaging acquired wave during rapid filling
ECG	Electrocardiogram
EF	Ejection fraction
FCW	Forward compression wave
FEW	Forward expansion wave
h	Wall thickness
HCM	Hypertrophic cardiomyopathy
HR	Heart rate
I	Iliac occlusion
IVC	Isovolumic contraction
IVR	Isovolumic relaxation
L	length/distance
L	Left ventricle long axis (base to apex)
LA	Left atrium
L_i	Inflection point on the left ventricle long axis velocity of shortening plot
L_{maxU}	Maximum shortening velocity of the left ventricle long axis
LV	Left ventricle
LVH	Left ventricle hypertrophy

M	Left ventricle minor axis (septum to free wall)
MA1	Left ventricle mid-level anterioseptal myocardial segment
MA2	Left ventricle mid-level inferiolateral myocardial segment
$\mathbf{M_i}$	Inflection point on the left ventricle minor axis velocity of shortening plot
$\mathbf{M_{maxU}}$	Maximum shortening velocity of the left ventricle minor axis
MR	Mitral regurgitation
ODE	Ordinary differential equation
P	Pressure
P wave	Atria electrical activation
Pb	Backward pressure
PDE	Partial differential equation
$\mathbf{P_{ex}}$	Excess/ wave only pressure
$\mathbf{P_f}$	Forward pressure
$\mathbf{P_{LV}}$	Left ventricle pressure
$\mathbf{P_{max}}$	Peak pressure
PU-Loop	Pressure-Velocity loop
PVR	Peripheral vascular resistance
PW	Pulsed wave Doppler
PWK	Reservoir pressure
Q	Flow
QRS	Electrical activation of the ventricles
R	Resistance
r	Radius
R	Riemann invariant
r	Pearson's correlation coefficient
RA	Right atrium
Reflection	Backward compression wave (only in this thesis is this always the case)
RV	Right ventricle
S or A	Cross-sectional area
S1	Tissue Doppler imaging acquired wave during isovolumic contraction
S2	Tissue Doppler imaging acquired wave during ejection
STE	Speckle tracking echocardiography
t	time
T	Thoracic occlusion
T wave	Depolarisation of the ventricles
TDI	Tissue Doppler Imaging
U	Velocity
$\mathbf{U_f}$	Forward velocity
$\mathbf{U_f}$	Backward velocity
$\mathbf{U_i}$	Inflection point on the velocity wave form
$\mathbf{U_{max}}$	Peak velocity
V	Volume
W/m2	Energy flux per unit area
WIA	Wave Intensity Analysis
wk	Windkessel
x	space
X wave	Forward expansion wave found in the carotid artery
Z	Arterial impedance

Appendices

Appendix 3.1: Individual average velocities and timings of all long and minor axes movement during ejection.

Dog	AVO (s)	Minor axis onset (s)	Long axis onset (s)	M_{maxU} (t)	L_{maxU} (t)	M_{maxU} (m/s)	L_{maxU} (m/s)	M_i	L_I
1	0.067	0.06	0.094	0.0745	0.1552	-0.011	-0.008	0.203	0.203
2	0.053	0.046	0.077	0.1071	0.1776	-0.01	-0.01	0.174	0.174
3	0.086	0.065	0.122	0.1047	0.1226	-0.014	-0.005	0.208	0.235
4	0.036	0.047	0.058	0.2174	0.139	-0.017	-0.009	0.184	0.186
5	0.055	0.058	0.103	0.1065	0.15432	-0.009	-0.006	0.214	0.214
6	0.073	0.066	0.113	0.0993	0.1318	-0.02	-0.005	0.193	0.191
7	0.04	0.028	0.074	0.0917	0.1143	-0.02	-0.009	0.160	0.159
8	0.019	0.022	0.045	0.0897	0.1285	-0.02	-0.024	0.181	0.178
9	0.051	0.044	0.058	0.1036	0.163	-0.017	-0.015	0.195	0.186
10	0.059	0.05	0.089	0.0886	0.1677	-0.019	-0.007	0.175	0.175
11	0.058	0.072	0.099	0.1318	0.1614	-0.011	-0.006	0.187	0.189
Mean	**0.054**	**0.051**	**0.085**	**0.110**	**0.147**	**-0.015**	**-0.009**	**0.189**	**0.190**
±SD	**0.018**	**0.016**	**0.025**	**0.04**	**0.02**	**0.004**	**0.005**	**0.02**	**0.02**

Appendix 3.2: Timings of individual hemodynamic events during ejection

Dog	dI_{-c}	U_{max}	dI_{-C}	dI_{+e1}	P_f	U_f	Plv	dI_{+e2}	P_{max}	U_i	
1	0.0495	0.0794	0.135	0.1652	0.18108	0.1809	0.152	0.202	0.202	0.205	
2	0.12365	0.136	0.124	0.1846	0.1821	0.182	0.147	0.179	0.184	0.175	
3	0.0996	0.1238	0.168	0.1295	0.1395	0.1395	0.192	0.214	0.263	0.209	
4	0.2028	0.2274	0.1	0.134	0.1291	0.1291	0.1	0.185	0.182	0.183	
5	0.0582	0.1017	0.126	0.1488	0.1342	0.1341	0.145	0.221	0.204	0.22	
6	0.1089	0.1242	0.139	0.1324	0.127	0.127	0.152	0.194	0.191	0.19	
7	0.1067	0.1023	0.111	0.1093	0.1043	0.1043	0.123	0.157	0.158	0.163	
8	0.0745	0.0894	0.09	0.1335	0.1334	0.1334	0.115	0.178	0.173	0.177	
9	0.1137	0.1156	0.118	0.163	0.158	0.158	0.138	0.194	0.196	0.199	
10	0.1081	0.133	0.134	0.1677	0.1689	0.1689	0.153	0.182	0.182	0.176	
11	0.1292	0.1442	0.122	0.1674	0.182	0.1809	0.163	0.191	0.178	0.194	
Mean	**0.107**	**0.125**	**0.124**	**0.149**	**0.149**	**0.149**	**0.144**	**0.191**	**0.192**	**0.190**	
±SD	**0.041**	**0.039**	**0.021**	**0.023**	**0.027**	**0.027**	**0.025**	**0.018**	**0.027**	**0.017**	

Appendix: 4.1: Wave speed (c) measured using the PU-loop method before and during thoracic, diaphragm, abdominal and iliac occlusions.

	c (m/)s BEFORE OCCLUSION	**c (m/s) DURING OCCLUSION**	**Difference**	**% Change**
T1	6.2713	9.4435	3.1722	50.58%
T3	5.1187	9.9831	4.8644	95.03%
T4	6.0197	13.7126	7.6929	127.80%
T5	4.8698	7.0707	2.2009	45.19%
T6	6.9205	14.4653	7.5448	109.02%
T7	4.4774	8.4591	3.9817	88.93%
T8	3.7698	6.1916	2.4218	64.24%
T9	5.8057	17.5966	11.7909	203.09%
T10	7.383	11.5494	4.1664	56.43%
T12	9.1369	11.5115	2.3746	25.99%
Average	**5.98m/s**	**11m/s**	**5.02m/s**	**83.95%**
±SD	**±5.64m/s**	**±7.51 m/s**	**±1.87 m/s**	
D1	5.6372	7.5075	1.8703	33.18%
D2	5.5346	6.894	1.3594	24.56%
D3	4.1995	4.092	-0.1075	-2.56%
D4	5.3382	7.7795	2.4413	45.73%
D5	4.1312	4.2876	0.1564	3.79%
D6	7.2864	7.4275	0.1411	1.94%
D7	5.3853	5.4568	0.0715	1.33%
D8	4.7997	6.2902	1.4905	31.05%
D9	6.6259	7.0638	0.4379	6.61%
D10	5.2525	4.71919	-0.53331	-10.15%
D12	5.2793	5.2397	-0.0396	-0.75%
Average	**5.41m/s**	**6.07m/s**	**0.66m/s**	**12.20%**
±SD	**±0.93 m/s**	**±1.36 m/s**	**±0.96 m/s**	
A1	5.3348	5.4126	0.0778	1.46%
A2	4.6747	4.7988	0.1241	2.65%
A3	4.6537	5.2457	0.592	12.72%
A4	5.5048	4.4974	-1.0074	-18.30%
A5	4.1261	3.4358	-0.6903	-16.73%
A6	9.0347	7.8137	-1.221	-13.51%
A7	5.6432	4.8449	-0.7983	-14.15%
A8	5.6985	4.3436	-1.3549	-23.78%
A12	6.4887	6.7463	0.2576	3.97%
Average	**5.68m/s**	**5.24m/s**	**-0.45m/s**	**-7.75%**
±SD	**±1.44 m/s**	**±1.32 m/s**	**±0.72 m/s**	
I1	5.4019	5.0165	-0.3854	-7.13%
I3	4.6603	4.8821	0.2218	4.76%
I4	5.0761	5.2093	0.1332	2.62%
I5	3.892	4.5064	0.6144	15.79%
I7	5.5686	6.9831	1.4145	25.40%
I8	4.4177	4.6028	0.1851	4.19%
I9	5.4305	5.9895	0.559	10.29%
I10	5.3745	5.4093	0.0348	0.65%
I12	6.713	5.1959	-1.5171	-22.60%
Average	**5.17m/s**	**5.31m/s**	**0.14m/s**	**2.71%**
±SD	**±0.80 m/s**	**±0.77 m/s**	**±0.80 m/s**	

Appendix 4.2: Average wave magnitudes during control and all four occlusions both before and after aortic reservoir subtraction. Proximal occlusion reduces the magnitude of the forward waves and augments the magnitude of the BCW. After reservoir subtraction the energy carried by the FCW and BCW are reduced while that of the FEW increases.

	CONTROL	**THORACIC OCCLUSION**		**DIAPHRAGM OCCLUSION**		**ABDOMINAL OCCLUSION**		**ILIAC OCCLUSION**	
	(J/m^2)	Original WIA (J/m^2)	After reservoir subtraction (J/m^2)	Original WIA (J/m^2)	After reservoir subtraction (J/m^2)	Original WIA (J/m^2)	After reservoir subtraction (J/m^2)	Original WIA (J/m^2)	After reservoir subtraction (J/m^2)
FCW	295±198	232±209	159±132	147±70	111±54	285±218	186±171	273±210	187±121
BCW	-42±13	-213±40	-14±10	-91±52	-36±19	-46±22	-26±13	-38±21	-10±7
FEW	120±57	78±64	98±28	51±26	58±32	107±66	113±52	127±59	139±54

Appendix 4.3: Individual times to peak aortic flow ($\mathbf{U_i}$), peak aortic pressure ($\mathbf{P_{max}}$), the rapid increase in energy of the FEW both before ($\mathbf{dI_{e+2}}$)and after aortic reservoir subtraction (Wk$\mathbf{dI_{e+2}}$) and the inflection points of both axes (M_i, $\mathbf{L_i}$) . All events occur simultaneously.

	$\mathbf{U_i}$	$\mathbf{P_{max}}$	$\mathbf{dI_{+e2}}$	Wk$\mathbf{dI_{+e2}}$	M_i	L_i
Thoracic	0.181	0.184	0.185	0.181	0.171	0.176
	0.212	0.219	0.219	0.219	0.214	0.228
	0.191	0.191	0.195	0.195	0.190	0.188
	0.229	0.229	0.229	0.229	0.222	0.229
	0.175	0.175	0.175	0.176	0.172	0.176
	0.170	0.200	0.185	0.170	0.170	0.170
	0.208	0.212	0.203	0.212	0.208	0.203
	0.156	0.176	0.176	0.157	0.156	0.157
	0.225	0.226	0.226	0.226	0.218	0.218
	0.196	**0.204**	**0.201**	**0.198**	**0.194**	**0.196**
	0.027	**0.021**	**0.022**	**0.028**	**0.025**	**0.028**
Diaphragm	0.187	0.204	0.200	0.196	0.186	0.186
	0.194	0.203	0.203	0.203	0.198	0.198
	0.215	0.215	0.215	0.211	0.207	0.215
	0.198	0.203	0.203	0.203	0.202	0.194
	0.308	0.303	0.307	0.307	0.293	0.293
	0.219	0.222	0.219	0.220	0.214	0.219
	0.173	0.174	0.173	0.168	0.166	0.163
	0.204	0.203	0.205	0.205	0.199	0.207
	0.217	0.217	0.218	0.212	0.201	0.201
	0.182	0.183	0.182	0.182	0.173	0.187
	0.220	0.201	0.194	0.190	0.182	0.190
	0.211	**0.212**	**0.211**	**0.209**	**0.202**	**0.205**
	0.036	**0.033**	**0.035**	**0.036**	**0.034**	**0.033**
Abdominal	0.176	0.172	0.176	0.176	0.167	0.172
	0.169	0.170	0.169	0.169	0.164	0.169
	0.206	0.202	0.206	0.206	0.200	0.206
	0.150	0.145	0.148	0.148	0.150	0.150
	0.258	0.258	0.258	0.258	0.250	0.258
	0.178	0.199	0.184	0.178	0.193	0.194
	0.160	0.155	0.155	0.155	0.150	0.160
	0.169	0.159	0.169	0.169	0.159	0.163
	0.178	0.178	0.178	0.178	0.178	0.178
	0.182	0.182	0.182	0.178	0.177	0.177
	0.170	0.166	0.170	0.170	0.177	0.174
	0.181	**0.180**	**0.181**	**0.180**	**0.179**	**0.182**
	0.029	**0.031**	**0.030**	**0.030**	**0.029**	**0.030**
Iliac	0.214	0.210	0.218	0.218	0.220	0.214
	0.212	0.216	0.227	0.227	0.202	0.202
	0.166	0.175	0.174	0.174	0.159	0.169
	0.189	0.184	0.207	0.207	0.218	0.228
	0.171	0.166	0.171	0.171	0.171	0.171
	0.203	0.193	0.203	0.203	0.193	0.203
	0.182	0.182	0.182	0.182	0.172	0.177
	0.182	0.182	0.182	0.182	0.177	0.182
	0.210	0.200	0.210	0.210	0.210	0.206
	0.192	**0.190**	**0.197**	**0.197**	**0.191**	**0.195**
	0.018	**0.016**	**0.020**	**0.020**	**0.022**	**0.021**

Appendix 4.4: Wave speed calculated using the PU-Loop method before and after reservoir subtraction during control conditions and each occlusion. T=thoracic, D=diaphragm, A=abdominal and I=iliac

Dog	**BEFORE**				**DURING**			
	Original	Reservoir subtracted	Difference	% difference	Original	Reservoir subtracted	Difference	% Difference
T1	6.2713	5.5067	-0.7646	-12.19	9.4435	6.1967	-3.2468	-34.38
T3	5.1187	4.9434	-0.1753	-3.42	9.9831	7.5571	-2.426	-24.30
T4	6.0197	4.7959	-1.2238	-20.33	13.7126	7.1123	-6.6003	-48.13
T5	4.8698	4.5341	-0.3357	-6.89	7.0707	4.9778	-2.0929	-29.60
T7	4.4774	4.1084	-0.369	-8.24	8.4591	5.2188	-3.2403	-38.31
T8	3.7698	3.1821	-0.5877	-15.59	6.1916	2.0721	-4.1195	-66.53
T9	5.8057	4.3452	-1.4605	-25.16	17.5966	10.7542	-6.8424	-38.88
T10	7.383	6.6365	-0.7465	-10.11	11.5494	6.6692	-4.8802	-42.26
T12	9.1369	8.8213	-0.3156	-3.45	11.5115	7.5481	-3.9634	-34.43
Average	**5.87**	**5.21**	**-0.66**	**-11.24**	**10.61**	**6.46**	**-4.16**	**-39.21**
±SD	**1.62**	**1.66**	**0.44**	**27.16**	**3.51**	**2.35**	**1.68**	
D1	5.6372	4.2553	-1.3819	-24.51	7.5075	3.2569	-4.2506	-56.62
D2	5.5346	4.6091	-0.9255	-16.72	6.894	4.2602	-2.6338	-38.20
D3	4.1995	4.1494	-0.0501	-1.19	4.092	3.436	-0.656	-16.03
D4	5.3382	3.7688	-1.5694	-29.40	7.7795	3.2682	-4.5113	-57.99
D5	4.1312	3.2246	-0.9066	-21.95	4.2876	3.159	-1.1286	-26.32
D6	8.9194	8.3203	-0.5991	-6.72	7.4275	5.3624	-2.0651	-27.80
D7	5.3853	4.7907	-0.5946	-11.04	5.4568	4.138	-1.3188	-24.17
D8	4.7997	4.2655	-0.5342	-11.13	6.2902	5.0535	-1.2367	-19.66
D9	6.6259	5.7774	-0.8485	-12.81	7.0638	4.173	-2.8908	-40.92
D10	5.2525	4.4724	-0.7801	-14.85	4.71919	3.342	-1.37719	-29.18
D12	6.272	5.6974	-0.5746	-9.16	5.2397	3.7833	-1.4564	-27.80
Average	**5.65**	**4.85**	**-0.8**	**-14.16**	**6.07**	**3.93**	**-2.14**	**-35.26**
±SD	**1.32**	**1.37**	**0.42**	**31.82**	**1.36**	**0.75**	**1.29**	
A1	5.3348	4.6019	-0.7329	-13.74	5.4126	4.9041	-0.5085	-9.39
A2	4.6747	3.5521	-1.1226	-24.01	4.7988	3.5651	-1.2337	-25.71
A3	4.6537	4.3274	-0.3263	-7.01	5.2457	5.0865	-0.1592	-3.03
A4	5.5048	3.9222	-1.5826	-28.75	4.4974	3.2512	-1.2462	-27.71
A5	4.1261	3.8777	-0.2484	-6.02	3.4358	2.7771	-0.6587	-19.17
A6	9.0347	8.0919	-0.9428	-10.44	7.8137	7.7271	-0.0866	-1.11
A7	5.6432	5.8701	0.2269	4.02	4.8449	4.3917	-0.4532	-9.35
A8	5.6985	5.2078	-0.4907	-8.61	4.3436	4.4033	0.0597	1.37
A12	6.4887	6.1397	-0.349	-5.38	6.7463	6.2475	-0.4988	-7.39
Average	**5.68**	**5.07**	**-0.619**	**-10.90**	**5.24**	**4.71**	**-0.53**	**-10.11**
±SD	**1.44**	**1.45**	**0.54**	**37.50**	**1.32**	**1.54**	**0.46**	
I1	5.4019	4.0043	-1.3976	-25.87	5.0165	3.7371	-1.2794	-25.50
I3	4.6603	4.5245	-0.1358	-2.91	4.8821	4.7365	-0.1456	-2.98
I4	5.0761	3.2557	-1.8204	-35.86	5.2093	3.5094	-1.6999	-32.63
I5	3.892	3.8351	-0.0569	-1.46	4.5064	4.3318	-0.1746	-3.87
I7	5.5686	5.0926	-0.476	-8.55	6.9831	6.4125	-0.5706	-8.17
I8	4.4177	3.8188	-0.5989	-13.56	4.6028	4.1708	-0.432	-9.39
I9	5.4305	4.7636	-0.6669	-12.28	5.9895	5.7466	-0.2429	-4.06
I10	5.3745	4.7104	-0.6641	-12.36	5.4093	4.7707	-0.6386	-11.81
I12	6.713	6.4279	-0.2851	-4.25	5.1959	4.1202	-1.0757	-20.70
Average	**5.17**	**4.49**	**-0.68**	**-13.15**	**5.31**	**4.62**	**-0.7**	**-13.18**
±SD	**0.8**	**0.93**	**0.58**	**72.50**	**0.77**	**0.94**	**0.54**	

Appendix 5.1: Patient Information sheet

KENSINGTON, CHELSEA & WESTMINSTER HEALTH AUTHORITY

PATIENT INFORMATION

WAVE INTENSITY ANALYSIS: A NEW APPROACH TO CORONARY HAEMODYNAMICS

What is the purpose of this study?

This study will use new techniques only recently developed to study blood flow within the arteries of the heart to see how this is affected by diseases.

Why have I been chosen?

You are already scheduled, for your own benefit, for coronary angiography and/or angioplasty for investigation and treatment of your cardiac symptoms.

What will the angiogram/angioplasty entail?

This involves applying a small amount of local anaesthetic into the skin and a small plastic tube being inserted into either the leg or arm. Following identification of each coronary blood vessel, a small amount of dye is injected and X-ray pictures being taken. This shows if the arteries are narrowed.

What additional procedure will the research involve?

It will involve making some extra measurements during the angiography procedure by using a tiny additional probe introduced into the coronary artery to measure pressure and flow. It will lengthen your procedure by about 5 minutes (the procedure length itself varies very much between patients, typically between 30 minutes and 2 hours). It will not prevent any treatment from being carried out.

Are there any risks?

You have already had the risks of the angiogram/angioplasty explained to you. In addition to these there is a very small risk that the tiny probe used to measure the pressure may cause some damage to the arterial wall.

If damaged what treatment will I receive?

In the event of any damage occurring to the arterial wall at any stage of the procedure, a small metal framework (Stent) will be inserted into the artery to close the hole.

What are the benefits?

On top of the information we obtain from the coronary angiogram, the pressure tracings may help us to identify problems in your coronary circulation independent from those seen by the angiogram. This may lead to changes in your medications.

Will my taking part in the study be kept confidential?

Yes, your records will be kept strictly confidential by your doctors and the research team.

What will happen to the results of the research study?

The additional information will be analysed and may help us to understand differences in blood flow to the heart independent of coronary artery disease. This may go onto be published in scientific journals.

Who has reviewed the study?

Hospital ethics committee.

Do I have to take part?

You are under no obligation to agree to have these extra measurements. Even if you initially agree to participate in the study, you remain free to withdraw at any time. If you decide not to participate or to withdraw from the study, this will not affect the medical care you receive.

Appendix 5.2 : Patient Consent Form

KENSINGTON & CHELSEA AND WESTMINSTER HEALTH AUTHORITY
ST MARY'S LOCAL RESEARCH ETHICS COMMITTEE

CONSENT FORM

AGREEMENT TO PARTICIPATE IN RESEARCH PROJECT

I, (name of subject) ……...

Of (address) ……

Agree to take part (or agree that my child/ward may take part in the research project:

WAVE INTENSITY ANALYSIS: A NEW APPROACH TO CORONARY HAEMODYNAMICS

I confirm that the nature and demands of the research have been explained to me and I understand and accept them. I understand that my consent is entirely voluntary and that I may withdraw from the research project if I find that I am unable to continue for any reason and this will not affect my medical care.

Signed: ……. Print Name: …….

Witness: …….. Print Name: ……

Date: ……..

Investigator's Statement:
I have explained the nature, demands and foreseeable risks of the above research to the subject:

Signature: ……. Date: ……. 2002

Appendix 5.3 Individual long axis peak velocities values during systole measured from 5 mitral annular segments. The septal, lateral and inferior walls are relatively uniform while the anterior wall reaches lower velocities and the posterior wall reaches higher shortening velocities during systole

.

Subject	Septum (cm/s)	Lateral (cm/s)	Inferior (cm/s)	Anterior (cm/s)	Posterior (cm/s)
N1	7.240	7.300	7.833	5.850	8.200
N2	7.940	8.310	8.210	7.373	9.083
N3	7.480	7.530	7.087	5.057	7.120
N4	7.207	7.040	7.273	7.140	8.373
N5	7.437	7.473	7.573	7.840	7.940
N6	7.707	7.207	7.080	7.440	8.130
N7	7.510	7.570	7.093	7.570	8.747
N8	9.013	9.550	9.317	7.413	10.957
N9	7.570	8.040	7.080	7.003	9.247
N10	7.027	6.890	7.307	4.723	7.473
N11	8.073	8.643	7.337	7.337	7.663
Average	**7.655**	**7.778**	**7.563**	**6.795**	**8.448**
±SD	0.546	0.795	0.684	1.072	1.057

Appendix 5.4: Calculated aortic wave speeds for each subject before and after aortic reservoir subtraction. Wave speed is always reduced after aortic reservoir subtraction.

Subject	c (m/s) Before	c (m/s) After	Difference (m/s)	% change
N1	10.65	7.01	-3.64	-34
N2	6.88	4.79	-2.09	-30
N3	10.63	7.86	-2.77	-26
N4	8.25	6.90	-1.35	-16
N5	3.35	2.49	-0.85	-25
N6	6.81	5.39	-1.41	-21
N7	7.83	6.45	-1.38	-18
N8	6.54	4.26	-2.28	-35
N9	9.15	6.63	-2.52	-28
N10	3.94	2.70	-1.24	-31
N11	7.14	4.98	-2.17	-30
Average	**7.378**	**5.407**	**-1.971**	**-26.727**
±SD	**2.341**	**1.764**	**0.818**	**6.246**

Appendix 5.5: Individual time intervals between the R of the QRS complex and the onset of the FEW both before and after aortic reservoir subtraction in addition to the time interval to peak systolic

Subject	FEW onset (ms)	Peak S2 (ms)	FEW onset after reservoir subtraction(ms)
N1	273	240	268
N2	267	230	261
N3	199	216	189
N4	197	206	179
N5	263	261	276
N6	251	261	236
N7	228	222	211
N8	261	253	261
N9	272	281	251
N10	249	274	270
N11	322	302	314
Average	**253**	**250**	**247**
±SD	**35**	**30**	**40**

Appendix 5.6: Individual time intervals between the R of the QRS complex and the rapid increase in energy of the FEW and the onset of slope 3 on the TDI systolic wave.

Subject	FEW rapid increase (ms)	Slope 3 onset (ms)	Difference (ms)
N1	329	355	-26
N2	339	365	-26
N3	345	340	5
N4	361	345	16
N5	361	365	-4
N6	348	350	-2
N7	413	420	-7
N8	355	372	-17
N9	425	407	18
N10	333	343	-10
N11	335	341	-6
Average	**359**	**364**	**-5**
±SD	**32**	**27**	**15**

Appendix 6.1: PICCOLA study protocol

Ploglitazone on Cardiac funCtiOn and Large Arteries (PICCOLA STUDY)
Protocol: EU-IIT-006

Outline of proposed study

The study will be conducted at the International Centre for Circulatory Health, St Mary's Hospital, London, UK. 24 subjects with type 2 diabetes mellitus will be recruited. Subjects with known coronary heart disease, uncontrolled hypertension (i.e. >160 mmHg systolic or >95 diastolic), systolic dysfunction (ejection fraction <50%), heart valve disease, proliferative or pre-proliferative retinopathy, severe hepatic or renal impairment, possible pregnancy, malignancy or receiving insulin therapy will be excluded. Subjects will be receive pioglitazone (45 mg/day) or placebo in addition to current therapy for 12 weeks in a crossover protocol using a prospective, randomized, double blind design following a run-in period $\geq$ 1 week with a 2 week washout period. Measurements will be made at the start and at the end of each crossover period (M1 - M4 in Figure 1).

Standard echocardiographic measures of left ventricular function and long and short axis TDI will be performed using an ATL HDI 5000 ultrasound system and digital cineloops recorded for offline analysis. Carotid blood flow velocity will be measured using pulsed Doppler ultrasound with an ATL HDI 5000 ultrasound system and carotid blood pressure measured using applanation tonometry. Wave intensity analysis will be performed using custom written software as previously described. In addition, at baseline (visit R) fasting blood samples will be drawn for lipids (total cholesterol, HDL cholesterol, triglyceride), glucose, creatinine, liver function tests and HbA1c. At completion of each limb of the crossover study measurements of fasting glucose, liver function tests and HbA1c will be repeated.

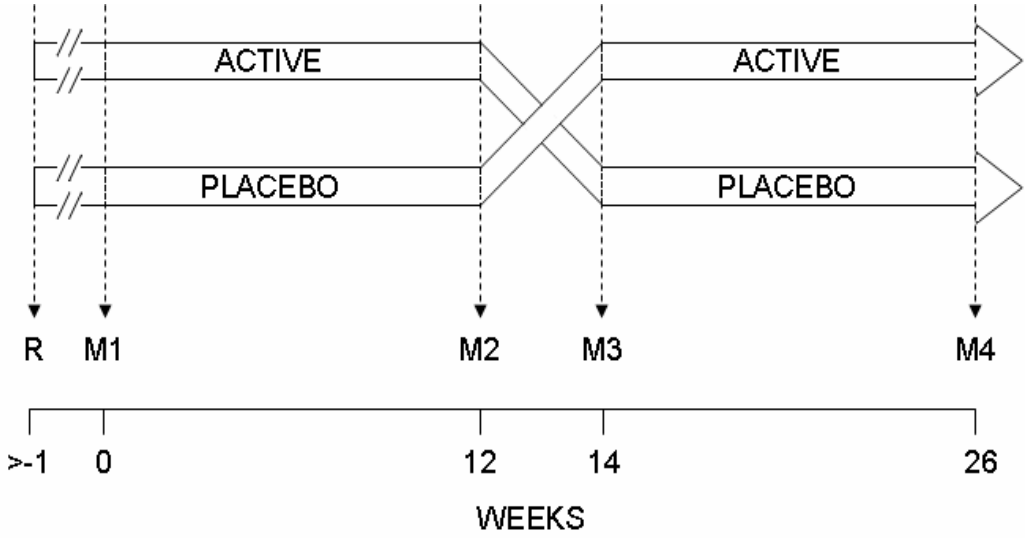

Figure 1. Study design. R = recruitment and consent, M1 – M4 = measurements.

Analysis and Statistics

Sample size estimates are based on published data[15] and additional unpublished data from our group. The primary TDI endpoints will be E´ and E/E´ ratio, a relatively preload independent measure of left ventricular filling pressure.[24] In wave intensity studies the major wave peaks (the systolic compression wave (a measure of LV systolic function), the expansion wave (a measure of LV diastolic function) and the reflected wave (measure of the arterial reflections) and wave speed (a measure of arterial stiffness)[22] will be measured. Data will be analysed using analysis of variance to look for treatment*period interaction and if absent treatment groups (placebo vs. active treatment) will be compared using a paired t-test; if there is evidence of carry-over, analysis will be performed on data from only the initial phase prior to washout..

Appendix 6.2: PICCOLA PARTICIPANT CONSENT FORM
The effect of pioglitazone on cardiac and large artery function (PICCOLA Study)

The participant should complete the whole of this sheet him or herself

(please tick each statement if it applies to you)

I have read the Information Sheet (version __ .__) ☐

I have been given the opportunity to ask questions and discuss this study ☐

I have received satisfactory answers to all my questions ☐

I have received enough information about this study ☐

This study has been explained to me by: Prof/Dr/Nurse _____

I understand that I am free to withdraw from the study at any time without having to give a reason for withdrawing and without affecting my future medical care. ☐

I agree to take part in this study, to be contacted for follow up and blood samples to be stored for later analysis. ☐

I consent for my medical records to be reviewed by authorised personnel and that confidentiality will be maintained ☐

I consent to the test results being sent to my GP ☐

I understand that information held by the NHS and records maintained by the General Register Office may be used to keep in touch with me and follow up my health ☐

Women only:

I confirm that I am not pregnant and will use a reliable contraceptive for the duration of the study if appropriate. ☐

Signed ……. Date …….

NAME IN BLOCK CAPITALS .....

Investigators signature ..... Date .....

NAME IN BLOCK CAPITALS .....

Appendix 6.3: Baseline Characteristics for each subject in addition to minor axis segment peak velocities (MA1, MA2) and long axis peak velocities (septum, lateral and inferior wall) during isovolumic contraction. All three long axis segments reach higher velocities than the minor axis segments measured.

Subject	Age	EF	Hypertensive	MA1 (cm/s)	MA2 (cm/s)	SEPTUM (cm/s)	LATERAL (cm/s)	INFERIOR (cm/s)
N1	66	>50%	no	5.93	6.04	7.29	8.51	7.02
N2	72	>50%	no	6.12	5.11	6.03	9.98	6.24
N3	67	>50%	yes	4.2	4.87	5.79	7.13	6.28
N4	69	>50%	no	6	6.07	8.25	10.52	6.13
N5	60	>50%	no	6.36	7.84	9.05	9.95	8.5
N6	66	>50%	yes	4.79	5.44	6.06	6.79	5.09
N7	74	>50%	no	6.3	5.1	7.87	11.3	4.58
N8	42	>50%	yes	6.03	4.22	4.32	7.77	4.96
N9	62	>50%	yes	3.54	4.01	5.82	8.09	5.62
N10	59	>50%	yes	5.19	8.98	9.99	10.05	8.97
N11	75	>50%	no	6.203	5.827	9.047	9.047	9.713
Average	**65**			**5.51**	**5.77**	**7.23**	**9.01**	**6.65**
±SD	**9**			**0.95**	**1.49**	**1.76**	**1.47**	**1.72**

Appendix 6.4: Minor axis segment peak velocities (MA1, MA2) and long axis segment peak velocities (septum, lateral and inferior wall) during ejection. Long axis segments reach higher velocities than the minor axis segments measured.

Subject	MA1 (cm/s)	MA2 (cm/s)	SEPTUM (cm/s)	LATERAL (cm/s)	INFERIOR (cm/s)
N1	4.65	6.28	6.57	7.82	6.66
N2	6.27	6.36	7.72	9.56	5.92
N3	4.35	4.4	5.15	5.98	6.24
N4	3.5	7.11	7.76	9.66	7.54
N5	6.01	6.77	6.11	6.95	6.35
N6	5.02	5.3	5.37	7.25	5.04
N7	6.33	4.71	7.51	8.75	7.57
N8	4.34	4.03	9.01	10.96	9.55
N9	4.02	5.11	7	9.26	6.66
N10	3.5	7.11	7.76	10.82	7.92
N11	6.56	6.54	7.27	9.22	7.54
Average	**4.8**	**5.72**	**7**	**8.7**	**6.95**
±SD	**1.15**	**1.12**	**1.14**	**1.59**	**1.2**

Appendix 6.5: Individual average differences in peak velocity of movement during IVC and ejection. Peak S1 during IVC is always similar to peak S2 during systolic ejection.

Subject	MA1 (cm/s)	MA2 (cm/s)	SEPTUM (cm/s)	LATERAL (cm/s)	INFERIOR (cm/s)
N1	1.28	-0.24	0.72	0.69	0.36
N2	-0.15	-1.25	-1.69	0.42	0.32
N3	-0.15	0.47	0.64	1.15	0.04
N4	2.5	-1.04	0.49	0.86	-1.41
N5	0.35	1.07	2.94	3	2.15
N6	-0.23	0.14	0.69	-0.46	0.05
N7	-0.03	0.39	0.36	2.55	-2.99
N8	1.69	0.19	-4.69	-3.19	-4.59
N9	-0.48	-1.1	-1.18	-1.17	-1.04
N10	1.69	1.87	2.23	-0.77	1.05
N11	-0.357	-0.713	1.777	-0.173	2.173
	0.65	**0.05**	**0.05**	**0.31**	**-0.61**
	1.04	**0.97**	**2.11**	**1.73**	**2.06**

Appendix 6.6: Individual time intervals from the R of the QRS complex to

- Peak aortic flow measured by applying continuous Doppler wave through the aorta.
- Peak S2 of the mid-anterioseptal (MA1) and mid- inferiolateral (MA2) segments.
- Peak S2 of the mitral annular septum, lateral and inferior walls.

The time of Peak aortic flow coincides with the time to minor axis peak S2 in both MA1 and MA2.

Subject	Peak Aortic Flow (ms)	MA1 (ms)	MA2 (ms)	Septum (ms)	Lateral wall (ms)	Inferior wall (ms)
N1	124±2	118±3	122±2	176±21	141±0	177±5
N2	137±0	128±2	138±2	155±10	162±30	210±12
N3	124±2	129±2	128±6	121±2	148±7	190±13
N4	128±6	124±5	129±1	126±6	192±16	173±8
N5	115±8	118±6	111±3	186±45	133±22	170±33
N6	103±3	102±11	117±12	150±10	153±10	150±5
N7	90±5	95±18	110±17	152±16	128±15	185±10
N8	125±5	123±6	120±5	177±23	172±10	180±18
N9	143±3	135±10	140±6	202±89	150±30	205±22
N10	128±8	127±8	125±5	130±15	145±22	138±8
N11	130±5	122±7	126±10	163±13	167±10	170±6
Average	**122**	**120**	**124**	**156**	**155**	**177**
±SD	**16**	**12**	**10**	**27**	**19**	**22**

Appendix 7.1: Study Protocol

A trial to compare the effects of nebivolol versus atenolol on various cardiovascular measurements including insulin sensitivity

Background

Retrospective studies of treated hypertensive cohorts have strongly implicated beta blocker therapy as increasing the risk of developing new-onset diabetes[1]. In 2002 the LIFE trial showed a significant 15% excess of new-onset diabetes over 5 years when the beta blocker, atenolol, was directly compared to the angiotensin receptor blocker, losartan[2].

Concerns over the adverse metabolic effects of traditional beta blockers (in particular impaired glucose tolerance and dyslipidaemia, notably reduced high density lipoprotein cholesterol and raised triglycerides) have led to the latest British Hypertension Society guidelines advising caution when using beta blockers, particularly in combination with thiazide-like diuretics, and have placed the 'B' of the ABCD treatment algorithm in brackets[3]. This to some extent conflicts with the latest hypertension guidance from the National Institute of Clinical Excellence that recommends the combination of a beta-blocker and thiazide-like diuretic in patients who are not at increased risk of developing diabetes[4].

Nebivolol is a new class of vasodilating beta blocker. It lowers blood pressure by selectively blocking beta-1 receptors and stimulating the production of nitric oxide in the lining of the blood vessel walls[5]. There is some evidence to suggest that, unlike traditional beta blockers, nebivolol does not impair insulin sensitivity. These studies have mostly been conducted in patients with pre-existing impaired glucose tolerance and have been single drug comparator studies[6,7]. There is little compelling evidence for the effect of nebivolol in patients with normal glucose tolerance[8,9]. To our knowledge, no study has looked at the effect on insulin sensitivity when nebivolol is used in combination with a thiazide-like diuretic. This is the drug combination that has raised the most concerns about increasing the risk of new onset diabetes.

In addition there is some evidence that beta blockers are not as effective at preventing stroke as other drugs. This may be due to reduced cerebral blood flow. It has been postulated that the vasodilatory action of nebivolol may improve cerebral blood flow and thus potentially lead to improved stroke protection.

Rationale

It is important to determine the effect of nebivolol in combination with a thiazide-like diuretic on insulin sensitivity in a large cohort of non-diabetic hypertensive patients. Of additional interest is to study the 24 hour blood pressure profile of nebivolol and to quantify its effects on lipid profiles, body

weight and wellbeing. It is also of interest to further explore cerebral blood flow as a possible mechanism for improved stroke protection.

Aim of the study

The aim of the study is to conduct a randomised trial to compare the insulin sensitivity, 24 hour blood pressure profile and tolerability of nebivolol + thiazide-like diuretic versus atenolol + thiazide-like diuretic.

Patients

Patients will be recruited from the Peart-Rose Cardiovascular Disease Prevention Clinic at St Mary's Hospital, London, UK. This clinic routinely sees approximately 80 patients with hypertension every week.

Inclusion criteria

1. Male or female of any age

2. Systolic blood pressure ≤ 160mmHg and Diastolic blood pressure ≤ 90mmHg on one antihypertensive drug

   OR Systolic blood pressure ≤ 150mmHg and Diastolic blood pressure ≤ 90mmHg on two antihypertensive drugs

   OR Systolic blood pressure ≥ 140 and ≤ 170 mmHg and Diastolic blood pressure ≥ 90 and ≤ 100 mmHg on no antihypertensive drugs.

Exclusion criteria

1. Compelling indication for treatment with a beta blocker.

2. Contraindication to, or previous history of, major intolerance to treatment with a beta blocker or thiazide-like diuretic.

3. Asthma.

4. Diabetes.

5. Concurrent treatment with verapamil and diltiazem.

6. Heart failure.

7. Bradycardia with heart rate less than 60 beats per minute.

8. AV conduction disturbances.

9. Atrial fibrillation.

10. Concomitant clinically important haematological, gastrointestinal, hepatic, renal, respiratory or other condition which, in the opinion of the investigator, will interfere with the treatment or the patient's ability to complete the study.

Design

This is a double-blind randomised cross over study comparing nebivolol + thiazide-like diuretic with atenolol + thiazide-like diuretic in 50 volunteer patients. The study involves a 4 week open label run-in phase on a low dose thiazide-like diuretic only. This is followed by two 8 week double-blind study treatment phases separated by a 4 week open label washout phase on a low dose thiazide-like diuretic only. Patients will be randomised double blind, to one of two treatment sequences. Either nebivolol-atenolol or atenolol-nebivolol. At the start of each study treatment phase patients will receive either nebivolol 2.5mg or atenolol 50mg in addition to the low dose thiazide-like diuretic. After 2 weeks of active treatment if the systolic blood pressure is ≥ 140mmHg or the diastolic blood pressure is ≥ 90mmHg the dose of nebivolol will be increased to 5mg and atenolol to 100mg. Investigations to assess insulin sensitivity, blood pressure and cerebral blood flow will be carried out at the end of each washout and study treatment phase (4 sets of investigations in total).

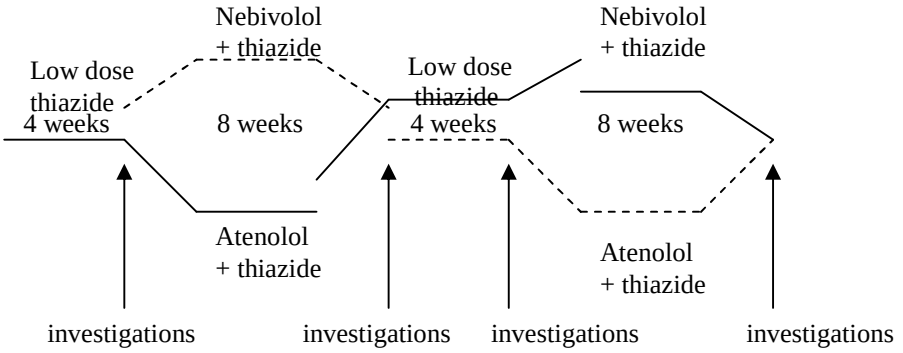

Treatment Schedule

1) Randomise patient
2) Treat with low dose thiazide-like diuretic only for 4 weeks
3) *Investigations 1*
4) Add nebivolol 2.5mg or atenolol 50mg to thiazide-like diuretic
5) After 2 weeks if systolic blood pressure ≥ 140mmHg or the diastolic blood pressure is ≥ 90mmHg increase dose of nebivolol to 5mg or atenolol to 100mg
6) Continue treatment for 6 weeks
7) *Investigations 2*
8) Continue on thiazide only for 4 weeks
9) *Investigations 3*
10) Add nebivolol 2.5mg or atenolol 50mg to thiazide-like diuretic
11) After 2 weeks if systolic blood pressure ≥ 140mmHg or the diastolic blood pressure is ≥ 90mmHg increase dose of nebivolol to 5mg or atenolol to 100mg

12) Continue treatment for 6 weeks

13) Investigations 4

14) END OF STUDY (24 weeks)

Sample size

The study has 80% power at the 5% level (α = 0.05) to detect a 20% difference in insulin sensitivity index if 46 patients are randomised to the trial. To allow for a modest 10% drop out rate, 50 patients will be randomised to the trial.

Primary End Point

Difference in insulin sensitivity index as defined by oral glucose tolerance test after 8 weeks intervention and at baseline. This endpoint will be compared between atenolol and nebivolol.

Secondary End Points

Differences in 24 hour blood pressure control, cholesterol, $HbA1_c$, body weight, FEV1, wellbeing and cerebral blood flow after 8 weeks intervention and at baseline. These endpoints will be compared between atenolol and nebivolol.

Investigations to be carried out after each washout and active treatment phase (4 in total)

1) Demographic information via administered questionnaire.

2) In men only: self administered questionnaire to assess erectile function.

3) Blood sample (total 60 mls includes 48 mls for oral glucose tolerance test):

   a. Fasting lipid profile (3mls)

   b. $HbA1_c$ (4mls)

   c. Plasma and serum stored at –70C for 5 years (5mls) on one occasion only.

4) Oral glucose tolerance test (OGTT). After a 12 hour fast, a cannula will be inserted into the subject's vein and 2 fasting blood samples will be taken 15 minutes apart, for insulin (6mls) and glucose (2mls). The subjects will then be given a drink containing 75g glucose in a volume of 300mls. Blood samples for the measurement of glucose and insulin will be drawn from the cannula at 30, 60, 90 and 120 minutes (total 48mls).

5) Three seated clinic blood pressure measurements using OMRON HEM 705 CP. The mean of the last two blood pressure measurements will be used in the analyses.

6) 24 hour ambulatory blood pressure monitoring.

7) Height and Weight.

8) Forced expiratory volume (FEV1).

9) Carotid dopplers to assess cerebral blood flow.

Statistical Analysis

Insulin sensitivity index (ISI) will be calculated used the standard method for oral glucose tolerance testing described in the paper by Matsuda and DeFronzo[10]. That is: ISI = 10,000 / √ [(fasting plasma glucose × fasting plasma insulin) × (mean OGTT glucose concentration × mean OGTT insulin concentration)]**One tailed student's paired t test will be used to compare the difference in insulin sensitivity index between baseline and the end of the treatment period for nebivolol and atenolol. One way analysis of variance will be used to detect differences between the two therapies. A p value < 0.05 will be considered statistically significant.**

References

[1] Opie LH, Schall R. Old antihypertensives and new diabetes. Journal of Hypertension 2004; 22:1453-1458

[2] Williams B, Poulter NR, Brown MJ, Davids M, McInnes GT, Potter JF etal. Guidelines for management of hypertension: report of the fourth working party of the British Hypertension Society, 2004-BHS IV. Journal Human Hypertension. 2004;18(3):139-85

[3] Dahlof B, Devereux RB, Kjeldsen SE, Julius S, Beevers G, de Faire U, Fyhrquist F et al. Cardiovascular morbidity and mortality in the Losartan Intervention for Endpoint reduction in hypertension study (LIFE): a randomised trial against atenolol. Lancet 2002;359:995-1003.

[4] National Institute for Clinical Excellence 2004. Hypertension: management of hypertension in adults in primary care. www.nice.org.uk/CG018NICEguideline accessed on 24th August 2004.

[5] Cockcroft J. Nebivolol: a review. Expert Opinion Pharmacotherapy 2004;5:893-899.

[6] Poirier L, Cleroux J. Nadeau A, Lacourciere Y. Effects of nebivolol and atenolol on insulin sensitivity and haemodynamics in hypertensive patients. Journal of Hypertension 2001; 19: 1429-1435

[7] Fogari R, Zoppi A, Lazzari P, Mugellini A, Lusardi P, Preti P, Van Nueten L, Vertommen C. Comparative effects of nebivolol and atenolol on blood pressure and insulin sensitivity in hypertensive subjets with type II diabetes. Journal of Human Hypertension 1997; 11:753-757

[8] Pesant Y, Marc-Aurele J, Bielmann P, Alaupovic P, Cartier P, Bichet D, Thibault G, Lupien PJ. Metabolic and antihypertensive effects of nebivolol and atenolol in normometabolic patients with mild-to-moderate hypertension. American Journal Therapeutics 1999; May;6(3):137-47.

[9] Rizos E, Bairaktari E, Kostoula A, Hasiotis G, Achimastos A, Ganotakis E, Elisaf M, Mikhailidis D. The combination of Nebivolol plus Pravastatin is associated with a more beneficial metabolic profile compared to that of atenolol plus pravastatin in hypertensive patients with dyslipidemia: a pilot study. Journal of Cardiovascular Pharmacological Therapy 2003; 8(2):127-34

[10] Matsuda M, DeFronzo R. Insulin sensitivity indices obtained from oral glucose tolerance testing. Diabetes Care 1999; 22(9) 1462-1470

***Appendix 7.2: PATIENT* CONSENT FORM**

AGREEMENT TO PARTICIPATE IN RESEARCH PROJECT

I, (name of subject)

……

Of (address)

……

……

……

Agree to take part in the research project:

A trial to compare the effects of nebivolol versus atenolol on various cardiovascular measurements including insulin sensitivity

I confirm that the nature and demands of the research have been explained to me and I understand and accept them. I understand that my GP will be informed that I am participating in this study and that my test results will be sent to my GP. I understand that my identity will not be disclosed and that any information collected will remain confidential. I agree that my clinical records may be examined by representatives of the sponsor and by people working on behalf of the sponsor, members of the Ethics Committee and by representatives of regulatory authorities. I understand that my consent is entirely voluntary and that I may withdraw from the research project if I find that I am unable to continue for any reason and this will not affect my medical care.

Signed: ……. Date…….

Investigator's Statement:

I have explained the nature, demands and foreseeable risks of the above research to the subject:

Signed: ……..
Date……

Print name: ……

Appendix 7.2: Individual Baseline characteristics for each volunteer involved in the study. Ethnic groups: 1=Caucasian, 2= Black of African decent, 3= South-Asian/Indian subcontinent, 4= mixed race, 5= other.

Subject ID	Sex	Drug Sequence	Age (yrs)	Ethnicity	Diastolic BP (mmHg)	Systolic BP (mmHg)
204	Male	Nebivolol-Atenolol	62	1	**86**	**141**
222	Female	Atenolol-Nebivolol	74	1	**74**	**132**
233	Male	Nebivolol-Atenolol	56	1	**90**	**143**
241	Male	Nebivolol-Atenolol	65	1	**91**	**135**
242	Female	Atenolol-Nebivolol	66	1	**76**	**127**
243	Male	Nebivolol-Atenolol	73	1	**77**	**123**
256	Female	Atenolol-Nebivolol	68	1	**84**	**131**
263	Female	Atenolol-Nebivolol	65	1	**78**	**127**
264	Female	Atenolol-Nebivolol	79	1	**78**	**108**
275	Female	Atenolol-Nebivolol	65	5	**90**	**157**
276	Female	Atenolol-Nebivolol	67	1	**75**	**135**
279	Male	Nebivolol-Atenolol	67	5	**76**	**123**
283	Male	Nebivolol-Atenolol	48	3	**96**	**134**
286	Female	Atenolol-Nebivolol	70	1	**71**	**150**
290	Male	Nebivolol-Atenolol	57	5	**82**	**121**
313	Female	Atenolol-Nebivolol	78	1	**81**	**156**
316	Female	Atenolol-Nebivolol	40	1	**92**	**131**
317	Male	Nebivolol-Atenolol	56	3	**93**	**143**
331	Male	Nebivolol-Atenolol	65	1	**86**	**122**
333	Male	Nebivolol-Atenolol	35	1	**75**	**131**
337	Male	Nebivolol-Atenolol	57	1	**82**	**125**
347	Female	Atenolol-Nebivolol	77	2	**71**	**126**
349	Female	Atenolol-Nebivolol	51	2	**82**	**110**
357	Female	Atenolol-Nebivolol	74	1	**78**	**128**
362	Male	Nebivolol-Atenolol	67	1	**88**	**144**
365	Male	Nebivolol-Atenolol	56	2	**89**	**128**
367	Female	Atenolol-Nebivolol	52	1	**90**	**154**
370	Female	Atenolol-Nebivolol	66	1	**78**	**118**
381	Female	Atenolol-Nebivolol	73	1	**80**	**143**
385	Female	Atenolol-Nebivolol	51	4	**94**	**123**
396	Male	Nebivolol-Atenolol	44	1	**92**	**138**
411	Female	Atenolol-Nebivolol	52	1	**91**	**133**
415	Male	Nebivolol-Atenolol	78	1	**85**	**123**
418	Male	Nebivolol-Atenolol	69	2	**111**	**167**
419	Female	Atenolol-Nebivolol	70	1	**82**	**125**
421	Female	Atenolol-Nebivolol	76	1	**88**	**131**
422	Male	Nebivolol-Atenolol	52	2	**96**	**148**
429	Female	Atenolol-Nebivolol	66	1	**74**	**123**
average			**63**		**84**	**133**
±SD			**11**		**8**	**13**

References

Alam M, Wardell J, Andersson E, Samad BA, Norlander R. Characteristics of mitral and tricuspid annular velocities determined by pulsed wave Doppler tissue imaging in healthy subjects. *J Am Soc Echocardiogr* 1999;**12**:618–28.

Allieve L. Allgenmeine Theorie uber die verandliche Bewegung des Wassers in Leitungen. Springer, Berlin.1909

Avolio AP. Ageing and wave reflection. *J of Hypertension*.;10:S83-S86.1992

Bergeron L. Etude des variations de régime dans les conduites d'eau. Solution graphique générale." ("Study of state changes in water-filled conduits. General graphical solution.") *Revue générale de l'Hydraulique* 1(1), 12-25 (in French) 1935

Binder TH. Three- Dimensional Echocardiography-Principles and Promises. *J Clin Basic Cardiol* ; 5:149-152. 2002

Bleasdale R.A, Parker K.H, Jones C.J.H. Chasing the wave. Unfashionable but important new concepts in arterial wave travel. *AJP-Heart and Circulatory Physiology* 284:H1879-H1855. 2003

Bom N, Hugenholtz PG, Kloster FE, Roelandt J, Popp RL, Pridie RB, Sahn DJ. Evaluation of structure recognition with the multiscan echocardiograph. A cooperative study in 580 patients. *Ultrasound Med Biol*;1:243-25.1974.

Borg AN, Harrison JL, Argyle RA, Ray SG. Left ventricle torsion in primary chronic mitral regurgitation. Heart 94:597-603. 2008

Brixius K, Bundkirchen A, Bolck B, Mehlorn U, Schwinger RH. Nebivolol, bucindolol, metoprolol and carvedilol are devoid of intrinsic sympathomimetic activity in human myocardium. *Br J Pharmacol*;133:1330-1338. 2001

Broeders MAW, Doevendans PA, Bekkers BC, et al. Nebivolol: a third generation beta-blocker that augments vascular nitric oxide release. *Circulation*;102:677-84.2000

Brutsaert DL, Sys SU. Relaxation and diastole of the heart. *Physiol Rev* 69:1228-1351. 1989

Burns AT, McDonald G, Thomas TD, Maclsaac A, Prior D. Doin' the twist: new tools for an old concept of myocardial function. *Heart* 94:978-983. 2008

Burt VL, Whelton P, Roccella EJ, Brown C, Cutler JA, Higgins M, Horan MJ, Labarthe D. Prevalence of hypertension in the adult US population. Results from the third national health and nutrition examination survey 1988-91. *Hypertension* 25:305-313. 1995

Celik T, Iyisoy A, Kursaklioglu H, Kardesoqlu E, Kilic S, Turham H, Yilmaz MI, Ozcan O, Yaman H, Isik E, Fici F. Comparative effects of nebivolol and metoprolol

oxidative stress, insulin resistance, plasma adiponectin and soluble P-selectin levels in hypertensive patients. *J Hypertens*;24:591-596. 2006

Chobanian AV, Bakris GL, Black HR, Cushman WC, Green LA, Izzo JL Jr, Jones DW, Materson BJ, Oparil S, Wright JT Jr, Roccella EJ; National Heart, Lung, and Blood Institute; National High Blood Pressure Education Program Coordinating Committee. Seventh report of the Joint National Committee on Prevention, Detection, Evaluation, and Treatment of High Blood Pressure .*Hypertension.* 2003 Dec;42(6):1206-52. 2003

Cockcroft JR, Chowienczyk PJ, Brett SE, Chen CP, Dupont AG, Van Nueten L, Wooding SJ, Ritter JM. Nebivolol vasodilates human forearm vasculature: evidence for an L-arginine/NO-dependent mechanism. *J Pharmacol Exp Ther*;274(3):1067-71.1995

Cruickshank J. Are we misunderstanding beta-blockers. *Intl J Cardiol***;** 120 (1):10-27.2007

Curtis SL, Zambanini A, Mayet J, McG Thom SA, Foale R, Parker KH, Hughes AD. Reduced systolic wave generation and increased peripheral wave reflection in chronic heart failure. *Am J Physiol Heart Circ Physiol.;*293(1):H557-62. 2007

Cushman WC Are there benefits to specific antihypertensive drug therapy?*Am J Hypertens*;16(11 Pt 2):31S-35S. 2003

Davis JS, Hassanzadeh S, Winitsky S, et al. The overall pattern of cardiac contraction depends on a spatial gradient of myosin regulatory light chain phosphorylation *Cell*;107:631-641.2001

Davies JE, Whinnett ZI, Francis DP, Willson K, Foale RA, Malik IS, Hughes AD, Mayet J. Use of simultaneous pressure and velocity measurements to estimate arterial wave speed at a single site in humans. *Am J Physiol Heart Circ Physiol* 290: H878–H885. 2006

Davies JE, Hadjiloizou N, Leibovich D, Malaweeera A, Alastruey-Arimon J, Whinnett ZI, Manisty CH, Francis DP, Aguado-Sierra, Foale R, Malik IS, Parker KH ,Mayet J, Hughes AD. Importance of the aortic reservoir in determining the shape of the arterial pressure waveform-the forgotten lessons of Frank. *Artery Research;* 1: 40-45. 2007

Davies JE, Parker KH, Francis DP, Hughes AD, Mayet J: What is the role of the aorta in determining coronary blood flow? *Heart***.** (12):1545-7.2008

De Simone G, Ganau R, Roman MJ, Devereux RB. Relation of left ventricular longitudinal and circumferential shortening to ejection fraction in the presence or in the absence of mild hypertension. *J Hypertens*;(9):1011-7.1997

Dolber PC, Bauman RP, Rembert JC, Greenfield jr.JC, Regional changes in myocyte structure in model of canine right atrial hypertrophy. *Am J Physiol*;267:H1279-H1287.1994

Duncan AM, Lim E, Clague J, Gibson DG, Henein MY. Comparison of segmental and global markers of dyssynchrony in predicting clinical response to cardiac resynchronization. *Eur Heart J*.;27(20):2426-32. 2006

Edler I. The diagnostic use of ultrasound in heart disease. *Acta Med Scand Suppl*;308:32. 1955

Edler I and Gustafson A. Ultrasonic cardiogram in mitral stenosis; preliminary communication. *Acta Med Scand.*;159(2):85-90. 1957

Edvardsen T, Gerber BL, Garot J, Bluemke DA, Lima JAC, Smiseth OA. Quantitative Assessment of Intrinsic Regional Myocardial Deformation by Doppler Strain Rate Echocardiography in Humans. Validation Against Three-Dimensional Tagged Magnetic Resonance Imaging. *Circulation*; 106:50-56. 2000

Edvardsen t, Helle-Valle T, Smiseth OA. Systolic Dysfunction in Heart Failure with Normal Ejection Fraction: Speckle-Tracking Echocardiograpohy.Progress in *Cardiovascular Diseases*;49,3:207-214. 2006

Einthoven W. Un nouveau galvanometre. *Arch Neerl Sc Ex Nat* ; 6:625. 1901

Emilsson K, Wandt B. The Relation between Left Ventricular ejection fraction and mitral annulus motion changes with age and heart size. *Clin Physiol*; 20:38-43. 2000

Euler L. Principia pro motu sanguinis per arterias derterminado: opera posthuma mathematica et physica anno 1884 detecta, ediderunt **Fruss PH** et **Fruss N**. Pertropoli Apud Eggers et Socios.

Feng J and Khir AW. Determination of wave intensity in flexible tubes using measured diameter and velocity. *Conf Proc IEEE Eng Med Biol Soc.*;985-8. 2007

Fitch RM, Vergona R, Sullivan ME, Wang Y-X. Nitric oxide synthase inhibition increases aortic stiffness measured by pulse wave velocity in rats, *Cardiovasc Res;*51:351-8.2001

Folkow B. Physiological aspects of primary hypertension *Physiological Reviews*; 62 (2): 347-504.1982

Fonseca CG, Dissanayake M, Doughty RN, Whalley GA, Gamble GD, Cowan BR, Occleshaw CJ, Young AA. Three-Dimensional Assessment of Left Ventricular Systolic Strain in Patients with Type 2 Diabetes Mellitus, Diastolic Dysfunction, and Normal Ejection Fraction *Am J Cardiol.;*94(11):1391-5. 2004

Frank O. Die Grundform des Arteriellen Pulses. *Erste AbhandlungMathematische Analyse Z Biol*;37:483-526.1899

Frank O. Der puls inden arterien. *Z Biol*;46:441-553.1905

Franklin SS, Jacobs MJ, Wong ND, L'Italien GJ, Lapuerta P. Predominance of isolated systolic hypertension among middle-aged and elderly US hypertensives: analysis

based on National Health and Nutrition Examination Survey (NHANES) III. *Hypertension*.; 37: 869–874.2001

Fujimoto S, Mizuno R, Saito Y, Nakamura S. Clinical application of wave intensity for the treatment of essential hypertension. *Heart Vessels*;19:19-22. 2004

Galderis M, Cattaneo, Mandillo S. Doppler Echocardiography and myocardial dyssynchrony: a practical update of old and new ultrasound technologies.*Cardiovascular Ultrasound*; 5: 28. 2007

Galiuto L, Ignone G, DeMaria AN. Contraction and relaxation velocities of the normal left ventricle using pulsedwave tissue doppler echocardiography. *Am J Cardiol* ;**81**:609–14.1998

Gibbon JH, Jr. Artificial maintenance of circulation during experimental occlusion of the pulmonary artery. *Arch Surg;*34*:*1105-1131.1937

Gleason TJ, Cragg AH, DeJong SC, Smith TP. Results of thermal balloon angioplasty in a canine model. *Radiology*; 173:148. 1989

Gosgnach W, Boixel C, Nevo N, Poiraud T, Michel JB. Nebivolol induces calcium-independent signaling in endothelial cells by a possible ß-adrenergic pathway. *J Cardiovasc Pharmacol* ;38:191-9.2001

Gleason TJ, Cragg AH, Smith TP, Landas SK, DeJong SC. Preliminary results of thermal balloon angioplasty in a canine model. *J Vasc Intervent Radiol* 1:121-126.1990

Greenbaum RA, Ho SY, Gibson DG, Becker AE, Anderson RH. Left Ventricular fibre architecture in man. *Br Heart J* 45:248-63.1981

Gress TW, Nieto FJ, Shahar E, Wofford MR, Brancati FL. For the Atherosclerosis Risk in Community Study. Hypertension and anti-hypertensive therapy as risk factors for type 2 diabetes mellitus. *N Engl J Med*; 342:905-912. 2000

G**ulati VK, Katz WE, Follansbee WP, Gorcsan J.** Mitral Annular Descent Velocity by Tissue Doppler Echocardiography as an index of Global Left Ventricular Function. *Am J Cardiol;*77:979-984.1996

Giugliano D, Acampora R, Marfella R et al. Metabolic and Cardiovascular effects of carvedilol and atenolol in non-insulin-dependent diabetes mellitus and hypertension. A randomized, controlled trial. *Ann Intern Med*;126:955-959.1997

Harada A, Okada T, Sugawara M, Niki K. Development of a Non-invasive measurement system of Wave Intensity. *IEEE Ultrasonics symposium*.2000

Hasenfuss G. Animal models of human cardiovascular disease, heart failure and hypertrophy.*Cardiovascular Res*;39:60-76.1998

Hawthorne EW. Instantaneous dimensional changes of the left ventricle in dogs. *Circ Res*;**9**:110–19.1961

Heger JJ, Weyman AE, Wann LS, Dillon JC, Feigenbaum H. Crosssectional echocardiography in acute myocardial infarction: detection and localization of regional left ventricular asynergy. *Circulation*;60:531-8. 1979

Henderson Y. The volume curve of the ventricles of the mammalian heart and the significance of this curve in respect to the mechanics of the heart beat and the filling of the ventricles. *Am J Physiol*. 16:325-367. 1906

Henein MY, Gibson DG. Abnormal subendocardialfunction in restrictive left ventricular disease. Br Heart J. sep;**72**(3):237-42. 1994

Henein MY, Das SK, O'Sullivan C, Kakkar VV, Gillbe CE, Gibson DG. Effect of acute alterations in afterload on left ventricular function in patients with combined coronary artery and peripheral vascular disease. *Heart.*;75(2):151-8. 1996

Henein MY, Gibson DG. Normal long axis function. *Heart* 81:111-113. 1999

Henien MY, Gibson DG. Long axis function in disease *Heart* 81:229-231. 1999

Helle-Valle T, Crosby J, Edvardsen Y, Lyseggen E, Amundsen BH, Smith HJ, Rosen BD, Lime JA, Torp H, Ihlen H, Smiseth OA. New Non-invasive Method for Assessment of Left Ventricle Rotation: Speckle Tracking Echocardiography. *Circulation*; 15:3149-315654. 2005

Helm RH, Byrne M, Helm PA, Daya SK, Osman NF, Tunin R, Halperin HR, Berger RD, Kass DA, Lardo AC. Three-dimensional mapping of optimal left ventricular pacing site for cardiac resynchronization. *Circulation*. 27;115(8):953-61.2007

Ho CY and Solomon SD. A Clinicians Guide to Tissue Doppler Imaging. *Circulation*: 113: e396-e398. 2006

Ignaro LJ. Experimental evidences of nitric oxide-dependent vasodilatory activity of nebivolol, a third generation beta-blocker *Blood Presure*;13 (1):2-16.2004

Ingels Jr. NB, Hansen DE, Daughters 2nd GT, Stinson EB, Alderman EL, Miller DC. Relation between longitudinal, circumferential, and oblique shortening and torsional deformation in the left ventricle of the transplanted human heart. *Circ Res* ;64:915-927.1989

Jacob S, Rett K, Henriksen EJ. Anti-hypertensive therapy and insulin sensitivity: do we have to redefine the role of beta-blocking agents? *Am J Hypertension*;11:1258-1265.1998

Janssens WJ, Van de Water A, Xhonneux R, Renemann RS, Van Nueten JM, Janssens PA. Nebivolol is devoid of intrinsic sympathomimetic activity.*Eur J Pharmacol*;159:89-95.1989

Jones CJH, Raposo L, Gibson DG. Functional importance of the long axis dynamics of the human left ventricle. *Br Heart J*;63:215-20.1990

Jones CJH, Parker KH, Hughes R, Sheridan DJ. Nonlinearity of human arterial pulse wave transmission. *J Biomech Eng*;114(1):10-4. 1992

Jones CJH, Sugawara M. "Wavefronts" in the aorta- implications for the mechanisms of left ventricular ejection and aortic valve closure. *Cardiovas Res* 27:1902-1905. 1993

Jones CJH, Sugawara M, Davis RH. Arterial wave intensity: physical meaning and physiological significance. 1994 travel. *Heart Vessels*;15:247-255. 2000

Jones CJH, Sugawara M, Kondoh Y, Uchida K, Parker KH. Compression and expansion wavefreont travel in the canine ascending aortic flow: wave intensity analysis. *Heart Vessels*;16:91-8.2002

JoukowskI N. Über den hydraulischen Stoss in Wasserleitungsröhen'(On the hydraulic hammer in water suply pipes). *Memoires de l'Aacademie Imperiale des Sciences de St-Petersbourg.* Series 8,9(5);1-71. 1900

Kakoki M, Hirata Y, Hagakawa H. Effects of vasodilatory beta-adrenoceptor antagonists on endothelium-derived nitric oxide release in rat kidney. *Hypertension*;33(II): 467-71.1999

Kapal E, Martini F, Wetterer E. Über die Zuverlassigkeit der bishrigen Bestimmungsartder Pulswellen geschwindigkeit. *Z Biol*;104:75-86.1951

Kapetanakis S, Kearney MT, Siva A, Gall N, Cooklin M, Monaghan MJ. Real-time three-dimensional echocardiography: a novel technique to quantify global left ventricular mechanical dyssynchrony. *Circulation*. 2005 Aug 16;112(7):992-1000. 2005

Karliner JS, Gault JH, Eckberg D, Mullins CB, Ross JR. Mean Velocity of fibre shortening- a simplified measure of left ventricular myocardial contractility. *Circulation* 44:323-33. 1971

Kendal MJ. Clinical Relevance of pharmacokinetic differences between beta-blockers. *Am J Cardiol*;80:15J-19J.1997

Khan NA, Hemmelgarn B, Herman RJ, Rabkin SW, McAlister FA, Bell CM, Touyz RM, Padwal R, Leiter LA, Mahon JL, Hill MD, Larochelle P, Feldman RD, Schiffrin EL, Campbell NR, Arnold MO, Moe G, Campbell TS, Milot A, Stone JA, Jones C, Ogilvie RI, Hamet P, Fodor G, Carruthers G, Burns KD, Ruzicka M, dechamplain J, Pylypchuk G, Petrella R, Boulanger JM, Trudeau L, Hegele RA, Woo V, McFarlane P, Vallée M, Howlett J, Katzmarzyk P, Tobe S, Lewanczuk RZ; Canadian Hypertension Education Program. The 2008 Canadian Hypertension Education Program recommendations for the management of hypertension: part 2 – therapy. *Can J Cardiol.;*24(6):465-75. 2008

Keith A. The functional anatomy of the heart. *BMJ* i:361-3. 1918

Koide M,Nagatsu M, Zile MR, Hamawaki M, Swindle MM, Keech G, DeFreyte G, Tagawa H, Cooper G 4th , Carabello BA. Premorbid determinants of left ventricular

dysfunction in a novel model gradually induced pressure overload in the adult canine. *Circulatio*n:95:1601-1610.1997

Khir AW, Henien MY, Koh T, Das SK, Parker KH, Gibson DG. Arterial waves in humans during peripheral vascular surgery. *Clin Sci (LON)*;101:749-57.2001

Khir AW, **Parker KH.** Measurements of wave speed and reflected waves in elastic tubes and bifurcations .*J Biomech*.;35 (6):775.2002

Khir AW, Zambanini A, Parker KH. Local and Regional wave speed in the aorta: effects of arterial occlusion. *Medical Engineering and Physics* 26: 23-29. 2004

Khir AW and Parker. Wave Intensity in the ascending aorta: effects of arterial occlusion. *Journal of Biomechanics* 38:647-655.2005

Koh, TW, Pepper JR, De Souza AC, and Parker KH. Analysis of wave reflections in the arterial system using wave intensity: a novel method for predicting the timing and amplitude of reflected waves. *Heart Vessels* 13: 103-113. 1998

Kolyva C, Spaan JA, Piek JJ, Siebes M. Windkesselness of coronary arteries hampers assessment of human coronary wave speed by single-point technique. *Am J Physiol Heart Circ Physiol*.;295(2):H482-90. 2008

Korteweg DJ. Über die Fortpflanzungesgechwindigkeit des Schalles in elastischen Rohern. *Annals of physics and Chemistry* (NS);5:525-527.1878

Lang RL, Mor-Avi V, Sugeng L, Niemann PS, Sahn DJ. Three-Dimensional Echocardiography: The Benefits of Additional Dimension. *Journal of the American College of Cardiolog:*;48(10): 2053-69. 2006

Laskey WK and Kussmaul WG. Arterial wave reflection in heart failure. *Circulation*. 75(4):711-22. 1987

Laurent S, Cockcroft J, Bortel LV, Boutouyrie P, Giannattasio C, Hayoz D, Pannier B, Vlachopoulos C, Wilkinson I, Struijker-Boudier H. Abridged version of the expert consensus document on arterial stiffness. *Artery Research*;1:2-12.2007

Lehman ED, Parker JR, Hopkins KD, Taylor MG, Gosling RG. Validation and reproducibility of pressure-corrected aortic distensibility measurements using pulse-wave-velocity Doppler ultrasound. *J Biomed Eng*;15:221-8.1993

Lewington S, Clarke R, Qizilbash N, Peto R, Collins R; Prospective Studies Collaboration. Age-specific relevance of usual blood pressure to vascular mortality: a meta-analysis of individual data for one-million adults in 61 prospective studies. *Lancet.* 14;360 (9349):1903-13. 2002

Lompre AM, Mercadier JJ, Wisnewsky, Bouveret P, Pantaloni C. Species and age-dependent changes in the relative amount of cardiac myosin isozymes in mammals. *Dev Biol;*84:286-290.1981

Lin LIK A concordance correlation coefficient to evaluate reproducibility. *Biometrics* 45:255-268.1989

Lindholm LH, Carlberg B, Samuelsson O. Should beta blockers remain first choice in the treatment of primary hypertension? A meta-analysis. *Lancet*; 4;366(9496):1545-53. BHS NICE.2005

Lindqvist P, Waldenstro A, Wikstro G, Kazzam E. Potential use of isovolumic contraction velocity in assessment of left ventricular contractility in man: A simultaneous pulsed Doppler tissue imaging and cardiac catheterization study. *Eur J Echocardiography* ;8: 252-258.2007

Lund-Johansen P, Omvik P, Nordrehaug. Long-term hemodynamic effects of antihypertensive treatment. *JE Clin Investig*;70 Suppl 1:S58-64. 1992

Maffei A, Vecchione C, Aretini A et al. Characterisation of nitric oxide release by nebivolol and its metabolites. *Am J Hyertens*;19:579-586.2006

Mason RP, Kalinowski L, Jacob RF, Jacoby AM, Malinsky T. Nebivolol reduces nitroxidative stress and restores nitric oxide bioavailability in endothelium of black Americans. *Circulation*;19:579-586. 2006

Mason RP, Kubant R, Jacob RF, Walter MF, Boychuk B, Malinski T. Effect of nebivolol on endothelial nitric oxide and peroxynitrite release in hypertensive animals: role of antioxidant activity. *J Cardiovasc Pharmacol*;48:862-869.2006

Manisty CH, Willson K, Wensel R, Whinnett ZI, Davies JE, Oldfield WL, Mayet J, Francis DP. Development of respiratory control instability in heart failure: a novel approach to dissect the pathophysiological mechanisms. J *Physiol*.;577:387-401. 2006

McDonald DA. The relation of the pulsatile pressure to flow in the arteries. *J Physiol*;127:533-52.1955b

McDonald IG. The shape and movements of the human left ventricle during systole. *Am J Cardiol*;26: 221-230.1970

McEniery CM, Schmitt M, Qasem A, Webb DJ, Avolio AP, Wilkinson IB, Cockcroft JR. Nebivolol increases arterial distensibility in vivo. *Hypertension*. ;44(3):305-10. 2004

Melbin J, Detweiler DK, Riffle RA, Noordergraaf A. Coherence of cardiac output with rate changes. *Am J Physiol*; 243(4):H499-504. 1982

Messerli FH. The LIFE study: the straw that should break the camels back. *Eur Heart J*;24:487-489. 2003

Moens AI. Die Pulskurve;Leiden.1878

Monaghn MJ.Role of real time 3D echocardiography in evaluating the left ventricle. *Heart* 92;131-136, 2006

Moore CC, Lugo-Olivieri CH, McVeigh ER, Zerhouni EA. Three-dimensional Systolic Strain Patterns in the Normal Human Left Ventricle: Characterisation with Tagged MR Imaging. *Radiology*;214: 453-4. 2000

Newton I. Principia Mathematica.1687

Nichols WW and Edwards DG. Arterial elastance and wave reflection augmentation of systolic blood pressure: deleterious effects and implications for therapy *J Cardiovasc Pharmacol Ther.;*6(1):5-21.2001

Niki K, Sugawara M, Uchida K, Tanaka R, Tanimoto K, Imamura H, Sakomura Y , Ishizuka N, Koyanagi H, Kasanuki H. A non-invasive method of measuring wave intensity, a new hemodynamic index: application to the carotid artery in patients with mitral regurgitation before and after surgery. *Heart Vessels* 14:263-271. 1999

Niki K, Sugawara M, Chang D, Harada A, Okada T, Tanaka R. Effect of sublingual nirtoglycerin on working conditions of the heart and arterial system: analysis using wave intensity analysis. *J Med Ultrasound* ;32:145-52.2005

Nikitin NP, Witte KKA, Thackray SDR, Clark AL, Cleland JGF. Longitudinal ventricular function: Normal values of atrioventricular annular and myocardial velocities measured with colour tissue Doppler imaging. Eur Heart J:23(abstract suppl). 57. 2002

Nikitin NP, Witte KKA. Application of Tissue Doppler Imaging in Cardiology. Cardiology;101:170-184.2004

Noble M. The Contribution of Blood Momentum to Left Ventricular Ejection in the Dog. *Circ. Res* 23:663-670. 1968

Notomi Y, Martin-Miklovic MG, Oryszak SJ, Shiota T, Deserranno D. Popovic ZB, Garcia MJ, Greenberg NL, Thomas JD. .Enhanced ventricular untwisting during exercise: a mechanistic manifestation of elastic recoil described by Doppler tissue imaging. *Circulation* 113:2524-2533; 2006

Ohte N, Narita H, Akita S, Kurokawa K, Hayano J, Sugawara M, Kimura G. The Mechanism of Emergence and Clinical Significance of Apically Directed Intraventricular Flow During Isovolumic Relaxation. *J Am Soc Echo*;15,7:715-723. 2002

Oki T; Tabata T; Mishiro Y; Yamada H; Abe M; Onose Y; Wakatsuki T; Iuchi A; Ito S. Pulsed tissue Doppler imaging of left ventricular systolic and diastolic wall motion velocities to evaluate differences between long and short axes in healthy subjects**.** J Am Soc of Echocardiography; 12 (5): 308-313. 1999

Oki T; Fukuda K; Tabata T; Mishiro Y; Yamada H; Abe M; Onose Y; Wakatsuki T; Iuchi A; Ito **S**Effect of an acute increase in afterload on left ventricular regional wall motion velocity in healthy subjects**.***Am Soc Echocardiography*;12(6):476-83. 1999

Onose Y, Oki T, Mishuno Y, *et al*. Influence of aging on systolic left ventricular wall motion velocities along the long and short axes in clinically normal patients determined by pulsed tissue Doppler imaging. *J Am Soc Echocardiogr*;**12**:921–6.1999

Opie LH, **Schall R**. Old antihypertensives and new diabetes *J Hypertens.*;22(8):1453-8.2004

O'Rourke MF. Pulsatile arterial haemodynamics in hypertension.*Aust N Z J Med*.;6 suppl 2:40-8. 1976

Pai RG and Gill KS. Amplitudes, Durations, and Timings of Apically Directed Left Ventricular Myocardial Velocities: 1. Their Normal Pattern and Coupling to Ventricular Filling and Ejection. *Am Soc Echocardiogrphy*. 105-111. 1998

Papaioannou TG, Vlachopoulous CV, Alexopoulos NA, Dima I, Pietri PG, Protogerou AD, Vyssoulis GG, Stefanadis CI. The Effect of Heart Rate on Wave Reflections May be Determined by the level of Aortic Stiffness: Clinical and Technical Implications. *Am J Hypertension*; 21:334-340. 2008

Parker K.H, Jones C.J.H. Forwards and Backwards Running waves in the arteries: Analysis Using the Method of Characteristics. *Journal of Biomechanical Engineering* 112: 322-326. 1990

Parker K.H, Jones C.J.H, Dawson J.R, Gibson D.G. What stops the flow of blood from the heart? *Heart Vessels* 4:241-245. 1988

Patterson SW, Piper H, Starling EH. The regulation of the heartbeat and the filling of the ventricles. *J Physiol* (London);48:465-513. 1914

Peiper HP. Catheter-tip instrument for measuring left ventricular diameter in closed-chest dogs. *J Appl Physiol*;21:1412-1416. 1966

Pettigrew JB. On the arrangement of the muscle fibres in the ventricles of the vertebrate heart, with physiological remarks. *Phil Trans Roy Soc*;154:445-500. 1865

Picard MH, Popp RL, Weyman AE. Assessment of Left Ventricular Function by Echcardiography: A technque of Evolution. *J Am Soc Echocardiogr* :21(1): 14-21. 2007

Popp RL, Wolfe SB, Hirata T, Feigenbaum H. Estimation of right and left ventricular size by ultrasound: a study of the echoes from the interventricular septum. *Am J Cardiol*;24:523-30. 1969

Przewlocka-Kosmala M, Kosmala W, Mazurek W. Left ventricular circumferential function in patients with essential hypertension. *J Hum Hypertens* 20:666-71. 2006

Price DJA, Wallbridge DR, Stewart MJ. Tissue Doppler imaging: current and potential clinical applications *Heart*;84 (Supp II) ii 1-ii18. 2000

Ramsey MW, Sugawara M. Arterial wave intensity and ventriculo-arterial interaction. *Heart Vessels* 12:128-134. 1997

Rankin JS, McHale PA, Arentzen CE, Ling D, Greenfield JC Jr, Anderson RW. The three-dimensional dynamic geometry of the left ventricle in the conscious dog. *Circulation Res*;39(3):304-13.1976

Reimann B., Gesammelte mathematische Werke un wissenschaftlicher Nachlass 1860

Remmington JW, O'Brien LJ. Construction of aortic flow pulse from pressure pulse. *Am J Physiol*;218,2:437-447.1970

Rosen BD, Gerber BL, Edvardsen T, Castillo E, Amado LC, Nasir K, Kraitchman DL, Osman NF, Bluemke DA, Lima JAC. Late systolic onset of regional LV relaxation demonstrated in three-dimensonal space by MRI tissue tagging. *Am J Physiol Heart Circ Physiol:* HI740-H1746. 2004

Rushmer RF, Crystal DK, Wagner C. The functional anatomy of ventricular contractioh. *Circ Res;* 1:162-70. 1952

Rushmer RF. Initial phase of ventricular systole: asynchronous contraction. *Am J Physiol*;184: 188-194. 1956

Rushmer RF Initial Ventricular Impulse. *Circulation*;XIX:268-283,1964.

Sandler H, Alderman E. Determination of left ventricular size and shape. *Circ Res*;34:1-8.1974

Savitzky A and Golay MJE. *Analytical Chemistry* 36:1627-1639, 1964

Scher AM .Studies of the electrical activity of the ventricles and the origin of the QRS complex. *Acta cardiologica* 50(6):429-65. 1995

Schnyder 0. "Über Druckstöße in Rohrleitungen." ("On water hammer in pipe lines.")*Wasserkraft und Wasserwirtschaft* 27(5), 49-54; 27(6), 64-70; 27(8), 96 in German . 1932

Schulman SP, Becker LC, Kass DA. et al. L-argenine therapy in acute myocardial infarction. *JAMA*;295:58-64. 2006

Senac JB, *Traité de la structure du coeur*, J Vincent, Paris. 1749

Sengaputa PP, Korinek J, Belohlavek M, Narula J, Vannan MA, Jahangir A, Khadheria BK. Left ventricular structure and function: basic science for cardiac imaging.*J Am Coll Cardio*l. Nov 21;48(10):1988-2001. Epub 2006 Oct 31. 2000

Sengupta PP, Khandheria BK, Korinek J, Wang J, Belohlavek M. Biphasic tissue Doppler waveforms during isovolumic phases are associated with asynchronous deformation of subendocardial and subepicardial layers *J Appl Physiol* ;99:1104-1111.2005

Sengaputa PP, Krishnamoorthy VK, Korinek J, Narula J, Vannan MA, **Lester SJ, Tajik TA, Steward JB, Khadheria BK, Belohlavek M,** Left ventricular form and function revisited: applied translational science to cardiovascular ultrasound imaging.. *J Am Soc Echocardiogr*.May;20(5):539-51.2007

Sherwin SJ, Franke V, Peiro J, Parker KH. One-dimensional modelling of a vascular network in space-time variables. *J Eng Math;*47:217-50.2003

Smiseth OA, Ihlen H. Strain rate imaging: Why do we need it? *J Am Coll Cardiol*; 42(9):1574-83.2003

Spencer MD and Greiss FC. Dynamics of Ventricular ejection. *Circulation Res;*10:274.1962

Staessen J, Wang J, Bianchi G, Birkenhäger W. Essential hypertension. *The* Lancet;367:9369,1629-1641.2003

Stensen N, *De musculis et glandulis observationum specimen, cum epistolis anatomica*, P le Grand, Amsterdam p. 90.1664

Stergiopulos N, Young DF, Rogge TR. Computer simulation of arterial flow with applications to arterial and aortic stenoses. *J of Biomech*;25:1477-1488.1992

Stergiopulos, N.; Westerhof, B.E.; Meister, J.-J.; Westerhof, N. The four-element Windkessel.Engineering in Medicine and Biology Society, 1996. *Proceedings of the 18th Annual International Conference of the IEEE* Volume 4, Issue 31:1715 - 1716 vol.4.1996

Streeter DD Jr, Spotnitz HM, Patel DJ, Ross J Jr. Sonnenblick EH: Fibre orientation in the canine left ventricle during diastole and systole. *Circ Res*:24: 339-347.1969

Sugawara M, Uchida K, Kondoh Y, Magosaki N, Niki K, Jones C.J.H, Sugimachi M, Sunagawa K. Aortic blood momentum-the more the better for the ejecting heart in vivo? *Cardiovascular Research* 33:433-446. 1997.

Sugawara M, Niki K, Furuhata H, Ohnishi S, Suzuki S. Relationship between the pressure and diameter of the carotid artery in humans. *Heart and Vessels*; 15:49-51.2000

Sugawara M, Niki K, Ohte N, Okada T, Harada A. Clinical usefulness of wave intensity analysis. *Med Biol Eng Comput* 47:197-206. 2009.

Sugeng L, Mor-Ai V, Weinert L, Niel J, Ebner C, Steringer-Mascherbauer R, Schmidt F, Galuschky C, Schummers G, Lang RM, Nesser HJ. Quantative Assessment of Left Ventricular Size and Function: Side-by-Side Comparison of Real-Time Three-Dimensional Echocardiography and Computed Tomography with Magnetic Resonance Reference. *Circulation*; 114: 654-661. 2006

Sun Y, Anderson TJ, Parker KH, Tyberg JV. Wave intensity analysis : a new approach to coronary hemodynamics. *J Appl Physiol* 89:1639-1644. 2000

Swillens A, Segers P. Assessment of arterial pressure wave reflection: Methodological considerations *Artery Research.*4 (2); 122-131.2008

Taber LA, Yang M, Podszus WW. Mechanics of ventricular torsion *J Biomech* ;29:745-752. 1996

Tanimoto M, Pia RG. Effect of isolated left atrial enlargement of mitral annular size and valve competence. *Am J Cardiol*:77:769-774. 1996

Tarnawski M, Cybulski G, Doorly D, Dumoulin C, Darrow R, Caro CG. Non-invasive determination of local wave speed and distensibility of the femoral artery by comb-excited Fourier velocity-encoded magnetic resonance imaging: measurements on athletic and non-athletic human subjects. *Heart Vessels*;9:194-201.1994

Taylor MG. Wave Transmission through an assembly of randomly branching elastic tubes. *Biophysical journal*;6:697-716. 1966

Teske AJ, De Boeck BW, Melman PG, Sieswerda GT, Doevendans PA, Cramer MJM. Echocardiographic quantification of Myocardial function using tissue deformation imaging, a guide to image acquisition and analysis using tissue Doppler and Speckle tracking. *Cardiovascular Ultrasound* ; 5: 27. 2007

Toda N. Vasodilating B-adrenoceptor blockers as cardiovascular therapeutics. *Pharmacol Ther*; 100:215-234. 2003

Tsutsui H, Spinale FG, Nagatsu M, **Schmid PG, Ishihara K, DeFreyte G, Cooper G 4th,Carabello BA.** Effects of chronic beta-adrenergic blockage on the left ventricular and cardiomyocyte abnormalities of chronic canine mitral regurgitation.*J Clin Invest*;93:2639-2648.1994

Urheim S, Edvardsen T, Torp H, Angelsen B, Smiseth OA: Myocardial Strain by Doppler Echocardiography: Validation of a New Method to Quantify Regional Myocardial Function. *Circulation* ; 102: 115-1164. 2000

Van Dalen BM, Kauer F, Soliman OLL, Vletter WB, Michels M, Ten Cate FJ, Geleijnse ML. Influence of the pattern of hypertrophy on left ventricular twist in hypertrophic cardiomyopathy. *Heart* 95:657-661.2009

Van Den Bos GC, Westerhof N, Elzinga G, Spikema P. Reflection in the systemic arterial system: effects of aortic and carotid occlusion. *Cardiovascular Research* 10:565-573.1976

Vogel M, Schmidt MR, Kristiansen SB, Cheung M, White PA, Sorensen K, et al. Validation of myocardial acceleration during isovolumic contraction as a novel non invasive index of right ventricular contractility: comparison with ventricular pressure-volume relations in an animal model. *Circulation*;105(14):1693-9.2002

Wang JJ, O'Brien AB, Shrive NG, Parker KH, Tyberg JV. Time-domain representation of ventricular-arterial coupling as a windkessel and wave system. . *Am J Physiol Heart Circ Physiol* 284:H1358-H1368. 2003

Wang JJ, Parker KH. Wave propagation in a model of the arterial circulation. J *Biomech*;37:457-470.2004

Westerhof N, Sipkema P, Van den Bos G.C, Elzinga G. Forward and Backward waves in the arterial system. *Cardiovascular Research* 6:648-656. 1972

Westerhof N, Bosman F, De Vries CJ, Noordergraaf A. Analogue studies of the human systemic arterial tree.*J of Biomech*;2:121-143.1969

Wetterer E. Wetterer, Die Wirkung der Herztatigkeit auf die Dynamik des Arteriensystems, *Verhandlungen der Duetchen Gesellschaft fur krieslaufforschungen* **22**, pp. 26–60.1956

Wiggers CJ. Studies on the Consecutive Phases of the Cardiac cycle.I The duration of the consecutive phases of the cardiac cycle and the criteria for their precise determination. *Am J Physiol* 56: 415–459. 13.1921

Wiggers CJ, Katz LN. The contour of the ventricular volume curves under different conditions. *Am J Physiol*;58:439-475.1921

Wiggers CJ. The interpretation of the intraventricular pressure curve on the basis of rapidly summated fractionate contractions. *Am J Physiol*; 80:1 –11. 1927

Wilkinson I, McEniery C. Arterial Stiffness, Endothelial unction and Novel Pharmacological Approaches. *Clinical and Experimental Phar and Phys:*31;795-799. 2004

Wilkinson I, McEniery C, Cockcroft J.Atenolol and cardiovascular risk: an issue close to the heart**.** *The Lancet*;367: 9511:627-629. 2006

Williams B, Lacy PS, Thom SM, Cruickshank K, Stanton A, Collier D, Hughes AD, Thurston H, O'Rourke M; CAFE Investigators; Anglo-Scandinavian Cardiac Outcomes Trial Investigators; CAFE Steering Committee and Writing Committee. Differential impact of blood pressure-lowering drugs on central aortic pressure and clinical outcomes: principal results of the Conduit Artery Function Evaluation (CAFE) study. Circulation. 2006 Mar 7;113(9):1213-25.2006

Winslow JB. Observations sur les fibres du coeur et sur ses valvules. Histoire (et Mémoires) de l'Academie Royale des Sciences (Paris) pt 2:151-6. 1711 (1714)

Woods RH. A few applications of a physical theorem to membranes in the human body in a state of tension. *J Anat Physiol*;26:362-370.1892

Womersley JR. Method for calculation of velocity, rate of flow and viscous drag in arteries when the pressure gradient is known. *J Physiol*,127(3):553-63.1955

Yanada A, Ohte N, Narita H, Akita S, Takada N, Goto T, Mukai S, Hayano J, Kimura G.)The role of apically directed intraventricular isovolumic relaxation flow in

speeding early diastolic left ventricular filling.*J Am Soc Echocardiogr*;16(12):1226-30.2003

Yang L ; Qiu Q ; Zhang HZ; Xia JX ; Characteristics of myocardial postsystolic shortening in patients with coronary artery disease assessed by strain rate imaging . *Chinese Medical Journal*;120(21):1894-1897.2007

Yoshidu T, Ohte N, Narita H, Sakata S, Wakami K, Asada K, Miyabe H, Saeki T, Kimura G. Lack of inertia force of late systolic aortic flow is a cause of left ventricular isolated diastolic dysfunction in patients with coronary artery disease. *J Am Col Cardio*;48,5:983-91.2006

Young T. On the functions of the heart and arteries: the Croonian Lecture. *Philosophical Transactions of Royal Society* **99**, pp. 1–31.1809

Yu CM, Fung JW, Zhang Q, et al. Tissue Doppler imaging is superior to strain rate imaging and postsystolic shortening on the prediction of reverse remodelling in both ischemic and nonischemic heart failure after cardiac resynchronization therapy. *Circulation* 73:110:66. 2004

Yu CM, Zhang Q, Fung JW, Chan HC, Chan YS, Yip GW, Kong SL, Lin H, Zhang Y, Sanderson JE. A novel tool to assess systolic asynchrony and identify responders of cardiac resynchronization therapy by tissue synchronization imaging. *J Am Coll Cardiol*. 1;45(5):677-84.2005

Yu CM, Sanderson JE, Marwick TH, Oh JK. Tissue Doppler Imaging: A New Prognosticator for Cardiovascular Diseases. *J Am Col of Cardio*. 49.19. 1903-14.2007

Yusuf S, Peto R, Lewis J, Collins R, Sleight P. Beta-blockade during and after myocardial infarction: an overview of the randomized trials. *Prog Cardiovasc Dis*; XVII(5):335-71. 1985

Zambanini A, Cunningham SL, Parker KH, Khir AW, Thom SAM, Hughes AD. Wave-energy patterns in the carotid, brachial and radial arteries: a non-invasive approach to using wave-intensity analysis. *Am J Phisiol;289*: H270-H276.2005

Bibliography

Allender S, Scarborough P, Peto V and Rayner M. European Cardiovascular Disease Statistics 2008, Edition 3. 2008

Harvey W, An anatomical disquisition on the motion of the heart and blood in animals (1628). In: F.A. Willis and T.E. Keys, Editors, *Cardiac classics*, Henry Kimpton, London p17–19.1941

Khir AW. The Haemodynamic Effects of Aortic Clamping .PhD thesis, University of London, London: 1999

Latham RD. Pulse propagation in the systemic arterial tree. In Westerhof N, Gross DR. (Eds) *Vascular Dynamics*. Plenum press. London (Chapter 4) .1998

McDonald DA. Blood flow in arteries. *Monog.Physiol.Soc*. London: Edward Arnold: Baltimore:Williams and Wilkins. 1982

O'Rourke MF and **Nichols WW.** McDonald's Blood Flow in Arteries-Theoretical , Experimental and Clinical Principles. 4th ED. London, United Kingdom: Arnold;1998

Page CP, Curtis**, M. Sugger, M. Walker, M. Hoffman, B** Integrated pharmacology. 2nd Edition Mosby, London. 1997

Websites

British Heart Foundation . www.heartstats.org

NICE clinical guidelines 34. Hypertension management of hypertension in adults in primary care. www.nice.org.uk , ISBN 1-84629-222-0. 2006

.